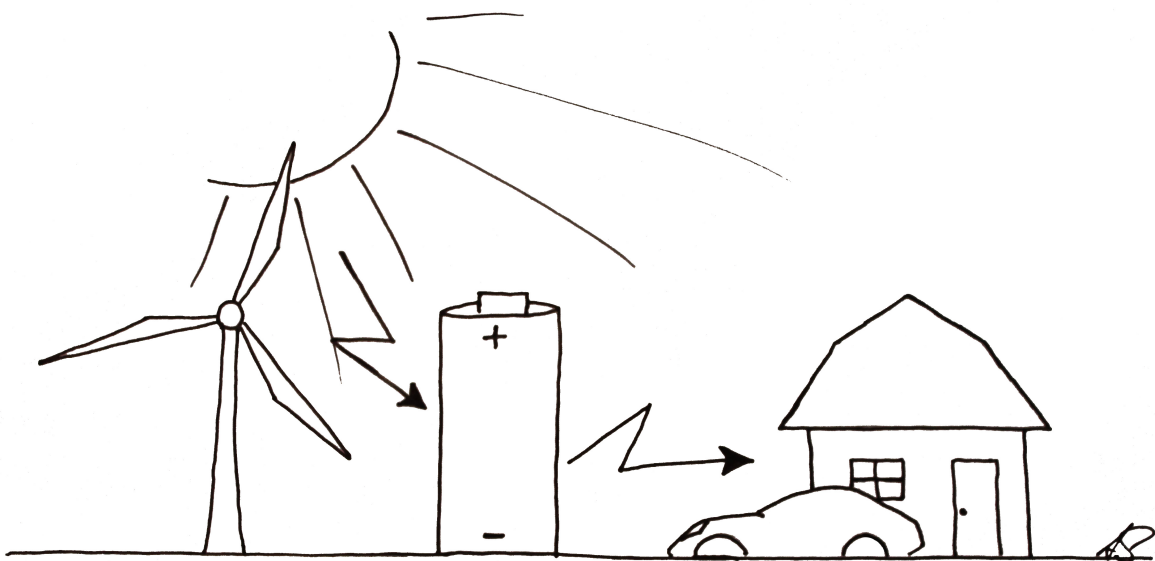


**Investigation of the reaction mechanisms during Li uptake and release of spinel oxide nanoparticles  $M^{II}M^{III}FeO_4$  ( $M^{II} = Mn, Mg, Co, Ni$ ;  $M^{III} = Mn, Fe$ ) for application as anode materials in Lithium ion batteries**



A thesis submitted to the

**Faculty of Mathematics and Natural Sciences of the  
Christian-Albrechts-Universität zu Kiel**

for the degree of

**Doctor rer. nat.**

by

**Stefan Permien**

Kiel, 2016



Cover picture by Annika Sellin:

Electro vehicles and large-scale energy storage systems to save the energy of renewables are the applications of the future for the next-generation of Lithium ion batteries.

Referent:.....Prof. Wolfgang Bensch  
Koreferent:.....Prof. Christian Näther  
Tag der mündlichen Prüfung:.....05.10.2016  
Zum Druck genehmigt:.....05.10.2016

Prof. Dr. Natascha Oppelt, Dekanin

## Abstract

Lithium ion batteries (LIBs) have achieved great success as portable power supply for consumer electronic devices. New applications for LIBs in the near future are electric vehicles and stationary energy storage systems. Therefore, higher energy density and simultaneously cost reduction is needed. Materials should also be earth abundant and environmental friendly. Actually commercialized materials exhibit a capacity limit due to the fact that just a limited number of  $\text{Li}^+$  ions can be intercalated/deintercalated per formula unit. Alternative materials were investigated during the past decades. Conversion materials exhibit 2 - 5 times larger capacities because more Li per formula unit can be stored. Intensively investigated materials are e.g. spinel oxides  $\text{M}^{\text{II}}\text{M}^{\text{III}}_2\text{O}_4$  ( $\text{M}^{\text{II}} = \text{Co, Cu, Mn, Mg, Co, Ni}$ ;  $\text{M}^{\text{III}} = \text{Mn, Fe, Co}$ ). The reactions occurring during electrochemical cycling are complex affecting both the crystal structure and the electronic properties, which were not investigated in detail.

In the thesis the synthesis of several spinel oxide nanoparticles  $\text{MnFe}_2\text{O}_4$ ,  $\text{MgFe}_2\text{O}_4$ ,  $\text{CoFe}_2\text{O}_4$ ,  $\text{CoMnFeO}_4$  and  $\text{NiMnFeO}_4$  are reported. In addition, composites were synthesized including  $\text{NiFe}_2\text{O}_4$  interconnected with a network made of carbon nanotubes and  $\text{CoFe}_2\text{O}_4$  deposited on reduced graphite oxide. The materials were intensively characterized and processed as electrodes for testing their electrochemical performance applying galvanostatic cycling and cyclic voltammetry (CV).

The focus of this thesis is the investigation of the reaction mechanisms occurring during Li uptake and release of this new class of anode materials. Different methods including *ex situ* and *operando* X-ray diffraction and X-ray absorption spectroscopy, as well as solid state nuclear magnetic resonance spectroscopy, transmission electron microscopy and Mössbauer spectroscopy were used. For the first time lognormal size distributions and anisotropic crystallite sizes could be determined from X-ray powder patterns to investigate the development of the particle morphology and the particle size during the chemical reactions. The results of the combined methods allow formulation of detailed reaction mechanisms for Li uptake and release during the first and subsequent cycles. The spinel oxides are transformed into an intermediate NaCl-like structure after uptake of about 2 Li per formula unit. Further Li uptake leads to the successive formation of amorphous metallic nanoparticles embedded in a  $\text{Li}_2\text{O}$  matrix. After the charge process the spinel structure is not recovered. The metallic nanoparticles are oxidized to bivalent and/or trivalent cations. Further cycling and investigation of samples cycled 2-10 times showed stable redox reactions over many cycles. Additional small improvements of cycling stability were realized, e.g. by the substitution of hazardous PVDF binder by environmental-friendly and water-soluble alternatives.

The last part of the thesis reports results about the synthesis and characterization of  $\text{Fe}_3\text{S}_4$  nanoparticles and the performance of the material as anode material for sodium ion batteries. The  $\text{Fe}_3\text{S}_4$  nanoparticles exhibit good cycling stability accompanied by very large capacities. It seems that the uptake of Na is accompanied by formation of mackinawite as intermediate phase.

## Kurzzusammenfassung

Lithium-Ionen-Batterien (LIBs) werden mit großem Erfolg als tragbare Stromversorgungen für elektronische Geräte genutzt. Neue Anwendungen in naher Zukunft stellen Elektrofahrzeuge und stationäre Energiespeichersysteme dar. Für deren breite Anwendung ist eine Erhöhung der Energiedichte bei gleichzeitiger Reduktion der Kosten erforderlich. Zudem sollten die Materialien in großen Mengen verfügbar und umweltfreundlich sein. Aktuell kommerzialisierte Materialien weisen eine natürliche Kapazitätsgrenze auf, da nur eine begrenzte Anzahl von  $\text{Li}^+$ -Ionen pro Formeleinheit aufgenommen werden kann. Materialien, die auf einer „Konversionsreaktion“ basieren, zeigen 2 - 5 Mal höhere Kapazitäten, da mehr  $\text{Li}^+$  pro Formeleinheit gespeichert werden kann. Interessante und intensiv untersuchte Konversionsmaterialien sind z.B. die Spinelloxide  $\text{M}^{\text{II}}\text{M}^{\text{III}}_2\text{O}_4$  ( $\text{M}^{\text{II}} = \text{Co, Cu, Mn, Mg, Co, Ni}$ ;  $\text{M}^{\text{III}} = \text{Mn, Fe, Co}$ ). Die Reaktionen, die beim elektrochemischen Entladen und Laden auftreten, sind von komplexen Reaktionen begleitet, die sowohl die Kristallstruktur als auch die elektronischen Eigenschaften beeinflussen, was bisher nur ungenügend untersucht wurde.

In der Doktorarbeit wird über die Synthese verschiedener Spinell-Nanopartikel mit den Zusammensetzungen  $\text{MnFe}_2\text{O}_4$ ,  $\text{MgFe}_2\text{O}_4$ ,  $\text{CoFe}_2\text{O}_4$ ,  $\text{CoMnFeO}_4$  und  $\text{NiMnFeO}_4$  berichtet. Außerdem wurden Komposite aus  $\text{NiFe}_2\text{O}_4$  mit Kohlenstoff-Nanoröhren hergestellt und  $\text{CoFe}_2\text{O}_4$  auf reduziertem Graphit-Oxid deponiert. Die Materialien wurden umfassend charakterisiert und anschließend zu Elektroden weiterverarbeitet, um die elektrochemischen Eigenschaften mit galvanostatischem Entladen/Laden und Cyclovoltammetrie zu untersuchen.

Der Schwerpunkt dieser Arbeit liegt auf der Untersuchung der Reaktionsmechanismen, die während der Aufnahme und Abgabe von Li ablaufen. Dafür wurden *ex situ* und *operando* Röntgenbeugung und Röntgenabsorptionsspektroskopie sowie Festkörper-Kernresonanzspektroskopie, Transmissionselektronenmikroskopie und Mössbauer-Spektroskopie eingesetzt. Außerdem konnten erstmalig die Lognormal Größenverteilungen und die anisotropen Kristallitgrößen aus Röntgenbeugungsdaten extrahiert werden, um die Entwicklung der Partikelmorphologie und der Teilchengrößen während der chemischen Reaktionen zu verfolgen. Die Ergebnisse der verschiedenen analytischen Methoden ermöglichten es, detaillierte Reaktionsmechanismen für die Aufnahme und Freisetzung von Li zu formulieren. Die Spinelloxide werden nach Aufnahme von ca. 2 Li pro Formeleinheit in eine intermediäre Kochsalz-Struktur umgewandelt. Bei weiterer Erhöhung des Li-Gehaltes tritt die sukzessive Bildung von amorphen, metallischen Nanopartikeln ein, welche in einer  $\text{Li}_2\text{O}$  Matrix eingebettet sind. Nach dem Ladevorgang wird die Spinell-Struktur nicht wieder zurückgebildet, stattdessen werden die metallischen Nanopartikel zu zwei- und/oder

dreiwertigen Kationen oxidiert. Untersuchungen nach 2-10 Zyklen ergaben stabile Redox-Reaktionen. Zudem wurden weitere kleine Verbesserungen der Zyklenstabilität realisiert, z.B. durch die Substitution von gesundheitsschädlichem PVDF-Binder durch umweltfreundliche und wasserlösliche Alternativen.

Der letzte Teil dieser Arbeit beschäftigt sich mit der Synthese und Charakterisierung von  $\text{Fe}_3\text{S}_4$  Nanopartikeln und deren Eigenschaften als Anodenmaterial für Natrium-Ionen-Batterien.  $\text{Fe}_3\text{S}_4$  Nanopartikeln weisen eine gute Zyklenstabilität auf verbunden mit sehr großen Kapazitäten. Die Untersuchungen weisen darauf hin, dass Mackinawit als intermediäre Phase auftritt.

## Table of Contents

---

### Table of Contents

<b>1</b>	<b>Introduction</b>	<b>1</b>
1.1	Motivation	1
1.2	Scientific Background	4
1.2.1	Lithium ion batteries (LIBs)	4
1.2.2	Cathodes (commercial)	5
1.2.3	Anodes (commercial)	5
1.2.4	Conversion reaction materials	7
1.2.5	Oxides with spinel structure as anode material in LIBs	8
1.2.6	Why investigation of the reaction mechanisms?	11
1.2.7	Sodium - an alternative to Lithium	14
<b>2</b>	<b>Experimental Section</b>	<b>15</b>
2.1	Investigation of the electrochemical performance	15
2.1.1	Preparation of the electrodes	15
2.1.2	Swagelock test cell	16
2.2	Investigations with synchrotron radiation	17
2.2.1	Synchrotron light	17
2.2.2	The <i>in situ</i> cell	17
2.2.3	X-Ray absorption spectroscopy (XAS)	18
2.3	Rietveld refinement	21
2.4	Transmission electron microscopy	23
2.5	Mössbauer spectroscopy	24
2.6	Solid state $^7\text{Li}$ NMR spectroscopy	25
2.7	Standard methods for sample characterization	26
<b>3</b>	<b>Publications</b>	<b>27</b>
3.1	Electrochemical insertion of Li into nanocrystalline $\text{MnFe}_2\text{O}_4$ : A study of the reaction mechanism	27

## Table of Contents

---

3.2	Is there a universal reaction mechanism of Li insertion into oxidic spinels: a case study using $\text{MgFe}_2\text{O}_4$ .....	42
3.3	What happens structurally and electronically during the Li conversion reaction of $\text{CoFe}_2\text{O}_4$ nanoparticles: An <i>operando</i> XRD and XAS investigation .....	56
3.4	Elucidation of the Conversion Reaction of $\text{CoMnFeO}_4$ Nanoparticles in Lithium Ion Battery Anode via Operando Studies.....	68
3.5	The role of reduced graphite oxide in transition metal oxide nanocomposites used as anode material: A case study on $\text{CoFe}_2\text{O}_4/\text{rGO}$ .....	82
<b>4</b>	<b>Further Projects (will be submitted soon) .....</b>	<b>92</b>
4.1	The Lithiation and Delithiation Process of Nanocomposite Materials Consisting of $\text{NiFe}_2\text{O}_4$ Nanoparticles and Carbon Nanotubes .....	92
4.1.1	Short Introduction .....	92
4.1.2	Synthesis of $\text{NiFe}_2\text{O}_4$ and $\text{NiFe}_2\text{O}_4/\text{CNT}$ .....	93
4.1.3	Characterization of as-prepared $\text{NiFe}_2\text{O}_4/\text{CNT}$ and $\text{NiFe}_2\text{O}_4$ .....	93
4.1.4	Electrochemical performance.....	96
4.1.5	<i>Operando</i> XRD and XAS .....	97
4.1.6	$^7\text{Li}$ MAS NMR .....	102
4.1.7	<i>Ex situ</i> XAS .....	103
4.1.8	Conclusion of chapter 4.1 .....	104
4.2	The exceptional reaction mechanism during Li uptake into and release out of $\text{Ni}^{\text{II}}\text{Fe}^{\text{III}}\text{Mn}^{\text{III}}\text{O}_4$ nanoparticles .....	105
4.2.1	Short introduction .....	105
4.2.2	Synthesis of $\text{NiFeMnO}_4$ Nanoparticles .....	106
4.2.3	Characterization of the as-prepared product.....	106
4.2.4	Electrochemical performance.....	108
4.2.5	<i>Operando</i> XAS .....	109
4.2.6	<i>Ex situ</i> XAS .....	111
4.2.7	<i>Ex situ</i> Li MAS NMR.....	113
4.2.8	<i>Operando</i> XRD.....	113



## Table of Contents

---

4.2.9	TEM investigations after uptake of 2 Li / NiMnFeO <sub>4</sub> .....	116
4.2.10	Conclusion of chapter 4.2 .....	116
4.3	Fe <sub>3</sub> S <sub>4</sub> nanoparticles - a new anode material for sodium ion batteries .....	118
4.3.1	Short introduction .....	118
4.3.2	Synthesis of Greigite (Fe <sub>3</sub> S <sub>4</sub> ) nanoparticles .....	119
4.3.3	Characterization of the Greigite (Fe <sub>3</sub> S <sub>4</sub> ) nanoparticles.....	119
4.3.4	Electrochemical properties of Fe <sub>3</sub> S <sub>4</sub> nanoparticles .....	122
4.3.5	Elucidation of the reaction mechanism .....	123
4.3.6	Conclusion of chapter 4.3 .....	126
<b>5</b>	<b>Conclusions and Outlook.....</b>	<b>128</b>
<b>6</b>	<b>References.....</b>	<b>130</b>
<b>7</b>	<b>Appendix.....</b>	<b>139</b>
7.1	Reports for beamtime at synchrotron sources .....	139
7.2	Acknowledgements .....	148
7.3	List of Publications .....	149
7.4	Curriculum Vitae.....	150
7.5	Erklärung.....	151

## 1 Introduction

### 1.1 Motivation

Fossil fuels make our life very comfortable, because they enable cheap and fast travelling by car, bus and plane. Additionally heating of houses, output of industrial plants and generation of electricity is also based on fossil fuels. The worldwide total primary energy supply doubled from 1972 to 2012 (Figure 1 left). Coal, oil and natural gas represent the main part (81.7 %). Whereas renewable energies like hydro, geothermal, wind and solar energy contribute just a small part of the energy supply (~3.5 %). Fossil fuels exhibit the disadvantage that world occurrence of coal, oil and natural gas is limited. It is assumed that within the next centuries these non-renewable energy reserves will be consumed. Another drawback is the undesired environmental long-term effect due to CO<sub>2</sub> emission from large scale burning of fossil fuels.<sup>[1]</sup> For measures against the climate change, emission of greenhouse gases like CO<sub>2</sub> should be minimized. Nuclear power plants produce energy without emission of global warming gases. Nevertheless, the storage of atomic waste is worldwide still an unsolved problem. Nuclear accidents in Tschernobyl and Fukushima showed the limited controllability of this technology. An element of risk always remains and can be only suppressed via nuclear phase-out. Worldwide, specifically in third world countries greenhouse gases are produced for heating, production of electricity and cooking. In industrial countries like, e.g. Germany, CO<sub>2</sub> is mainly emitted by power industry (~45 %) and the traffic sector (~20 %), which is illustrated in Figure 1 right. One strategy reducing emission of CO<sub>2</sub> is an enlargement of the energy production based on renewable sources such as sunlight, wind, tidal energy and geothermal heat. In the last years production of renewable energies was significantly increased. In Germany the ratio of renewable energies was more than quadrupled from 2000 (2.5 %) to 2014 (11.3 %).<sup>[2]</sup>

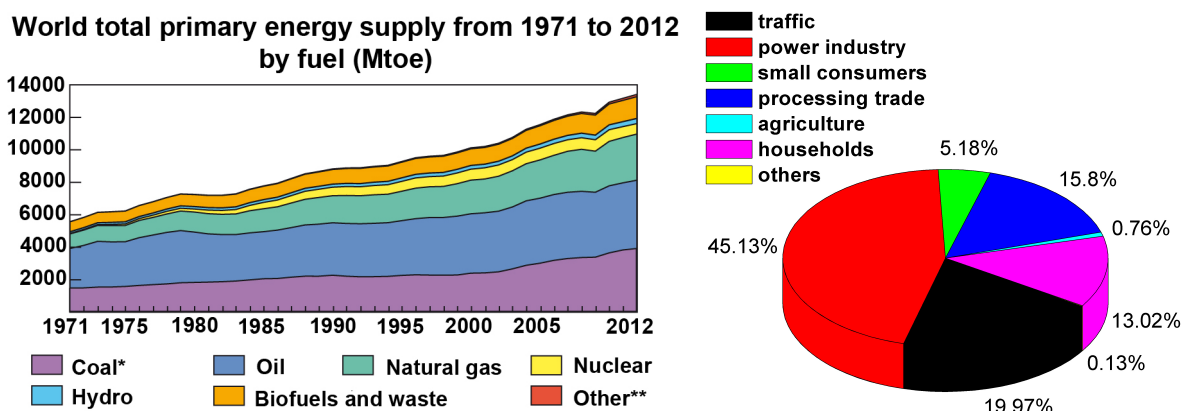


**Figure 1: World total energy supply showing contributions of different energy sources (left). Peat and oil shale are aggregated as “coal” and “others” include wind, solar and geothermal (toe = tonne of oil equivalent).<sup>[3]</sup> CO<sub>2</sub> emission in Germany (2013) in percentages (right, data from Bundesministerium for economics and energy).**

But production of electricity from renewable sources has a pronounced drawback: they are based on forces of nature, which are variable in time and strength/intensity. Figure 2 presents consumption and production of electricity from renewable sources in Germany at two days in the last year: supply of electricity was between 10 and almost 30 %. In summer overall less energy is needed but solar power plants supply more energy than in winter times (Figure 2, left). During winter months more energy is needed and solar power plants produce less energy. However, the main problem is a constant supply on a daily basis. Much energy is needed from 6 am to 8 pm, which cannot be sufficiently supplied by renewable energy sources (Figure 2, right). The variable production of wind and solar power plants have to be balanced in the future for substitution of all conventional power plants by renewable energy sources.<sup>[4]</sup> Therefore, it is important to identify an efficient method for large-scale energy storage for private households as well as supplier for electric energy.<sup>[5]</sup>

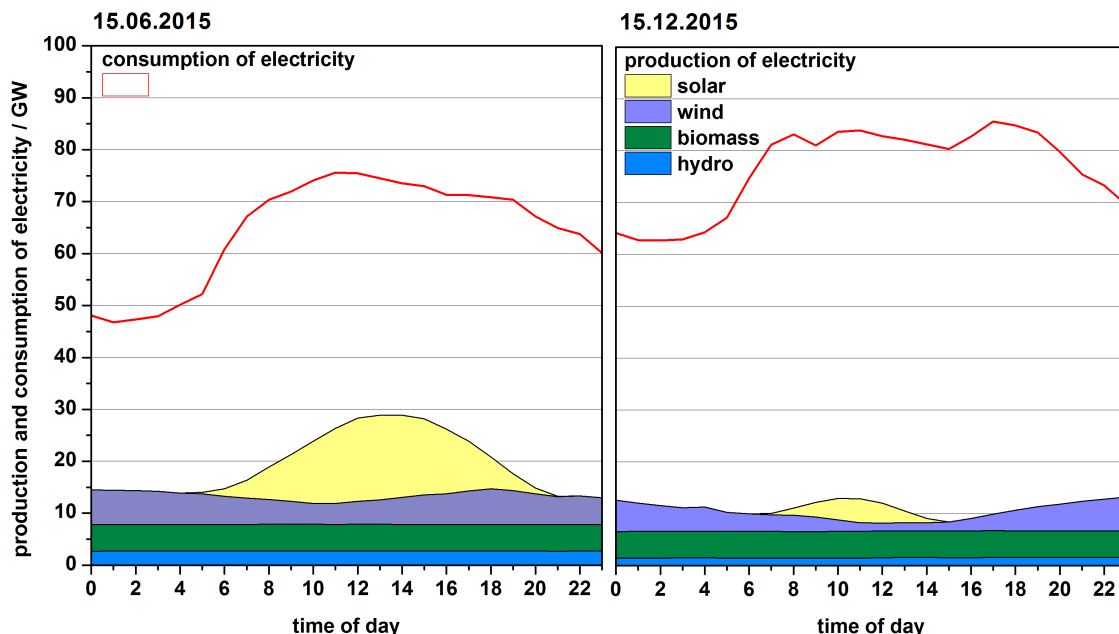


**Figure 2: Production and consumption of electricity produced by renewable energies in Germany showcase for two days 15.06.2015 (left) and 15.12.2015.<sup>[6]</sup>**

As mentioned above about one-fifth of CO<sub>2</sub> gas is emitted by the traffic sector. If Hybrid and full electric vehicles (HEVs, EVs) would replace the majority of gasoil-powered vehicles, the greenhouse gas emission would be significantly reduced. But actual EVs are not competitive to vehicles with combustion engines due to poor driving range and high asset costs. The high asset costs are in fact a result of high prices for lithium ion batteries (LIBs). Raising production of LIBs leads also to rapid increase of the price for lithium carbonate on the world market. An alternative to LIBs are sodium ion batteries (SIBs). The potential (-2.7 V against standard hydrogen electrode; only 0.3 V above that of lithium) is very suitable.<sup>[7,8]</sup> Due to unlimited abundance the price for sodium carbonate is a factor of 10 cheaper compared to Li<sub>2</sub>CO<sub>3</sub>. Unfortunately, standard carbon anodes cannot be used for SIBs without special

electrolytes or templating strategies.<sup>[9]</sup> In addition, the capacity of carbon-based anodes for SIBs is low. Therefore, the commercialisation of rechargeable batteries based on sodium is essentially depending on research success for suitable anode materials.

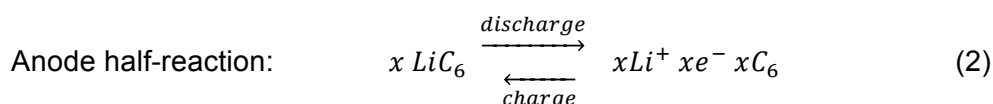
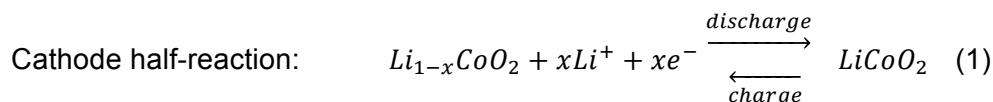
LIBs are actually used for portable electronic devices like e.g. smart phones, laptops, cordless electric screwdriver, electric shaver, electric bicycles and also in hybrid and full electric vehicles. For large-scale energy storage and competitive electric vehicles new batteries are needed, combining higher capacity, lighter weight and good cycling stability, consisting of cheap and environmental friendly materials. In my PhD studies the first part was the synthesis of nanosized materials and composites. Then the products were tested for their application as anode material for LIBs and SIBs, respectively. Besides optimization of the electrochemical performance, the focus was on the investigations of the detailed reaction mechanisms during electrochemical cycling. The new class of materials presented here show differing mechanisms, which was not investigated in detail before. The last project is about a new anode material for SIBs.

## 1.2 Scientific Background

### 1.2.1 Lithium Ion Batteries (LIBs)

In general, batteries contain a cathode and an anode, which are separated by an electrolyte-filled membrane. Commercial LIBs consist mostly of layered materials or substances with empty sites in their crystal structure.  $\text{Li}^+$  ions can reversibly intercalate into the empty sites in the structures. In 1991, Sony commercialized the first  $\text{LiCoO}_2/\text{C}$  LIB (Figure 3). This was a revolution because the energy stored in this LIB ( $\sim 180 \text{ Wh kg}^{-1}$ ) was five times larger than for lead-acid batteries at an average potential of 3.8 V.<sup>[10]</sup>  $\text{LiCoO}_2$  is a layered oxide which is used as cathode. Graphite is used as anode material because Li metal is “unsafe” and not used for commercial batteries. Anode and cathode are in contact via a non-aqueous electrolyte. The most common organic electrolyte is  $\text{LiPF}_6$ , which is dissolved in carbonate solvents like e.g. ethylene carbonate (EC), diethyl carbonate (DEC), dimethyl carbonate (DMC) or propylene carbonate (PC).

During discharging  $\text{Li}^+$  ions are deintercalated from the graphite layer, move through the separator and are intercalated into the cobalt oxide layer on the cathode site. The electrons move through an external electric circuit from the anode to the cathode, where  $\text{Co}^{4+}$  is reduced to  $\text{Co}^{3+}$ . The charge process is the other way around. From a chemical point of view the following equations can be formulated (eq. 1 and 2):



In a LIB  $\text{Li}^+$  ions simply shuttle back and forth between the electrodes. These types of batteries are also known as “rocking chair” batteries.<sup>[11]</sup>

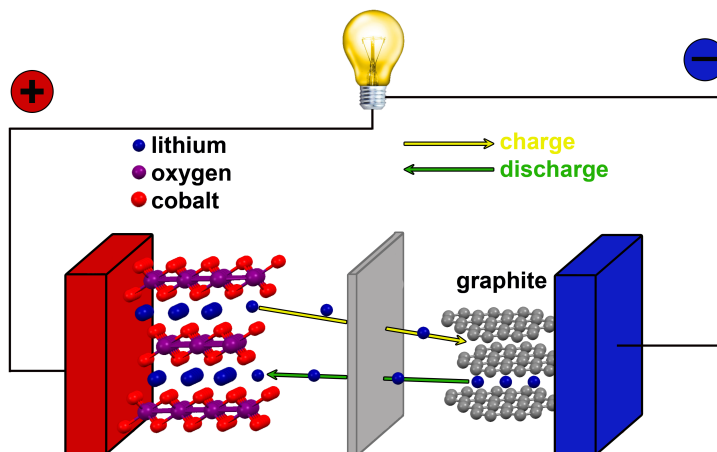


Figure 3: Schematic illustration of the reaction mechanism during charge and discharge process in a LIB. The illustrated LIB consists of a graphite anode, a separator and a  $\text{LiCoO}_2$  cathode.

### 1.2.2 Cathodes (commercial)

As already mentioned LIBs consist of anode, cathode, separator and electrolyte. The following materials are commercialized as cathode materials: lithium-cobalt oxide (LCO), lithium-nickel-cobalt-aluminium (NCA), lithium-nickel-manganese-cobalt (NMC), lithium-manganese-spinel (LMO), lithium-iron phosphate (LFP) and lithium-titan-sulphide (LTS). The currently most successful commercialized technology is LCO, which was introduced by Goodenough 1980 and commercialized by Sony one year later.<sup>[12]</sup> LCO is very attractive due to high theoretical capacity, low self-discharge, high discharge voltage and good cycling performance.<sup>[13]</sup> But this cathode is expensive because of the high cost for Co. The NCA ( $\text{LiNi}_{0.8}\text{Co}_{0.15}\text{Al}_{0.05}\text{O}_2$ ) cathode is used for example by Panasonic for Tesla EVs. NCA has a higher usable discharge capacity and long storage calendar life compared to other layered Co-based oxide cathodes. Problems are micro-cracks at grain boundaries and capacity fade due to solid electrolyte interphase (SEI) formation.<sup>[14,15]</sup> An attractive material with very similar capacity but being less expensive compared to LCO is  $\text{Li}(\text{Ni}_{0.5}\text{Mn}_{0.5})\text{O}_2$ . Adding a small amount of Co into the material  $\text{Li}(\text{Ni}_{0.33}\text{Mn}_{0.33}\text{Co}_{0.33})\text{O}_2$  (NMC) improves the stability of the crystal structure and the reversible theoretical and experimental capacity is slightly larger than for LCO.<sup>[16]</sup> Besides layered transition metals lithium manganese spinel is a very attractive cathode material consisting of cheap and environmental friendly manganese ions. But insufficient long-term stability, resulting from irreversible side reactions with the electrolyte, are a big disadvantage of  $\text{LiMn}_2\text{O}_4$ .<sup>[17,18]</sup>  $\text{LiTiS}_2$  (LTS) shows high gravimetric energy density and long cycle life (1000+ cycles). Unfortunately, the operating voltage is only in the range of 2 V, which is the lowest potential of all mentioned cathode materials.<sup>[19,20]</sup>

### 1.2.3 Anodes (commercial)

Pure Li metal would be an ideal anode for LIBs due to an extremely high specific capacity ( $3860 \text{ mAh g}^{-1}$ ) and the lowest negative potential. Unfortunately, Li metal forms dendrites and exhibits poor cycle life during Li deposition (limited Coulombic efficiency). Uncontrollable dendritic growth can cause short circuit and start a thermal runaway leading to explosion like reactions and/or bursting.<sup>[21]</sup> Therefore, it is necessary to use safer materials as an anode.

The anode material of choice for commercial LIBs is carbon. It is environmental friendly, highly abundant, cost saving and is characterized by long cycle life.  $\text{Li}^+$  ion diffusion and electrical conductivity is high, while the delithiation potential vs.  $\text{Li}/\text{Li}^+$  is relatively low (0.1-0.2 V).<sup>[22]</sup> Graphite is a layered material consisting of carbon layers stacked along the c-axis.  $\text{Li}^+$  ions are intercalated between 2D graphene layers. (Figure 4.1) One Li can be stored per 6 C (theoretical capacity:  $372 \text{ mAh g}^{-1}$ ), resulting in a volume expansion of only about 10 %.<sup>[23]</sup> A disadvantage is the relative low capacity (compared to conversion materials). Also graphitic carbons cannot be combined with PC electrolyte because a co-intercalation with  $\text{Li}^+$

between the graphene layers occurs. As a consequence graphite starts to exfoliate resulting in irreversible capacity loss. In addition, the performance of these materials is poor at high charge-discharge rates.<sup>[24]</sup>

LTO is a successfully commercialized alternative because of its superior thermal stability, high rate stability and high cycle life. High cycling rate stability and long-life are a result of the Li insertion/extraction mechanism. LTO crystallizes in spinel structure ( $Fd\bar{3}m$ ), oxygen ions are face-centred cubic packed. Lithium ions occupy all tetrahedral sites (8a), while remaining  $\text{Li}^+$  and  $\text{Ti}^{4+}$  (ratio 1:5) occupy the octahedral sites (16d). Three additional  $\text{Li}^+$  can be inserted per formula unit which occupy free octahedral 16c sites. Simultaneously,  $\text{Li}^+$  on tetrahedral sites move also to 16c sites thus avoiding too short separations of two neighbored  $\text{Li}^+$  ions of  $< 2 \text{ \AA}$  leading to strong repulsive interactions. The resulting structure can be described also in a cubic space group ( $Fd\bar{3}m$ , also it is possible to describe it as an rocksalt-structure  $Fd\bar{3}m$ ). The volume change during lithiation/delithiation is only 0.2 % and therefore LTO is known as a “zero-strain” anode. Drawbacks of LTO are the higher asset cost for Ti, the reduced cell potential and lower capacity ( $175 \text{ mAh g}^{-1}$ ).

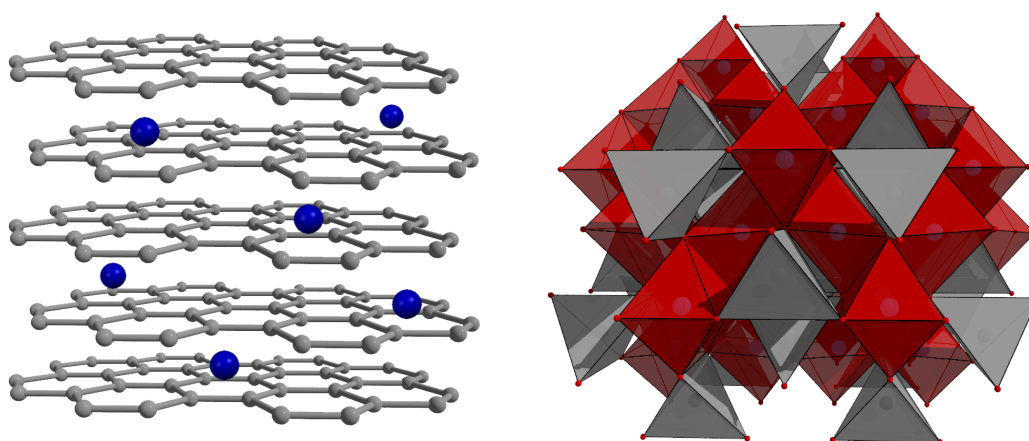


**Figure 4: Schematic illustration of lithiated graphite (left) and crystal structure of  $\text{Li}_4\text{Ti}_5\text{O}_{12}$  (right).**

Commercial anodes and cathodes consist in the main part of layered materials (LCO, NCA, NMC, LTS and graphite). Lithium is de-/intercalated in empty sites between the layers. These materials can be described as “intercalation materials”. LMO, LFP and LTO in contrast are not composed of layers. But in the structures empty sites are available for reversible  $\text{Li}^+$  insertion/extraction. Therefore, this type of materials can be regarded as “insertion materials”. For both material classes the number of lithium converted per formula unit of the active material is strictly limited. The experimental capacities range between  $148 \text{ mAh g}^{-1}$  (LCO) and  $199 \text{ mAh g}^{-1}$  (LCA) for cathodes and is  $372 \text{ mAh g}^{-1}$  (graphite) and  $175 \text{ mAh g}^{-1}$  (LTO) for commercialized anode materials.<sup>[22]</sup> The reaction rate is limited by diffusion of the guest ions ( $\text{Li}^+$ ) for insertion and intercalation materials. The need for better batteries is the main driving force for the search and investigation of new suitable materials.

### 1.2.4 Conversion reaction materials

An alternative class of materials are so-called “conversion” materials. This type of materials can be sub-divided into two types: Transition metal (TM) compounds which form  $\text{Li}_y\text{X}_z$  salts ( $\text{X} = \text{O}, \text{S}, \text{N}, \text{P}, \text{F}, \text{Cl}$ ) are referred as “Type A”. “Type B” are materials forming alloys with Li like e.g. Sn, Si and Zn. Electrode materials based on conversion reactions can be used as cathode or as anode depending on the potential level. Conversion cathode materials are metal fluorides<sup>[25–28]</sup> (MF) and chlorides<sup>[29,30]</sup> (MCl) and lithium sulphide<sup>[31]</sup> ( $\text{Li}_2\text{S}$ ). Also elemental sulphur<sup>[32]</sup> (S) and selenium<sup>[33]</sup> (Se) are investigated for its application as cathode in LIBs. Because the focus of the present work is on anode materials this topic will not be further discussed.

The capacity for conversion anode materials is much larger compared to carbon and LTO (Figure 5) because significantly more Li can be cycled with respect to the formula unit. Typical conversion anode materials belonging to Type B are Si, Sn and Zn. Among the alloying materials, Si has received the most attention due to the extremely high capacity and low delithiation potential.<sup>[34,35]</sup> A drawback is the large volume expansion (>300 %) resulting in electrically disconnection of the particles.<sup>[36–38]</sup> Sn has a smaller capacity compared to Si, but crack formation in the electrode is avoided if nanoparticles of about 10 nm are used.<sup>[39–41]</sup> Relatively few studies have been reported of zinc forming a  $\text{LiZn}$  phase during Li uptake.<sup>[42]</sup> But poor kinetics and short cycle life make Zn unpractical as negative electrode so far.<sup>[43,44]</sup> For further information I’ll recommend a much more detailed review of type B electrodes.<sup>[45]</sup>

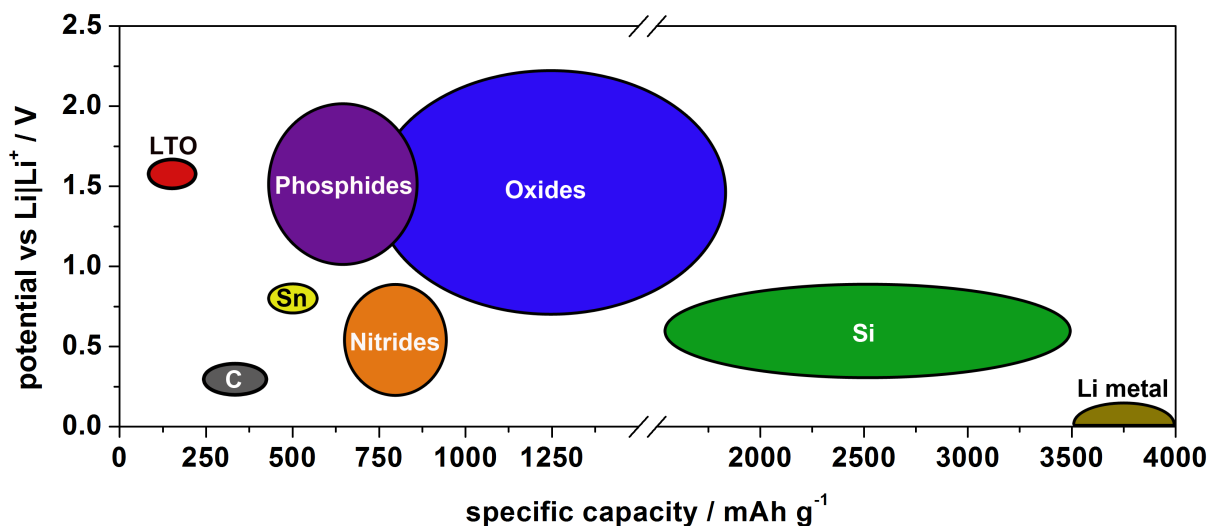


Figure 5: Approximate range of average discharge potentials and specific capacity of the most common conversion type anodes compared to Li metal and commercial anodes (experimental).

Type A conversion anode materials mainly consist of transition metal oxides, sulphides, nitrides or phosphides. Phosphides show capacities up to about  $650 \text{ mAh g}^{-1}$ , but also the operating voltage is higher compared to graphite and a large potential hysteresis of about 1 V is observed.<sup>[46–50]</sup> Nitrides were investigated enthusiastically 15 years ago.<sup>[51–53]</sup> But the



difficult synthesis and preparation made this type of electrodes unattractive.<sup>[54]</sup> Transition metal sulphides are not very intensively investigated compared to oxides. The specific capacity is slightly smaller due to the larger atomic weight of sulphur.<sup>[55–58]</sup> In addition, the potential level is higher as can be directly evidenced comparing  $\text{Fe}_3\text{S}_4$  and  $\text{Fe}_3\text{O}_4$ .<sup>[59,60]</sup>

In the year 2000 Poizot et al. reported for the first time about the application of nanosized transition metal oxides (CoO, FeO, NiO) as an anode for LIBs.<sup>[61]</sup> These types of anodes can store 2 Li per formula unit resulting in a capacities of  $700 \text{ mAh g}^{-1}$ .<sup>[62]</sup> For Type A conversion anode materials especially oxides were in focus of research over the past 15 years. Oxides can be easily synthesized and handled during electrode preparation. In addition to rock salt-structured oxides, also oxides with the spinel structure ( $\text{M}^{\text{II}}\text{M}^{\text{III}}_2\text{O}_4$ ,  $\text{M}^{\text{II}} = \text{Co, Fe, Ni, Zn, Mn}$ ;  $\text{M}^{\text{III}} = \text{Co, Fe, Mn}$ ) moved into the focus of research in the past 10 years, caused by the large theoretical and experimental capacities. In addition Ti, Mo, Sn and Sb oxides were investigated for its applications in LIBs.<sup>[63]</sup>

### 1.2.5 Oxides with spinel structure as anode material in LIBs

Transition metal oxides with spinel structure (space group:  $Fd\bar{3}m$ ) are highly interesting anode materials because of their large theoretical and experimental capacity.<sup>[63]</sup> In the spinel structure  $\text{O}^{2-}$  ions are cubic closed packed (face-centred cubic – fcc) as displayed in Figure 6. The  $\text{M}^{2+}$  ions occupy 1/8 of the tetrahedral sites (8a) and 1/2 of the octahedral sites (16d) is occupied by  $\text{M}^{3+}$ . For inverse spinels the half of the trivalent ions  $\text{M}^{3+}$  occupies the tetrahedral 8a sites and  $\text{M}^{2+}$  and the other half of  $\text{M}^{3+}$  occupy the octahedral 16d sites in equal proportion. For nanosized particles a mixture of inverse and normal spinel is often observed.

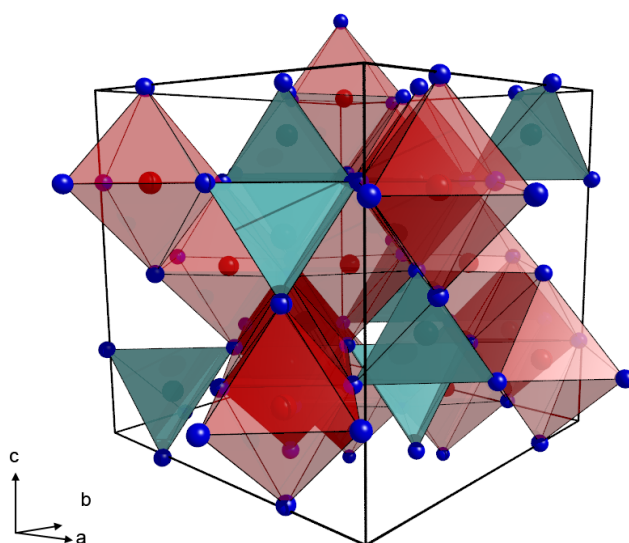


Figure 6: General crystallographic illustration of the spinel oxide structure,  $\text{O}^{2-}$  ions in blue,  $\text{M}^{\text{II}}\text{O}_4$ -tetrahedra in green,  $\text{M}^{\text{III}}\text{O}_6$ -octahedra in red and unit cell (black).

The structure is called partially inverse spinel structure and can be described as  $(M_{1-2\lambda}^{II} M_{2\lambda}^{III})_A [M_{2\lambda}^{II} M_{2(1-\lambda)}^{III}]_B O_4$  (A, B = tetrahedral and octahedral sites) with  $\lambda$  as inversion parameter.<sup>[64–67]</sup>

$Co_3O_4$ ,  $Fe_3O_4$  and  $Mn_3O_4$  crystallize with the inverse spinel structure. These materials are of great interest as anode materials because of their high theoretical capacity values ( $Co_3O_4$ :  $890 \text{ mAh g}^{-1}$ ;  $Fe_3O_4$ :  $928 \text{ mAh g}^{-1}$ ;  $Mn_3O_4$ :  $936 \text{ mAh g}^{-1}$ ). The group of Tarascon first reported  $Co_3O_4$  as an anode conversion material, which is easily synthesized and shows high stable and reversible capacities of  $800 - 900 \text{ mAh g}^{-1}$  (Table 1). Several reports proved the good cycle stability of  $Fe_3O_4$ , e.g. nanostructured  $Fe_3O_4$  rods grown on Cu substrate.<sup>[60]</sup>  $Mn_3O_4$  in comparison shows smaller reversible capacities which is explained by the fact that metallic Mn nanoparticles can only be oxidized to  $Mn^{II}$  after the first cycle.<sup>[68]</sup> All three mixed-valent oxides have been extensively investigated as anode materials. Synthesis of nanoparticles, nanowires, nanospheres, and other 2D and 3D structures, as well as addition of reduced graphite oxide (rGO) and carbon coatings improved the cycling stability significantly (Table 1).

**Table 1: Electrochemical Li cycling Data of  $M_3O_4$  (M = Co, Fe, Mn).**

Composition	size, morphology, additives	Capacity first discharge	Capacity after x cycles	Reference
$Co_3O_4$	Porous particles	$1100 \text{ mAh g}^{-1}$	$800 \text{ mAh g}^{-1}$ , 15 <sup>th</sup> cycle	[69]
$Co_3O_4$	Micrometre particles	$1130 \text{ mAh g}^{-1}$	$800 \text{ mAh g}^{-1}$ , 60 <sup>th</sup> cycle	[70]
$Co_3O_4/rGO$	Nanoparticles on reduced graphite oxide	$1100 \text{ mAh g}^{-1}$	$935 \text{ mAh g}^{-1}$ , 30 <sup>th</sup> cycle	[71]
$Fe_3O_4/C$	carbon-coated (30 wt % C)	$1000 \text{ mAh g}^{-1}$	$600 \text{ mAh g}^{-1}$ , 200 <sup>th</sup> cycle	[72]
$Fe_3O_4$	Single wall nanotubes	$1400 \text{ mAh g}^{-1}$	$1000 \text{ mAh g}^{-1}$ , 50 <sup>th</sup> cycle	[73]
$Fe_3O_4/rGO$	Nanoparticles on graphene nanosheets	$1390 \text{ mAh g}^{-1}$	$700 \text{ mAh g}^{-1}$ , 100 <sup>th</sup> cycle	[74]
$Mn_3O_4$	Nanofibers of 20-25 nm nanoparticles	$880 \text{ mAh g}^{-1}$	$450 \text{ mAh g}^{-1}$ , 50 <sup>th</sup> cycle	[75]
$Mn_3O_4/rGO$	Nanoparticles on reduced graphite oxide	$1320 \text{ mAh g}^{-1}$	$730 \text{ mAh g}^{-1}$ , 40 <sup>th</sup> cycle	[76]
$Mn_3O_4$	Spongelike nanoparticles	$1300 \text{ mAh g}^{-1}$	$\sim 800 \text{ mAh g}^{-1}$ , 40 <sup>th</sup> cycle	[77]

Because literature reports demonstrated the good Li cyclability of  $Co_3O_4$  and  $Fe_3O_4$  and their high capacities, researchers started to substituted Co and Fe by other transition metals. The group of Tirado published the first report about  $NiCo_2O_4$  used as negative electrode in 2002.<sup>[78]</sup> Afterwards several studies have been published about the performance of  $MCo_2O_4$  (M = Cu, Fe, Mg, Mn, Ni and Zn) as well as  $MFe_2O_4$  (M = Cu, Co, Mg, Mn, Ni and Zn) in LIBs. The oxides crystallize in normal, inverse or partially inverse spinel structures and show good capacities (summarized in Table 2). Spinel oxides including Zn can host one additional Li per formula unit due to the formation of a LiZn alloy at low potentials.<sup>[79,80]</sup> The morphology

## Introduction

and porosity of the particles as well as carbon coatings and addition of rGO improve the long-life stability of the electrodes (Table 2).

Please note Tables 1 & 2 are in no case complete and just a variety of results are presented.

For more information I recommend more detailed review articles.<sup>[63,81,82]</sup>

**Table 2: Electrochemical Li Cycling Data of AB<sub>2</sub>O<sub>4</sub> (A = Cu, Co, Mg, Mn, Ni and Zn; B = Co, Fe, Mn).**

Composition	size, morphology, additives	Capacity first discharge	Cycling stability	Reference
NiCo <sub>2</sub> O <sub>4</sub>	Nanoparticle, 8 nm	1250 mAh g <sup>-1</sup>	884 mAh g <sup>-1</sup> , 2 <sup>nd</sup> cycle	[78]
NiCo <sub>2</sub> O <sub>4</sub>	Mesoporous microspheres	1280 mAh g <sup>-1</sup>	705 mAh g <sup>-1</sup> , 50 <sup>th</sup> cycle	[83]
MnCo <sub>2</sub> O <sub>4</sub>	Submicrometer	1190 mAh g <sup>-1</sup>	500 mAh g <sup>-1</sup> , 49 <sup>th</sup> cycle	[84]
MnCo <sub>2</sub> O <sub>4</sub>	Mesoporous microspheres	1480 mAh g <sup>-1</sup>	553 mAh g <sup>-1</sup> , 200 <sup>th</sup> cycle	[85]
FeCo <sub>2</sub> O <sub>4</sub>	Submicron sized particles	902 mAh g <sup>-1</sup>	747 mAh g <sup>-1</sup> , 50 <sup>th</sup> cycle	[86]
FeCo <sub>2</sub> O <sub>4</sub>	Nanoflakes on Ni Foam	2445 mAh g <sup>-1</sup>	905 mAh g <sup>-1</sup> , 170 <sup>th</sup> cycle	[87]
CuCo <sub>2</sub> O <sub>4</sub>	100-500 nm particles	1187 mAh g <sup>-1</sup>	740 mAh g <sup>-1</sup> , 40 <sup>th</sup> cycle	[88]
ZnCo <sub>2</sub> O <sub>4</sub>	Nanoparticles 15-20 nm	1200 mAh g <sup>-1</sup>	900 mAh g <sup>-1</sup> , 60 <sup>th</sup> cycle	[79]
ZnCo <sub>2</sub> O <sub>4</sub>	Nanowire arrays on carbon cloth	1600 mAh g <sup>-1</sup>	1200 mAh g <sup>-1</sup> , 160 <sup>th</sup> cycle	[89]
NiFe <sub>2</sub> O <sub>4</sub> /rGO	Nanoparticles on reduced graphite oxide	1350 mAh g <sup>-1</sup>	850 mAh g <sup>-1</sup> , 50 <sup>th</sup> cycle	[90]
NiFe <sub>2</sub> O <sub>4</sub> /CNT	Linked with single wall nanotubes	1448 mAh g <sup>-1</sup>	788 mAh g <sup>-1</sup> , 50 <sup>th</sup> cycle	[91]
CoFe <sub>2</sub> O <sub>4</sub>	150 nm	1090 mAh g <sup>-1</sup>	740 mAh g <sup>-1</sup> , 75 <sup>th</sup> cycle	[92]
CoFe <sub>2</sub> O <sub>4</sub>	Hollow nanospheres	2264 mAh g <sup>-1</sup>	1185 mAh g <sup>-1</sup> , 50 <sup>th</sup> cycle	[93]
3CoO/CoFe <sub>2</sub> O <sub>4</sub>	nanocomposite	1260 mAh g <sup>-1</sup>	844 mAh g <sup>-1</sup> , 30 <sup>th</sup> cycle	[94]
CoFe <sub>2</sub> O <sub>4</sub>	graphene	1174 mAh g <sup>-1</sup>	1047 mAh g <sup>-1</sup> , 160 <sup>th</sup> cycle	[95]
CoFe <sub>2</sub> O <sub>4</sub> /C	carbon-coated (30 wt % C)	1700 mAh g <sup>-1</sup>	700 mAh g <sup>-1</sup> , 200 <sup>th</sup> cycle	[72]
MnFe <sub>2</sub> O <sub>4</sub> /rGO	MnFe <sub>2</sub> O <sub>4</sub> -graphene nanocomposite	1585 mAh g <sup>-1</sup>	1017 mAh g <sup>-1</sup> , 90 <sup>th</sup> cycle	[96]
MnFe <sub>2</sub> O <sub>4</sub> /C	Carbon-coated nanospheres	1222 mAh g <sup>-1</sup>	646 mAh g <sup>-1</sup> , 50 <sup>th</sup> cycle	[97]
MgFe <sub>2</sub> O <sub>4</sub>	Nanoparticles 11 nm	1001 mAh g <sup>-1</sup>	493 mAh g <sup>-1</sup> , 50 <sup>th</sup> cycle	[98]
MgFe <sub>2</sub> O <sub>4</sub>	Nanoparticles 33 nm	1123 mAh g <sup>-1</sup>	635 mAh g <sup>-1</sup> , 50 <sup>th</sup> cycle	[99]
CuFe <sub>2</sub> O <sub>4</sub> /C	Hollow CuFe <sub>2</sub> O <sub>4</sub> spheres encapsulated in carbon	1100 mAh g <sup>-1</sup>	550 mAh g <sup>-1</sup> , 70 <sup>th</sup> cycle	[100]
ZnFe <sub>2</sub> O <sub>4</sub>	Hollow spheres out of Nanoparticles 10-20 nm	1200 mAh g <sup>-1</sup>	900 mAh g <sup>-1</sup> , 50 <sup>th</sup> cycle	[80]
ZnFe <sub>2</sub> O <sub>4</sub> /C	Carbon-coated Nanoparticles <100 nm	1450 mAh g <sup>-1</sup>	>1000 mAh g <sup>-1</sup> , 60 <sup>th</sup> cycle	[101]
CoMn <sub>2</sub> O <sub>4</sub>	Triple-shelled	1007 mAh g <sup>-1</sup>	709 mAh g <sup>-1</sup> , 200 <sup>th</sup> cycle	[102]
ZnMn <sub>2</sub> O <sub>4</sub> /rGO	Graphene-wrapped nanorods	1412 mAh g <sup>-1</sup>	707 mAh g <sup>-1</sup> , 50 <sup>th</sup> cycle	[103]

While high capacities and good cycling stability of several binary spinel oxide composites have been demonstrated, studies concerning structural and electronic changes occurring during Li uptake and release are scarce. This holds also for spinel oxides composed of three TM ions.

In this work spinel oxides were investigated with the focus on elucidation of the reaction mechanisms occurring during Li uptake and release, especially under *operando* / *in-situ* conditions. The theoretical capacities of the investigated materials are summarized in Table 3 evidencing that the values are 2 - 5 times larger compared to the commercialized anode materials graphite or LTO.

**Table 3: Theoretical capacity of graphite and lithium titanate (anode materials used in commercial batteries) compared to spinel oxides and sulphides (based on conversion reactions).**

Formula unit active material	Li converted per formula unit	Theoretical capacity / mAh g <sup>-1</sup>
Li <sub>4</sub> Ti <sub>5</sub> O <sub>12</sub>	3	175
C (graphite)	1/6	372
MnFe <sub>2</sub> O <sub>4</sub>	8	930
MgFe <sub>2</sub> O <sub>4</sub>	6	804
CoFe <sub>2</sub> O <sub>4</sub>	8	914
CoMnFeO <sub>4</sub>	8	917
NiMnFeO <sub>4</sub>	8	918
NiFe <sub>2</sub> O <sub>4</sub>	8	915
Fe <sub>3</sub> S <sub>4</sub>	8	725

### 1.2.6 Why investigation of the reaction mechanisms?

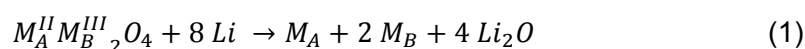
Spinel oxides show a high potential for its application as anode material in LIBs. But for commercialization these types of electrodes have to be improved significantly, especially enhancing cycle stability and reducing the irreversible capacity loss during the first cycle. Therefore a deep understanding of the reaction mechanisms is very important. The actual focus of research is mainly the synthesis of materials with special morphologies, combinations of carbon species with TM oxides or variation and improvement of electrode preparation.<sup>[104]</sup> All these studies are important, but such investigations do not contribute to the understanding of the fundamental reaction mechanisms occurring during cycling. Nowadays, only little is known about structural and electronic alterations during Li uptake and release of such conversion materials.

On the other hand, to improve the performance of LIBs based on intercalation/insertion reactions, *ex situ*, *in situ* and *operando* studies were performed.<sup>[105–118]</sup> The detailed investigation of the reactions helped to improve the performance significantly. But as mentioned above the capacity of these compounds is limited requiring the development of next-generation LIBs with larger capacities.<sup>[119]</sup>

In general a conversion reaction for an anode material proceeds as follows: i) During Li uptake transition metals ions are reduced to the metallic state. Simultaneously a Li<sub>2</sub>X (X = O, S) salt matrix is formed in which the metallic nanoparticles are embedded. ii) During

subsequent charge process  $\text{Li}^+$  and electrons are released from the anode material, *i.e.* metallic nanoparticles are oxidized and form M-X bonds (M = transition metal; X = O, S). The structure of the pristine (nano-)crystalline material is not formed back. Hence, the electrochemically active phases are generated *in-situ* during the first cycle.<sup>[10,120]</sup> Therefore, it is important to investigate the first cycle and to identify and characterize the resulting new species in detail.

For spinel oxides with the composition  $\text{M}^{\text{II}}\text{M}^{\text{III}}_2\text{O}_4$  (M<sup>II</sup> = Mn, Fe, Co, Ni, Cu; M<sup>III</sup> = Co, Fe, Mn) the mechanism is related to these general processes (Figure 7). During discharge (Li uptake) TMs cations are reduced to the metallic state and  $\text{Li}_2\text{O}$  is formed. At the end of the discharge process the spinel structure is completely transformed to small metallic nanoparticles embedded in the  $\text{Li}_2\text{O}$  matrix (*eq. 1*).



During subsequent charging (Li release) the spinel structure is not formed back. But bivalent and trivalent oxides are formed without structural long-range order. Subsequent discharge-charge cycling differs from the first cycle.<sup>[63]</sup> The proposed reaction pathways are mainly based on interpretation of cyclic voltammetry (CV) curves and galvanostatic cycling. But these nanocrystalline or amorphous oxides, oxidation states or local environments of Li and TMs were rarely evidenced by appropriate experimental investigations. The CV curves show more than one signal for each charge/discharge operation, indicating that intermediate phases are generated excluding the one-step conversion reaction formulated in *eq. 1*.<sup>[96,121–123]</sup>

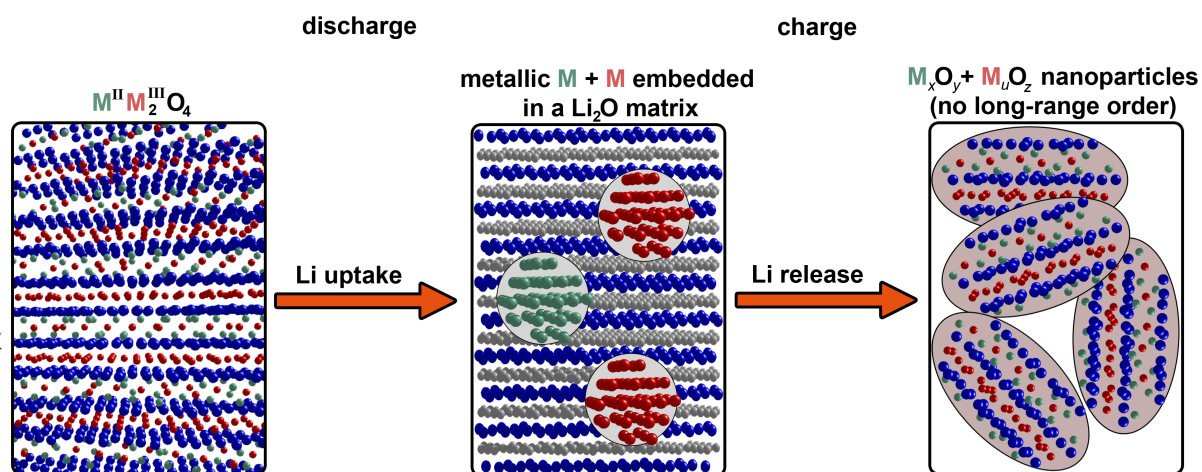


Figure 7: Schematic representation of the reaction mechanism during Li uptake and release of a spinel oxide  $\text{M}^{\text{II}}\text{M}^{\text{III}}_2\text{O}_4$ . Per Formula unit 8 Li are converted.

During Li uptake/release, new species are generated which are sensitive to air or moisture. To minimize the risk of contamination or formation of unwanted chemical species it is necessary working under inert gas atmosphere. For detailed investigations of complex reactions it is also required to synthesize many samples of different lithiation / delithiation

steps which is time consuming and cost ineffective. Elegant solutions are *in situ / operando* investigations. *In situ* experiments are performed with an interruption of the reaction for data collection and measurement in the same cell or reactor. During *operando* investigations a reaction is followed coupled with simultaneously collecting data. The presented different investigations were realized simultaneously during charge and discharge of the conversion anode materials and are so-called “*operando*” experiments. In literature the terms *operando* and *in situ* are not strictly distinguished and become blurred. Independent from terms and definitions, in the last years the power of such experiments was demonstrated by several groups.<sup>[105,124–136]</sup>

For the Li uptake of  $\text{Fe}_3\text{O}_4$  the group of Goodenough postulated the following reaction pathway. First, empty octahedral 16c sites are entered by  $\text{Li}^+$  ions, followed by a movement of the Fe cations located on the tetrahedral 8a sites to empty 16c sites. After uptake of 1 Li per formula unit a NaCl-like structure is generated. 1d sites are occupied by Fe cations and 16c sites are occupied Fe and Li, similar to the Li insertion mechanism of LTO. But the increase of the volume of the  $\text{Fe}_3\text{O}_4$  unit cell is larger (2.8 %) than for LTO.<sup>[137]</sup> Chen and Greenblatt investigated the Li insertion into  $\text{MMn}_2\text{O}_4$  (M = Cd, Ni and Zn) spinels. Similar to  $\text{Mn}_3\text{O}_4$  a new tetragonal compound  $\text{LiM}[\text{Mn}^{\text{II}}\text{Mn}^{\text{III}}]\text{O}_4$  is formed after insertion of 1 Li per formula unit caused by a strong Jahn-Teller distortion.<sup>[138]</sup>

The group of Larcher et al. reported two different competing reaction mechanisms depending on the particle size and current density. Smaller particles or lower intermitted applied discharge rate lead to direct formation of CoO and  $\text{Li}_2\text{O}$ . Large domains and fast discharge rates favour the formation of a  $\text{Li}_x\text{Co}_3\text{O}_4$  intermediate phase.<sup>[139]</sup>

The group of Passerini *et al.* investigated the first discharge mechanism of  $\text{ZnFe}_2\text{O}_4$  nanoparticles (particle size: 53 nm) via *in situ* XRD. The first 0.4 Li per formula unit are inserted into empty octahedral 16c sites. Further Li uptake leads to hopping of  $\text{Zn}^{\text{II}}$  into neighbouring 16c sites and simultaneously occupancy of 16c with Li until the composition  $[\text{Li}_{0.9}\text{Zn}]_{16\text{c}}[\text{Fe}]_{16\text{d}}\text{O}_4$  is reached. Afterwards up to 1.45 Li per formula unit are located on tetrahedral sites 8a/48f. Unfortunately,  $^7\text{Li}$  MAS NMR investigations did not evidence the formation of Zn/Fe-O-Li bonds. Further Li uptake forms  $\text{Li}_2\text{O}$  and a mixed monoxide  $\text{Zn}_{0.33}\text{Fe}_{0.66}\text{O}$  which could not be well-defined to the  $[\text{Li}_{0.55}]_{8\text{a}/48\text{f}}[\text{Li}_{0.9}\text{Zn}]_{16\text{c}}[\text{Fe}]_{16\text{d}}\text{O}_4$  phase. The final discharge state includes metallic Fe nanoparticles and LiZn alloy embedded in a  $\text{Li}_2\text{O}$  matrix. Information about the charge process were not available due to the amorphous character of the new species.<sup>[140]</sup>

Lowe and Abruna proposed the following reaction mechanism for 15 nm  $\text{Mn}_3\text{O}_4$  particles. The first Li uptake takes place on the surface into an amorphous manganese oxide layer of the nanoparticles. In a second step  $\text{LiMn}_3\text{O}_4$  is formed by reduction of manganese  $\text{Mn}^{\text{III}}$  to  $\text{Mn}^{\text{II}}$  and movement of the cations to neighbouring octahedral sites. In the next step MnO



crystallized in a defect NaCl-like structure and  $\text{Li}_2\text{O}$  is formed during uptake of  $2 \text{Li}^+$  per formula unit. At the end of the discharge process metallic Mn (1 nm) is embedded in a  $\text{Li}_2\text{O}$  matrix. During charge operation NaCl-like MnO is reversibly formed. The capacity fading during the first cycle could be attributed to oxidation of Mn to only  $\text{Mn}^{\text{II}}$  instead of  $\text{Mn}^{\text{III}}$ .<sup>[68]</sup>

### 1.2.7 Sodium - an alternative to Lithium

Lithium is the lightest metallic element and has the lowest redox potential (-3.0 V versus standard hydrogen electrode).  $\text{Li}^+$  has a small ionic radius and therefore exhibits good diffusion velocity in solids. But the pronounced production increase of LIBs leads to raising demand and prices for Lithium. Significant Li reserves are located in remote or in politically unstable areas.<sup>[7]</sup>

On the search for an alternative, sodium is the most promising element, which may replace Li. Due to its low standard potential (-2.7 V against standard hydrogen electrode), relatively low atomic weight (please note for stationary energy storage the weight is regardless), and the nearly unlimited availability guaranteeing a low price are factors which may finally lead to a future SIB based technology. In the last years mainly oxidic compounds were identified as suitable cathode materials for SIBs.<sup>[141–146]</sup> But the success of SIBs mainly depends on the research for safe and efficient anode materials.<sup>[8]</sup> Graphite is the common negative electrode in LIBs (see section 1.2.3). But it cannot be used as an anode for SIBs because the size of the  $\text{Na}^+$  ion is not suitable for intercalation between the graphene layer.<sup>[147,148]</sup> Recent studies showed that the problem can be overcome by using a co-intercalation process. Reversible capacity of about  $100 \text{mAh g}^{-1}$  were reached with a dyglime-based electrolyte.<sup>[149]</sup> Another approach used expanded graphite and it was shown that the capacity strongly depends on the distance between the graphene layer. For an optimized layer to layer separation of  $4.3 \text{ \AA}$  a reversible capacity of  $280 \text{mAh g}^{-1}$  was obtained.<sup>[150]</sup>

Conversion anode materials for SIBs enable much higher capacities and good cycling stability. In the focus of research are alloys (Sn, Sb, Ge, In - based materials), phosphides and transition metal oxides.<sup>[151]</sup> Studies about TM sulphides used as anode materials are scarce, and only a limited number of reports is available. The impressively long-life stability of Pyrite ( $\text{FeS}_2$ ) is the motivation for us to investigate Greigite ( $\text{Fe}_3\text{S}_4$ ) nanoparticles as anode material for sodium batteries.<sup>[152–154]</sup>

## 2 Experimental Section

Various methods were applied for characterization of the as-prepared materials and resulting products occurring during Li/Na uptake and release. Special methods are described in detail and used equipment is illustrated in section 2.7.

### 2.1 Investigation of the electrochemical performance

For investigation of the electrochemical performance the active material was mixed with carbon and a polymer binder. The mixture was processed to an electrode and measured in a Swagelock-type or *in situ* cell.

#### 2.1.1 Preparation of the electrodes

For electrochemical measurements the active materials were mixed with carbon Super C65 (Timcal) in a Retsch MM400 ball mill for 30 min at 10 or 15 Hz. As binder sodium carboxymethyl cellulose (NaCMC, Dow Chemicals) or sodium alginate (NaAlginate, Sigma Aldrich) was dissolved in water (1.5 wt. % binder in H<sub>2</sub>O) and added to the mixture of active material and carbon. The slurry was ball milled for another 30 min.

Polyvinylidene fluoride (PVDF, Solvay) or sodium polyacrylate acid (NaPAA, Sigma Aldrich) were also used as binder by mixing the powders directly with active material and carbon. The mixture with PVDF (3 wt. %) was dissolved in N-methyl-pyrrolidone (NMP, Sigma-Aldrich), while NaPAA (1.5 wt. %) was dissolved in water.

The suspensions were painted on dendritic copper foils (Schlenk, Germany) or smooth copper foils (Goodfellow, Germany). A small puddle was formed at one site of the copper foil and a “notch bar” (120 μm spreader gap) was used to spread the slurry evenly across the foil (Figure 8).<sup>[155]</sup> The electrode films were then dried at room temperature for 24 h. From the electrode films circles (10 mm in diameter) were punched out and used as electrode in Swagelock test cells.

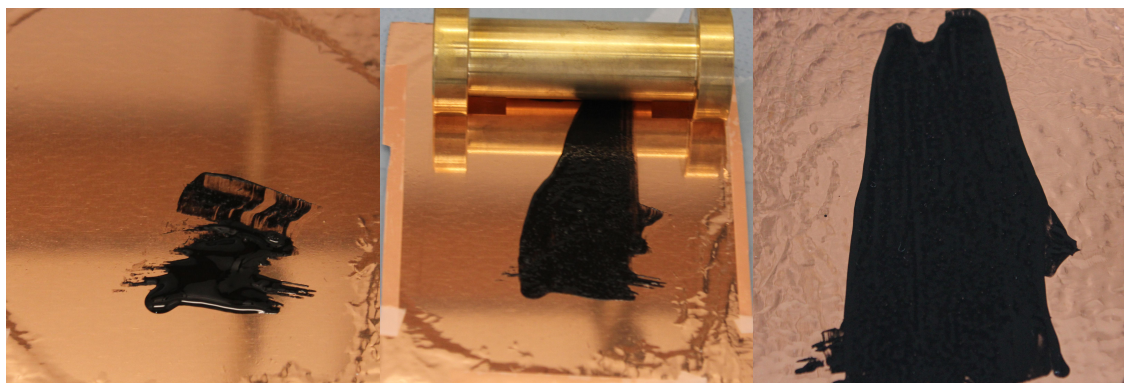


Figure 8: Preparation of the electrode film: Puddle of slurry on copper foil (left), wet slurry outspread with notch bar (middle) and dried electrode film (right).



### 2.1.2 Swagelock test cell

For galvanostatic cycling and cyclic voltammetry (CV) Swagelock-type test cells were used. The components of the cells were dried at 80 °C and transferred into an argon filled glovebox (MBraun, <1 ppm of O<sub>2</sub>, <1 ppm of H<sub>2</sub>O). The electrode consisting of active material, carbon and binder on a copper foil was weighted and used as cathode. Li (ABCR, 99.9 %) respectively Na (ABCR, 98 %) were used as anode materials. Whatman glass fibre filter discs (GE Health Care, United Kingdom) were used as Separator. For Li test cells 1 M LiPF<sub>6</sub> in ethylene carbonate/dimethyl carbonate (1:1, Merck) was used as electrolyte. 1 M NaCF<sub>3</sub>SO<sub>3</sub> in diglyme was used for Na test cells. After assembling the cells in the glovebox different measurements were performed. For galvanostatic cycling the current was calculated according to eq. 2:

$$I = \frac{x(\text{Li/Na})m F}{t M} \quad (2)$$

I ... current

x ... number of Li/Na ions converted per formula unit

m ... mass of the active material on the electrode

F ... Faraday constant

t ... time

M ... molecular weight of active material

During cycling at constant current the potential of the cell and the time were recorded. The time can be converted into capacity and Li / Na amount per formula unit by knowledge of the mass of the active material. This provides information about the capacity and cycling stability of the materials.

For CV the cell potential ramps linearly versus time. The scan rate is the potential change over time, e.g. 0.05 mV s<sup>-1</sup>. The current at the working electrode is monitored and plotted against the cell potential. Signals in the CV provide information about redox processes during charging and discharging.

### 2.2 Investigations with synchrotron radiation

#### 2.2.1 Synchrotron light

For *operando* X-ray diffraction (XRD) the “PDIFF” beamline at ANKA (Karlsruhe) and beamline “B18” at Diamond Light source (Oxford) were used. For *operando* X-ray absorption spectroscopy (XAS) the “XAS” beamline at ANKA (Karlsruhe), “KMC-2” at BESSY II (Berlin) and beamline “B18” at Diamond Light source (Oxford) were used.

#### 2.2.2 The *in situ* cell

For *operando* XRD and XAS investigations, a custom-built cell was developed for experiments performed in transmission mode (Fig. 9). The cell consists of two round plates (40 mm in diameter) made of brass respectively aluminium with rectangular apertures (14 x 3 mm) in the centre. On each plate a Kapton foil window was glued.

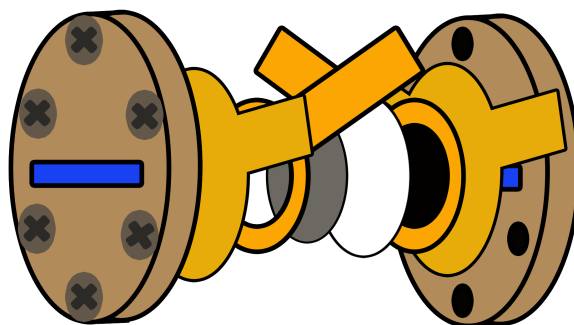


**Figure 9:** Schematic illustration of the *in situ* cell for XRD and XAS investigations. Design from left to right: top plate, Kapton window, copper ring, lithium/sodium metal, separator, copper foil with active material, Kapton window, and bottom plate.

The active anode material was mixed with carbon black (Super C65, Timcal) and PVDF in an agate mortar. The mixture was suspended in NMP, coated on 8  $\mu\text{m}$  copper foil (Goodfellow) and dried at room temperature for 24 h. A microporous polyethylene/polypropylene membrane (Celgard 2325) was used as separator and 1 M  $\text{LiPF}_6$  in ethylene carbonate/dimethyl carbonate (Merck) was applied as electrolyte. The counter electrode were Li metal respectively Na metal was used as counter electrode. The metal was attached on a ring as current collector made of copper foil. The two cell plates are bolt together with six Phillips screws. The cells were assembled in an argon filled glovebox and transferred to the beamline in a plastic bag. The same *in situ* cells were also used for *ex situ* XAS investigations. Galvanostatic Li/Na uptake/release was realized with a Biologic SP-300 in a voltage range from 3.0 to 0.1 V.

### 2.2.3 X-Ray absorption spectroscopy (XAS)

X-Ray absorption spectroscopy (XAS) provides information about the local geometry and electronic structure of the absorbing atom. The experiment is performed at a synchrotron light source with a beamline delivering high intensity and tuneable X-rays. XAS is not restricted to crystalline phases, but also highly disordered or amorphous samples can be investigated.<sup>[156]</sup>

The experimental setup is illustrated in Figure 10. The synchrotron storage ring is shown on the left hand side, the beam is passing a double crystal monochromator (Si(111) or Si(311)) producing monochromatic light. The first and second ionization chambers measure the flux before and after the sample. A fluorescence detector can be installed 45 or 90 degree to the sample. The third ionization chamber measures continuously the appropriate metallic references foil to provide the correct energy calibration.

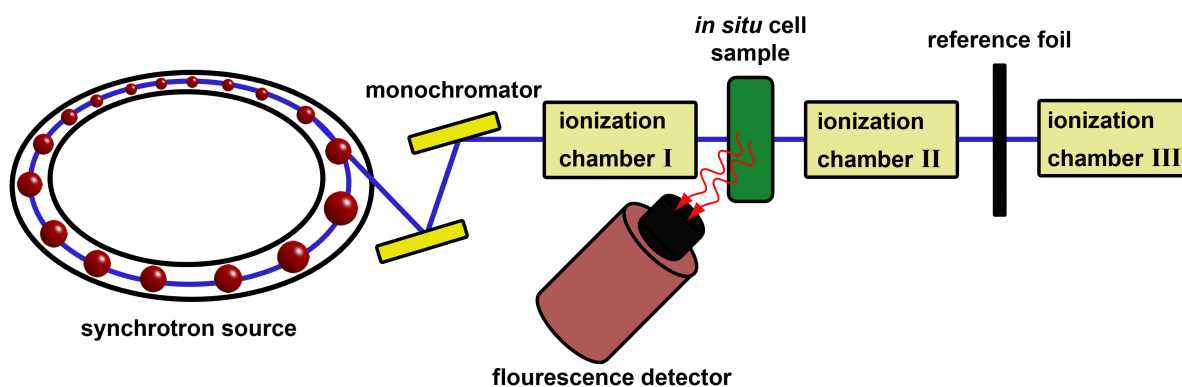


**Figure 10:** Schematic illustration of a XAS experiment (from left to right): Synchrotron light source, monochromator (Si crystal), first ionization chamber, sample (*in situ* cell), fluorescence detector (45 or 90 degree to the induced beam), second ionization, metallic reference foil, third ionization chamber.

Tuning the energy of the X-rays the absorption of the sample is continuously measured. If the incident beam has an energy equal to binding energy of a core level electron (such as 1s level) of the absorber atom, a sharp raise of the absorption is observed. The electron is promoted from the core level to the continuum (Figure 11 left). This phenomenon is called the photoelectric effect. The resulting XAS spectrum is the energy depending of  $\mu$  at the binding energy of a specific element. The emission of an electron leaves behind a core hole. There are two principal mechanisms after the absorption event. The core-hole can be filled by electrons from higher energy core-level(s) leading to emission of an X-ray photon with a fluorescence energy characteristic for the absorber atom (Figure 11 right). The second mechanism is the Auger Effect, where an electron drops from a higher energy level into the hole by simultaneously emission of an electron into continuum. The energy dependence of the absorption coefficient  $\mu$  can be measured both in transmission and fluorescence mode.<sup>[157]</sup>

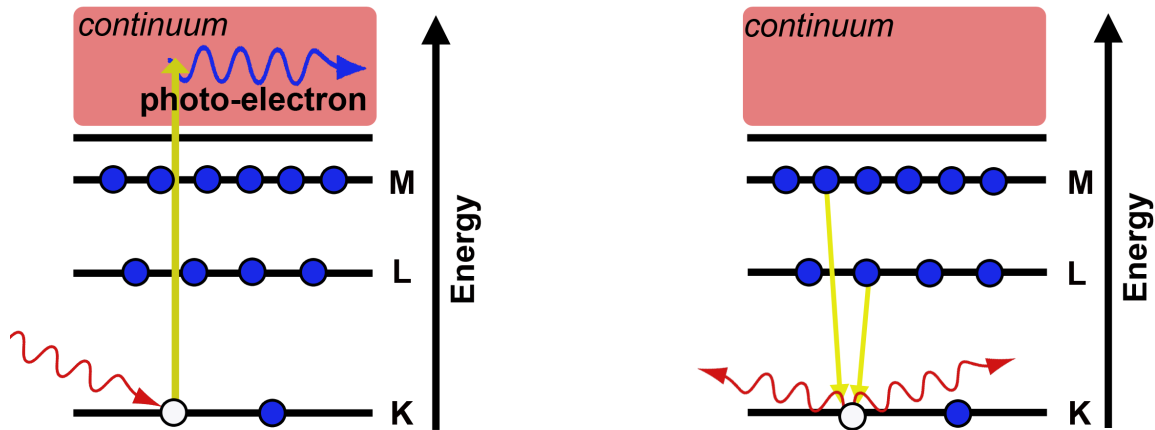


Figure 11: Schematic illustration of the photoelectric effect, where a core-level electron is promoted to continuum (left). Afterwards core-hole is recombined by X-ray fluorescence (right).

Independent whether the spectra are collected in transmission or fluorescence geometry, the data analysis and processing is identical: First the data are converted to absorption  $\mu(E)$ . Figure 12 left shows exemplarily the spectrum at Fe K-edge for NiFe<sub>2</sub>O<sub>4</sub> nanoparticles linked by carbon nanotubes. A smooth pre-edge line and the post edge line are fitted to the spectrum. In the next step the spectrum is normalized by transformation of  $\Delta\mu_0$  into  $\Delta 1$  (Figure 12 right). XAS spectra can be subdivided into two parts: 1) the X-ray Absorption Near-Edge Structure (XANES) (pre-edge and rising edge) is the energy range around the edge transition, delivering information about the oxidation state and environment of the absorbing atom. 2) Extended X-ray Absorption Fine Structure (EXAFS) sheds light on the local environment of the absorbing atom, providing information about atom type, bond length and coordination number of the first and second or further neighbours.<sup>[158]</sup>

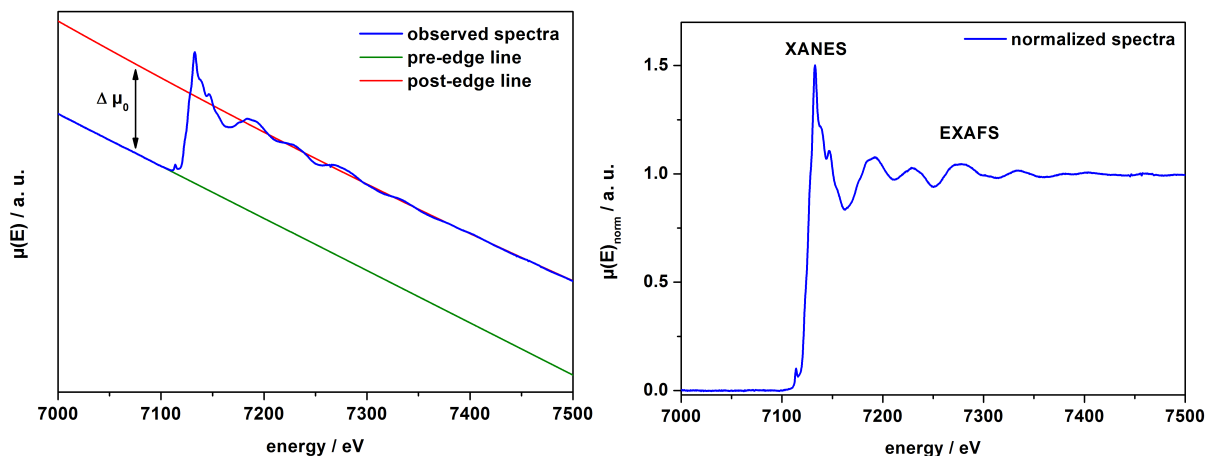


Figure 12: XAS data processing exemplary for Fe K-edge of NiFe<sub>2</sub>O<sub>4</sub> nanoparticles. Observed spectra with pre-edge and post-edge line (left) and normalized spectrum with EXAFS and XANES region (right).

The spectrum is calibrated with Fe reference foil measured between the second and third ionization chamber. In the exemplary spectra (Figure 12 right) a small pre-edge peak is located at 7114 eV and the energy value for the Fe K-edge is 7126 eV, which is discussed in detail later.

In the next step the EXAFS region is isolated  $\chi(k)$  by applying the relation  $k = \sqrt{2m(E - E_0)/\hbar^2}$ . Afterwards the spectrum is  $k^2$ -weighted (the weighting depends on different factors), which amplifies the oscillations at high  $k$  (Figure 13 left). In addition a window function is shown, which is multiplied by  $k^2\chi(k)$ . Finally EXAFS data are Fourier transformed into R-space ( $\chi(R)$ , Figure 13 right) which is the magnitude consisting of an imaginary and real part. In Figure 13 right the first maximum is located at 1.8 Å (not phase shift corrected) which corresponds to the Fe-O distance for Fe located on octahedral sites. The shoulder at about 1.6 Å is assigned to Fe-O for Fe on tetrahedral sites. The second maximum consists of two peaks at 3.0 and 3.3 Å, which are the Fe-O-M distances for Fe tetrahedral and octahedral sites. The XAS spectra were calibrated, normalized,  $k^2$ -weighted and Fourier transformed using the Athena Software package.<sup>[159]</sup>

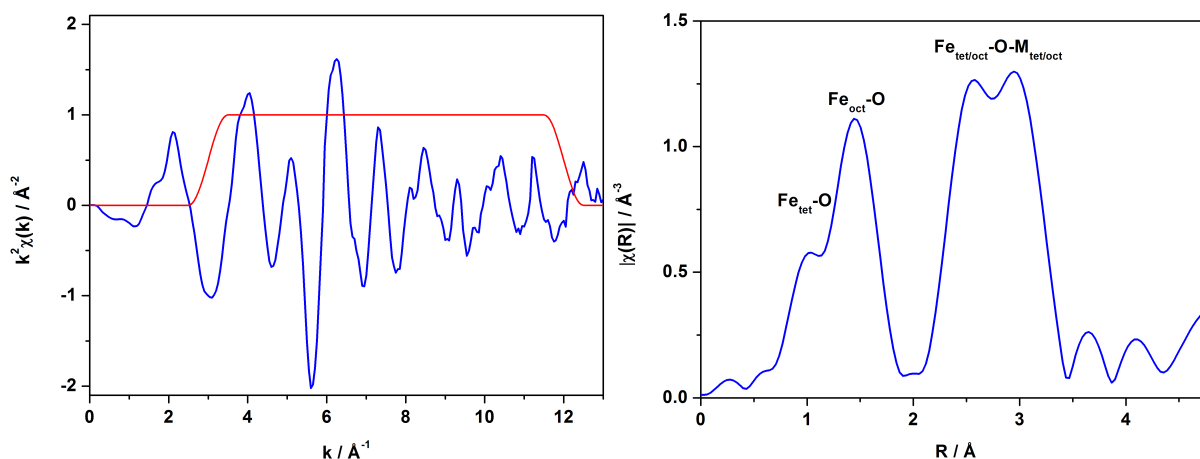


Figure 13: EXAFS region  $k^2$ -weighted (left) and Fourier transformed EXAFS region ( $\chi(R)$ ) (right).

### 2.3 Rietveld refinement

Rietveld Refinement is an important method for the detailed analysis of X-ray diffraction pattern data. The entire powder diffraction pattern is calculated based on a structure model including intensity, position, peak shape and background.<sup>[160]</sup> Based on the following equation:

$$y_i(\text{calc}) = y_{\text{Background}} + S \sum_{hkl} P_{hkl} A(2\theta) Lp(2\theta) |F_{hkl}|^2 \phi(2\theta - 2\theta_{hkl}) \quad (3)$$

Where  $y_{\text{Background}}$  describes the background intensity,  $S$  is the scale factor,  $hkl$  are the Miller indices for the given reflection,  $P_{hkl}$  is the preferred orientation correction,  $A(2\theta)$  is the absorption correction,  $Lp(2\theta)$  is the Lorentz-Polarisation correction,  $F_{hkl}$  represents the structure factor and  $\phi(2\theta - 2\theta_{hkl})$  is a function, which describes the reflection profile. Additional more correction functions can be added and the above mentioned corrections are just a selection.

The principle of the Rietveld method is to minimize the difference between the calculated pattern and observed data by a least square method.

For an ideal crystal (strain free, infinite crystallite size, without surface) measured at ideal conditions each reflection in the powder pattern would be infinitesimally narrow. The observed reflections exhibit a broadened peak shape due to the wavelength of the X-rays, the geometric instrument profile (together instrument profile function) and specimen broadening function from the sample. Broadening from the instrument can be subtracted using the fundamental parameter approach or by measuring the profile function of a line profile standard like e.g. NIST 660 LaB<sub>6</sub>.

Sample related broadening is caused by size and strain of the material, which can be distinguished according to their different dependence on the diffraction angle. Size-effects depend on  $1/\cos\theta$  and reflections are generally broadened by a Lorentz function, while strain-effects result in an enhancement of the Gaussian fraction of the peak profile and correlate with  $1/\tan\theta$ . In crystallites two types of strain can be observed. The uniform strain expands or contracts the unit cell in an isotropic way and no broadening is observed. Reflection broadening depending on non-uniform strain originates from a systematic shift of atoms from their equilibrium positions. There are different approaches to determinate the influence of size and strain on the broadening.

For nanocrystalline materials one way to determine the particle size (more precisely: the sizes of coherently scattering domains) uses the Scherrer equation:<sup>[161]</sup>

$$\Delta(2\theta) = \frac{K \lambda}{d \cos\theta} \quad (4)$$

Where  $\Delta(2\theta)$  is the full width at half maximum (FWHM) of the reflection, after subtracting the instrumental line broadening,  $K$  is the shape factor, which is 0.9 for cubic particles,  $\lambda$  is the wavelength of the X-rays and  $d$  is the domain size. According to the Scherrer equation the

FWHM increases with the diffraction angle. Properly speaking  $d$  is an apparent area weighted domain size. Strain effects are not considered in this simple model.

A more sophisticated approach to distinguish size and strain components in the powder pattern is the Williamson-Hall plot.<sup>[162]</sup> The reflection widths are plotted as a function of  $2\theta$ . From the resulting linear fit of the data the strain can be extracted from the slope, while the crystallite size is determined from the y-intercept of the fit. Additionally isotropic and anisotropic size and strain can be distinguished visually in Figure 14.

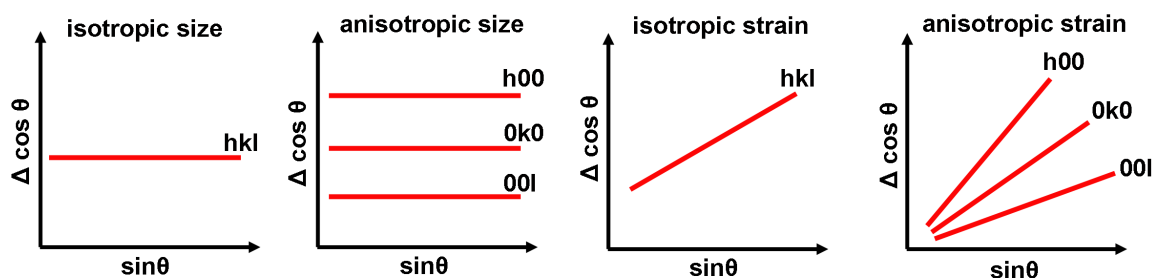


**Figure 14: Schematic illustration of Williamson Hall plots concerning isotropic and anisotropic size and strain broadening.**

Each reflection in the diffraction pattern consists of a Lorentz and a Gaussian term. In the Rietveld refinement a pseudo-Voigt function models the reflection profile for extraction of the size and strain parameters.<sup>[163]</sup> As a result the volume-weighted average particle size and anisotropic strain is obtained from the refinement.

For the characterization of nanocrystalline materials, refinement cannot rely on the average domain size alone due to its polydisperse particle size distribution. Therefore Whole Powder Pattern Modelling (WPPM) is more appropriate. WPPM is based on the direct modelling of the experimental data using physical models of the microstructure and lattice defects.<sup>[164,165]</sup> For any broadening source (including particles of different sizes) the corresponding Fourier transform is calculated. As a result the domain size distribution can be presented as a histogram. Instead of using the PM2K software, a macro implemented in TOPAS academic was used.<sup>[166,167]</sup>

The particle morphology is determined by calculation of the  $hkl$ -dependent anisotropic particle size (see also Figure 14), which is implemented in TOPAS academic.<sup>[168]</sup>

For rapid collection of powder patterns synchrotron X-ray radiation was used. *Operando* XRD data were collected at the PDIFF beamline (ANKA, Germany) operated at 16 keV ( $\lambda = 0.77490 \text{ \AA}$ ) with a Princeton CCD Detector. The 2D powder patterns were calibrated and transformed using Area Diffraction machine.<sup>[169]</sup> For *operando* XRD of the  $\text{NiFe}_2\text{O}_4/\text{CNT}$  samples the beamline B18 (Diamond Light Source, England) was operated at 8940 eV ( $\lambda = 1.3868 \text{ \AA}$ ) using a Mythen 6K detector for data collection.

### 2.4 Transmission electron microscopy

With the transmission electron microscopy (TEM) technique particles and structures within the range of nanometers or even smaller can be investigated and characterized. In a TEM the electrons are accelerated at *e.g.* 300 keV in an electric field. The electron beam is focused on the sample using magnetic lenses. The electrons interact with the sample and pass through. The image is magnified and focussed onto a fluorescent screen or a sensor (*e.g.* CCD Camera). Images occur by occlusion and absorption of the electrons, which is called bright field mode.<sup>[170]</sup>

Electrons are also diffracted by the solid specimen resulting in an image with spots for single crystals or a series of rings for polycrystalline samples. This technique is called selected area electron diffraction (SAED, Figure 15).

TEM can be also combined with energy-dispersive X-ray spectroscopy, which is a technique to analyse the chemical composition of the sample with high resolution. Additionally a mapping of a selected area or a line scan can be performed, which is very useful to evidence the homogeneity of a sample.

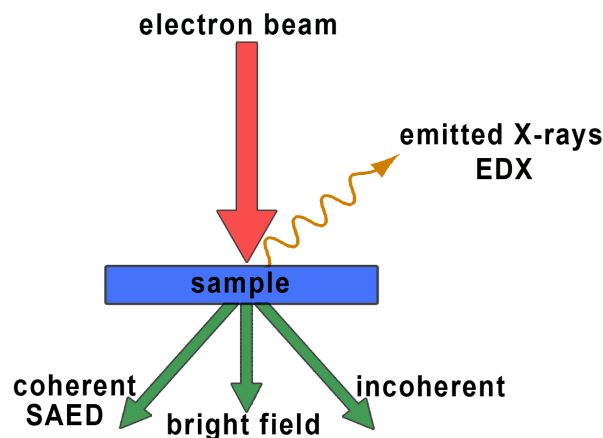


Figure 15: Schematic illustration of selected interactions between electron beam and sample in a transmission electron microscopy (TEM).



## 2.5 Mössbauer spectroscopy

Mössbauer spectroscopy is based on the Mössbauer effect discovered back in 1958. A radioactive source is emitting  $\gamma$ -radiation by transition from an excited state into the ground state. The gamma quantum can be absorbed by a nucleus with the same number of protons and neutrons. If the local environment of the emitting and absorbing nuclei is exactly the same, the nuclear transition energies would be identical. Chemical differences in the local environment of the absorber nucleus lead to tiny energy shifts. The two nuclei can be brought back into resonance by changing slightly the energy of the  $\gamma$ -radiation using the Doppler effect. General three different interactions can be observed:

The isomer shift is caused by the different s-electron densities in the emitting and absorbing atoms. The s-electron density is affected by the oxidation state and the nature of the ligands respectively atoms/ions in the local environment of the absorber atom.

All nuclei with an angular momentum  $I > 1/2$  have a non-spherical charge distribution. This produces an asymmetrical electric field, which splits the nuclear energy levels. A nuclear quadrupole moment is produced. For e.g.  $^{57}\text{Fe}$  the  $3/2$  to  $1/2$  transition is split into two substates ( $m_I = 1/2$  and  $m_I = 3/2$ ) leading to occurrence of a doublet in the spectrum. Quadrupole splitting is measured as the distance between the two observed peaks.

Hyperfine splitting is an interaction between the nucleus and surrounding internal and external magnetic fields. This dipolar interaction is known as Zeeman effect. For e.g.  $^{57}\text{Fe}$  with  $I = 3/2$  and  $1/2$  the signals split into 6 sub-states (Figure 16) so that a sextet is observed in the spectrum.

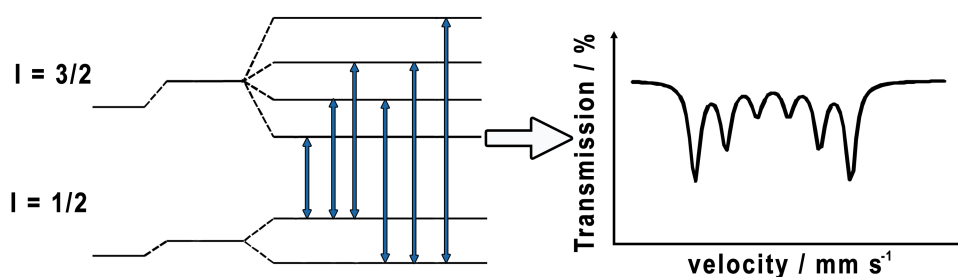


Figure 16: Schematic illustration of the possible transitions in a Mössbauer spectrum, which can be observed for e.g.  $\text{Fe}^{3+}$  ions in a spinel structure.

$^{57}\text{Fe}$  Mössbauer spectroscopic measurements were performed at room temperature using a constant acceleration spectrometer with a  $^{57}\text{Co}(\text{Rh})$  source. Isomer shifts are given relative to that of  $\alpha\text{-Fe}$  at room temperature.

### 2.6 Solid state $^7\text{Li}$ NMR spectroscopy

Atoms with an odd number of protons or neutrons have a nuclear spin which is associated with a magnetic dipole moment. This dipole moment can interact with local and external magnetic fields and thus leads to additional contributions to the energy levels of the nucleus resulting in the so-called Zeeman splitting. Solid state nuclear magnetic resonance (NMR) makes use of transitions between the Zeemann levels and is thus able to probe the interactions of these nuclei with its environment and is able to give information about these environments. Solid state NMR spectra are characterized by very broad lines in comparison to those obtained for liquid samples because of anisotropic interactions in the crystal lattice.<sup>[171]</sup> The anisotropic dipolar interactions can be suppressed by artificial motion of the solid. The sample is rotated around an axis oriented at an angle of  $54.74^\circ$  with respect to the external magnetic field, which is called magic-angle spinning (MAS). The spinning rate must be equal to or larger than the dipolar line width (1 to 100 kHz).<sup>[172,173]</sup>

$^7\text{Li}$  MAS NMR spectroscopy was performed at room temperature on a Bruker Avance 200 MHz spectrometer at a magnetic field of 4.7 T corresponding to a Larmor frequency of  $\nu_L = 77.8$  MHz. A spinning speed of 60 kHz was applied using 1.3 mm rotors in a dry nitrogen atmosphere. An aqueous 1 M LiCl solution served as  $^7\text{Li}$  reference (0 ppm). The typical value for the recycling delay was 1 s.  $^7\text{Li}$  MAS NMR experiments were implemented with a rotor-synchronized Hahn-echo sequence ( $\pi/2$ - $\tau$ - $\pi$ - $\tau$ -acquisition) and a typical  $\pi/2$  pulse length of 2  $\mu\text{s}$ .

### 2.7 Standard methods for sample characterization

Additional various standard characterization methods were performed to investigate the as-prepared and Li/Na containing materials. These methods are: X-ray powder diffraction (XRD), Scanning electron microscope (SEM), energy-dispersive X-ray spectroscopy (EDX), Elemental analysis (EA), Raman spectroscopy, N<sub>2</sub> physical adsorption and atomic absorption spectroscopy (AAS). Table 4 summarizes the equipment for characterization.

**Table 4: Overview of the used equipment.**

Method	Equipment	Description
XRD	PANalytical X'Pert Pro	Reflection geometry, Cu-K <sub>α</sub> and Cu-K <sub>β</sub> radiation (ratio 2:1), pixcel detector
XRD	Stoe Stadi P	Transmission geometry, Mo-K <sub>α</sub> radiation, Mythen 1k detector
SEM/EDX	Philips ESEM XL 30	Scanning electron microscope with EDAX New XL-30 EDX detector
EA	Eurovektor EuroEA Elemental Analyzer	Analysis of carbon, hydrogen, nitrogen and sulphur via combustion analysis, carrier gas: He
Raman	Horiba LaRam Evolution HR	Nd:YAG solid state laser 532 nm (10 mW)
Physical adsorption	BELSORP Max from BEL Japan INC.	N <sub>2</sub> , Samples were activated for 14 h at 200 °C under vacuum (0.1 mbar)
AAS	Perkin Elmer Analyst 3000	Flame atomizer (air-acetylene)
TEM	Tecnai F30 G <sup>2</sup> -STwin	300 kV, field emission cathode, Si/Li detector for nanoprobe EDX
Mössbauer	-	Transmission geometry, γ-ray source: <sup>57</sup> Co(Rh), reference: α-Fe-foil
NMR spectroscopy	Bruker Avance 200 MHz	Magnetic field: 4.7 T, Larmor frequency $\nu_L = 77.8$ MHz, 60 kHz spinning speed with 1.3 mm rotors
CV	Zahner XPot	Potentiostat/galvanostat
Galvanostatic cycling	Material Mates MM510	Potentiostat/galvanostat
Galvanostatic cycling	MTI BST8-MA	8 channel galvanostat

### 3 Publications

#### 3.1 Electrochemical insertion of Li into nanocrystalline $\text{MnFe}_2\text{O}_4$ : A study of the reaction mechanism

In the publication the investigation of the mechanisms occurring during Li uptake of partially inverse spinel  $\text{MnFe}_2\text{O}_4$  nanoparticles is presented. Using X-ray diffraction, in-situ Quick X-ray Absorption Spectroscopy, Mössbauer Spectroscopy, High Resolution Transmission Electron Microscopy,  $^7\text{Li}$ -MAS NMR, and electrochemical measurements the formulation of a detailed reaction mechanism from the beginning of Li uptake is possible. The capacity of the material is 1.5 times larger than expected, an observation made frequently for the type of conversion reactions. During cycling the capacity is decreasing to  $266 \text{ mAh g}^{-1}$  in the 100<sup>th</sup> cycle. At the very early stage of Li uptake  $\text{Fe}^{3+}$  ions located on the tetrahedral site are reduced and simultaneously move to empty octahedral sites. For 1  $\text{Li}/\text{MnFe}_2\text{O}_4$  the X-ray powder pattern could only be refined assuming a two phase mixture: a monoxide formed by movement of the cations from the tetrahedral site to empty octahedral sites and remaining spinel. The formation of the monoxide is accompanied by a decrease of the size of the coherent scattering domains of the spinel. Reaching 2  $\text{Li}/\text{MnFe}_2\text{O}_4$  the reflections of the spinel phase disappeared and only those of the monoxide could be detected via XRD and HRTEM. Increasing the amount of  $\text{Li}/\text{MnFe}_2\text{O}_4$  beyond 2, a conversion reaction occurs. After uptake of 8 Li per f.u. metallic Mn and Fe are embedded in a matrix of  $\text{Li}_2\text{O}$  evidenced by TEM and  $^7\text{Li}$  NMR. Mn, Fe and  $\text{Li}_2\text{O}$  are homogeneously distributed in the discharged material. During charging (Li release) metallic Mn and Fe are oxidized.

Following research article is reproduced by permission of The Royal Society of Chemistry  
**2013**

Original citation:

Stefan Permien, Holger Hain, Marco Scheuermann, Stefan Mangold, Valeriu Mereacre, Annie K. Powell, Sylvio Indris, Ulrich Schürmann, Lorenz Kienle, Viola Duppel, Svenja Harm, Wolfgang Bensch, *RSC Advances*, **2013**, 3, 23001-23014. – published by the Royal Society of Chemistry

DOI:10.1039/c3ra44383c

## Electrochemical insertion of Li into nanocrystalline MnFe<sub>2</sub>O<sub>4</sub>: a study of the reaction mechanism†

Cite this: *RSC Adv.*, 2013, **3**, 23001

Stefan Permien,<sup>a</sup> Holger Hain,<sup>b</sup> Marco Scheuermann,<sup>b</sup> Stefan Mangold,<sup>c</sup> Valeriu Mereacre,<sup>d</sup> Annie K. Powell,<sup>d</sup> Sylvio Indris,<sup>b</sup> Ulrich Schürmann,<sup>e</sup> Lorenz Kienle,<sup>e</sup> Viola Duppel,<sup>f</sup> Svenja Harm<sup>a</sup> and Wolfgang Bensch<sup>a</sup>

The study of the mechanism of Li insertion into nanosized partially inverse spinel MnFe<sub>2</sub>O<sub>4</sub> applying X-ray diffraction, *in situ* quick X-ray absorption spectroscopy, Mössbauer spectroscopy, high resolution transmission electron microscopy, <sup>7</sup>Li MAS NMR, and electrochemical measurements yields a comprehensive picture of the individual steps occurring during Li uptake. At the very early beginning of the reaction Fe<sup>3+</sup> on the tetrahedral site is reduced and moves to empty octahedral sites. Increasing the amount of Li to 0.7 per MnFe<sub>2</sub>O<sub>4</sub>, further Fe<sup>3+</sup> is reduced and Mn<sup>2+</sup> residing on the tetrahedral site moves to empty octahedral sites thus forming a defect NaCl-type structure. At least for 2 Li per MnFe<sub>2</sub>O<sub>4</sub> reflections of the spinel disappeared in the X-ray powder pattern and only those of a monoxide are observed. No indications were found for a phase separation and Fe and Mn are homogeneously distributed over the sample. Further Li uptake leads to a stepwise conversion of the material and after insertion of 8 Li/MnFe<sub>2</sub>O<sub>4</sub> only nanosized Mn, Fe, and Li<sub>2</sub>O are detected. After a capacity loss at the beginning of Li insertion, a constant capacity of about 266 mA h g<sup>-1</sup> is reached after 100 cycles discharging–charging the material.

Received 14th August 2013  
Accepted 23rd September 2013

DOI: 10.1039/c3ra44383c

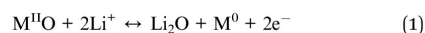
[www.rsc.org/advances](http://www.rsc.org/advances)

### 1. Introduction

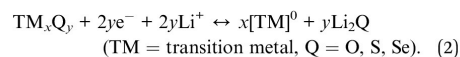
In the search for batteries with higher capacity, faster charging and more power for portable consumer electronics or the next generation of electro-mobility vehicles new materials are intensively investigated.<sup>1–4</sup> The first commercialized lithium-ion battery introduced in 1991 was based on a graphite (Li<sub>x</sub>C<sub>6</sub>) anode and a layered-oxide (LiCoO<sub>2</sub>) cathode.<sup>5</sup> State of the art, challenges and perspectives of Li based batteries were recently reviewed in several articles.<sup>6–13</sup>

Besides investigating the electrochemical properties of a large variety of solids with respect to their performance in Li based batteries, new approaches were developed like hierarchical structuring or nanostructuring of cathode and anode materials. The advantages and disadvantages of nanomaterials

in Li batteries were discussed in detail.<sup>6,14</sup> It was demonstrated that a careful control of the nanoparticle size and shape can greatly improve the performance, capacity and cyclability of nanoparticle based Li batteries.<sup>15</sup> The reaction mechanism of classical Li battery materials like LiCoO<sub>2</sub>/graphite is based on intercalation/deintercalation of Li<sup>+</sup> ions. But it was also reported that so-called “conversion” reactions may be an attractive alternative to the classical reaction mechanism.<sup>16</sup> The reversible electrochemical reaction mechanism of Li with transition-metal oxides like MO (M = Co, Ni, Cu or Fe) proceeds like a displacive redox reaction (eqn (1)).<sup>17,18</sup>



Such conversion reactions are not limited to oxides and they can be generally formulated with eqn (2):



At the end of the conversion reaction nanosized metal particles are embedded in a Li<sub>2</sub>Q matrix. The advantage of such conversion reactions is that specific capacities beyond 500 mA h g<sup>-1</sup> can be achieved because 2y/x Li ions can be converted per TM ion. The capacity is much higher compared to that of commercial electrode materials like LiCoO<sub>2</sub> (160 mA h g<sup>-1</sup>) or graphite (370 mA h g<sup>-1</sup>). A disadvantage of conversion reactions is that the formation of a new phase may lead to large volume changes.

<sup>a</sup>Institute of Inorganic Chemistry, University of Kiel, Max-Eyth-Straße 2, 24118 Kiel, Germany

<sup>b</sup>Institute of Nanotechnology, Karlsruhe Institute of Technology, P.O. Box 3640, 76021 Karlsruhe, Germany

<sup>c</sup>Institute of Synchrotron Radiation, Karlsruhe Institute of Technology, P.O. Box 3640, 76021 Karlsruhe, Germany

<sup>d</sup>Institute of Inorganic Chemistry, Karlsruhe Institute of Technology, Engesser Str. 15, 76131 Karlsruhe, Germany

<sup>e</sup>Institute for Materials Science, University of Kiel, Kaiserstraße 2, 24143 Kiel, Germany

<sup>f</sup>Max-Planck-Institute for Solid Research, Heisenbergstr. 1, 70569 Stuttgart, Germany

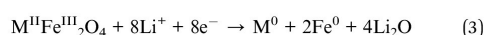
† Electronic supplementary information (ESI) available. See DOI: 10.1039/c3ra44383c

Especially the formation of nanoparticles can lead to side-reactions with the electrolyte resulting in poor calendar life, strong capacity fading, and loss of contact to the current collector.<sup>19</sup>

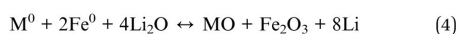
Nevertheless, conversion reactions offer the opportunity to tune the capacity by selecting compounds with TM ions in high oxidation states. Moreover, the strength of the metal–oxygen bond is related to the potential of a battery cell.<sup>15</sup> For a complete conversion reaction of *e.g.* MnO the theoretical value for the capacity amounts to 755 mA h g<sup>-1</sup>. However, a rapid capacity loss after the first cycle was reported in ref. 20. MnO powders with particle sizes of ≈ 1 μm showed the best results after 150 cycles with a reversible capacity of about 650 mA h g<sup>-1</sup>. The capacity loss during the first discharge cycle is related to the conversion reaction and the formation of the solid-electrolyte interface (SEI).<sup>21</sup> For Fe<sub>2</sub>O<sub>3</sub> a theoretical value for the capacity of 1080 mA h g<sup>-1</sup> is reported in ref. 22. The conversion reaction of α-Fe<sub>2</sub>O<sub>3</sub> and γ-Fe<sub>2</sub>O<sub>3</sub> proceeds in the same way,<sup>23</sup> but interestingly using nanosized powders the capacity in first discharge was as high as 1838 mA h g<sup>-1</sup> and remained at the very high level of 900 mA h g<sup>-1</sup> after 50–100 cycles.<sup>24,25</sup>

Spinel AB<sub>2</sub>O<sub>4</sub> may be viewed as a combination of monoxides and sesquioxides containing A<sup>2+</sup> and B<sup>3+</sup> ions on different sublattices. Hence, spinels should be able to combine the properties observed for the monoxides and sesquioxides. Indeed, it was shown that *e.g.* ZnMn<sub>2</sub>O<sub>4</sub> exhibits a good recoverable capacity of about 615 mA h g<sup>-1</sup>,<sup>26,27</sup> while for FeCo<sub>2</sub>O<sub>4</sub> and MgCo<sub>2</sub>O<sub>4</sub> a first charge capacity of 827 mA h g<sup>-1</sup> was reported.<sup>28</sup> These capacities are even more than twice of the theoretical capacity of graphite.

Several investigations with MnFe<sub>2</sub>O<sub>4</sub> nanoparticles as energy storage material were performed in electrochemical capacitors with organic Li<sup>+</sup> or NaCl electrolytes.<sup>29–32</sup> Micron-sized MnFe<sub>2</sub>O<sub>4</sub> octahedra with an average diameter of 1 μm showed capacities between 893 and 972 mA h g<sup>-1</sup> depending on the current density. Such large values correspond to a Li uptake of 7.7 to 8.4 per formula unit.<sup>33</sup> Obviously, the electrochemical uptake of eight lithium ions per formula unit should result in a complete reduction of both Fe and Mn to the metallic state (1 Mn<sup>2+</sup> and 2 Fe<sup>3+</sup>). Until now the conversion reaction pathways of ferrite spinels MFe<sub>2</sub>O<sub>4</sub> (ref. 34–38) with M = Co, Cu, Mg, Ni or Zn were studied using different analytical methods and a general pathway was proposed for the first discharge reaction:



In subsequent charge–discharge cycles reversible redox processes involve Fe and M metals and their oxides:



For M = Zn and Ni intermediates were identified in XRD patterns recorded *ex situ* after insertion of 0.5 and 2 Li per formula unit MFe<sub>2</sub>O<sub>4</sub> (M = Ni or Zn), *i.e.* cubic Li<sub>0.5</sub>MFe<sub>2</sub>O<sub>4</sub> and Li<sub>2</sub>MFe<sub>2</sub>O<sub>4</sub> (ref. 39) but no details on the reaction mechanism were reported.

MnFe<sub>2</sub>O<sub>4</sub> is a partially inverse spinel and the percentage of the A site occupied by Fe<sup>3+</sup> determines the degree of inversion.<sup>40</sup>

The Mn<sup>2+</sup>/Fe<sup>3+</sup> distribution depends on the size of the particles, the synthesis route and the temperature.<sup>40–42</sup>

While a number of spinel-type materials were investigated with respect to the electrochemical performance as conversion materials as anode or cathode, detailed investigations of the individual reaction steps occurring during the conversion are scarce. To establish detailed reaction mechanisms starting from the very early beginning of Li uptake up to full conversion a variety of complementary analytical tools must be used probing the long-range and local structural properties, the electronic and chemical/compositional changes during discharge of the material. Here we report a detailed reaction mechanism for the conversion of MnFe<sub>2</sub>O<sub>4</sub> during Li uptake obtained by X-ray powder diffraction (XRD), energy dispersive X-ray (EDX), atomic absorption spectroscopy (AAS), transmission electron microscopy (TEM), Mössbauer spectroscopy, X-ray absorption spectroscopy (XAS), cyclic voltammetry (CV), and <sup>7</sup>Li NMR spectroscopy.

## 2. Experimental section

### 2.1 Synthesis

All chemicals were of analytical grade and used without purification. The MnFe<sub>2</sub>O<sub>4</sub> nanoparticles were synthesized in an easy “bottom up” approach. 4.5 mmol MnCl<sub>2</sub>·4H<sub>2</sub>O (99%, Merck) and 9.0 mmol FeCl<sub>3</sub>·6H<sub>2</sub>O (98%, Grüssing) were dissolved in 30 mL distilled water. The solution was slowly dropped into 40 mL of 4 M NaOH solution. Afterwards the solution was stirred under reflux for 2 h. The black powder was filtered, washed with water, and dried for 24 h at 80 °C.<sup>42</sup> AAS and EDX analyses yield Mn to Fe ratios of 1 : 2 (ESI<sup>†</sup>) in accordance with the expected composition.

The MnFe<sub>2</sub>O<sub>4</sub> bulk material was synthesized in a high-temperature reaction. A stoichiometric mixture of MnO (99.99%, ABCR) and Fe<sub>2</sub>O<sub>3</sub> (99%, Grüssing) was treated in a ball mill for 1 h (Fritsch Pulverisette, with 15 mm agate balls, at 100 rpm in air) and pressed into a pellet which was sintered in an evacuated silica glass ampoule at 1200 °C for 2 days and quenched in ice-cold water.<sup>43</sup> Afterwards the product was ground in a ball mill for 10 min at 500 rpm.

### 2.2 Materials characterisation

XRD patterns of MnFe<sub>2</sub>O<sub>4</sub> nanoparticles and bulk material were recorded on a X'PERT PRO PANalytical instrument with a Göbel mirror and PIXcel detector using Cu radiation. SEM images and EDX spectra were obtained using a Philips ESEM XL 30 equipped with an EDX detector from EDAX. Atomic absorption spectroscopy (AAS) was performed with a Perkin Elmer Analyst 3000 system. TEM investigations were performed in a Tecnai F30 G<sup>2</sup>-STwin microscope at 300 kV with a field emission gun cathode and a Si/Li detector (Thermo Fisher, NSS). For TEM preparation, MnFe<sub>2</sub>O<sub>4</sub> nanoparticles were suspended in *n*-butanol and treated in ultrasonic bath to induce particle separation and the dispersion was dropped onto a holey-carbon copper grid.



### 2.3 Electrochemical measurements

For the electrochemical characterization 80 wt%  $\text{MnFe}_2\text{O}_4$  was mixed with 10 wt% SP Carbon (Timcal, Suisse) and 10 wt% PVDF as binder. The compounds were mixed with *N*-methyl-2-pyrrolidone, painted on copper foil, dried over night at room temperature and sintered at 90 °C for 12 h. Afterwards 14 mm discs were cut with about 2 mg of active material. Test cells were discharged with 80–100 mA being equivalent to 8 Li per formula unit  $\text{MnFe}_2\text{O}_4$  in 20 h. Cyclic voltammetry and galvanostatic charge–discharge experiments were performed with a Biologic VMP3 potentiostat/galvanostat.

For XRD and NMR experiments on lithiated samples, pure  $\text{MnFe}_2\text{O}_4$  powder was used as the cathode in a Swagelok type test cell, using lithium metal as the anode, glass fiber filter disks (Whatman, UK) as the separator, and a solution of 1 M  $\text{LiPF}_6$  in an ethylene carbonate–dimethyl carbonate mixture (Ferro Fine Chemicals, USA) as electrolyte. The cells were assembled in an argon filled glove box (<1 ppm  $\text{O}_2$ , <1 ppm  $\text{H}_2\text{O}$ ). A test cell was discharged with 500  $\mu\text{A h}^{-1}$  until the desired formal composition  $\text{Li}_x\text{MnFe}_2\text{O}_4$  ( $x = 0.5, 1, 1.5, 2, 8$  and 9.5) was reached. Experiments were performed with a Materials Mates 510 DC. The cells were opened in the glove box (<1 ppm  $\text{O}_2$ , <1 ppm  $\text{H}_2\text{O}$ ) and the recovered powders were used for further measurements without purification. Typically 25 mg of Li containing powder could be obtained in a 10 mm Swagelok cell. The materials were transferred to an iron sample holder and protected with a Kapton foil.

For Mössbauer experiments on lithiated samples,  $\text{MnFe}_2\text{O}_4$  powder was mixed with 20% conductive carbon. The test cell was discharged with C/20 rate, *i.e.* insertion of 8 lithium ions per formula unit within 20 hours, until a cut-off potential of 0.8, 0.5, or 0.05 V was reached. Subsequently, the cells were opened in the glove box and the powder was used for further measurements without purification. Typically 30 mg of the material could be obtained in a 12 mm Swagelok cell.

### 2.4 Characterization of the lithiated samples

The *in situ* analysis of the oxidation state of Fe and Mn during Li uptake was performed at the XAS beamline of the synchrotron ANKA (Karlsruhe, Germany) in special battery cells. A polyimide foil with a thickness of 25  $\mu\text{m}$  (Goodfellow, UK) was used as window material. The active material film consisting of 60%  $\text{MnFe}_2\text{O}_4$ , 20% conductive carbon, and 20% PVDF as a binder was cast on a sputtered gold film of 20 nm thickness on one of the polyimide foils. Lithium metal was used as anode, porous polyethylene–polypropylene foil (Celgard, USA) was used as separator, and the electrolyte was a solution of 1 M  $\text{LiPF}_6$  in ethylene carbonate–dimethyl carbonate. During repeated quick-XAFS scans of both the Mn and Fe K absorption edge at 6.55 and 7.12 keV, respectively, this cell was discharged with a rate of C/10 using a  $\mu\text{III}$ -Autolab (Metrohm, Switzerland). The energy was calibrated using a Fe foil and checked before and after the measurement. The fluorescence XAFS data were corrected for the background and normalized. XRD measurements of the intercalated samples were recorded on the X'PERT PRO PANalytical instrument mentioned above.  $^7\text{Li}$  magic-angle spinning (MAS)

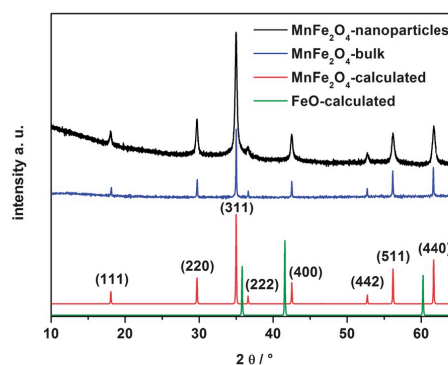
NMR was performed at room temperature on a Bruker Avance 200 MHz spectrometer at a magnetic field of 4.7 T corresponding to a Larmor frequency of  $\nu_L = 77.8$  MHz. A spinning speed of 60 kHz was applied using 1.3 mm rotors in a dry nitrogen atmosphere. A 1 M LiCl solution served as  $^7\text{Li}$  reference (0 ppm). The typical value for the recycling delay of  $^7\text{Li}$  was 1 s.  $^7\text{Li}$  MAS NMR experiments were implemented with a rotor-synchronized Hahn-echo sequence ( $\pi/2$ – $\tau$ – $\pi$ – $\tau$ –acquisition) and a typical  $\pi/2$  pulse length of 2  $\mu\text{s}$ . SAED (selected area electron diffraction) patterns and high resolution images of intercalated samples were taken with a Phillips CM30/ST microscope (operated at 300 kV,  $\text{LaB}_6$  cathode) using a GATAN slow scan CCD camera. Larger magnetic particles were removed before the observation with the aid of a magnet. The specimens were prepared by grinding the samples in Ar atmosphere and spreading the powders onto a perforated carbon film supported by a copper grid. For elemental analyses by EDX performed in the TEM a nanoprobe mode was adjusted (Si/Li detector, system Noran NSF 7).

## 3. Results

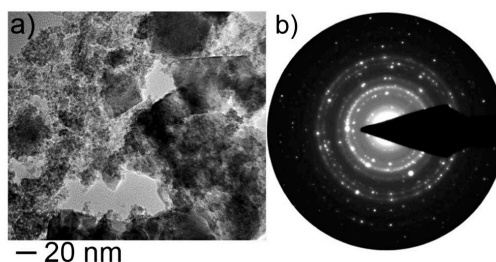
### 3.1 Characterisation of the $\text{MnFe}_2\text{O}_4$ bulk material and nanoparticles

Fig. 1 shows the XRD patterns of nanosized and bulk  $\text{MnFe}_2\text{O}_4$  together with the calculated diagram. The patterns of both samples show only reflections of cubic  $\text{MnFe}_2\text{O}_4$  in the pristine material and no reflections of FeO or any other impurity could be observed. The reflections of the nanoparticles are significantly broadened compared to the bulk material indicating coherent scattering domains in the nanoregime.

The average size of the coherent scattering domains was estimated from the X-ray powder pattern using the fundamental approach implemented in the TOPAS-5 software<sup>44</sup> yielding 37(2) nm for the domain size. The refined lattice parameter  $a$  of 8.491(1) Å is in good agreement with the value of 8.4983 Å reported in ref. 45. For smaller particles with an average size of 9 nm the value for  $a$  was 8.499 Å.<sup>42</sup>



**Fig. 1** XRD patterns of the prepared nanoparticles and bulk material. The calculated X-ray pattern of  $\text{MnFe}_2\text{O}_4$  is shown for comparison and the calculated X-ray pattern of FeO is included to demonstrate the absence of FeO in the pristine materials.



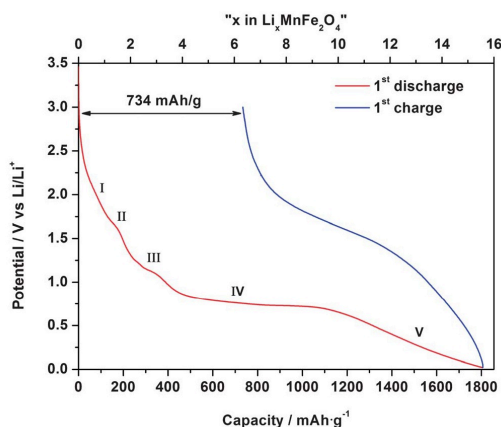
**Fig. 2** (a) TEM bright field image of a pristine  $\text{MnFe}_2\text{O}_4$  sample showing bimodal size distribution of the particles; (b) corresponding SAED pattern.

Fig. 2a shows a TEM bright field image of the pristine nanoparticles. As can be seen the sample is characterized by a bimodal size distribution of particles. Nanoprobe EDX analyses gave no indication for a chemical inhomogeneity, *i.e.* larger and smaller nanoparticles can be both assigned to the spinel-type phase of  $\text{MnFe}_2\text{O}_4$ . The smaller nanoparticles forming aggregates show typical sizes below 5 nm. These particles were not observed in XRD analyses due to strong confinement of the coherently scattering areas.

In contrast, the nearly rectangular and larger particles exhibit an average particle size of 37 nm as determined *via* statistical analysis, and this value matches well with that obtained from Rietveld refinement. The coexistence of larger and smaller spinel-type particles is additionally supported *via* SAED (Fig. 2b, TEM). The Bragg reflections and diffuse intensity (for the smaller nanoparticles) each on concentric circles can be assigned to larger and smaller nanoparticles, respectively.

### 3.2 Electrochemical performance of the $\text{MnFe}_2\text{O}_4$ nanoparticles compared to its bulk counterpart

The first discharge curve of nanocrystalline  $\text{MnFe}_2\text{O}_4$  shows five regions (Fig. 3). In the first region (region I) the potential drops



**Fig. 3** First discharge and charge curve of nanocrystalline  $\text{MnFe}_2\text{O}_4$  against  $\text{Li}|\text{Li}^+$ . The capacity is shown in the bottom axis and the corresponding Li uptake in the top.

fast. The insertion of one  $\text{Li}^+$  in  $\text{MnFe}_2\text{O}_4$  corresponds to a capacity of  $116 \text{ mA h g}^{-1}$ , suggesting that less than 1 Li is inserted in the first reaction step. A not well resolved “plateau” appears at about 1.7 V with a length of *ca.*  $70 \text{ mA h g}^{-1}$  (region II), followed by a longer plateau ( $114 \text{ mA h g}^{-1}$ , region III) at 1.15 V, and the fourth one at about 0.7 V with a length of about  $702 \text{ mA h g}^{-1}$  (region IV). After the long plateau there is a fifth region with a length of about  $680 \text{ mA h g}^{-1}$ .

For bulk  $\text{MnFe}_2\text{O}_4$ , only two plateaus can be identified with the first one occurring at 1.15 V being much smaller (length:  $20 \text{ mA h g}^{-1}$ ) than region II of the nanosized material (Fig. S1†). The second plateau at a slightly lower voltage of 0.6 V has a length of about  $389 \text{ mA h g}^{-1}$ , corresponding to an uptake of 3.4 Li (Fig. S1†). The present observations are in remarkable contrast to that reported in ref. 33 where only one long plateau at about 0.7 V was observed with a corresponding capacity of  $893 \text{ mA h g}^{-1}$  ( $0.1 \text{ mA cm}^{-2}$ ) or  $972 \text{ mA h g}^{-1}$  ( $0.2 \text{ mA cm}^{-2}$ ). The former value corresponds to an uptake of 7.7  $\text{Li}^+$  and the latter to 8.4  $\text{Li}^+$  per formula unit. The theoretical discharge capacity is about  $933 \text{ mA h g}^{-1}$  per mole  $\text{MnFe}_2\text{O}_4$  assuming a full conversion of  $\text{Mn}^{2+}$  and  $\text{Fe}^{3+}$  to the metals. Our nanocrystalline  $\text{MnFe}_2\text{O}_4$  sample shows an entire capacity of  $1806 \text{ mA h g}^{-1}$  which is almost twice of the bulk material and much larger than expected. Similar high values were reported for other nanosized oxides like  $\text{CoMn}_2\text{O}_4$  ( $1650 \text{ mA h g}^{-1}$ ),<sup>46</sup>  $\text{CoFe}_2\text{O}_4$  ( $1782 \text{ mA h g}^{-1}$ )<sup>35</sup> or  $\text{ZnFe}_2\text{O}_4$  ( $1805 \text{ mA h g}^{-1}$ ).<sup>37</sup> The extra capacity is most likely caused by irreversible reactions with the electrolyte when the potential approaches 0 V vs.  $\text{Li}|\text{Li}^+$  forming passivating layers on the surface of the particles, *i.e.* the formation of a solid electrolyte interface (SEI).<sup>21,47</sup>

In the first charge curves no distinct plateaus occur at about 1.5 V for the bulk material and at 1.75 V for the nanomaterial. This behaviour may be explained by the oxidation of metallic Mn and Fe to  $\text{MnO}$  and  $\text{Fe}_2\text{O}_3$ , respectively.<sup>34–39,48</sup> After the first discharge–charge cycle the capacity loss of the bulk material is  $563 \text{ mA h g}^{-1}$ , *i.e.* the reversible capacity is  $410 \text{ mA h g}^{-1}$  (42%), while the reversible capacity of nanocrystalline  $\text{MnFe}_2\text{O}_4$  amounts to  $1070 \text{ mA h g}^{-1}$  (59%, irreversible capacity loss:  $734 \text{ mA h g}^{-1}$ ) corresponding to an uptake of 9.2  $\text{Li}^+$  per formula unit. The 1.2 excess  $\text{Li}^+$  may be reversibly inserted into the conductive carbon, or it may be adsorbed at the large surface of the small nanoparticles.<sup>49–51</sup>

During further cycling the first two plateaus disappeared for both materials and the potential decreased continuously until a potential of about 0.7 V was reached (Fig. 4).

In addition, the capacity dropped during the first discharging–charging cycles reaching a constant value of  $250 \text{ mA h g}^{-1}$  for the nanosized spinel and  $240 \text{ mA h g}^{-1}$  for the bulk material (Fig. 5). At the beginning of the cycling the nanoparticles exhibit a higher capacity than the microcrystalline sample.

After about 60 cycles the capacity of the nanomaterial slightly increases reaching  $266 \text{ mA h g}^{-1}$  after 100 cycles. The  $\text{MnFe}_2\text{O}_4$  nanoparticles seem to perform slightly better than bulk material which may be explained by the smaller particle sizes. The slight increase of the capacity after 60 cycles may be due to the formation of more interfaces where some excess Li can be stored.<sup>49–51</sup>



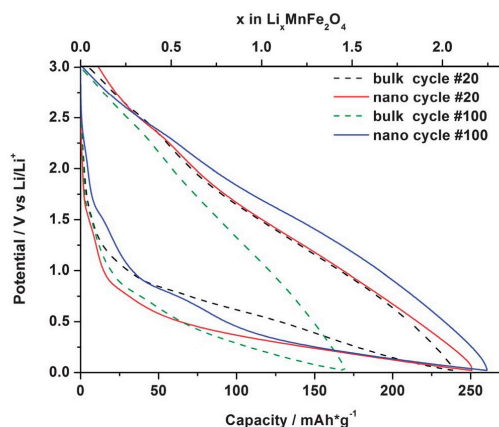


Fig. 4 Discharge and charge curves of bulk and nanocrystalline  $\text{MnFe}_2\text{O}_4$  during cycles number 20 and 100.

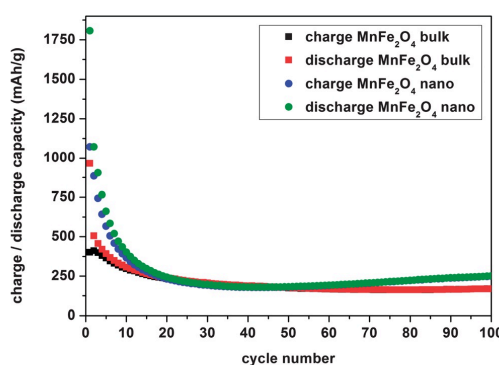


Fig. 5 Capacity as a function of cycle number for nanocrystalline and bulk  $\text{MnFe}_2\text{O}_4$ .

Fig. 6 shows the cyclic voltammograms for  $\text{MnFe}_2\text{O}_4$  nanoparticles against Li metal at different sweep rates and different voltage windows. Cycling in the large voltage window from 0.05 to 4.5 V leads to a strong capacity fading even at a slow rate of  $0.1 \text{ mV s}^{-1}$ . The broad cathodic and anodic peaks at 0.5 and 1.9 V, respectively, show a strong fading during progressive cycling.

A second anodic peak at about 2.0 V corresponds to the short plateaus observed during galvanostatic cycling (Fig. 6) and is visible only in the very first few cycles. Reducing the voltage window to 0.5–4.5 V results in a strong improvement of the cycling stability, even at an enhanced sweep rate of  $1 \text{ mV s}^{-1}$ . Stable cathodic and anodic peaks are visible at 1.5 and 2.4 V, respectively. A further reduction of the voltage window (1.0 to 4.0 V) leads to even better reversibility. Cycling with a high rate of  $10 \text{ mV s}^{-1}$  results in a very stable behaviour with the cathodic and anodic peaks being shifted to even lower ( $<1.0 \text{ V}$ ) and higher voltages (2.9 V), respectively.

### 3.3 *Ex situ* XRD on lithiated nanocrystalline $\text{MnFe}_2\text{O}_4$

Fig. 7 shows the *ex situ* XRD patterns of pure nanocrystalline  $\text{MnFe}_2\text{O}_4$  after electrochemical insertion of 0.5, 1, 1.5, 2, 8, and 9.5 Li per formula unit and after a full charge–discharge cycle.

It is essential to note that for these experiments no binders and no carbon were added to the material. After insertion of 0.5 Li (Fig. 3, region I) and 1 Li (beginning of region II) all peaks shift to lower scattering angles which is typical for an intercalation process leading to an expansion of the unit cell dimensions. For  $\text{Li}_{0.5}\text{MnFe}_2\text{O}_4$  the refined value for the  $a$ -axis of  $8.516(1) \text{ \AA}$  (expansion:  $\approx 0.3\%$ ) is larger than for the pristine material. The average size of the coherent scattering domains decreased to  $28(1) \text{ nm}$ . Increasing the Li content to 1 per formula unit required a two phase refinement of the powder pattern. The second phase was identified as monoxide, *i.e.* a substitutional mixed crystal  $\text{MnFe}_2\text{O}_3$  (with cubic symmetry, space group:  $Fm\bar{3}m$ ) where the metal cations are octahedrally coordinated by  $\text{O}^{2-}$  ions with a slightly larger Mn/Fe–O bond length compared to the spinel-type phase (FeO:  $2.144 \text{ \AA}$ ; MnO:  $2.226 \text{ \AA}$ ;  $\text{MnFe}_2\text{O}_4$ :  $2.129 \text{ \AA}$  for Fe–O and  $1.844 \text{ \AA}$  for Mn–O).<sup>52</sup> The lattice parameter of the spinel is further enlarged to  $a = 8.542(1) \text{ \AA}$  (expansion:  $\approx 0.6\%$ ) while the size of coherently scattering domains remains constant ( $28(1) \text{ nm}$ ). The  $a$ -axis value for the monoxide was refined to  $4.291(1) \text{ \AA}$  and the crystallite size to  $8.3(3) \text{ nm}$ . According to the observation that a monoxide is formed if 1 Li per formula unit is introduced, the pattern of  $\text{Li}_{0.5}\text{MnFe}_2\text{O}_4$  was also refined with two phases. The data for the spinel phase are identical with the single phase refinement and for the monoxide the  $a$ -axis was obtained as  $4.298(4) \text{ \AA}$  with an average domain size of  $3.0(2) \text{ \AA}$ . The assumption that a monoxide is formed for low Li uptake is justified by the decrease of the pre-edge feature in the XANES spectra even at very low Li insertion (see below).

A further decrease of the intensity of the reflections of the spinel occurs for the sample containing 1.5 Li per formula unit (region II), while the intensity of the reflections of the monoxide increased. The two phase Rietveld refinement yields  $a = 8.551(2) \text{ \AA}$  (expansion:  $\approx 0.71\%$ ) for the spinel with a size of the coherent scattering domains of  $19(1) \text{ nm}$ . The  $a$ -axis length of the monoxide was determined to be  $4.299(1) \text{ \AA}$  and the domain size is  $15.7(3) \text{ nm}$ . In the powder pattern of the sample with 2 Li per formula unit (region III) it cannot be decided whether small amounts of the spinel phase still exist. Hence the powder pattern was refined either with two phases or with the monoxide only. For the two phase refinement the estimated standard deviations obtained for the spinel phase are very large indicating that the amount of  $\text{MnFe}_2\text{O}_4$  is very low. Hence the pattern was refined with only one phase yielding  $a = 4.303(1) \text{ \AA}$  and  $22(1) \text{ nm}$  for the domain size. The XRD patterns of the samples after insertion of 4 and 6 Li per formula unit show a decrease of the intensity of the peaks of the monoxides during the long plateau at about 0.7 V (see Fig. 3, region IV), while in the pattern of the sample with 8 Li/ $\text{MnFe}_2\text{O}_4$  (beginning of region V) very weak peaks are seen, and finally no reflections can be detected for the material containing 9.5 Li per formula (end of region V). The very broad peak at  $44^\circ 2\theta$  could belong to metallic Mn or Fe. During

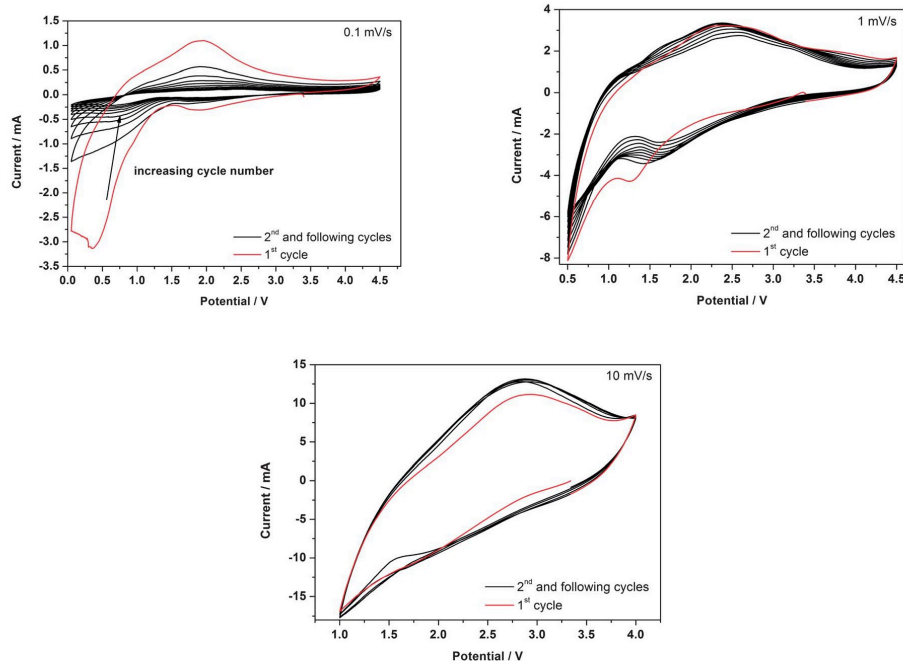


Fig. 6 Cyclic voltammetry on nanocrystalline  $\text{MnFe}_2\text{O}_4$  for different sweep rates and different voltage ranges.

the long plateau at 0.7 V the monoxides are converted to an amorphous product or the crystallites are too small to be detected by XRD. After the first full charge–discharge cycle no crystalline phases could be detected.

### 3.4 *In situ* quick EXAFS on nanocrystalline $\text{MnFe}_2\text{O}_4$

The K absorption edges of Fe and Mn have only a small energy difference of about 0.6 keV allowing quick EXAFS measurements in just one cell. The beam was optimized for an energy of 7 keV and the K edge absorption spectra of Mn and Fe were measured subsequently during battery cycling. The discharge curve monitored simultaneously shows features similar to those obtained from the Swagelok-type cell for *ex situ* XRD experiments, but the pronounced plateau below 0.8 V is not visible (see Fig. 8a). This is ascribed to the less effective cycling in the *in situ* cells where the regions irradiated by the X-ray beam are not compressed by a spring and therefore full conversion is not reached.

The XANES spectra of nanocrystalline  $\text{MnFe}_2\text{O}_4$  are shown in Fig. 8b and c. The maximum for the Mn K-edge is at 6558 eV, the threshold energy at 6550 eV and the pre-edge peak is located at 6541 eV (Fig. 8b). The analogous values for the Fe K-edge are at 7132 eV, 7127 eV, and 7114 eV. These values match exactly those reported for  $\text{Fe}^{3+}$  and  $\text{Mn}^{2+}$  in  $\text{MnFe}_2\text{O}_4$  nanoparticles.<sup>53,54</sup>

In XAFS spectra the shape, intensity, and position of pre-edge peaks deliver information about the local symmetry and oxidation state of the absorber atom. Such pre-edge peaks are

caused by  $1s \rightarrow 3d$  transitions and are very weak for absorbers in a centrosymmetric environment. A reduction of the local symmetry leads to more intense pre-edge features due to  $3d-4p$  mixing as well as mixing between metal d states with ligand p states.

The occurrence of the pre-edge peak in both spectra demonstrates the presence of  $\text{Mn}^{2+}$  and  $\text{Fe}^{3+}$  ions on the tetrahedral site (*cf.* Mössbauer spectra).<sup>55</sup> During discharge both absorption spectra exhibit changes of the shape and the maximum of the absorption edge. The alteration of the different spectral features can be observed from the beginning of the discharge at both edges. The intensity of the Mn pre-edge feature at 6541 eV is reduced continuously and the maximum absorption moves to lower energies (see Fig. 8b). A similar behaviour is observed for the Fe XANES spectra (see Fig. 8c). The drop of the intensity of the pre-edge peaks is a clear hint that the symmetry around the absorber atoms is changing, *i.e.*  $\text{Mn}^{2+}/\text{Fe}^{3+}$  move from the tetrahedral site to the more symmetric octahedral site. The edge position of the Fe K-edge shifts from the beginning of the electrochemical insertion reaction, while a significant shift of the Mn K-edge occurs at later stages of Li uptake. Such a decrease is expected for the reduction of the transition metal centres.<sup>53,56,57</sup>

The spectra also show isosbestic points at 6543.2 eV and 6557.0 eV for Mn during Li uptake (Fig. 8b), indicating that this reaction involves two local environments at equilibrium, being in agreement with  $\text{Mn}^{2+}$  in tetrahedra and octahedra. At the

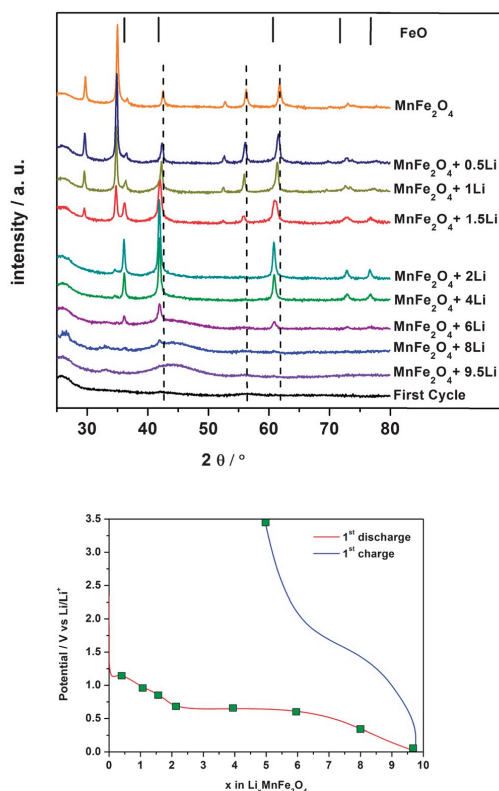


**Fig. 7** XRD patterns of nanocrystalline  $\text{MnFe}_2\text{O}_4$  after insertion of 0.5, 1, 2, 8, and 9.5 Li and after the first discharge–charge cycle. Bottom: electrochemical voltage profile during the first discharge–charge cycle of  $\text{MnFe}_2\text{O}_4$ . Green squares mark the point where the inset was stopped for XRD measurements.

beginning of Li insertion no such isosbestic points are visible for the Fe K-edge spectra. But for the spectra acquired at 1.0 V and lower voltages an isosbestic point is visible at 7115.6 eV, suggesting that also Fe centres are present in two distinct chemical environments, *i.e.*  $\text{Fe}^{2+}$  and elemental Fe may be present at this stage of the reaction.

### 3.5 $^{57}\text{Fe}$ Mössbauer spectra of nano, bulk and lithiated samples

The room-temperature  $^{57}\text{Fe}$  Mössbauer spectrum (Fig. 9a) of the nanocrystalline sample consists of a broad sextet and a central doublet with broadened lines, suggesting a mixture of magnetic and superparamagnetic particles with the isomer shift values,  $\delta$ , being characteristic for  $\text{Fe}^{3+}$  (Table 1). The very small value for the quadrupole splitting of the doublet is typical for  $\text{Fe}^{3+}$  in a highly symmetric environment. The broad asymmetric lines of the sextet have to be described in terms of a distribution of hyperfine fields with a maximum at 45 T (Fig. 9a). This Mössbauer spectrum is very similar to that of  $\text{MnFe}_2\text{O}_4$

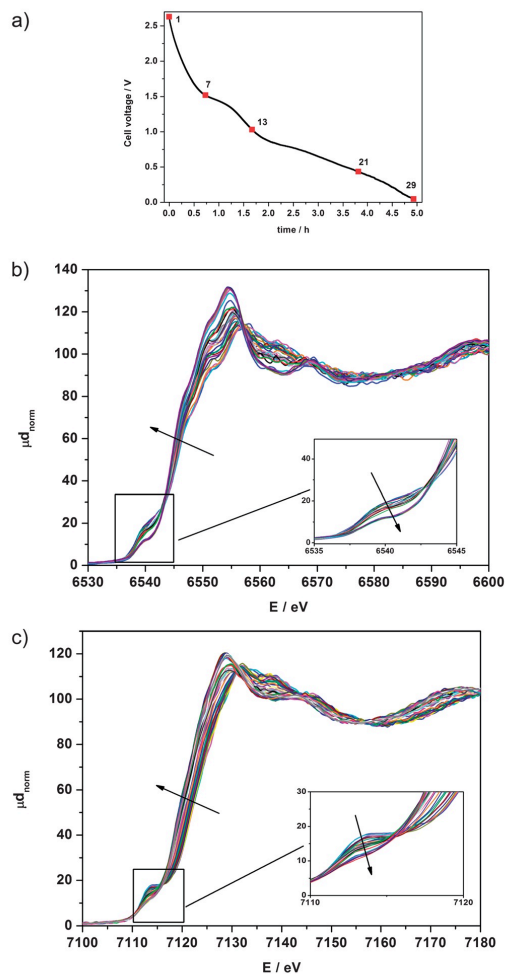


**Fig. 8** (a) Voltage profile and *in situ* XAS measurements on (b) Mn K-edge and (c) Fe K-edge of nanocrystalline  $\text{MnFe}_2\text{O}_4$  during discharging against  $\text{Li}^+/\text{Li}$ .

nanoparticles (4 nm and 50 nm) published in ref. 42. In other studies, for very small particles of  $\approx 16$  nm size the sextet was not observed in the room temperature spectrum and just two doublets with slightly different quadrupole splitting were seen<sup>58</sup> while in another investigation of particles with a size of 7.4 nm only one doublet could be detected.<sup>59</sup> The absence of the sextet in the spectra was explained with the presence of superparamagnetic particles. In contrast, bulk  $\text{MnFe}_2\text{O}_4$  shows just a broadened sextet without the central doublet (Fig. 9b), also reported in literature for samples calcinated at 1150 °C and 1300 °C.<sup>60</sup>

At 3 K, a magnetic ordering (sextet) is seen in the Mössbauer spectrum both for nanocrystalline and bulk  $\text{MnFe}_2\text{O}_4$  (Fig. 10, upper spectra) confirming that these particles are  $\text{MnFe}_2\text{O}_4$ . The

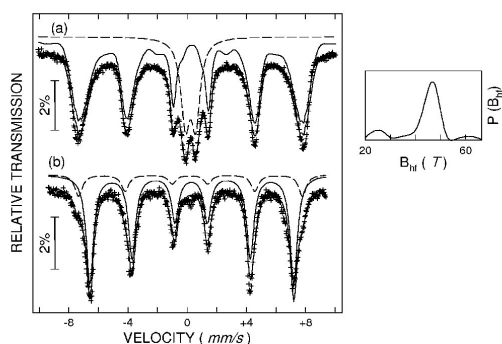


**Fig. 9** Mössbauer spectrum of (a) nanocrystalline and (b) bulk  $\text{MnFe}_2\text{O}_4$  reference sample measured at room temperature.

broadened absorption lines imply that the sextet is a superposition of two individual sextets corresponding to tetrahedral (A) and octahedral (B)  $\text{Fe}^{3+}$  contributions. But the resolution is not

good enough to evaluate the relative fractions of these two contributions. To separate the absorption lines caused by  $\text{Fe}^{3+}$  on A and B sites, an external magnetic field was applied to the sample perpendicular to the  $\gamma$ -ray direction, allowing resolving the hyperfine structure into well-defined two-site absorption lines (sextets), as expected for the ferrimagnetic behaviour of  $\text{MnFe}_2\text{O}_4$  (Fig. 10, lower spectra). The Mössbauer spectra of the samples were evaluated by a least-squares fitting to two hyperfine sextets of the following model,  $(\text{Mn}_x\text{Fe}_{1-x})_A[\text{Mn}_{1-x}\text{Fe}_{1+x}]_B\text{O}_4$ , where the subscripts A and B denote the tetrahedral and octahedral sites, respectively. For bulk  $\text{MnFe}_2\text{O}_4$  the fitting procedure suggests a distribution of cations according to  $(\text{Mn}_{0.89}\text{Fe}_{0.11})_A[\text{Mn}_{0.11}\text{Fe}_{1.89}]_B\text{O}_4$  (Table 1). We note that different distributions for  $\text{Mn}^{2+}/\text{Fe}^{3+}$  were reported like  $(\text{Mn}_{0.81}\text{Fe}_{0.19})_A[\text{Mn}_{0.19}\text{Fe}_{1.81}]_B\text{O}_4$  or  $(\text{Mn}_{0.86}\text{Fe}_{0.20})_A[\text{Mn}_{0.20}\text{Fe}_{1.80}]_B\text{O}_4$ .<sup>61,62</sup> For nanosized  $\text{MnFe}_2\text{O}_4$  the inversion degree is even higher  $(\text{Mn}_{0.71}\text{Fe}_{0.29})_A[\text{Mn}_{0.29}\text{Fe}_{1.71}]_B\text{O}_4$ , and depending on the synthesis conditions and particle sizes the presence of nearly inverse spinels were also reported in literature.<sup>40,42,53,58,61–63</sup>

The values for the isomer shift of bulk and nano  $\text{MnFe}_2\text{O}_4$  fit well to  $\text{Fe}^{3+}$ .<sup>62</sup> The linewidth of nanocrystalline  $\text{MnFe}_2\text{O}_4$  is

**Table 1** Fitted in-field Mössbauer parameters for nanocrystalline and bulk  $\text{MnFe}_2\text{O}_4$  particles at 3 K and applied field of 4 T: isomer shift ( $\delta$ ) relative to  $\alpha$ -Fe at 300 K, quadrupole shift ( $\epsilon$ ), line width ( $\Gamma$ ), effective  $H_{\text{eff}}$  and hyperfine  $H_{\text{hyp}}$  fields,  $\theta$  – angle between  $H_{\text{eff}}$  and direction of  $\gamma$ -rays, and relative proportion of each  $\text{Fe}^{\text{III}}$  component with A-sites tetrahedral and B-sites octahedral lattice

Site	$\delta$ , $\text{mm s}^{-1}$	$\epsilon$ , $\text{mm s}^{-1}$	$\Gamma$ , $\text{mm s}^{-1}$	$\theta$ , $^\circ$	$H_{\text{eff}}$ , T	$H_{\text{hyp}}$ , T	Ratio, %
<b>Nanocrystalline</b>							
A	0.44(1)	0.03(1)	0.58(1)	63.9 <sup>a</sup>	56.1	52.1	29.5
B	0.46(1)	−0.01(1)	0.73(1)	63.9 <sup>a</sup>	48.7	52.7	70.5
<b>Bulk</b>							
A	0.41(1)	−0.01(1)	0.40(1)	60.3 <sup>a</sup>	56.1	52.1	11.0
B	0.51(1)	0.01(1)	0.58(1)	60.3 <sup>a</sup>	47.4	51.4	89.0

<sup>a</sup> Constrained to the same value for both sites.

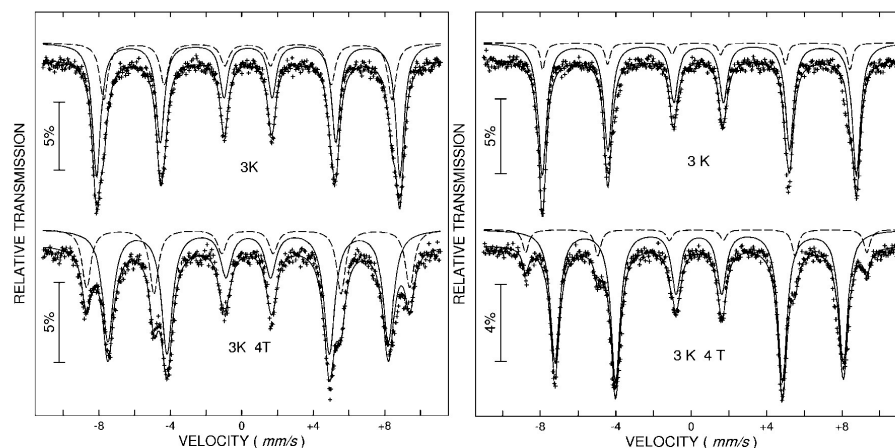


**Fig. 10** Fe Mössbauer spectra of nanocrystalline (left) and bulk (right)  $\text{MnFe}_2\text{O}_4$  at 3 K with an external field of 4 T (bottom) and without field.



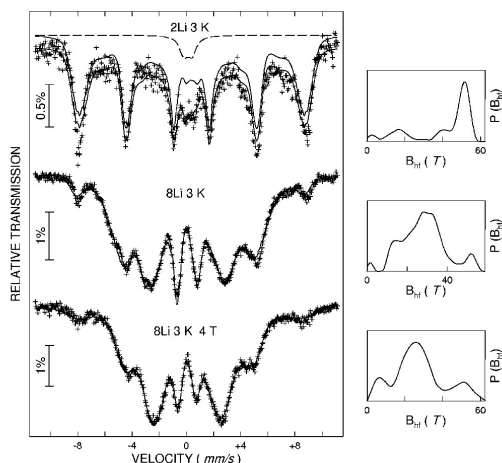


**Fig. 11** Fe Mössbauer spectra of  $\text{MnFe}_2\text{O}_4$  after insertion of 2 and 8 Li at 3 K and applied field 4 T.

about  $0.2 \text{ mm s}^{-1}$  larger than that of the bulk material (Table 1), which was also reported for, *e.g.*, nanosized  $\text{Fe}_2\text{O}_3$  (ref. 64) or  $\text{CuFe}_2\text{O}_4$ ,  $\text{MnFe}_2\text{O}_4$ , and  $\text{NiFe}_2\text{O}_4$ .<sup>64</sup>

The Mössbauer spectrum acquired at 3 K and zero field after insertion of 2 Li (Fig. 11) consists of a broad sextet with hyperfine parameters similar to those obtained for pristine nanocrystalline and bulk samples and a broad central onset.

The central onset might be assigned to FeO paramagnetic particles also observed in the XRD pattern. This is also supported by the spectrum at room temperature (Fig. 12), which

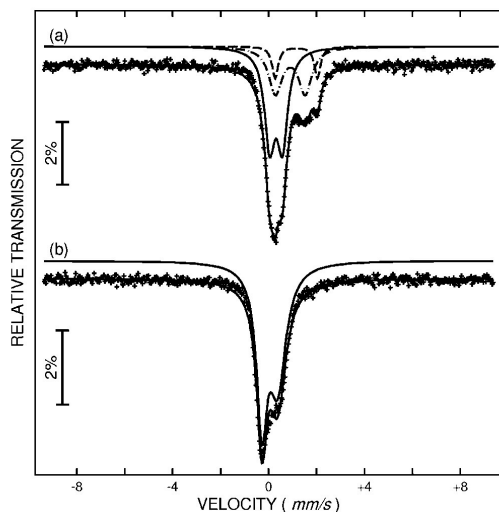


**Fig. 12** Fe Mössbauer spectra of  $\text{MnFe}_2\text{O}_4$  after insertion of (a) 2 and (b) 8 Li at room temperature.

shows a broad absorption between  $+1$  and  $+2 \text{ mm s}^{-1}$ . The broad sextet of the original nanoparticles disappeared like the peaks of the spinel phase in the XRD patterns (Fig. 7). The two overlapping doublets in the room temperature spectrum were also reported for  $\text{FeO}$ .<sup>65</sup>

After insertion of 8 Li the XRD pattern exhibits no structural information due to the amorphous nature of the material (Fig. 7). In contrast, more information can be extracted from Mössbauer spectra collected at room and low temperature (Fig. 11 and 12). The room temperature spectrum (Fig. 12) is an overlap of a series of doublets with isomer shifts close to  $0 \text{ mm s}^{-1}$ , which was also observed for fully discharged  $\text{CuFe}_2\text{O}_4$ .<sup>66</sup> The low temperature zero-field spectrum measured without an external magnetic field (Fig. 11) exhibits two weak absorptions at  $-8$  and  $+9 \text{ mm s}^{-1}$  in addition to a distribution of magnetic fields with average hyperfine fields close to 33 T. These absorptions are assigned to the first and sixth lines of the spectrum for the remained, not converted  $\text{MnFe}_2\text{O}_4$  particles, which constitutes less than 10% of the total quantity. The two absorption lines are further broadened under application of an external field (Fig. 11). This broadening represents the splitting of the first and sixth lines in agreement with the ferrimagnetic structure of  $\text{MnFe}_2\text{O}_4$  as discussed above. The central distribution with an average internal field of 33 T is assigned to iron nanoparticles with a broad size distribution giving a broad distribution of magnetic fields. When an external magnetic field is applied, the position of the absorptions shifts slightly inwards, *i.e.*, the hyperfine field is reduced. This is typical for ferromagnetic materials where an alignment of the magnetic moments along the external field,  $H_{\text{ext}}$ , with a concomitant rotation of the internal field such as to reduce the nuclear hyperfine field is expected. This is an unambiguous indication that the central absorption lines correspond to Fe metal nanoparticles, *i.e.* metallic Fe is formed during insertion of 8 Li per formula unit, which are not isolated but rather intimately dispersed with  $\text{Li}_2\text{O}$  (see TEM results). The observations made here are similar to those reported for lithiated  $\text{CuFe}_2\text{O}_4$  with a similar weakly split signal compared to a stronger split signal in lithiated  $\text{CoFe}_2\text{O}_4$ .<sup>66,67</sup>

### 3.6 *Ex situ* $^7\text{Li}$ NMR spectra

Fig. 13 shows  $^7\text{Li}$  MAS NMR spectra of lithiated nanocrystalline samples after insertion of 0.5, 1, 2, 8, and 10 Li per formula unit.

Solid state NMR in common provides a probe for the local environment of lithium ions.<sup>68,69</sup> It is well known that paramagnetic ions in the surrounding of the lithium ions can have strong effects on the NMR spectra due to the Fermi-contact interaction, *i.e.* the transfer of spin density from the unpaired electrons of the paramagnetic ions to the lithium nucleus. The value of the resulting hyperfine shift depends on the specific local environment. Furthermore, dipolar coupling between the lithium nuclei and the unpaired electrons constitutes a major source of large spinning sideband manifolds in MAS spectra.<sup>68,70</sup> In lithium manganese oxides with manganese oxidation states varying from (iii) to (iv) observed hyperfine shifts are ascribed primarily to a Fermi-contact shift mechanism.<sup>71</sup> Comparatively small – though well above 0 ppm – shifts

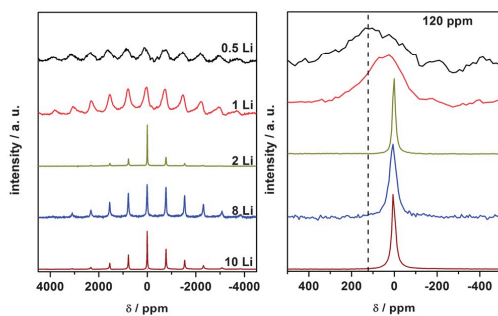


Fig. 13  ${}^7\text{Li}$  MAS NMR spectra of nanocrystalline  $\text{MnFe}_2\text{O}_4$  after insertion of 0.5, 1.5, 2, 8, and 10 Li.

in rock-salt related compounds with stoichiometry  $\text{LiMnO}_2$  are due to a shift reduction caused by Jahn–Teller distortions and strong antiferromagnetic interactions.<sup>59</sup> Likewise, antiferromagnetic interactions are responsible for reduced shifts of about 500 ppm in the NMR spectra of  $\alpha$ - and  $\beta$ - $\text{LiFeO}_2$ .<sup>68</sup> Additional consideration of the 317 ppm shift in  $\alpha$ - $\text{LiFeO}_2$  suggests a lower limit of 20 ppm per Li–O–Fe bond in suchlike ternary compounds.<sup>72</sup> During electrochemical lithiation of  $\text{FeF}_2$  and  $\text{FeF}_3$  a conversion reaction is observed resulting in nanosized  $\alpha$ -Fe metal, LiF, and – in the latter case – some unidentifiable lithium iron fluoride.<sup>73</sup> Cycling of nano-sized transition-metal oxides MO was reported to involve the formation and decomposition of  $\text{Li}_2\text{O}$  while metal nanoparticles are reduced and oxidized, respectively.<sup>17</sup>

After insertion of 0.5 Li per formula unit  $\text{MnFe}_2\text{O}_4$ , (Fig. 13) the  ${}^7\text{Li}$  MAS NMR spectrum reveals a broad peak with a large isotropic shift of 120 ppm and an extremely broad pattern of spinning sidebands extending over several thousand ppm corresponding to several hundred kHz in the frequency regime (Fig. 13). This clearly shows that Li is incorporated into  $\text{MnFe}_2\text{O}_4$  which is consistent with the findings of the XRD measurements (Fig. 7). Electronic spin density of Mn and Fe is transferred *via* Mn/Fe–O–Li bonds to the Li ions resulting in the large shifts and the presence of Mn/Fe as next nearest neighbors results in strong variations of the local magnetic fields giving rise to the broad spinning sideband manifolds. The presence of  $\text{Mn}^{2+}/\text{Fe}^{2+}/\text{Fe}^{3+}$  ions that are connected to the Li ions *via* Mn/Fe–O–Li bonds results in a large variety of local environments around the Li probe nuclei and therefore superposition of the different contributions results in the broad isotropic peak and the single environments can not be resolved. For 1 Li per formula unit, the broad peak shifts to 27 ppm because successively the  $\text{Fe}^{3+}$  neighbors around the Li ions are reduced to  $\text{Fe}^{2+}$ . As can be also seen from the reduced intensity of the peaks in the XRD pattern of this sample (Fig. 7), the crystal structure of  $\text{MnFe}_2\text{O}_4$  is partially converted and a rock-salt like phase is formed. Some Li ions are still linked *via* Mn/Fe–O–Li bonds to Fe/Mn but also diamagnetic  $\text{Li}_2\text{O}$  has started to form.

After insertion of 2, 8, and 10 Li ions per formula unit, the  ${}^7\text{Li}$  MAS NMR spectra are characterized by a quite narrow isotropic

peak with a very small NMR shift close to 0 ppm and again very broad spinning sideband patterns. The shift close to 0 ppm reveals that the local environment of the lithium nuclei is diamagnetic<sup>68,69</sup> and in accordance with the results discussed above the existence of direct Li–O–Fe/Mn bonds can be excluded now. Taking into account the nanoscale nature of the  $\text{MnFe}_2\text{O}_4$  powder, an interpretation following Poizot *et al.*<sup>17</sup> seems to be most likely. Both Fe and Mn ions are reduced to the metallic state while diamagnetic  $\text{Li}_2\text{O}$  is created. Consistently, the huge width of the spinning sideband manifold is caused by the presence of metallic Fe and Mn particles close to the Li ions. The width of the sideband manifold grows significantly and also the width of the isotropic peak increases when the number of incorporated lithium ions per formula unit increases from 2 to 8 because more and more Mn/Fe metal particles are formed. The decrease of the width of the sideband pattern and the reduced width of the isotropic peak at the maximum lithium content might be explained by a growth of the  $\text{Li}_2\text{O}$  particles and thus an increase of the average distance between the  $\text{Li}^+$  and the Fe/Mn metal particles.

### 3.7 *Ex situ* TEM investigations of intercalated samples

Intercalated samples with 2, 8, and 9.5 Li per formula unit were investigated with high resolution TEM. Note that the samples were magnetically filtered as described in the experimental section. Thus, extended magnetic components are excluded from the examinations. All samples consist of irregularly shaped and laterally extended particles. These particles are built from different components depending on the degree of lithiation. In case of the specimen with the nominal composition  $\text{Li}_2\text{MnFe}_2\text{O}_4$  well-faceted crystals were observed, particularly at the edges of the extended particles, *cf.* arrows in the bright field image of Fig. 14a. The structure of these crystals can be assigned to the spinel-type phase by characteristic electron diffraction patterns (not shown). Due to the minute changes of the  $d$ -values in course of Li incorporation in the spinel-type structure one can not determine the degree of lithiation of these crystals by conventional electron diffraction. The particles contain larger aggregates of crystallites with irregular shape which are kept together by an amorphous matrix material. Independent from the analyzed area, the ratio of Mn : Fe is always determined to be 1 : 2 by nanoprobe EDX. A representative electron diffraction pattern from an aggregate of particles is depicted in Fig. 14b. The pattern can be assigned to the cubic monoxide-type structure (space group  $Fm\bar{3}m$ ,  $d(hkl)$  exp./calc. in Å:  $d(111) = 2.50/2.5172$ ,  $d(002) = 2.17/2.1800$ ,  $d(022) = 1.54/1.5415$ ,  $d(222) = 1.26/1.2586$ ,  $d(004) = 1.14/1.0900$ ,  $d(240) = 0.98/0.9749$ ,  $d(242) = 0.895/0.8900$ ).

Note that the diffracted intensity concentrates into Bragg reflections located on concentric rings, thus proving the presence of several extended crystallites within each of the transmitted circular areas of the sample (diameter 250 nm). Due to superimposition of the crystallites their individual sizes can hardly be determined by analyzing projections.

Upon insertion of 8 Li per formula unit (nominal composition:  $\text{Li}_8\text{MnFe}_2\text{O}_4$ ) the overall crystallinity of the particles is

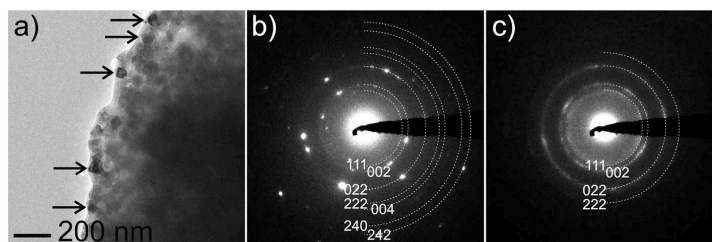


**Fig. 14** (a) TEM bright field image of sample  $\text{Li}_2\text{MnFe}_2\text{O}_4$ . The arrows highlight some of the spinel-type crystals segregating at the particle edge, see text. (b) SAED pattern with indices recorded on a particle of sample  $\text{Li}_2\text{MnFe}_2\text{O}_4$ . (c) SAED pattern with indices recorded on a particle of sample  $\text{Li}_9\text{MnFe}_2\text{O}_4$ .

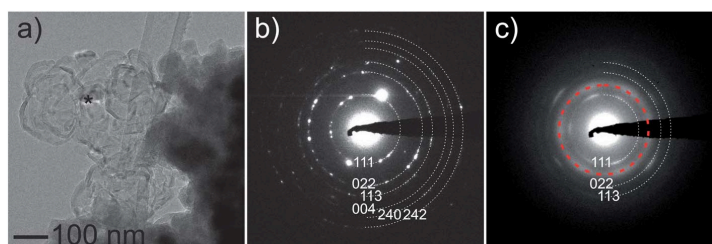


**Fig. 15** (a) TEM bright field image recorded on the edge of a particle of sample  $\text{Li}_{9.5}\text{MnFe}_2\text{O}_4$ . The asterisk mark segregating particles of crystalline  $\text{Li}_2\text{O}$ , see text. (b) Electron diffraction pattern of  $\text{Li}_2\text{O}$  (area marked by asterisk in (a)) with indices. (c) Electron diffraction pattern recorded on the central part of a particle displaying diffuse intensity (highlighted by dotted red circle) assigned to pure metal phases (Mn or Fe). Indices are given for those intensities assigned to poorly crystalline  $\text{Li}_2\text{O}$ .

reduced. The cubic monoxide-type structure can still be identified within the extended particles maybe due to incomplete conversion of the spinel phase which is only observed in exceptional cases. The coherently scattering areas of the monoxide crystallites appear to be smaller since the Bragg intensities are frequently streaked by diffuse intensity, cf. electron diffraction pattern in Fig. 14c. This sample also contains hardly crystalline  $\text{Li}_2\text{O}$  as indicated by combined electron diffraction and nanoprobe EDX examination. In this case the EDX spectra do not show any characteristic peak of metal atoms since Li can not be identified.

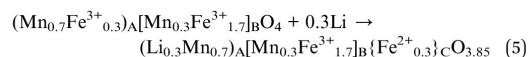
The crystallinity of the particles is further decreased upon insertion of 9.5 Li (nominal composition  $\text{Li}_{9.5}\text{MnFe}_2\text{O}_4$ ). Larger areas of  $\text{Li}_2\text{O}$  and only traces of the crystalline monoxide were observed, cf. bright field image in Fig. 15a. The electron diffraction pattern of Fig. 15b was recorded on an isolated and exceptional example of highly crystalline  $\text{Li}_2\text{O}$  particles, cf. asterisk in Fig. 15a. Space group  $Fm\bar{3}m$ ,  $d(hkl)$  exp./calc. in Å:  $d(111) = 2.71/2.6674$ ,  $d(022) = 1.67/1.6334$ ,  $d(113) = 1.42/1.3930$ ,  $d(004) = 1.18/1.1550$ ,  $d(240) = 1.08/1.0800$ ,  $d(242) = 0.97/0.9700$ .

As a rule, the  $\text{Li}_2\text{O}$  is poorly crystalline, consequently, the SAED patterns recorded on the particles contain diffuse rings of intensity with diameters correlating to the  $d$ -values of  $\text{Li}_2\text{O}$ , cf. Fig. 15c. Additionally, the patterns show intensity for  $d = 2.1$  Å (see red circle in Fig. 15c) which can not be indexed on the basis of  $\text{Li}_2\text{O}$ . The  $d$ -value according to the diameter of the broad ring matches well with the high intensity (111) reflection of Fe and/or Mn. This finding potentially indicates that despite magnetic

filtering some small particles of the metals are captured inside the particles after full conversion. The lateral resolution of the nanoprobe EDX analyses is not sufficient to resolve the dispersed metal, but exhibits a Mn : Fe ratio of 1 : 2 like for the less lithiated samples.

#### 4. Discussion

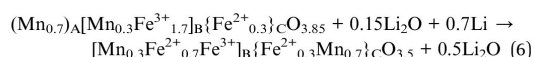
At least for the sample with nominal composition  $\text{LiMnFe}_2\text{O}_4$  a Rietveld refinement with only one phase is significantly less reliable than assuming the presence of two phases (Fig. S2†). In the structure of  $\text{MnFe}_2\text{O}_4$  the  $\text{Li}^+$  ions can enter empty tetrahedral (48f) or octahedral (16c) sites. But for both sites  $\text{Li}^+ - \text{Mn}^{2+}/\text{Fe}^{3+}$  distances are below 2 Å leading to strong repulsive interactions. The expansion of the lattice of the spinel at the beginning of Li insertion indicates that some  $\text{Li}^+$  can be incorporated. But we note that the expansion of the unit cell of the spinel may be also caused by the reduction of the sizes of coherent scattering domains as observed for many oxides,<sup>74</sup> which is most probably the case here. The Li atoms reduce  $\text{Fe}^{3+}$  on 8a site to  $\text{Fe}^{2+}$  which moves from the tetrahedral site to the octahedral 16c site. According to the degree of inversion obtained by Mössbauer data  $((\text{Mn}_{0.71}\text{Fe}_{0.29})_{\text{A}}[\text{Mn}_{0.29}\text{Fe}_{1.71}]_{\text{B}}\text{O}_4)$ , after uptake of about 0.3 Li all  $\text{Fe}^{3+}$  on the 8a site are reduced and are moved to the 16c site (eqn (5)).





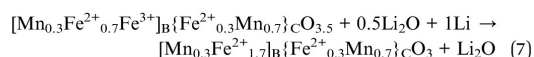
The XANES spectra show a more pronounced shift for the Fe K-edge and a decrease of the pre-edge feature from the beginning of the reaction in accordance with the proposed first step. The uptake of 0.3 Li is accompanied by a significant drop of the potential in the discharge curve (see Fig. 5, beginning of region I). The occupation of the 16c site leads to the formation of a rock-salt like structure being accompanied by a reduction of the size of coherent scattering domains of the spinel phase. The  $^7\text{Li}$  NMR data (see Fig. 13) suggest the existence of Li–O–Fe/Mn bonding interactions, *i.e.* a small amount of Li is inserted in the host material.

In the next reaction step it is most likely that the insertion of further 0.7 Li forces the  $\text{Mn}^{2+}$  ions on the A site to move to the 16c site while an appropriate amount of  $\text{Fe}^{3+}$  on the 16d site is reduced and the reaction may be formulated according to eqn (6):



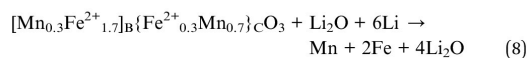
After insertion of 1 Li per  $\text{MnFe}_2\text{O}_4$  the rock-salt type oxide domains are large enough to be clearly detected in the XRD pattern and the Rietveld refinement indicates a further reduction of the coherent scattering domains of the spinel and an increase for the NaCl-type domains. In addition the formation of the NaCl-like phase may induce some strain which may also contribute to the broadening of the reflections. The XANES spectra exhibit a further decrease of the intensity of the pre-edge feature indicating a change of the local symmetry of both absorber atoms. In addition, the absorption edges shift to lower energies which is more pronounced for the Fe K-edge. The Li uptake is also accompanied by a further drop in the discharge curve (Fig. 3, end of region I). The generation of appreciable amounts of  $\text{Li}_2\text{O}$  in this reaction step is evidenced by the  $^7\text{Li}$  NMR results.

The insertion of another Li reduces the remaining  $\text{Fe}^{3+}$  ions and leads to the formation of the defective/distorted NaCl-type structure according to eqn (7):



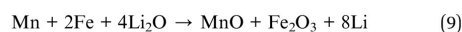
This assumption is supported by the disappearance of the spinel reflections in the XRD pattern, the increased size of the coherent scattering domains of the monoxide, and the nearly disappeared pre-edge peaks in the XANES spectra. Moreover, the Mössbauer spectrum of the sample containing 2 Li shows the signature of paramagnetic FeO, the electron diffraction pattern can be indexed on the basis of a cubic NaCl-type structure and the  $^7\text{Li}$  NMR spectrum is dominated by a narrow line due to the presence of  $\text{Li}_2\text{O}$ . The Mn/Fe ratio of the NaCl-type oxide should be 1 : 2 leading to  $\text{Mn}_{0.33}\text{Fe}_{0.66}\text{O}$  for which  $a = 4.36 \text{ \AA}$  (ref. 76) was reported being larger than the values refined from the powder patterns. The discrepancy may be due to the presence of a non-stoichiometric monoxide, and the well documented decrease of the lattice parameter with decreasing Fe content in  $\text{Fe}_{1-x}\text{O}$ . In addition, it can be expected that the monoxide contains a large amount of defects and also some distortion which also affect the lattice parameter.

The insertion of another 6 Li per formula unit leads to a successive reduction of  $\text{Fe}^{2+}$  and  $\text{Mn}^{2+}$  to the metals and the formation of  $\text{Li}_2\text{O}$  according to eqn (8):



This reaction occurs during the long plateau in the discharge curve (Fig. 3, region IV). The continuous conversion of the monoxide is clearly demonstrated by the decrease of the intensity of the reflections in the X-ray powder patterns. The formation of nanosized Fe particles is observed in the Mössbauer spectrum after insertion of 8 Li into  $\text{MnFe}_2\text{O}_4$  and the occurrence of  $\text{Li}_2\text{O}$  could be evidenced by TEM and  $^7\text{Li}$  NMR. The TEM investigations also demonstrate that Fe/Mn are homogeneously distributed in the reaction products throughout the whole Li insertion steps. In the X-ray powder pattern no reflections are seen indicating that the sizes of coherent scattering domains are very small.

During the charging cycle the Fe/Mn particles are partially oxidized to iron/manganese oxides according to eqn (9):



But these oxide particles are too small to be detected in X-ray powder patterns. The oxidation of Fe to  $\text{Fe}_2\text{O}_3$  was postulated in several publications,<sup>35,38,39</sup> but we cannot present evidences that  $\text{Fe}_2\text{O}_3$  was formed during charging.

The postulated mechanism should be briefly compared to reaction pathways reported in literature. For the Li insertion reaction of  $\text{ZnFe}_2\text{O}_4$  it was postulated that up to 0.4 Li per formula unit enter the empty octahedral 16c site and for Li contents >0.4 the repulsive interactions between  $\text{Li}^+$  on 16c and  $\text{Zn}^{2+}$  on 8a forces a movement of the latter cations to empty 16c sites.<sup>77,78</sup> For  $\text{Li}_{0.9}\text{ZnFe}_2\text{O}_4$  a further lattice expansion was observed being explained as ongoing Li intercalation and the simultaneous displacement of  $\text{Zn}^{2+}$  into octahedral 16c sites. The lattice expansion occurs up to  $\text{Li}_{1.45}\text{ZnFe}_2\text{O}_4$  and for larger Li contents a phase transition to a rock-salt phase is postulated. At 2 Li per formula unit it is proposed that the partially lithiated  $\text{Li}_{1.45}\text{ZnFe}_2\text{O}_4$  decomposes to  $\text{Li}_2\text{O}$  and a new rock-salt phase metal oxide containing only  $\text{Fe}^{2+}$ . This scenario is similar to that proposed for the reaction of Li with  $\text{Fe}_3\text{O}_4$ .<sup>75</sup> For  $\text{Li}_{1.5}\text{Fe}_3\text{O}_4$  all Fe cations reside on octahedral sites and half of the 16c site is occupied by  $\text{Li}^+$  while the excess Li cations are on the 48f site. According to the evaluation and comparison of the reflection intensities of  $\text{Fe}_3\text{O}_4$  and  $\text{Li}_{1.5}\text{Fe}_3\text{O}_4/\text{Li}_{1.7}\text{Fe}_3\text{O}_4$  a structure intermediate between spinel and rock-salt was proposed, but predominantly rock-salt. On the basis of a similar analysis of the reflection intensities and peak positions phase pure  $\text{Li}_2\text{Fe}_3\text{O}_4$  was postulated.<sup>79</sup> An identical high Li content was obtained for  $\text{NiFe}_2\text{O}_4$  and a very small lattice expansion of the host of about 0.12% was observed. But the change of the intensity ratios (220/440) and (400/422) led to the conclusion that cations moved from the 8a site to the octahedral 16c sites. The maximum Li content for  $\text{MnFe}_2\text{O}_4$  was given as 1.5 per formula unit being accompanied by a lattice expansion of about 0.8%, similar to the value obtained in the present study.



A detailed picture of insertion of Li into the distorted spinel  $\text{Mn}_3\text{O}_4$  was reported recently.<sup>48</sup> At the early stage Li reacts with an amorphous oxide on the surface of the particles. After insertion of 0.5 Li into  $\text{Mn}_3\text{O}_4$  a significant reduction of the domain size and an increased strain was observed.<sup>48</sup> At this stage of Li uptake  $\text{LiMn}_3\text{O}_4$  could be identified in the powder pattern which exhibits a strong tensile strain along one axis. All data suggest that chemical reduction occurs first and mainly at the surface of the nanocrystallites. After insertion of 1  $\text{Li}/\text{Mn}_3\text{O}_4$  an appreciable amount of the spinel is still present (ca. 25%), indicating a concurrent reaction which was identified as the increase of the amount of  $\text{LiMn}_3\text{O}_4$  and the occurrence of nanosized MnO explaining the charge storage during this step. Between 1 and 2 Li per formula unit the three oxides coexist with varying proportions depending on the Li content. The formation of MnO was accompanied by a continuous shift of reflections of  $\text{LiMn}_3\text{O}_4$  due to reduction of  $\text{Mn}^{3+}$  to  $\text{Mn}^{2+}$  in the spinel, while the reflection of MnO stayed constant. This observation indicates that reduction of  $\text{LiMn}_3\text{O}_4$  involves structural formation of MnO, and nucleation and growth of a distinct phase in the spinel particles is highly unlikely. It was also noted that formation of MnO from  $\text{LiMn}_3\text{O}_4$  requires removal of Li which may proceed via  $\text{Li}_2\text{O}$  extrusion. In the distorted spinel  $\text{Mn}_3\text{O}_4$  a 2D network of tunnels is observed and the empty octahedral sites are large enough to host  $\text{Li}^+$  ions and enable movement of the ions. After a distinct Li uptake  $\text{Mn}^{2+}$  ions shift to octahedral sites closing the tunnels retarding  $\text{Li}^+$  ion mobility.<sup>48</sup>

## 5. Conclusions

The results of the multi-method approach to understand the detailed reaction mechanisms occurring during Li uptake by the nanosized spinel material  $\text{MnFe}_2\text{O}_4$  allowed formulation of individual structural and electronic reaction steps after insertion of well-defined amounts of Li. The data highly suggest that only a small amount of Li can be inserted into the spinel phase. The Li uptake is simultaneously accompanied by the formation of a second phase (monoxide with NaCl-type structure) due to the movement of  $\text{Fe}^{2+}$  which is formed by reduction of the  $\text{Fe}^{3+}$  ion from the tetrahedral site to empty octahedral sites. Increasing the Li content the amount of the monoxide phase increases on cost of the spinel type material. Above 2 Li per formula unit  $\text{MnFe}_2\text{O}_4$  a conversion reaction of the monoxide occurs and not of the spinel material. The results presented here demonstrate the necessity to investigate Li uptake reactions in detail applying a variety of analytical techniques probing the changes of structural features on different length scales and simultaneously the electronic alterations being accompanied by Li insertion into anode materials.

## Acknowledgements

We are grateful to the Deutsche Forschungsgemeinschaft and to the German Federal Ministry of Education and Research for financial support. Beamtime allocation by ANKA (Karlsruhe) is thankfully acknowledged.

## References

- 1 B. Scrosati, *Nature*, 1995, **373**, 557–558.
- 2 L. F. Nazar, G. Goward, F. Leroux, M. Duncan, H. Huang, T. Kerr and J. Gaubicher, *Int. J. Inorg. Mater.*, 2001, **3**, 191–200.
- 3 J.-M. Tarascon and M. Armand, *Nature*, 2001, **414**, 359–367.
- 4 D. W. Murphy and P. A. Christian, *Science*, 1979, **205**, 651–656.
- 5 G. A. Nazri and G. Pistoia, *Lithium Batteries: Science and Technology*, Springer, US, 2008.
- 6 P. G. Bruce, B. Scrosati and J.-M. Tarascon, *Angew. Chem.*, 2008, **120**, 2972–2989.
- 7 R. Marom, S. F. Amalraj, N. Leifer, D. Jacob and D. Aurbach, *J. Mater. Chem.*, 2011, **21**, 9938–9954.
- 8 N.-S. Choi, Z. Chen, S. A. Freunberger, X. Ji, Y.-K. Sun, K. Amine, G. Yushin, L. F. Nazar, J. Cho and P. G. Bruce, *Angew. Chem., Int. Ed.*, 2012, **51**, 9994–10024.
- 9 J. B. Goodenough, *J. Solid State Electrochem.*, 2012, **16**, 2019–2029.
- 10 J. B. Goodenough and K.-S. Park, *J. Am. Chem. Soc.*, 2013, **135**, 1167–1176.
- 11 J. B. Goodenough and Y. Kim, *Chem. Mater.*, 2010, **22**, 587–603.
- 12 J.-M. Tarascon, N. Recham, J.-N. Chotard, P. Barpanda, W. Walker and L. Dupont, *Chem. Mater.*, 2010, **22**, 724–739.
- 13 B. L. Ellis, K. T. Lee and L. F. Nazar, *Chem. Mater.*, 2010, **22**, 691–714.
- 14 J. Maier, *Nat. Mater.*, 2005, **4**, 805–815.
- 15 A. S. Arico, P. Bruce, B. Scrosati, J.-M. Tarascon and W. van Schalkwijk, *Nat. Mater.*, 2005, **4**, 366–377.
- 16 M. Armand and J.-M. Tarascon, *Nature*, 2008, **451**, 652–657.
- 17 P. Poizot, S. Laruelle, S. Grugnon, L. Dupont and J.-M. Tarascon, *Nature*, 2000, **407**, 496–499.
- 18 J. Cabana, L. Monconduit, D. Larcher and M. Rosa Palacin, *Adv. Energy Mater.*, 2010, **22**, E170–E192.
- 19 W. Bensch, J. Opey, H. Hain, H. Gesswein, D. Chen, R. Mönig, P. A. Gruber and S. Indris, *Phys. Chem. Chem. Phys.*, 2012, **14**, 7509–7516.
- 20 M. J. Aragon, C. Perez-Vicente and J. L. Tirado, *Electrochem. Commun.*, 2007, **9**, 1744–1748.
- 21 K. Zhong, X. Xia, B. Zhang, H. Li, Z. Wang and L. Chen, *J. Power Sources*, 2010, **195**, 3300–3308.
- 22 F. Jiao, J. Bao and P. G. Bruce, *Electrochem. Solid-State Lett.*, 2007, **10**, A264–A266.
- 23 K. M. Abraham, D. M. Pasquariello and E. B. Willstedt, *J. Electrochem. Soc.*, 1990, **137**, 743–749.
- 24 P. C. Wang, H. P. Ding, T. Bark and C. H. Chen, *Electrochim. Acta*, 2007, **52**, 6650–6655.
- 25 J. Li, H. M. Dahn, L. J. Krause, D.-B. Le and J. R. Dahn, *J. Electrochem. Soc.*, 2008, **155**, A812–A816.
- 26 F. M. Courtel, H. Duncan, Y. Abu-Lebdeh and I. J. Davidson, *J. Mater. Chem.*, 2011, **21**, 10206–10218.
- 27 Y. Sharma, N. Sharma, G. V. S. Rao and B. V. R. Chowdari, *Electrochim. Acta*, 2008, **51**, 2380–2385.
- 28 Y. Sharma, N. Sharma, G. V. Subba Rao and B. V. R. Chowdari, *Solid State Ionics*, 2008, **179**, 587–597.

- 29 S.-L. Kuo and N.-L. Wu, *Electrochem. Solid-State Lett.*, 2005, **8**, A495–A499.
- 30 S.-L. Kuo and N.-L. Wu, *Electrochem. Solid-State Lett.*, 2007, **10**, A171–A175.
- 31 N. N.-L. Wu and Y.-H. Chen, *ECS Trans.*, 2008, **16**, 223–228.
- 32 Y.-P. Lin and N.-L. Wu, *J. Power Sources*, 2011, **196**, 851–854.
- 33 D. Zhang, X. Zhang, X. Ni, J. Song and H. Zheng, *Chem. Phys. Lett.*, 2006, **426**, 120–123.
- 34 Y. Ding, Y. Yang and H. Shao, *Solid State Ionics*, 2012, **217**, 27–33.
- 35 Z. H. Li, T. P. Zhao, X. Y. Zhan, D. S. Gao, Q. Z. Xiao and G. T. Lei, *Electrochim. Acta*, 2010, **55**, 4594–4598.
- 36 N. Sivakumar, S. R. P. Gnanakan, K. Karthikeyan, S. Amaresh, W. S. Yoon, G. J. Park and Y. S. Lee, *J. Alloys Compd.*, 2011, **509**, 7038–7041.
- 37 C. T. Cherian, M. V. Reddy, G. V. S. Rao, C. H. Sow and B. V. R. Chowdari, *J. Solid State Electrochem.*, 2012, **16**, 1823–1832.
- 38 X. Guo, X. Lu, X. Fang, Y. Mao, Z. Wang, L. Chen, X. Xu, H. Yang and Y. Liu, *Electrochem. Commun.*, 2010, **12**, 847–850.
- 39 Y. Ding, Y. Yang and H. Shao, *Electrochim. Acta*, 2011, **56**, 9433–9438.
- 40 Z. J. Zhang, Z. L. Wang, B. C. Chakoumakos and J. S. Yin, *J. Am. Chem. Soc.*, 1998, **120**, 1800–1804.
- 41 C. Pereira, A. M. Pereira, C. Fernandes, M. Rocha, R. Mendes, M. P. Fernández-García, A. Guedes, P. B. Tavares, J.-M. Grenèche, J. P. Araújo and C. Freire, *Chem. Mater.*, 2012, **24**, 1496–1504.
- 42 A. Yang, C. N. Chinnsamy, J. M. Grenèche, Y. Chen, S. D. Yoon, Z. Chen, K. Hsu, Z. Cai, K. Ziemer, C. Vittoria and V. G. Harris, *Nanotechnology*, 2009, **20**, 1–6.
- 43 J. F. Hu, H. W. Qin, Y. Z. Wang, S. G. Zhang and Z. X. Wang, *J. Mater. Sci. Lett.*, 2001, **20**, 1531.
- 44 A. A. Coelho, *Topas Academic Version 5*, 2013.
- 45 B. Antic, A. Kremenovic, A. S. Nikolic and M. Stoiljkovic, *J. Phys. Chem. B*, 2004, **108**, 12646–12651.
- 46 L. Wang, B. Liu, S. Ran, L. Wang, L. Gao, F. Qu, D. Chen and G. Shen, *J. Mater. Chem.*, 2013, **1**, 2139–2143.
- 47 D. Aurbach, K. Gamolsky, B. Markovsky, G. Salitra, Y. Gofen, U. Heider, R. Oesten and M. Schmidt, *J. Electrochem. Soc.*, 2000, **147**, 1322–1331.
- 48 M. A. Lowe, J. Gao and H. D. Abruna, *J. Mater. Chem. A*, 2013, **1**, 2094–2103.
- 49 L. Y. Beaulieu, D. Larcher, R. A. Dunlap and J. R. Dahn, *J. Electrochem. Soc.*, 2000, **147**, 3206–3212.
- 50 S. Laruelle, S. Grugeon, P. Poizot, M. Dollé, L. Dupont and J.-M. Tarascon, *J. Electrochem. Soc.*, 2002, **149**, A627–A634.
- 51 J. Jamnik and J. Maier, *Phys. Chem. Chem. Phys.*, 2003, **5**, 5215–5220.
- 52 H. Fjellvag, F. Gronvold, S. Stolen and B. Hauback, *J. Solid State Chem.*, 1996, **124**, 52–57.
- 53 D. Carta, M. F. Casula, A. Falqui, D. Loche, G. Mountjoy, C. Sangregorio and A. Corrias, *J. Phys. Chem. C*, 2009, **113**, 8606–8615.
- 54 M. J. Akhtar and M. Younas, *Solid State Sci.*, 2012, **14**, 1536–1542.
- 55 L. Galoisy, G. Calas and M. A. Arrio, *Chem. Geol.*, 2001, **174**, 307–319.
- 56 G. Jain, M. Balasubramanian and J. J. Xu, *Chem. Mater.*, 2006, **18**, 423–434.
- 57 K. Zhong, B. Zhang, S. Luo, W. Wen, H. Li, X. Huang and L. Chen, *J. Power Sources*, 2011, **196**, 6802–6808.
- 58 J. Li, H. Yuan, G. Li, Y. Liu and J. Leng, *J. Magn. Magn. Mater.*, 2010, **322**, 3396–3404.
- 59 A. J. Rondinone, C. Liu and Z. J. Zhang, *J. Phys. Chem. B*, 2001, **105**, 7967–7971.
- 60 M. H. Mahmoud, H. H. Handeh and H. M. Al-Attar, *Hyperfine Interact.*, 2006, **171**, 261–267.
- 61 M. Siddique and N. M. Butt, *Physica B*, 2010, **405**, 4211–4215.
- 62 J. P. Chen, C. M. Sorensen, K. J. Klabunde, G. C. Hadjipanayis, E. Devlin and A. Kostikas, *Phys. Rev. B: Condens. Matter Mater. Phys.*, 1996, **54**, 9288–9296.
- 63 J. L. Lopez, H.-D. Pfannes, R. Paniago and F. A. Tourinho, *J. Magn. Magn. Mater.*, 2001, 1878–1880.
- 64 J. M. D. Coey, *Phys. Rev. Lett.*, 1971, **27**, 1140–1142.
- 65 D. P. Johnson, *Solid State Commun.*, 1969, **7**, 1785–1788.
- 66 M. Bomio, P. Lavela and J. L. Tirado, *ChemPhysChem*, 2007, **8**, 1999–2007.
- 67 P. Lavela, J. L. Tirado, M. Womes and J. C. Jumas, *J. Phys. Chem. C*, 2009, **113**, 20081–20087.
- 68 C. P. Grey and N. Dupre, *Chem. Rev.*, 2004, 4493–4512.
- 69 C. P. Grey and Y. J. Lee, *Solid State Sci.*, 2003, **5**, 883–894.
- 70 S. Indris, J. Cabana, O. J. Rutt, S. J. Clarke and C. P. Grey, *J. Am. Chem. Soc.*, 2006, **128**, 13354–13355.
- 71 Y. J. Lee, F. Wang and C. P. Grey, *J. Am. Chem. Soc.*, 1998, **120**, 12601–12613.
- 72 J. Kim, U. G. Nielsen and C. P. Grey, *J. Am. Chem. Soc.*, 2008, **130**, 1285–1295.
- 73 N. Yamakawa, M. Jiang, B. Key and C. P. Grey, *J. Am. Chem. Soc.*, 2009, **131**, 10525–10536.
- 74 P. M. Diehm, P. Agoston and K. Albe, *ChemPhysChem*, 2012, **13**, 2443–2454.
- 75 M. M. Thackeray, W. I. F. David and J. B. Goodenough, *Mater. Res. Bull.*, 1982, **17**, 785–793.
- 76 A. H. Jay and K. W. Andrews, *J. Iron Steel Inst.*, 1946, **152**, 15–18.
- 77 C. J. Chen, M. Greenblatt and J. V. Waszczak, *Mater. Res. Bull.*, 1986, **21**, 609–619.
- 78 D. Bresser, E. Paillard, R. Kloepsch, S. Krueger, M. Fiedler, R. Schmitz, D. Baither, M. Winter and S. Passerini, *Adv. Energy Mater.*, 2013, **3**, 513–523.
- 79 C. J. Chen and M. Greenblatt, *Solid State Ionics*, 1986, **18 & 19**, 838–846.

### 3.2 Is there a universal reaction mechanism of Li insertion into oxidic spinels: a case study using $\text{MgFe}_2\text{O}_4$

This publication presents results of another investigation on the reaction mechanisms occurring during discharge (Li uptake) and charge (Li release) into an oxidic spinel-type material. The aim was establishing a universal reaction mechanism for oxidic spinels on the basis of our investigations and those published in literature. Two samples with differently sized  $\text{MgFe}_2\text{O}_4$  nanoparticles were synthesized and the pristine materials were characterized with XRD, EDX, SEM,  $\text{N}_2$ -sorption, TEM and Mössbauer spectroscopy. The electrochemical performance was investigated with galvanostatic cycling and cyclic voltammetry. The capacity of the first discharge of  $1232 \text{ mAh g}^{-1}$  and  $1118 \text{ mAh g}^{-1}$  for the larger particles exceeds the theoretical value which may be explained by side reaction with the electrolyte and SEI formation. According to Ex-situ XRD,  $^7\text{Li}$  NMR and Mössbauer spectroscopy the mechanisms for Li uptake seems to be different for particles with different sizes: In case of nanosized particles, the complex pathway of the discharge reaction seems to start with an intercalation of very small amounts of Li, in contrast to larger particles where no indication were found for intercalation. After insertion of 2 Li per formula unit the rock salt structure is formed by the movement of cations located on tetrahedra to empty octahedra. Simultaneously  $\text{Fe}^{3+}$  is reduced to  $\text{Fe}^{2+}$ . During further uptake of Li amorphous MgO and metallic Fe nanoparticles were formed being embedded in a  $\text{Li}_2\text{O}$  matrix. The  $\text{Mg}^{2+}$  ions could not be reduced to metallic Mg which makes Mg based spinel oxides unsuitable as anode material in Li batteries. After the charge process the spinel type structure with  $\text{Fe}^{3+}$  ions could not be observed. The results indicate that amorphous inactive MgO is separated from active materials FeO and Li.

Following research article is reproduced by permission of the Royal Society of Chemistry  
**2015**

Original citation:

Stefan Permien, Sylvio Indris, Marco Scheuermann, Ulrich Schürmann, Valeriu Mereacre, Annie K. Powell, Lorenz Kienle, Wolfgang Bensch, *Journal of Material Chemistry A*, **2015**, 3, 1549-1561. – published by the Royal Society of Chemistry

DOI: 10.1039/c4ta05054a



Cite this: *J. Mater. Chem. A*, 2015, 3, 1549

## Is there a universal reaction mechanism of Li insertion into oxidic spinels: a case study using $\text{MgFe}_2\text{O}_4$ †

Stefan Permien,<sup>a</sup> Sylvio Indris,<sup>b</sup> Marco Scheuermann,<sup>b</sup> Ulrich Schürmann,<sup>c</sup> Valeriu Mereacre,<sup>d</sup> Annie K. Powell,<sup>d</sup> Lorenz Kienle<sup>c</sup> and Wolfgang Bensch<sup>\*a</sup>

Structural and electronic changes during Li insertion into spinel-type  $\text{MgFe}_2\text{O}_4$  particles with different sizes were studied applying a multi-method approach yielding a detailed picture about distinct reaction steps during Li uptake. A small amount of Li is intercalated into the smaller particles (8 nm) at the beginning of the reaction while no such reaction step occurs for the large crystallites (ca. 100 nm). Li uptake is accompanied by a reduction of  $\text{Fe}^{3+}$  ions and simultaneous movement from the tetrahedral to an empty octahedral site. After uptake of 2 Li per formula unit all ions have moved from tetrahedral to free octahedral voids resulting in the formation of a disordered NaCl-type material. Insertion of 4 further Li atoms transforms the crystalline material to an amorphous and inhomogeneous product consisting of a  $\text{Li}_2\text{O}$  matrix with embedded nanosized metallic Fe and MgO particles. During the charge process Fe is oxidized to FeO and  $\text{Li}_2\text{O}$  is converted to Li.

Received 24th September 2014  
Accepted 19th November 2014

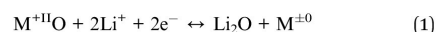
DOI: 10.1039/c4ta05054a

www.rsc.org/MaterialsA

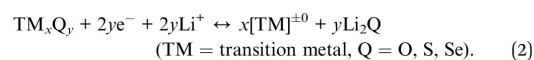
### 1. Introduction

Today's portable consumer electronics and electronic vehicles are under development and demand for new battery materials with high energy density and fast charge/discharge kinetics.<sup>1–4</sup> On the one hand new materials for Li-ion batteries (LiBs) need to be developed.<sup>5–7</sup> On the other hand characterization of reversible and irreversible phase transitions during charge and discharge is vital for the understanding of processes which determine the applicability of battery materials.<sup>8–10</sup> In conventional batteries graphite is used as an anode material, and Li intercalation and deintercalation are the basic reactions in this type of batteries.<sup>11</sup> Alternatives for graphite are nanomaterials like transition metal oxides. The advantages and disadvantages of nanomaterials in LiBs were discussed extensively in the literature.<sup>12–14</sup> A careful control of the nanoparticle size and shape can greatly improve the performance, capacity and cyclability of nanoparticle based Li batteries.<sup>13,15</sup> Using nanoparticulate metal oxides as anode materials leads to a change in the reaction mechanism from “classic” intercalation to a

so-called conversion reaction. The reversible electrochemical reaction mechanism of Li with transition metal oxides like MO (M = Co, Ni, Cu or Fe) proceeds like a displacive redox reaction (eqn (1)).<sup>16–18</sup>



Such conversion reactions are not limited to oxides and they can be generally formulated with eqn (2):



At the end of the conversion reaction a  $\text{Li}_2\text{Q}$  matrix is formed with embedded nanosized metal particles.  $2y/x$  Li ions can be converted per TM ion leading to specific capacities beyond  $500 \text{ mA h g}^{-1}$ . A disadvantage of conversion reactions is that the formation of a new phase may lead to large volume changes, often resulting in strong capacity fading during the first cycles, or even to the total loss of contact to the current collector.<sup>19</sup>

The conversion materials exhibit higher capacities if TM ions with higher oxidation states are applied, and the potential of the battery cell can be adjusted by the strength of the metal-oxygen bond.<sup>13</sup> Transition metal spinel oxides with the general formula  $\text{AB}_2\text{O}_4$  (A = Zn, Fe, Mn, Ni, Co; B = Fe, Co, Mn) are intensively investigated because their theoretical capacities are larger than  $1000 \text{ mA h g}^{-1}$ .<sup>20–24</sup> Ferrites with the formula  $\text{MFe}_2\text{O}_4$  (M = transition metal) with carbon coating, graphene supported surfaces and special morphology show good cycle stability over more than 100 cycles.<sup>25–30</sup>

<sup>a</sup>Institute of Inorganic Chemistry, University of Kiel, Max-Eyth-Straße 2, 24118 Kiel, Germany. E-mail: wbensch@ac.uni-kiel.de

<sup>b</sup>Institute for Applied Materials – Energy Storage Systems, Karlsruhe Institute of Technology, P.O. Box 3640, 76021 Karlsruhe, Germany

<sup>c</sup>Institute for Materials Science, University of Kiel, Kaiserstr. 2, 24143 Kiel, Germany

<sup>d</sup>Institute of Inorganic Chemistry, Karlsruhe Institute of Technology, Engesser Str. 15, 76131 Karlsruhe, Germany

† Electronic supplementary information (ESI) available. See DOI: 10.1039/c4ta05054a





MgFe<sub>2</sub>O<sub>4</sub> is environmentally friendly, non-toxic, based on earth abundant elements and hence the material is cheap. Some groups already investigated MgFe<sub>2</sub>O<sub>4</sub> nanoparticles as an anode material for LIBs: Sivakumar *et al.* used nanoparticles obtained *via* ball milling showing a capacity of 1480 mA h g<sup>-1</sup>, but the cycling performance was poor with only 300 mA h g<sup>-1</sup> after ten cycles.<sup>31</sup> Pan *et al.* synthesized nanoparticles by the sol-gel method by mixing nanoparticles with 20 wt% carbon black, leading to a better cyclic stability and after 50 cycles the capacity was still 493 mA h g<sup>-1</sup>.<sup>32</sup> Yin *et al.* prepared 33 nm particles mixed with 40 wt% Super P Carbon and 20 wt% PVDF showing an initial discharge capacity of 1123 mA h g<sup>-1</sup> and 635 mA h g<sup>-1</sup> after 50 cycles.<sup>33</sup> Gong *et al.* used carbon coated polydisperse nanoparticles (20 to 175 nm) providing a better cyclic stability after 50 cycles of about 600 mA h g<sup>-1</sup>.<sup>34</sup>

The capacity loss between the first and the following cycles is a general observation made for ferrites MFe<sub>2</sub>O<sub>4</sub> (Mn, Fe, Co, Ni). One reason may be that the elemental metallic nanoparticles formed in the Li<sub>2</sub>O matrix generate a large interface area where the formation of a solid-electrolyte interface (SEI) irreversibly consumes Li and significantly reduces the reversibility of Li introduction and extraction.<sup>20–30</sup>

In the last few years we investigated the Li insertion behavior of several compounds with the focus on the reaction mechanism, structural and magnetic properties as well as Li mobility properties.<sup>35–37</sup> The studies exhibited remarkable differences in Li insertion behavior for different selenides *e.g.* Cr<sub>4</sub>TiSe<sub>8</sub> or CuCr<sub>2</sub>Se<sub>4</sub> and the spinel MnFe<sub>2</sub>O<sub>4</sub>.<sup>19,38–42</sup> For MnFe<sub>2</sub>O<sub>4</sub> we were able to formulate a step-by-step reaction mechanism from the beginning of Li uptake until full conversion was reached applying a multi-method approach including *in situ* QuickXAFS, <sup>57</sup>Fe Mössbauer spectroscopy, X-ray diffraction, HRTEM, <sup>7</sup>Li MAS NMR spectroscopy and electrochemical experiments. The main findings of this investigation are: (i) only a very small amount of Li can be intercalated while simultaneously Fe<sup>3+</sup> on the tetrahedral site is reduced and moves to an empty octahedral site; (ii) insertion of 1 Li/MnFe<sub>2</sub>O<sub>4</sub> further reduces Fe<sup>3+</sup> which is accompanied by the movement of Mn<sup>2+</sup> to empty octahedral sites generating NaCl-like oxide domains and Li<sub>2</sub>O is simultaneously formed; (iii) after uptake of 2 Li per MnFe<sub>2</sub>O<sub>4</sub> all Fe<sup>3+</sup> ions are reduced and only NaCl-type monoxide and Li<sub>2</sub>O could be detected; (iv) full conversion of the monoxide into metallic Fe and Mn nanoparticles in a Li<sub>2</sub>O matrix is achieved after insertion of 8 Li/MnFe<sub>2</sub>O<sub>4</sub>; (v) during the charge cycle nanosized transition metal oxides are formed. The key question is whether oxidic spinels follow an identical Li insertion mechanism independent from the chemical composition. Because only a few investigations of the reaction mechanisms were reported until now, a detailed understanding of conversion reactions during Li insertion is important for systematic future battery development.<sup>19,38–42</sup> A suitable spinel to examine whether the reaction steps proceed in a similar or different way is MgFe<sub>2</sub>O<sub>4</sub> with Mg<sup>2+</sup> on the tetrahedral site exhibiting distinct electrochemical behavior compared to transition metal cations on this site. Here we report a detailed reaction mechanism for the conversion of MgFe<sub>2</sub>O<sub>4</sub> particles of two different sizes during Li uptake. The comparison of the progress of the

reaction applying one material with two different sizes should give hints about the advantages/disadvantages of using small nanoparticles compared to major large particles and its impact on the mechanisms. The pristine materials were thoroughly characterized using XRD, EDX, SEM, TEM and N<sub>2</sub>-sorption. Electrochemical performance was investigated by cyclic voltammetry (CV) and galvanostatic discharge/charge. Samples with distinct Li contents were characterized by XRD, <sup>7</sup>Li MAS NMR and <sup>57</sup>Fe Mössbauer spectroscopy.

## 2. Experimental section

### 2.1 Synthesis

MgFe<sub>2</sub>O<sub>4</sub> was synthesized applying a precursor route. All chemicals were of analytical grade and used without purification. 5.0 mmol Mg(NO<sub>3</sub>)<sub>2</sub>·6H<sub>2</sub>O (98%, ABCR), 10 mmol Fe(NO<sub>3</sub>)<sub>3</sub>·9H<sub>2</sub>O (98%, Riedel-de Haen) and 15 mmol citric acid (99%, Merck) were ball milled for 2 h in a Fritsch Pulverisette with 15 mm agate balls, at 500 rpm in air. The viscous product was transferred to an open cup and heated in a pre-heated oven at 500 °C (MgFe<sub>2</sub>O<sub>4\_A</sub>) and 1000 °C (MgFe<sub>2</sub>O<sub>4\_B</sub>) for 3 h.<sup>43</sup>

### 2.2 Characterization

XRD patterns were recorded with a X'PERT PRO PANalytical with a Göbel mirror and a PIXcel detector using Cu K<sub>α</sub> radiation. EDX spectra were recorded on a Philips ESEM XL 30 with an EDAX New XL-30 Detecting Unit. SEM images were taken in a Zeiss Ultra 55 with an FE-Cathode. Nitrogen sorption experiments were performed with a BELSORP Max from Bel Japan INC. The samples were activated for 14 h at 200 °C under a vacuum (0.1 mbar). TEM investigations were performed in a Tecnai F30 G2-STwin microscope at 300 kV with a field emission gun cathode and a Si/Li detector for nanoprobe EDX (EDAX system). For TEM experiments the samples were suspended in *n*-butanol and treated in an ultrasonic bath to induce particle separation. The dispersions were dropped onto a holey-carbon copper grid.

### 2.3 Electrochemical measurements

For the electrochemical characterization 80 wt% MgFe<sub>2</sub>O<sub>4</sub> powder was mixed with 10 wt% SUPER C65 Carbon (Timcal, Switzerland) and 10 wt% PVdF (Solvay, Germany). The mixture was dissolved with NMP (*N*-methyl-2-pyrrolidone), deposited on copper foil, dried overnight at room temperature and sintered at 100 °C for 24 h in a vacuum drying chamber. Afterwards 10 mm discs were cut with about 2 mg active material and applied as a cathode in a Swagelok type test cell, using Li metal as the anode, glass fiber filter disks (Whatman, United Kingdom) as the separator, and a solution of 1 M LiPF<sub>6</sub> in an ethylene carbonate/dimethyl carbonate mixture (Merck, Germany) as the electrolyte. Test cells were discharged/charged with C/10 rate, performed with a Materials Mates 510 DC.

For XRD, Mössbauer and <sup>7</sup>Li NMR experiments on lithiated samples, 70 wt% MgFe<sub>2</sub>O<sub>4</sub> was mixed with 15 wt% SUPER C65 Carbon and 15 wt% PVdF as a binder. The mixture was pressed into pellets (210 kg m<sup>-2</sup>) and used as a cathode in a Swagelok



type test cell with Li metal as the anode, glass fiber filter disks as the separator, and the electrolyte mentioned above. The cells were assembled in an argon filled glove box (<1 ppm O<sub>2</sub>, <1 ppm H<sub>2</sub>O). A test cell was discharged with C/20 rate until the desired formal composition Li<sub>x</sub>MgFe<sub>2</sub>O<sub>4</sub> was reached (Materials Mates 510 DC). The cells were opened in the glove box and the recovered powders were used for further measurements without purification. Typically about 25 mg of Li containing powder could be obtained in a 10 mm Swagelok cell. For XRD measurements, materials were transferred to an iron sample holder and protected with Kapton foil.

<sup>7</sup>Li magic-angle spinning (MAS) NMR was performed at room temperature on a Bruker Avance 200 MHz spectrometer at a magnetic field of 4.7 T corresponding to a Larmor frequency of  $\nu_L = 77.8$  MHz. A spinning speed of 60 kHz was applied using 1.3 mm rotors in a dry nitrogen atmosphere. A 1 M LiCl solution served as a <sup>7</sup>Li reference (0 ppm). The typical value for the recycling delay of <sup>7</sup>Li was 1 s. <sup>7</sup>Li MAS NMR experiments were implemented with a rotor-synchronized Hahn-echo sequence ( $\pi/2 - \tau - \pi - \tau - \text{acquisition}$ ) and a typical  $\pi/2$  pulse length of 2  $\mu$ s. <sup>57</sup>Fe Mössbauer spectra were acquired using <sup>57</sup>Co(Rh) as the  $\gamma$ -ray source in the transmission geometry. The velocity scale was calibrated with metallic  $\alpha$ -Fe foil. Isomer shifts are given relative to that of  $\alpha$ -Fe at room temperature.

### 3. Results

#### 3.1 Characterization of the pristine materials

In Fig. 1 X-ray powder patterns of the two samples together with the calculated diagram are shown. Only reflections of cubic MgFe<sub>2</sub>O<sub>4</sub> can be observed. Reflections of the sample MgFe<sub>2</sub>O<sub>4</sub>\_A are significantly broadened compared to MgFe<sub>2</sub>O<sub>4</sub>\_B indicating coherently scattering domains within the nanoregime and the average size of the domains was estimated from the XRD pattern using the fundamental approach implemented in the TOPAS-4 software<sup>44</sup> yielding 8(0.1) nm for MgFe<sub>2</sub>O<sub>4</sub>\_A. The refined lattice parameter *a* of sample A is 8.386(1) Å. The domain size of MgFe<sub>2</sub>O<sub>4</sub>\_B is 96(1) nm and the refined lattice

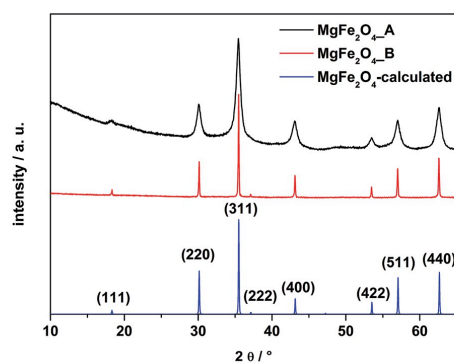


Fig. 1 XRD patterns of the as-prepared samples MgFe<sub>2</sub>O<sub>4</sub>\_A, MgFe<sub>2</sub>O<sub>4</sub>\_B and the calculated pattern of MgFe<sub>2</sub>O<sub>4</sub>.

parameter *a* is slightly larger (8.3955(1) Å). The smaller value for *a* for sample A could be attributed to defects and stress/strain as observed for MgO or CeO<sub>2</sub> (ref. 45 and 46) and also for nanoparticles of MgFe<sub>2</sub>O<sub>4</sub> with *a* between 8.386 and 8.430 Å,<sup>47,48</sup> depending on the synthesis conditions.

The EDX elemental analysis yields a ratio of Mg to Fe of about 1 : 1.71 for A and 1 : 1.97 for B (ESI†). The root mean square deviation of four measured locations is 3.5% for A and 4.4% for B, and therefore they are less than the experimental standard deviation of EDX analysis (about 5%).

SEM images of MgFe<sub>2</sub>O<sub>4</sub>\_B display spongy agglomerated particles with sizes in the range of micrometers (Fig. 2). The N<sub>2</sub>-sorption curve for MgFe<sub>2</sub>O<sub>4</sub>\_A shows a type-IV-isotherm (ESI†) typically for particles with textural porosity. The specific surface area according to the Brunauer–Emmett–Teller (BET) method is  $S_{\text{BET}} = 48 \text{ m}^2 \text{ g}^{-1}$  for A. The sample MgFe<sub>2</sub>O<sub>4</sub>\_B exhibits no N<sub>2</sub>-sorption due to a very small specific surface area.

TEM results of MgFe<sub>2</sub>O<sub>4</sub>\_A and MgFe<sub>2</sub>O<sub>4</sub>\_B are presented in Fig. 3 and 4, respectively. Nanoprobe EDX analyses gave no indication for chemical inhomogeneity, and the SAED pattern exhibits only reflections of cubic MgFe<sub>2</sub>O<sub>4</sub>. The SAED pattern of sample A shows smaller *d*-values compared to B as also observed in the XRD patterns. A polydisperse size distribution of particles ranging from about 4 to 14 nm with an average particle size of 8.7 nm as determined *via* statistical analysis is observed for sample A (Fig. 3, left). This value matches well with

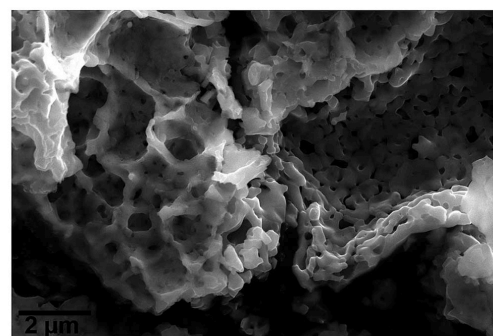


Fig. 2 SEM image of the sample MgFe<sub>2</sub>O<sub>4</sub>\_B.

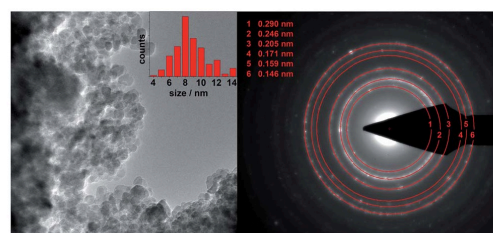


Fig. 3 TEM image of MgFe<sub>2</sub>O<sub>4</sub>\_A with statistical analysis (left) and the corresponding SAED pattern.



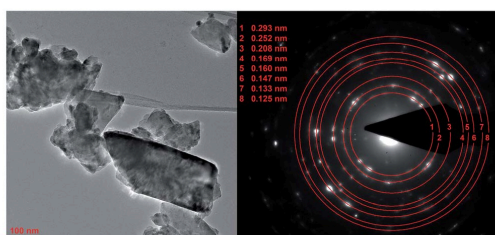


Fig. 4 TEM image of  $\text{MgFe}_2\text{O}_4\text{-B}$  with polydisperse size distribution (left) and the corresponding SAED pattern.

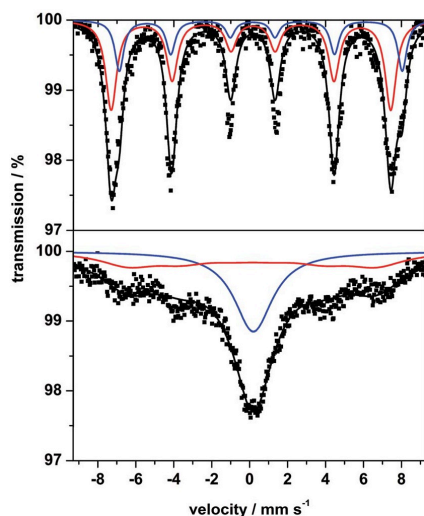


Fig. 5  $^{57}\text{Fe}$  Mössbauer spectrum of sample B (top) and sample A (bottom) measured at room temperature.

that estimated from the XRD data (8 nm).  $\text{MgFe}_2\text{O}_4\text{-B}$  mainly consists of particles larger than 100 nm, but also some smaller crystallites smaller than 100 nm can be identified.

The room temperature  $^{57}\text{Fe}$  Mössbauer spectrum of  $\text{MgFe}_2\text{O}_4\text{-B}$  (Fig. 5, top) is dominated by a broadened sextet without a central doublet. The sextet consists of two superimposed individual sextets caused by  $\text{Fe}^{3+}$  in tetrahedral (A) and octahedral (B) sites. In contrast, the spectrum of  $\text{MgFe}_2\text{O}_4\text{-A}$  (Fig. 5, bottom) exhibits a sextet and a central doublet with broadened lines, suggesting a mixture of magnetic and superparamagnetic particles with isomer shift (IS) values characteristic for  $\text{Fe}^{3+}$  (Table 1). The very small value for the quadrupole splitting (QS) of the doublet is typical for  $\text{Fe}^{3+}$  in a highly symmetric environment. The broad asymmetric lines of the sextet are caused by a distribution of hyperfine fields with a maximum of 41 T for sample A and about 46 T for B (Table 1). The spectrum of  $\text{MgFe}_2\text{O}_4\text{-B}$  (Fig. 5, top) is very similar to that reported in ref. 49 and 50 and also similar to the spectrum of 72 nm particles presented in ref. 51, while that for  $\text{MgFe}_2\text{O}_4\text{-A}$  is similar to the spectrum presented in ref. 52 for 20 nm particles. Smaller particles just lead to the broadened doublet because of superparamagnetic behavior of the particles.<sup>53</sup>

At 3 K, a sextet is seen in the Mössbauer spectrum for both samples due to magnetic ordering (Fig. 6, upper spectra). The width of the absorption lines indicates that the sextet is a superposition of two individual sextets corresponding to  $\text{Fe}^{3+}$  located on two different crystallographic positions (also seen in Fig. 5, upper spectrum). Because the resolution is not good enough to evaluate the relative fractions of the two contributions, an external field was applied vertical to the  $\gamma$ -ray direction. This experiment allows separation of the two sextets and two well-defined absorption lines can be seen, as expected for ferrimagnetic  $\text{MgFe}_2\text{O}_4$  (Fig. 6, middle and bottom). The two hyperfine sextets were least-squares fitted applying the following model,  $(\text{Mg}_x\text{Fe}_{1-x})_A[\text{Mg}_{1-x}\text{Fe}_{1+x}]_B\text{O}_4$ , where the subscripts A and B denote the tetrahedral and octahedral sites, respectively. The degree of inversion was calculated from the areas of the Mössbauer sub-spectra. For  $\text{MgFe}_2\text{O}_4\text{-A}$  a distribution of

Table 1 Mössbauer fit parameters: isomer shift (IS), quadrupole splitting (QS), line width, and hyperfine field ( $B_{\text{hf}}$ ). IS is given with respect to that of  $\alpha\text{-Fe}$

Sample	IS/mm s <sup>-1</sup>	QS/mm s <sup>-1</sup>	Line width/mm s <sup>-1</sup>	$B_{\text{hf}}/T$
$\text{MgFe}_2\text{O}_4\text{-A}$ (8 nm)	$0.305 \pm 0.011$	$-0.011 \pm 0.071$	$2.468 \pm 0.046$	$40.56 \pm 0.47$
	$0.252 \pm 0.052$		$3.601 \pm 0.300$	
$\text{MgFe}_2\text{O}_4\text{-B}$ (96 nm)	$0.228 \pm 0.009$	$0.111 \pm 0.020$	$0.709 \pm 0.017$	$45.73 \pm 0.02$
	$0.475 \pm 0.018$	$0.430 \pm 0.036$	$0.571 \pm 0.034$	$46.28 \pm 0.05$

Table 2 Overall capacities, reversible capacities and capacities of the regions I–III of samples A and B

Sample	Capacity	Region I	Region II	Region III	Charge capacity
$\text{MgFe}_2\text{O}_4\text{-A}$	1232 mA h g <sup>-1</sup>	1.5 V; 23 mA h g <sup>-1</sup>	0.8 V; 79 mA h g <sup>-1</sup>	0.4 V; 580 mA h g <sup>-1</sup>	798 mA h g <sup>-1</sup>
$\text{MgFe}_2\text{O}_4\text{-B}$	1118 mA h g <sup>-1</sup>	0.7 V; 44 mA h g <sup>-1</sup>	0.6 V; 83 mA h g <sup>-1</sup>	0.3 V; 600 mA h g <sup>-1</sup>	648 mA h g <sup>-1</sup>



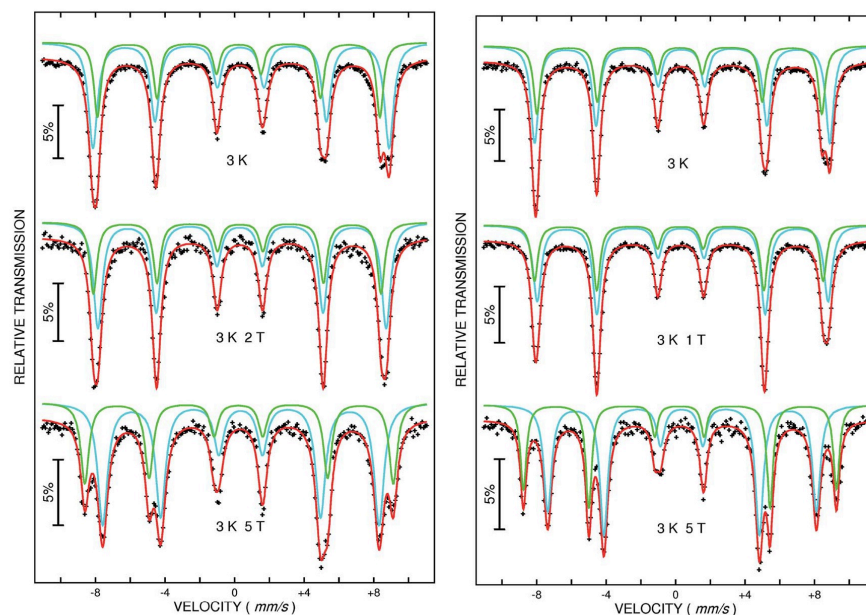


Fig. 6  $^{57}\text{Fe}$  Mössbauer spectra of  $\text{MgFe}_2\text{O}_4\text{-A}$  (left) and  $\text{MgFe}_2\text{O}_4\text{-B}$  (right) measured at 3 K without (top) and with an external field of 1 T, 2 T (middle) and 5 T (bottom) respectively.

cations according to  $(\text{Mg}_{0.30}\text{Fe}_{0.70})_{\text{A}}[\text{Mg}_{0.70}\text{Fe}_{1.30}]_{\text{B}}\text{O}_4$  is obtained and a quite similar distribution is observed for  $\text{MgFe}_2\text{O}_4\text{-B}$  with  $(\text{Mg}_{0.24}\text{Fe}_{0.76})_{\text{A}}[\text{Mg}_{0.76}\text{Fe}_{1.24}]_{\text{B}}\text{O}_4$ . We note that different  $\text{Fe}^{3+}/\text{Mg}^{2+}$  distributions are reported in the literature *e.g.*  $(\text{Mg}_{0.64}\text{Fe}_{0.36})_{\text{A}}[\text{Mg}_{0.36}\text{Fe}_{1.64}]_{\text{B}}\text{O}_4$  or  $(\text{Mg}_{0.12}\text{Fe}_{0.82})_{\text{A}}[\text{Mg}_{0.82}\text{Fe}_{1.12}]_{\text{B}}\text{O}_4$  depending on the synthesis conditions like calcination temperature and the preparation method.<sup>51–56</sup> The degree of inversion is comparable for the two samples while the lattice parameter differs and it can be assumed that the difference is an effect of the particle sizes as discussed above.

### 3.2 Electrochemical performance of the differently sized $\text{MgFe}_2\text{O}_4$ particles

The first discharge curve of both samples  $\text{MgFe}_2\text{O}_4\text{-A}$  and  $\text{MgFe}_2\text{O}_4\text{-B}$  shows four regions (Fig. 7). In the first region (region I) the potential drops very fast. The discharge curve of  $\text{MgFe}_2\text{O}_4\text{-A}$  exhibits a narrow plateau at 1.5 V with a length of *ca.*  $26 \text{ mA h g}^{-1}$ , while for  $\text{MgFe}_2\text{O}_4\text{-B}$  a broader plateau ( $44 \text{ mA h g}^{-1}$ ) at a lower potential of 0.74 V is observed. During discharge of  $\text{MgFe}_2\text{O}_4\text{-A}$  a second plateau at 0.8 V (region II,  $79 \text{ mA h g}^{-1}$ ) appears. The second plateau of sample B is located at 0.6 V (region II, length:  $83 \text{ mA h g}^{-1}$ ). Afterwards both samples exhibit a broad plateau at about 0.4 V with a length of  $580 \text{ mA h g}^{-1}$  (region III) for  $\text{MgFe}_2\text{O}_4\text{-A}$ , respectively at 0.3 V for  $\text{MgFe}_2\text{O}_4\text{-B}$  with a length of  $600 \text{ mA h g}^{-1}$  (region III). At this plateau for both samples a potential drop to 0.01 V follows (region IV). During charging the cell a not well resolved plateau at 1.6 V ( $\text{MgFe}_2\text{O}_4\text{-B}$ ) and 1.7 V

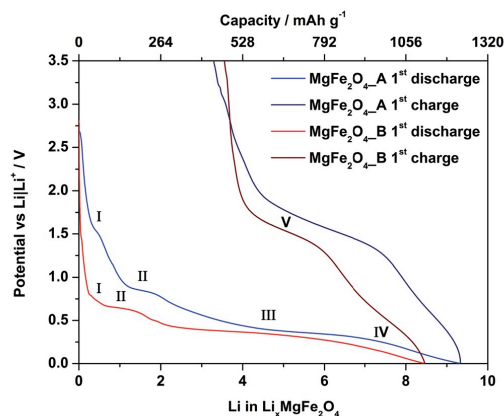


Fig. 7 First discharge/charge cycle of  $\text{MgFe}_2\text{O}_4\text{-A}$  (blue) and  $\text{MgFe}_2\text{O}_4\text{-B}$  (red).

( $\text{MgFe}_2\text{O}_4\text{-A}$ ) appears (region V). The insertion of 1  $\text{Li}^+$  into  $\text{MgFe}_2\text{O}_4$  corresponds to a capacity of  $132 \text{ mA h g}^{-1}$ . The theoretical discharge capacity is  $792 \text{ mA h g}^{-1}$  per  $\text{MgFe}_2\text{O}_4$  assuming a full conversion of  $\text{Fe}^{3+}$  to the metal. Pure  $\text{MgO}$  nanoparticles show no Li uptake (ESI,† Fig. 3) due to the fact that a conversion of  $\text{Mg}^{2+}$  cannot be realized.<sup>31,32</sup> Sample  $\text{MgFe}_2\text{O}_4\text{-A}$  exhibits an entire first discharge capacity of  $1232 \text{ mA h g}^{-1}$  which is larger than





theoretically expected. The phenomenon of an overcapacity is well documented and explained by additional capacitive charge storage at interfaces of nanoparticles<sup>57,58</sup> and/or electrolyte decomposition.<sup>59–62</sup> After the first discharge–charge cycle the reversible capacity of MgFe<sub>2</sub>O<sub>4</sub>\_A is 798 mA h g<sup>-1</sup> (35%, irreversible capacity loss: 434 mA h g<sup>-1</sup>) corresponding to an uptake of ≈6.04 Li per formula unit. The sample MgFe<sub>2</sub>O<sub>4</sub>\_B shows a somewhat lower entire capacity of 1118 mA h g<sup>-1</sup> and a reversible capacity of 648 mA h g<sup>-1</sup> (42%, irreversible capacity loss: 470 mA h g<sup>-1</sup>) corresponding to an uptake of 4.9 Li per formula unit. The capacity loss is most likely caused by irreversible reactions with the electrolyte when the potential approaches 0 V vs. Li/Li<sup>+</sup> forming passivating layers on the surface of the particles, *i.e.* the formation of a SEI.<sup>63</sup> During the discharge process Fe<sup>3+</sup> is reduced to Fe<sup>0</sup>, and charging can oxidize elemental Fe either to Fe<sup>3+</sup> or Fe<sup>2+</sup>. If Fe<sup>2+</sup> is formed the capacity loss amounts to 2 Li per formula unit.

### 3.3 Cyclic voltammetry (CV)

CV curves for MgFe<sub>2</sub>O<sub>4</sub>\_A and MgFe<sub>2</sub>O<sub>4</sub>\_B against Li metal are shown in Fig. 8. Cycling was performed in a range from 0.01 to 3.5 V at a slow sweep rate of 0.05 mV s<sup>-1</sup>. For the first cycle of MgFe<sub>2</sub>O<sub>4</sub>\_A (left) three cathodic peaks are visible at 1.6 V, 0.8 V and 0.3 V and two anodic peaks at 0.5 and 1.6 V, matching with the plateaus I–III and V in the galvanostatic cycling (Table 2). The second cycle is completely different, and only one cathodic peak at 0.6 V and an anodic peak at 1.6 V can be detected. For MgFe<sub>2</sub>O<sub>4</sub>\_B the first and second cycles are almost identical compared to first and second cycles of MgFe<sub>2</sub>O<sub>4</sub>\_A. There is just one difference at 1.6 V in the first cycle. Here the cathodic peak is missing in the CV curve of MgFe<sub>2</sub>O<sub>4</sub>\_B, in agreement with the galvanostatic cycling (Fig. 7) where also no plateau at 1.6 V was observed. The missing cathodic peak at 1.6 V for MgFe<sub>2</sub>O<sub>4</sub>\_B may be regarded as evidence that the first Li intercalation/insertion takes place at a lower potential, *i.e.* more energy is needed due to the lower surface area of sample B.

For both samples the first cycle is different compared to the second cycle being a clear hint that a new phase is formed. For similar spinel oxides the same phenomenon was reported.<sup>25,64</sup>

### 3.4 *Ex situ* XRD on lithiated MgFe<sub>2</sub>O<sub>4</sub>\_A

In Fig. 9 are displayed the *ex situ* XRD patterns of MgFe<sub>2</sub>O<sub>4</sub>\_A after electrochemical insertion of 0.3, 1, 1.5, 2, 3, 6 and 9 Li per formula unit and after the first charge/discharge cycle. Note that for these experiments pellets consisting of MgFe<sub>2</sub>O<sub>4</sub>\_A, a binder and carbon were prepared as described in Section 2.3.

After insertion of 0.3 Li (Fig. 7 and 8; region I) the reflections slightly shift to lower scattering angles which is typical for an intercalation reaction (ESI,† Fig. 4). For Li<sub>0.3</sub>MgFe<sub>2</sub>O<sub>4</sub> the refined value for the *a* axis of 8.4023(2) Å (expansion: ≈0.2%) is slightly larger than that for the pristine material which may be caused by intercalation of a small amount of Li. The average size of the coherently scattering domains amounts to 8(1) nm. Increasing the Li content to 1 per formula unit, a two phase refinement of the powder pattern was obtained. The second phase was identified as the monoxide, *i.e.* a mixed crystal Mg<sub>0.33</sub>Fe<sub>0.66</sub>O (cubic symmetry, space group: *Fm* $\bar{3}$ *m*) with all metal cations occupying octahedral sites with a slightly larger Mg/Fe–O bond length (2.1150 Å) compared to the spinel type phase (2.0631 Å for Fe/Mg–O on the octahedral site and 1.8887 Å for Fe/Mg–O on the tetrahedral site).<sup>65</sup> The *a* axis for the monoxide was refined to 4.222(5) Å, being between that of FeO (4.334 Å) and MgO (4.211 Å)<sup>65</sup> indicating the formation of a mixed Mg<sup>2+</sup>/Fe<sup>2+</sup>/Fe<sup>3+</sup> containing oxide. We note that the *a* axis is smaller than that reported for Mg<sub>0.24</sub>Fe<sub>0.76</sub>O of 4.296 Å exhibiting a composition near to that proposed here.<sup>66</sup> But one should keep in mind that after insertion of 1 Li into the host not all Fe<sup>3+</sup> cations are reduced to Fe<sup>2+</sup> with the former exhibiting a smaller ionic radius. In addition, the monoxide-like crystalline domains within the spinel material may be slightly non-stoichiometric, and it can be expected that the structure contains an appreciable number of defects and also some distortion which also affect the lattice parameter. The ratio of the spinel phase to monoxide is about 50 : 50% after insertion of 1 Li. For the spinel phase the *a* axis is slightly larger at 8.4078(3) Å and the size of coherent scattering domains is not significantly altered.

A further decrease of the intensity of the reflections of the spinel phase occurs for the sample containing 1.5 Li per formula unit (Fig. 7 and 8; region II), while the intensity of the reflections of the monoxide increased. The two phase Rietveld

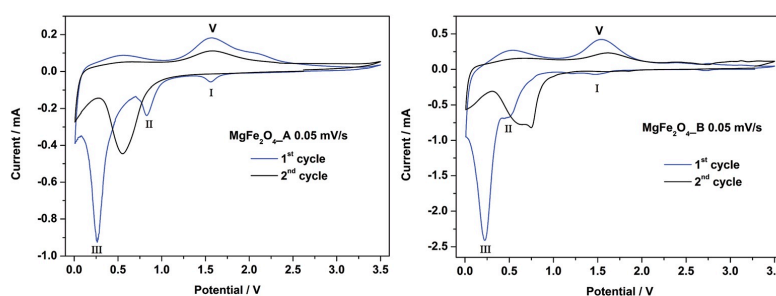


Fig. 8 CV curves for MgFe<sub>2</sub>O<sub>4</sub>\_A (left) and MgFe<sub>2</sub>O<sub>4</sub>\_B (right) in a potential range from 0–3.0 V with a scan rate of 0.05 mV s<sup>-1</sup>.



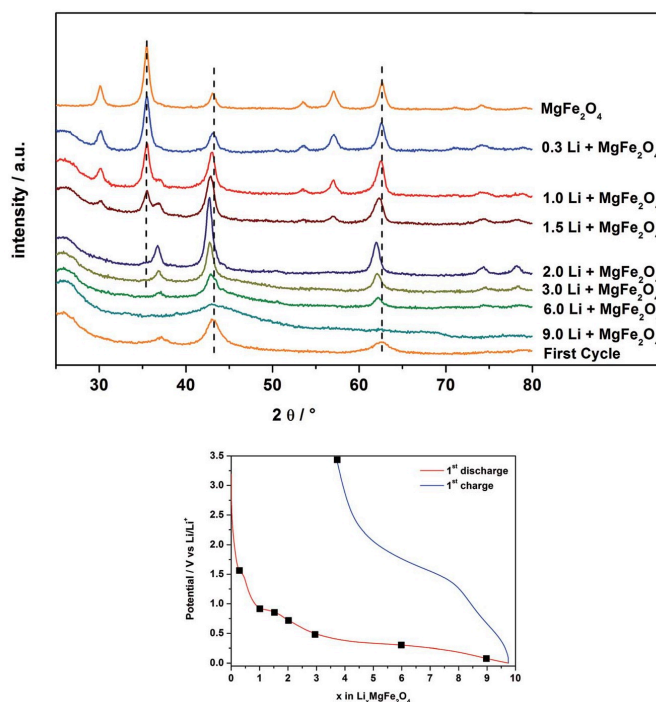


Fig. 9 XRD patterns of  $\text{MgFe}_2\text{O}_4\text{-A}$  after insertion of 0.3, 1, 1.5, 2, 3, 6, 9 Li and after the first discharge/charge cycle. Bottom: electrochemical voltage profile during the first discharge/charge cycle of  $\text{MgFe}_2\text{O}_4\text{-A}$ . Black squares mark the points where the Li insertion was stopped for XRD measurements.

refinement yields for the spinel type phase  $a = 8.411(4)$  Å and  $a = 4.231(2)$  Å for the monoxide. Increasing the Li content to 2 per formula unit (Fig. 7 and 8; beginning of region III) only small amounts of the spinel phase exist ( $\approx 1\%$ ), and the monoxide phase is dominating (99%) with  $a = 4.237(2)$  Å and 7(1) nm for the coherently scattering domains. The formation of a monoxide with a NaCl-type structure requires that Mg and Fe cations located on tetrahedral position 8a in the spinel move to the neighboring octahedral position 16c while  $\text{Fe}^{3+}$  is reduced to  $\text{Fe}^{2+}$ . When 16c and 16d are occupied in the spinel phase the symmetry changes and space group  $Fm\bar{3}m$  is adopted with about half of the  $a$  axis ( $8.4023$  Å/ $2 = 4.2012$  Å). Increasing the Li amount per formula unit leads to an increase of the size of the coherently scattering domains and an enlargement of the  $a$  axis due to the formation of larger particles with less defects, less strain and a monoxide consisting of  $\text{Mg}^{2+}$  and solely  $\text{Fe}^{2+}$  in the matrix of  $\text{O}^{2-}$  anions.

The XRD patterns of the samples after insertion of 3 and 6 Li per formula unit show a decrease of the intensity of the reflections of the monoxide during the long plateau at about 0.3 V (see Fig. 7 and 8, region III). The particle size is further reduced from 5.4(1) nm (3 Li) to 3.0(1) nm (6 Li). Finally, no reflections can be detected for the material containing 9.0 Li per formula

unit (Fig. 7 and 8; end of region IV). The very broad modulation centered at  $43^\circ$   $2\theta$  may be caused by nanosized metallic Fe. During the long plateau at 0.3 V the monoxide is converted to an amorphous product or the crystallites are too small to be detected by XRD. After the first charge/discharge cycle the reflections for the monoxide appear again, with a size of coherently scattering domains of 2.6(3) nm and a slightly smaller value for the  $a$  axis of 4.209(4) Å. The value for the  $a$  axis after the first cycle is very close to that of MgO (4.211 Å).<sup>65</sup>

### 3.5 Ex situ XRD on lithiated $\text{MgFe}_2\text{O}_4\text{-B}$

Fig. 10 shows the *ex situ* XRD patterns of  $\text{MgFe}_2\text{O}_4\text{-B}$ , after electrochemical insertion of 0.3, 1, 1.5, 2, 4, and 7 Li per formula unit and after a full charge/discharge cycle. The pellets of  $\text{MgFe}_2\text{O}_4\text{-B}$  were prepared as mentioned in Section 2.3.

After insertion of 0.3 Li (Fig. 7 and 8, corresponding to region I) the reflections do not shift in contrast to the observation made for sample A. For  $\text{Li}_{0.3}\text{MgFe}_2\text{O}_4$  the value for the  $a$  axis is 8.3969(3) Å, which is only about 0.02% larger than that for the pristine material and compared with sample A (expansion = 0.2%) the expansion can be neglected. The average sizes of the coherently scattering domains decreased to 74(2) nm, being 32% smaller than that for the starting material. The data



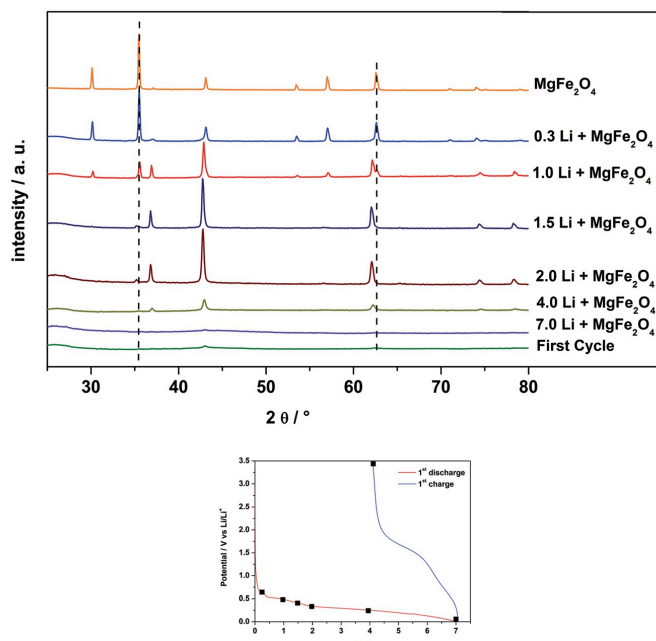


Fig. 10 XRD patterns of  $\text{MgFe}_2\text{O}_4\text{-B}$  after insertion of 0.3, 1, 1.5, 2, 4, 7 Li and after the first discharge/charge cycle. Bottom: electrochemical voltage profile during the first discharge/charge cycle of  $\text{MgFe}_2\text{O}_4\text{-B}$ . Black squares mark the point where the intercalation was stopped for XRD measurements.

suggest that no intercalation takes place in  $\text{MgFe}_2\text{O}_4\text{-B}$ . Despite that no shift of the reflection can be observed, the asymmetry of the (400) reflection (ESI,† Fig. 5) indicates the presence of small amounts of a second phase and the two phase Rietveld refinement yields better reliability factors. It seems that the monoxide phase is formed immediately by Li insertion in contrast to what is found for sample A. Increasing the Li content to 1 per formula unit, the amount of the second phase starts to grow. The  $a$  axis value for the monoxide was refined to 4.2288(2) Å and the particle size was obtained as 45(1) nm. For the spinel phase the size of coherent scattering domains decreases to 61(4) nm and the  $a$  axis is now slightly larger with  $a = 8.3993(5)$  Å. After insertion of 1.5 Li, the particle size of the monoxide is nearly constant at 46(1) nm, but the intensity of the reflections is enhanced, while the intensity of the reflections of the spinel phase decreases. Reflections of the spinel can hardly be detected in the XRD pattern after insertion of 2 Li per formula unit and the transformation to  $\text{Mg}_{0.33}\text{Fe}_{0.66}\text{O}$  ( $d = 36(1)$  nm) with a lattice parameter of 4.2278(4) Å seems to be completed. A possible explanation for the decrease of the crystallite size may be that some Li inserted into the material leads to the conversion of the domains to form nanosized metal particles.

The results of the Rietveld refinements suggest that the sizes of coherently scattering domains of the newly formed monoxide depend on the particle size of the pristine particles, indicating that the monoxide is directly formed out of the spinel structure

by movement of Fe and Mg cations from tetrahedral to octahedral sites. Compared to sample A, the  $a$  axis value is nearly identical at this stage of Li insertion (difference: 0.2%).

During the broad plateau (Fig. 7, region III) and the large peak in the CV curve (Fig. 8, III) the monoxide is converted to amorphous products as observed for sample A. After a full charge/discharge cycle the XRD pattern shows only reflections with very low intensity and a monoxide consisting of very small particles is formed as also seen for sample A (Section 3.4). But for sample B the particles are much smaller than A.

### 3.6 Ex situ Li-NMR spectra of $\text{Li}_x\text{MgFe}_2\text{O}_4$

$^7\text{Li}$  MAS NMR spectra of lithiated samples A and B are presented in Fig. 11. Solid state NMR in common provides a probe for the local environment of lithium ions.<sup>67,68</sup> It is well known that paramagnetic ions in the neighborhood of  $\text{Li}^+$  ions can have strong effects on the NMR spectra due to the Fermi-contact interaction, *i.e.* the transfer of spin density from the unpaired electrons of the paramagnetic ions to the Li nucleus. The value of the resulting hyperfine shift depends on the specific local environment. Furthermore, dipolar coupling between the Li nuclei and the unpaired electrons constitutes a major source of large spinning sideband manifolds in MAS spectra.<sup>67,69</sup> For the Li insertion of  $\text{MnFe}_2\text{O}_4$  nanoparticles a strong shift was observed for the samples with low Li content.<sup>42</sup>  $\text{MgFe}_2\text{O}_4\text{-A}$



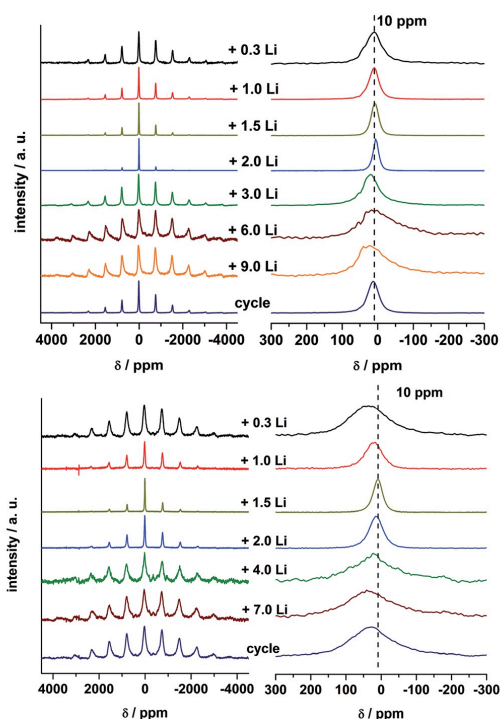


Fig. 11  ${}^7\text{Li}$  MAS NMR spectra of sample  $\text{MgFe}_2\text{O}_4\text{-A}$  after insertion of 0.3, 1, 1.5, 2, 3, 6, 9 Li and after the first discharge/charge cycle (top) and  ${}^7\text{Li}$  MAS NMR spectra of sample  $\text{MgFe}_2\text{O}_4\text{-B}$  after insertion of 0.3, 1, 1.5, 2, 4, 7 Li and after the first discharge/charge cycle (bottom).

(Fig. 11) does not show such a strong shift, because the paramagnetic  $\text{Mn}^{2+}$  ions are replaced by diamagnetic  $\text{Mg}^{2+}$  ions. For a Li content of 0.3 Li per formula unit the shift is 10 ppm with broad sideband patterns, indicating that Fe–O–Li bridges are formed. Small amounts of Li are intercalated into the spinel structure which is consistent with the results of XRD observations. Similar shifts in NMR spectra were also observed for  $o\text{-LiFeO}_2$  suggesting a lower limit of 20 ppm per Li–O–Fe linkage in such ternary compounds.<sup>70</sup> Increasing the Li amount up to 2 Li the shift is close to 0 ppm revealing that the local environment of the Li nuclei is diamagnetic. According to the results discussed above the existence of direct Li–O–Fe bonds can be now excluded and diamagnetic  $\text{Li}_2\text{O}$  is formed. In the next steps Fe is reduced to the metallic state and more diamagnetic  $\text{Li}_2\text{O}$  is generated. Consistently, the huge width of the spinning sideband manifold is caused by the presence of metallic Fe particles close to the  $\text{Li}^+$  ions. The width of the sideband manifold grows significantly and also the width of the isotropic peak increases when the number of incorporated  $\text{Li}^+$  ions per formula unit increases from 2 to 9 because more Fe metal particles are formed, as also reported for  $\text{MnFe}_2\text{O}_4$ .<sup>43</sup> For Li contents of 3, 6, and 9 Li, the Fe metal particles are growing in size and thus the

isotropic peaks are even broader than that of the sample with 0.5 Li and also the NMR shift is larger. After the first full cycle the width of the sideband pattern decreases and the width of the isotropic peak is reduced.

For  $\text{MgFe}_2\text{O}_4\text{-B}$  the shift is slightly larger after insertion of 0.3 Li per formula unit than for  $\text{MgFe}_2\text{O}_4\text{-A}$  (Fig. 11). The larger shift can be explained because the particles are not superparamagnetic but show strong ferrimagnetic interactions leading to a stronger shift of the peak maxima at the low Li content. XRD investigations evidenced that no Li intercalation into the particles occurred (Section 3.5), but Li–O–Fe can be formed at the surface of the particles. The formation of the monoxide in sample B takes place at a low Li content (Section 3.5) also seen by comparing Li NMR spectra of  $\text{MgFe}_2\text{O}_4\text{-B} + 1.5$  Li with spectra of  $\text{MgFe}_2\text{O}_4\text{-A} + 2$  Li. The shift of both spectra is 0 ppm and the spinning sidebands are very small. After insertion of 4 and 7 Li into sample B the Fe is reduced to the metallic state and more diamagnetic  $\text{Li}_2\text{O}$  is formed. Like for sample A the huge width of the spinning sideband manifold can be explained by the presence of metallic Fe particles close to the Li ions. After the first full cycle the width of the sideband pattern decreases and the width of the isotropic peak is reduced, but compared to sample A the effect is less pronounced.

### 3.7 ${}^{57}\text{Fe}$ Mössbauer spectroscopy on lithiated $\text{MgFe}_2\text{O}_4\text{-A}$

The  ${}^{57}\text{Fe}$  Mössbauer spectra of sample A collected at RT without external field after insertion of 2 and 9 Li and after the full discharge/charge cycle are displayed in Fig. 12. After uptake of 2 Li a broad absorption occurs between +1 and +2  $\text{mm s}^{-1}$  consisting of two doublets (Fig. 12, top). At this stage of Li insertion the reflections of the spinel phase in the XRD pattern (Fig. 9)

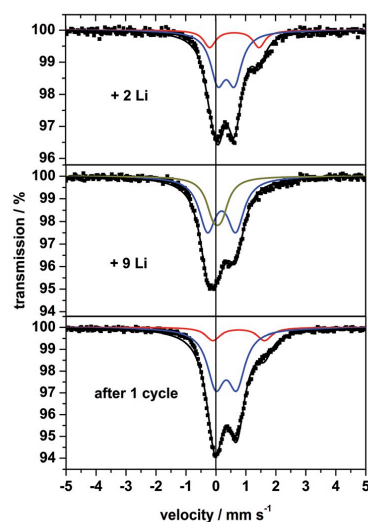


Fig. 12  ${}^{57}\text{Fe}$  Mössbauer spectra of nanocrystalline  $\text{MgFe}_2\text{O}_4\text{-A}$  measured at room temperature after insertion of 2, 9 Li and after the first discharge/charge cycle.

**Table 3**  $^{57}\text{Fe}$  Mössbauer fit parameters: isomer shift (IS), quadrupole splitting (QS), and line width. IS is given with respect to that of  $\alpha\text{-Fe}$

Sample	IS/mm s $^{-1}$	QS/mm s $^{-1}$	Line width/mm s $^{-1}$
MgFe $_2$ O $_4$ -A + 2Li	0.456 $\pm$ 0.002	0.560 $\pm$ 0.005	0.596 $\pm$ 0.011
	0.729 $\pm$ 0.008	1.648 $\pm$ 0.015	0.481 $\pm$ 0.024
MgFe $_2$ O $_4$ -A + 9Li	0.298 $\pm$ 0.007	0.943 $\pm$ 0.010	0.680 $\pm$ 0.017
	0.155 $\pm$ 0.006	0.270 $\pm$ 0.019	0.582 $\pm$ 0.090
MgFe $_2$ O $_4$ -A 1 cycle	0.449 $\pm$ 0.003	0.698 $\pm$ 0.005	0.690 $\pm$ 0.008
	0.867 $\pm$ 0.012	1.723 $\pm$ 0.023	0.585 $\pm$ 0.029

disappeared and the signature of two overlapping doublets appears in the Mössbauer spectrum being reminiscent of FeO.<sup>71</sup> The doublet with the larger QS value and the larger IS clearly belongs to Fe $^{2+}$  and the second doublet (with smaller QS and smaller IS) is caused by small amounts of Fe $^{3+}$ .

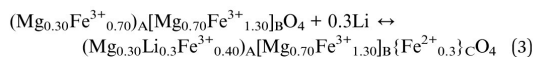
After insertion of 9 Li the XRD pattern exhibits no structural information due to the amorphous nature of the material (Fig. 9). More information can be extracted from the Mössbauer spectrum (Fig. 12, middle) being composed of two overlapping doublets with very small values for the IS (Table 3), which was also observed for fully discharged CoFe $_2$ O $_4$  and NiFe $_2$ O $_4$ .<sup>72,73</sup> The central absorption is caused by superparamagnetic metallic Fe nanoparticles, *i.e.* metallic Fe is formed during insertion of 9 Li per formula unit. These particles are not isolated but rather intimately dispersed in the Li $_2$ O matrix (see Li-NMR). The second doublet may be assigned also to metallic Fe atoms which are located at the surface of the particles being in a different environment compared to those in the centre of the particles. While fully converted CoFe $_2$ O $_4$  (ref. 72) exhibits a similar strong split signal, the splitting for converted MnFe $_2$ O $_4$  and CuFe $_2$ O $_4$  is less pronounced.<sup>42,72,74</sup>

After the first discharge/charge cycle the Mössbauer spectrum of MgFe $_2$ O $_4$ -A exhibits no sextet as expected for magnetic ordering, and is characterized by asymmetric broadened doublets which could be separated into two split signals (Fig. 12, bottom) similar to the spectrum after insertion of 2 Li per formula unit. The small particles are superparamagnetic with the doublet exhibiting the larger IS and QS values belonging to Fe $^{2+}$  and the second doublet is caused by a small amount of Fe $^{3+}$ . These observations indicate that during charging metallic Fe is oxidized to Fe $^{2+}$  as predicted in ref. 31 and 32.

#### 4. Discussion

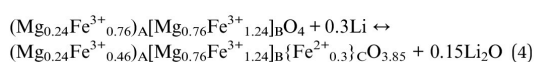
In the structure of MgFe $_2$ O $_4$  the Li $^{+}$  ions can either enter empty tetrahedral (8b and 48f) or octahedral (16c) sites. But for all sites Li $^{+}$ -Mg $^{2+}$ /Fe $^{3+}$  distances are below 2 Å leading to strong repulsive interactions (ESI,† Fig. 5 and 6). During Li uptake sample A consisting of nanosized crystallites shows an expansion of the lattice parameter, indicating that a small amount of Li can be incorporated. Further indication for the Li insertion is given by  $^7\text{Li}$  NMR spectra exhibiting a large shift of the resonance line which may be interpreted by magnetic interactions *via* Li-O-Fe bonds. But during Li insertion Fe $^{3+}$  is reduced to Fe $^{2+}$  which has

a larger ionic radius and the lattice parameter expansion may be caused by this effect. The intercalation takes place at 1.6 V visible by the cathodic peak in the CV curve (Fig. 8) and by the plateau in the galvanostatic discharge curve (Fig. 7, region I). The Li atoms reduce Fe $^{3+}$  on the tetrahedral site (8a) to Fe $^{2+}$ , which moves to the empty 16c site, as was observed in a previous study for MnFe $_2$ O $_4$ .<sup>42</sup> The uptake of the first 0.3 Li may then be formulated according to eqn (3):



Assuming that 0.3 Fe $^{3+}$  moved from the 8a site to the empty 16c site yielding the formula  $(\text{Mg}_{0.30}\text{Li}_{0.3}\text{Fe}^{3+}_{0.40})_{\text{A}}[\text{Mg}_{0.70}\text{Fe}^{3+}_{1.30}\{\text{Fe}^{2+}_{0.3}\}]_{\text{C}}\text{O}_4$  an average cation radius can be calculated for the three cations located on the tetrahedral site. Using the Shannon radii a value of 0.514 Å is calculated for the pristine material and an average radius of 0.544 Å for the intercalated sample. Hence, one would expect a lattice parameter expansion of about 5% instead of 0.2% obtained experimentally. Therefore, on the basis of this consideration one can assume that only a very small amount of Li is intercalated during this reaction step.

In contrast to sample A, sample B consists of larger particles (96 nm) and no expansion of the lattice parameter could be detected. This finding is in agreement with the CV curve of this material which shows no cathodic peak at 1.6 V. In addition, the absence of a plateau at 1.6 V in the galvanostatic discharge curve points to a different mechanism. The smaller surface of the larger particles may lead to a higher energy barrier for the intercalation process or just kinetic barriers caused by slow diffusion in the larger particles. The domain size of sample B is decreasing (30%) in comparison to sample A (no decrease in particle size) during the first Li uptake step. In  $^7\text{Li}$  NMR spectra a strong shift is visible, caused by Li-Fe-O bonds on the surface of the ferrimagnetic particles. XRD and NMR data suggest that a monoxide is deposited at the surface of the pristine particles while the core of the particles is still consisting of the spinel. In contrast to sample A, Li $_2$ O is formed from the beginning of Li uptake because Li $^{+}$  ions are not intercalated into the spinel structure (eqn (4)). Due to the strong shift in the  $^7\text{Li}$  NMR spectrum the newly formed small amounts of Li $_2$ O must be located close to the ferromagnetic spinel core.

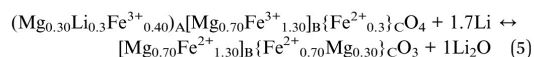


At this stage it is interesting to compare the behavior with Co $_3$ O $_4$  (particle size: 15–100 nm) where the trend of Li uptake occurs in the opposite way: larger particles lead to formation of an intercalated phase Li $_x$ Co $_3$ O $_4$  while smaller particles undergo a direct conversion.<sup>75</sup>

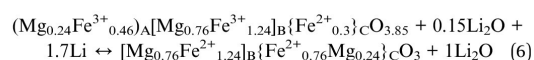
Subsequently, the insertion of 0.7 Li in sample A generates a rock salt type phase with sizes of the coherently scattering domains large enough to be clearly identified by XRD (Fig. 9). The Rietveld refinement indicates a further reduction of the sizes of coherently scattering domains of the spinel phase and



an increase of the NaCl-type domains. The generation of appreciable amounts of  $\text{Li}_2\text{O}$  in this reaction step is evidenced by the  $^7\text{Li}$  NMR results. During insertion of 1.5 and 2 Li per formula unit, for both samples the reflections of the spinel phase decrease and the intensity of the reflections of the rock salt phase increases in the XRD patterns. After insertion of 2 Li all  $\text{Fe}^{3+}$  are reduced to  $\text{Fe}^{2+}$  and all Mg/Fe ions are now on octahedral 16c sites. Moreover, the  $^{57}\text{Fe}$  Mössbauer spectrum of the sample containing 2 Li shows the signature of paramagnetic FeO and the  $^7\text{Li}$  NMR spectrum is dominated by a narrow line due to the presence of  $\text{Li}_2\text{O}$  for samples A and B. For sample A eqn (5) can be formulated as:



and for B eqn (6) may apply:



The occupation of all 16c sites changes the symmetry and space group  $Fm\bar{3}m$  is adopted by the monoxide with the chemical formula  $\text{Mg}_{0.33}\text{Fe}_{0.66}\text{O}$ . The formation of the monoxide takes place directly by rearrangement of the spinel structure. The formation of a rock salt structure during Li uptake has already been reported for  $\text{Fe}_3\text{O}_4$ ,  $\text{Co}_3\text{O}_4$  and  $\text{Mn}_3\text{O}_4$  proposing mechanisms being in remarkable difference to what is observed in the present study. According to the results obtained for  $\text{Fe}_3\text{O}_4$ , the first Li uptake step involves a movement of Fe from the tetrahedral site 8a to empty octahedral site 16c, a mechanism proposed also in our work. But further Li is intercalated occupying remaining 16c and accessible 8a/48f sites up to 2 Li per formula unit involving a 2.8% increase in the unit cell volume.<sup>76</sup> For  $\text{Co}_3\text{O}_4$  an even larger expansion of the unit cell volume of 8.6% was observed during Li intercalation within the stability range for  $\text{Li}_x\text{Co}_3\text{O}_4$  of  $1 < x < 1.92$ .<sup>77</sup> These findings are in contrast to our results where the maximum unit cell volume expansion is 0.9% for the nanosized sample A and only 0.14% for sample B with the larger crystallites. For tetragonally distorted  $\text{Mn}_3\text{O}_4$  different mechanisms must be formulated because of the formation of a non-cubic intermediate phase  $\text{LiMn}_3\text{O}_4$ .<sup>78</sup> But after insertion of 2 Li per formula unit the formation of a rock salt structured intermediate MnO was also observed.<sup>79</sup>

The particle sizes of the monoxide are determined by the particle sizes of the pristine material. In case of sample A the particle size is 8 nm, and the refined size of coherent scattering domains of the monoxide is 7 nm with the lattice parameter  $a = 4.237 \text{ \AA}$ , formed after insertion of 1.5 Li per formula unit. Starting with larger particles of 96 nm, larger coherently scattering domains of the monoxide ( $d_{\text{max}} = 46 \text{ nm}$ ) are obtained with a nearly identical parameter  $a = 4.2278 \text{ \AA}$  (difference between A and B: 0.2%). The refined  $a$  axis is slightly smaller than that reported in the literature ( $4.2710 \text{ \AA}$ ,  $\text{Mg}_{0.24}\text{Fe}_{0.76}\text{O}$ )<sup>66</sup> but confirms the existence of a mixed Mg/Fe oxide (see also Section 3.3).

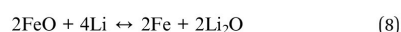
The insertion of another 4 Li per formula unit leads to reduction of  $\text{Fe}^{2+}$  to the metallic state according to eqn (7):



This reaction occurs in both samples during the intensive cathodic peak at 0.3 V in the CV curve (Fig. 8). During Li uptake, the intensity of the reflections of the monoxide decreases continuously during Li insertion as demonstrated by XRD. The Mössbauer spectrum evidences the presence of nanosized metallic Fe with an appreciable amount of Fe atoms on the surface of the particles. At the end of the first discharge metallic Fe nanoparticles are embedded in a  $\text{Li}_2\text{O}$  matrix as also described for  $\text{MnFe}_2\text{O}_4$ ,  $\text{NiFe}_2\text{O}_4$  and  $\text{ZnFe}_2\text{O}_4$ .<sup>42,80,81</sup> Assuming a statistical occupancy of the cationic sites in the monoxide by  $\text{Mg}^{2+}/\text{Fe}^{2+}$  the reaction formulated in eqn (5) requires destruction of long-range order and phase separation which explain the absence of reflections of MgO in the X-ray powder patterns.

A reduction of  $\text{Mg}^{2+}$  to  $\text{Mg}^0$  or formation of a Mg–Li alloy as reported for  $\text{Mg}_2\text{Si}$ <sup>82</sup> can be excluded due to the investigation of pure MgO (see ESI†). The stronger Mg–O bond in comparison to the Mg–Si bond may suppress the formation of  $\text{Mg}^0$ . The difference in capacity between samples A and B can be explained by the larger surface area of the nanoparticles. After discharge of the cell to 0.01 V metallic iron nanoparticles and amorphous MgO are embedded in a  $\text{Li}_2\text{O}$  matrix as schematically depicted in Fig. 13. Mössbauer spectra allow differentiation between iron atoms at the surface and in the core of the small particles.

During the charge process  $\text{Fe}^0$  can be oxidized to either  $\text{Fe}^{2+}$  or  $\text{Fe}^{3+}$ . Using  $\text{Fe}_2\text{O}_3$  as the pristine material Fe is oxidized to  $\text{Fe}^{3+}$  after the first cycle.<sup>83</sup> For other spinels with trivalent transition metals like  $\text{Mn}_3\text{O}_4$  the formation of MnO after the first cycle was reported.<sup>79</sup> According to the capacity fading after the first cycle, the different CV curves of the first and second cycle,  $^7\text{Li}$  NMR and the Mössbauer results, the charge process and following discharge/charge processes for both samples can be written according to eqn (8).



The formation of the iron monoxide was also proposed for converted  $\text{MgFe}_2\text{O}_4$ ,  $\text{Ca}_2\text{Fe}_2\text{O}_5$  and  $\text{Ca}_2\text{Co}_2\text{O}_5$ .<sup>31,84</sup> XRD investigations demonstrate that small particles of a monoxide are

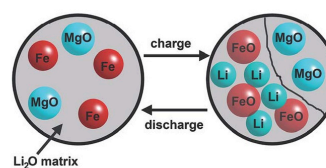


Fig. 13 Schematic illustration of metallic Fe nanoparticles and amorphous MgO embedded in the  $\text{Li}_2\text{O}$  matrix after discharge (left) and the charge/discharge process after the first cycle.





formed with NaCl-type during the charge process. The charge process is again accompanied by phase separation because only nanosized Fe particles are involved in this reaction while MgO is inactive. Such a phase separation phenomenon was reported as a mechanism for interfacial storage of lithium and may also proceed for the material investigated here.<sup>85</sup>

## 5. Conclusion

The present study highlights the value of combined and complementary chemical, structural and electronic characterization for the elucidation of the reaction pathways and ion-transport mechanisms interrelated with charge and discharge reactions of potential battery materials. According to the results obtained in the present study the mechanisms for Li insertion strongly depend on the average particle size of the host material. In case of nanosized particles, the complex pathway of the discharging reactions starts with an intercalation of very small amounts of Li. Subsequently, the successive formation of a NaCl-type ternary oxide is induced by movement of the cations located on tetrahedral sites to empty octahedral ones followed by successive conversion for Li contents larger than 2 per formula unit. Li cannot be intercalated into larger crystallites and the material is directly converted first to the NaCl-type monoxide material. Independent from the initial particle sizes, the formation of a composite consisting of a Li<sub>2</sub>O matrix with embedded Fe nanoparticles and nanosized MgO is observed during the final step of the discharging reaction. The particle sizes of the monoxide formed by conversion depend on those of the pristine spinel-type material due to the affinity between rock salt and the spinel structure. During the charge process Li is recovered and Fe is oxidized to FeO while MgO is not affected.

## Acknowledgements

We are grateful to the Deutsche Forschungsgemeinschaft and to the German Federal Ministry of Education and Research for financial support.

## References

- J.-M. Tarascon and M. Armand, *Nature*, 2001, **414**, 359.
- B. Scrosati, *Nature*, 1995, **373**, 557.
- V. Etacheri, R. Marom, R. Elazari, G. Salitra and D. Aurbach, *Energy Environ. Sci.*, 2011, **4**, 3243.
- J. B. Goodenough and K.-S. Park, *J. Am. Chem. Soc.*, 2013, **135**, 1167.
- N.-S. Choi, Z. Chen, S. A. Freunberger, X. Ji, Y.-K. Sun, K. Amine, G. Yushin, L. F. Nazar, J. Cho and P. G. Bruce, *Angew. Chem., Int. Ed.*, 2012, **51**, 9994.
- M. Armand and J.-M. Tarascon, *Nature*, 2008, **451**, 652.
- R. Marom, S. F. Amalraj, N. Leifer, D. Jacob and D. Aurbach, *J. Mater. Chem.*, 2011, **21**, 9938.
- P. Gibot, M. Casas-Cabanas, L. Laffont, S. Levasseur, P. Carlach, S. Hamelet, J.-M. Tarascon and C. Masquellier, *Nat. Mater.*, 2008, **7**, 741.
- A. Nyten, S. Kamali, L. Häggström, T. Gustafsson and J. O. Thomas, *J. Mater. Chem.*, 2006, **16**, 2266.
- J. B. Goodenough, *J. Solid State Electrochem.*, 2012, **16**, 2019.
- G. A. Nazri and G. Pistoia, *Lithium Batteries: Science and Technology*, Springer, US, 2008.
- P. G. Bruce, B. Scrosati and J.-M. Tarascon, *Angew. Chem., Int. Ed.*, 2008, **47**, 2930.
- A. S. Arico, P. Bruce, B. Scrosati, J.-M. Tarascon and W. van Schalkwijk, *Nat. Mater.*, 2005, **4**, 366.
- P. Poizot, S. Laruelle, S. Grugeron, L. Dupont and J.-M. Tarascon, *Nature*, 2000, **407**, 496.
- H. Long, T. Shi, S. Jiang, S. Xi, R. Chen, S. Liu, G. Liao and Z. Tang, *J. Mater. Chem. A*, 2014, **2**, 3741.
- J. Cabana, L. Monconduit, D. Larcher and M. R. Palacin, *Adv. Mater.*, 2010, **22**, 170.
- L. F. Nazar, G. Goward, F. Leroux, M. Duncan, H. Huang, T. Kerr and J. Gaubicher, *Int. J. Inorg. Mater.*, 2001, **3**, 191.
- D. W. Murphy and P. A. Christian, *Science*, 1979, **205**, 651.
- W. Bensch, J. Opey, H. Hain, H. Gesswein, D. Chen, R. Mönig, P. A. Gruber and S. Indris, *Phys. Chem. Chem. Phys.*, 2012, **14**, 7509.
- D. Larcher, G. Sudant, J.-B. Leriche, Y. Chabre and J.-M. Tarascon, *J. Electrochem. Soc.*, 2002, **149**, A234.
- P. Lavela and J. L. Tirado, *J. Power Sources*, 2007, **172**, 379.
- Y. Zhao, J. Li, Y. Ding and L. Guan, *J. Mater. Chem.*, 2011, **21**, 19101.
- C. T. Cherian, M. V. Reddy, G. V. S. Rao, C. H. Sow and B. V. R. Chowdari, *J. Solid State Electrochem.*, 2012, **16**, 1823.
- M. V. Reddy, G. V. Subba Rao and B. V. R. Chowdari, *Chem. Rev.*, 2013, **113**, 5364.
- Z. Ding, B. Yao, J. Feng and J. Zhang, *J. Solid State Electrochem.*, 2014, **18**, 19.
- T. Li, Y.-Y. Wang, R. Tang, Y.-X. Qi, N. Lun, Y.-J. Bai and R.-H. Fan, *ACS Appl. Mater. Interfaces*, 2013, **5**, 9470.
- F. Mueller, D. Bressler, E. Paillard, M. Winter and S. Passerini, *J. Power Sources*, 2013, **236**, 87.
- Y. Xiao, J. Zai, L. Tao, B. Li, Q. Han, C. Yu and X. Qian, *Phys. Chem. Chem. Phys.*, 2013, **15**, 3939.
- Z. Zhang, Y. Wang, M. Zhang, Q. Tan, X. Lv, Z. Zhong and F. Su, *J. Mater. Chem. A*, 2013, **1**, 7444.
- K. M. Shaju, F. Jiao, A. Debart and P. G. Bruce, *Phys. Chem. Chem. Phys.*, 2007, **9**, 1837.
- N. Sivakumar, S. R. P. Gnanakan, K. Karthikeyan, S. Amaresh, W. S. Yoon, G. J. Park and Y. S. Lee, *J. Alloys Compd.*, 2011, **509**, 7038.
- Y. Pan, Y. Zhang, X. Wei, C. Yuan, J. Yin, D. Cao and G. Wang, *Electrochim. Acta*, 2013, **109**, 89.
- Y. Yin, B. Zhang, X. Zhang, J. Xu and S. Yang, *J. Sol-Gel Sci. Technol.*, 2013, **66**, 540.
- C. Gong, Y.-J. Bai, Y.-X. Qi, N. Lun and J. Feng, *Electrochim. Acta*, 2013, **90**, 119.
- W. Bensch, T. Bredow, H. Ebert, P. Heitjans, S. Indris, S. Mankovsky and M. Wilkening, *Prog. Solid State Chem.*, 2009, **37**, 206.
- J. Wontcheu, W. Bensch, M. Wilkening, P. Heitjans, S. Indris, P. Sideris, C. P. Grey, S. Mankovsky and H. Ebert, *J. Am. Chem. Soc.*, 2008, **130**, 288.



- 37 J. Wontcheu, M. Behrens, W. Bensch, S. Indris, M. Wilkening and P. Heitjans, *Solid State Ionics*, 2007, **178**, 759.
- 38 M. Behrens, O. Riemenschneider, W. Bensch, S. Indris, M. Wilkening and P. Heitjans, *Chem. Mater.*, 2006, **18**, 1569.
- 39 M. Behrens, R. Kiebach, J. Ophey, O. Riemenschneider and W. Bensch, *Chem.-Eur. J.*, 2006, **12**, 6348.
- 40 S. Indris, J. Wontcheu and W. Bensch, *Phys. Chem. Chem. Phys.*, 2009, **11**, 3250.
- 41 M. Behrens, J. Wontcheu, R. Kiebach and W. Bensch, *Chem.-Eur. J.*, 2008, **14**, 5021.
- 42 S. Permien, H. Hain, M. Scheuermann, S. Mangold, V. Mereacre, A. K. Powell, S. Indris, U. Schürmann, L. Kienle, V. Duppel, S. Harm and W. Bensch, *RSC Adv.*, 2013, **3**, 23001.
- 43 B. Aslibeiki, P. Kameli, H. Salamati, M. Eshraghi and T. Tahmasebi, *J. Magn. Magn. Mater.*, 2010, **322**, 2929.
- 44 A. A. Coelho, *Topas Academic Version 4*, 2012.
- 45 A. Cimino, P. Porta and M. Valigi, *J. Am. Ceram. Soc.*, 1966, **49**, 152.
- 46 P. M. Diehm, P. Agoston and K. Albe, *ChemPhysChem*, 2012, **13**, 2443.
- 47 A. C. Druc, A. M. Dumitrescu, A. I. Borhan, V. Nica, A. R. Iordan and M. N. Palamaru, *Cent. Eur. J. Chem.*, 2013, **11**, 1330.
- 48 V. M. Khot, A. B. Salunkhe, M. R. Phadatare and S. H. Pawar, *Mater. Chem. Phys.*, 2012, **132**, 782.
- 49 E. de Grave, C. Dauwea, A. Govaert and J. de Sitter, *Phys. Stat. Sol.*, 1976, **73**, 527.
- 50 E. Wieser, H. Schröder and K. Kleinstück, *Phys. Stat. Sol.*, 1970, **1**, 749.
- 51 N. Sivakumar, A. Narayanasamy, J.-M. Greneche, R. Murugaraj and Y. S. Lee, *J. Alloys Compd.*, 2010, **504**, 395.
- 52 C. Liu, B. Zou, A. J. Rondinone and Z. J. Zhang, *J. Am. Chem. Soc.*, 2000, **122**, 6263.
- 53 Q. Chen, A. J. Rondinone, B. C. Chakoumakos and Z. J. Zhang, *J. Magn. Magn. Mater.*, 1999, **194**, 1.
- 54 P. Holec, J. Plocek, D. Niznansky and J. Poltieroova Vejpravova, *J. Sol-Gel Sci. Technol.*, 2009, **51**, 301.
- 55 S. Da Dalt, A. S. Takimi, T. M. Volkmer, V. C. Sousa and C. P. Bergmann, *Powder Technol.*, 2011, **210**, 103.
- 56 V. Šepelák, D. Baabe, F. J. Litterst and K. D. Becker, *J. Appl. Phys.*, 2000, **88**, 5884.
- 57 A. Ponrouch, P.-L. Taberna, P. Simon and M. R. Palacin, *Electrochim. Acta*, 2012, **61**, 13.
- 58 E. Bekaert, P. Balaya, S. Murugavel, J. Maier and M. Menetrier, *Chem. Mater.*, 2009, **21**, 856.
- 59 S. Laruelle, S. Grugeon, P. Poizot, M. Dolle, L. Dupont and J. M. Tarascon, *J. Electrochem. Soc.*, 2002, **149**, A627.
- 60 S. Grugeon, S. Laruelle, L. Dupont and J. M. Tarascon, *Solid State Sci.*, 2003, **5**, 895.
- 61 R. Dedryvere, S. Laruelle, S. Grugeon, P. Poizot, D. Gonbeau and J. M. Tarascon, *Chem. Mater.*, 2004, **16**, 1056.
- 62 L. Gireaud, S. Grugeon, S. Pilard, P. Guenot, J. M. Tarascon and S. Laruelle, *Anal. Chem.*, 2006, **78**, 3688.
- 63 P. Arora, R. E. White and M. Doyle, *J. Electrochem. Soc.*, 1998, **145**, 3647.
- 64 G. Li, Y. Wang, L. Yang, W. Ma and M. Wang, *Eur. J. Inorg. Chem.*, 2014, 845.
- 65 M. Boiocchi, F. Caucia, M. Merli, D. Prella and L. Ungaretti, *Eur. J. Mineral.*, 2001, **13**, 871.
- 66 A. H. Jay and K. W. Andrews, *J. Iron Steel Inst.*, 1946, **152**, 15.
- 67 C. P. Grey and N. Dupre, *Chem. Rev.*, 2004, **104**, 4493.
- 68 C. P. Grey and Y. J. Lee, *Solid State Sci.*, 2003, **5**, 883.
- 69 S. Indris, J. Cabana, O. J. Rutt, S. J. Clarke and C. P. Grey, *J. Am. Chem. Soc.*, 2006, **128**, 13354.
- 70 J. Kim, U. G. Nielsen and C. P. Grey, *J. Am. Chem. Soc.*, 2008, **130**, 1285.
- 71 D. P. Johnson, *Solid State Commun.*, 1969, **7**, 1785.
- 72 P. Lavela, J. L. Tirado, M. Womes and J. C. Jumas, *J. Phys. Chem. C*, 2009, **113**, 20081.
- 73 C. Vidal-Abarca, P. Lavela and J. L. Tirado, *J. Phys. Chem. C*, 2010, **114**, 12828.
- 74 M. Bomio, P. Lavela and J. L. Tirado, *ChemPhysChem*, 2007, **8**, 1999.
- 75 D. Larcher, G. Sudant, J.-B. Leriche, Y. Chabre and J.-M. Tarascon, *J. Electrochem. Soc.*, 2002, **149**, A234.
- 76 M. M. Thackeray, W. I. F. David and J. B. Goodenough, *Mater. Res. Bull.*, 1982, **17**, 785.
- 77 M. M. Thackeray, S. D. Baker, K. T. Adendorf and J. B. Goodenough, *Solid State Ionics*, 1985, **17**, 175.
- 78 M. M. Thackeray, W. I. F. David, P. G. Bruce and J. B. Goodenough, *Mater. Res. Bull.*, 1983, **18**, 461.
- 79 M. A. Lowe, J. Gao and H. D. Abruna, *J. Mater. Chem. A*, 2013, **1**, 2094.
- 80 F. Martinez-Julian, A. Guerrero, M. Haro, J. Bisquert, D. Bresser, E. Paillard, S. Passerini and G. Garcia-Belmonte, *J. Phys. Chem. C*, 2014, **118**, 6069.
- 81 R. Alcantara, M. Jaraba, P. Lavela, J. L. Tirado, J. C. Jumas and J. Olivier-Fourcade, *Electrochem. Commun.*, 2003, **5**, 16.
- 82 H. Kim, J. Choi, H.-J. Sohn and T. Kang, *J. Electrochem. Soc.*, 1999, **146**, 4401.
- 83 X. Zhu, Y. Zhu, S. Muralki, M. D. Stoller and R. S. Ruoff, *ACS Nano*, 2011, **5**, 3333.
- 84 N. Sharma, K. M. Shaju, G. V. Subba Rao and B. V. R. Chowdari, *Electrochim. Acta*, 2004, **49**, 1035.
- 85 J. Jamnik and J. Maier, *Phys. Chem. Chem. Phys.*, 2003, **5**, 5215.





### 3.3 What happens structurally and electronically during the Li conversion reaction of $\text{CoFe}_2\text{O}_4$ nanoparticles: An *operando* XRD and XAS investigation

In the publication the results of an *operando* XRD and XAS study using  $\text{CoFe}_2\text{O}_4$  nanoparticles as anode material in Lithium ion batteries is presented. The long-range structural changes occurring during the first discharge/charge cycle were investigated with *operando* XRD (ANKA, Karlsruhe) while the alterations of the local structure and electronic properties were followed by *operando* XAS studies at the Co and Fe K-edges (BESSY, Berlin). On the basis of all results we postulate that the first reaction during discharge is an uptake of Li by an amorphous surface layer covering the crystalline cores of the particles. Increasing the Li content a rock-salt like oxide is successively formed and the spinel structure disappeared after uptake of about 2 Li per formula unit. During this reaction  $\text{Fe}^{3+}$  is reduced to  $\text{Fe}^{2+}$  while  $\text{Co}^{2+}$  is not affected. The bivalent cations located on tetrahedra in the spinel structure move to empty octahedra yielding the structural arrangement of NaCl. Uptake of more Li leads to successive formation of amorphous Co and Fe metal nanoparticles embedded in a  $\text{Li}_2\text{O}$  matrix. The reduction of  $\text{Fe}^{2+}$  and  $\text{Co}^{2+}$  to the metallic state occurs simultaneously without any further intermediate reaction step. After the charge process oxides are formed which are either amorphous or crystallite sizes are too small to be detected by XRD. The XAS investigations evidence that metallic Co and Fe are oxidized to  $\text{Co}^{2+}$  and  $\text{Fe}^{3+}$  during charging. But extended cycling leads to a successive deactivation of metallic Co, i.e. after few cycles Co could not be oxidized. This is one reason for irreversible capacity loss observed during cycling.

Reprinted with permission from Stefan Permien, Sylvio Indris, Ulrich Schürmann, Lorenz Kienle, Stefan Zander Stephen Doyle, Wolfgang Bensch, *Chemistry of Materials*, **2016**, *28*, 434-444. DOI: 10.1021/acs.chemmater.5b01754 Copyright 2016 American Chemical Society.

## What Happens Structurally and Electronically during the Li Conversion Reaction of $\text{CoFe}_2\text{O}_4$ Nanoparticles: An Operando XAS and XRD Investigation

Stefan Permien,<sup>†</sup> Sylvio Indris,<sup>‡</sup> Ulrich Schürmann,<sup>§</sup> Lorenz Kienle,<sup>§</sup> Stefan Zander,<sup>||</sup> Stephen Doyle,<sup>⊥</sup> and Wolfgang Bensch<sup>\*,†</sup>

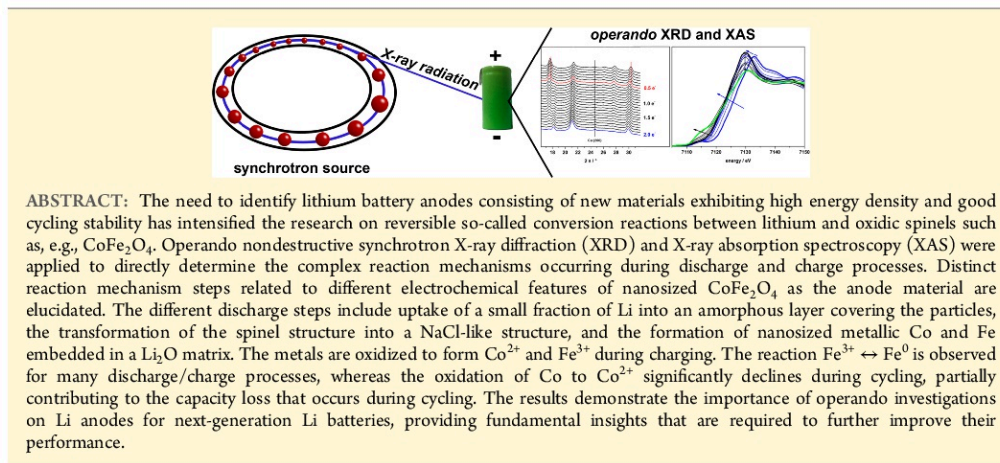
<sup>†</sup>Institute of Inorganic Chemistry, University of Kiel, Max-Eyth-Str. 2, 24118 Kiel, Germany

<sup>‡</sup>Institute for Applied Materials and <sup>⊥</sup>ANKA Synchrotron Radiation Facility, Karlsruhe Institute of Technology, P.O. Box 3640, 76021 Karlsruhe, Germany

<sup>§</sup>Institute for Materials Science, University of Kiel, Kaiserstr. 2, 24143 Kiel, Germany

<sup>||</sup>Helmholtz Center Berlin for Energy and Materials, Hahn-Meitner-Platz 1, 14109 Berlin, Germany

### Supporting Information



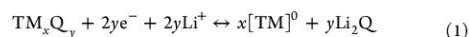
**operando XRD and XAS**

**ABSTRACT:** The need to identify lithium battery anodes consisting of new materials exhibiting high energy density and good cycling stability has intensified the research on reversible so-called conversion reactions between lithium and oxides such as, e.g.,  $\text{CoFe}_2\text{O}_4$ . Operando nondestructive synchrotron X-ray diffraction (XRD) and X-ray absorption spectroscopy (XAS) were applied to directly determine the complex reaction mechanisms occurring during discharge and charge processes. Distinct reaction mechanism steps related to different electrochemical features of nanosized  $\text{CoFe}_2\text{O}_4$  as the anode material are elucidated. The different discharge steps include uptake of a small fraction of Li into an amorphous layer covering the particles, the transformation of the spinel structure into a NaCl-like structure, and the formation of nanosized metallic Co and Fe embedded in a  $\text{Li}_2\text{O}$  matrix. The metals are oxidized to form  $\text{Co}^{2+}$  and  $\text{Fe}^{3+}$  during charging. The reaction  $\text{Fe}^{3+} \leftrightarrow \text{Fe}^{0}$  is observed for many discharge/charge processes, whereas the oxidation of Co to  $\text{Co}^{2+}$  significantly declines during cycling, partially contributing to the capacity loss that occurs during cycling. The results demonstrate the importance of operando investigations on Li anodes for next-generation Li batteries, providing fundamental insights that are required to further improve their performance.

### 1. INTRODUCTION

The need for better batteries for applications in several technologically important areas like plugin hybrid and fully electric vehicles, laptops, and smart phones can be regarded as the main driving force for the steadily increasing research efforts toward new electrode materials.<sup>1–6</sup> Li-based electrode materials in commercially available batteries work on the basis of intercalation/deintercalation reactions.<sup>7–12</sup> Depending on the cathode material, less than one Li per formula unit can be cycled per transition metal (TM) in the formula unit. An attractive alternative to intercalation/deintercalation is the conversion reaction of electrode materials, thus enabling specific capacities 2–10 times higher than those for commercialized graphite/ $\text{LiCoO}_2$  materials.<sup>13–16</sup> The significantly higher capacity is based on the cycling of much more Li with respect to the amount of TM.<sup>16–19</sup> During a conversion reaction, the cations of an electrode material are reduced to the metallic state, forming nanosized particles embedded in a

matrix of Li compound(s) consisting of Li and the corresponding anion.<sup>13–16,20</sup> Concerning materials for conversion electrodes, TM oxides and sulfides are a focus of current research. The redox reaction during reversible electrochemical Li uptake/release proceeds according to eq 1



where TM = transition metal and Q = O, S.

Besides oxides and sulfides, fluorides, phosphides, and nitrides were also investigated with respect to conversion reactions during Li uptake/release.<sup>21–28</sup> Among other compounds, spinel ferrites of the general formula  $\text{MFe}_2\text{O}_4$  (M = Co, Ni, Mn, Cu, and Zn) are promising high-capacity candidates because of the complete reduction of M and Fe to

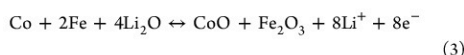
Received: May 11, 2015

Revised: December 7, 2015

Published: December 16, 2015

the metallic state.<sup>29–31</sup> Zn-containing TM oxides can reversibly host one additional Li by an alloying reaction, forming LiZn. One of the most promising spinel ferrites is CoFe<sub>2</sub>O<sub>4</sub>, with an initial capacity of more than 1200 mAh g<sup>-1</sup>.<sup>32,33</sup> These initial capacities are higher than the theoretical value (914 mAh g<sup>-1</sup>), which is related to partially reversible electrolyte decomposition, as discussed in detail later. However, one should consider the so-called extra capacity with care. In commercial devices, the amount of electrolyte is strictly limited; therefore, it is highly desirable to avoid electrolyte consumption by electrolyte decomposition. Using CoFe<sub>2</sub>O<sub>4</sub> with special morphologies like films,<sup>34</sup> nanosheets,<sup>35</sup> spheres,<sup>36</sup> or nanowires<sup>37</sup> leads to very good cycling stability with reversible capacities higher than 1000 mAh g<sup>-1</sup> even after 100 cycles. The stability of the electrode can be enhanced by adding carbon species. Cross-linked CoFe<sub>2</sub>O<sub>4</sub> particles with carbon nanotubes reached 1046 mAh g<sup>-1</sup> in the 100th cycle.<sup>38</sup> CoFe<sub>2</sub>O<sub>4</sub> particles deposited on graphene sheets yielded capacities of more than 1000 mAh g<sup>-1</sup> after 100 cycles,<sup>39–42</sup> and CoFe<sub>2</sub>O<sub>4</sub> particles coated with thermally decomposed carbon reached a capacity of ca. 700 mAh g<sup>-1</sup> in the 200th cycle.<sup>43</sup> All of these reports prove the excellent cycling stability of CoFe<sub>2</sub>O<sub>4</sub>- and CoFe<sub>2</sub>O<sub>4</sub>-based composites, but up to now, no operando study has been performed to follow the structural and electronic changes occurring during the conversion reaction.

In the past, formulating reaction mechanisms was attempted based on cyclic voltammetry (CV) or ex situ techniques. For Li uptake by and release from CoFe<sub>2</sub>O<sub>4</sub>, the following pathways (2 and 3) are proposed in the literature:<sup>32,38,39,44–46</sup>



However, in the galvanostatic discharge/charge curves during the first cycle, up to three plateaus occur, indicating that the mechanism is more complex than that suggested by eq 2. After the first cycle, a large irreversible capacity loss was reported that cannot be explained by eq 3. Additionally, the reaction mechanism during the first charge process has never been studied in detail, but this is the most important step for all of the subsequent charge/discharge cycles. The complexity of the conversion reaction together with the reactivity and sensitivity of the lithiated species requires in situ/operando investigations to achieve a detailed reaction mechanism.<sup>47,48</sup>

Over the past few years, the power of such experiments has been impressively demonstrated by several groups.<sup>49–63</sup> For MnFe<sub>2</sub>O<sub>4</sub><sup>64</sup> and MgFe<sub>2</sub>O<sub>4</sub><sup>65</sup> nanoparticles, we studied the reaction mechanism in detail: During the first discharge, the first step consists of intercalation of a very small amount of Li (~0.3 Li). After uptake of 1 Li per MnFe<sub>2</sub>O<sub>4</sub>, one Fe<sup>3+</sup> is reduced to Fe<sup>2+</sup> per formula unit and the process is accompanied by the movement of ions on the tetrahedral sites to empty neighboring octahedral sites, thus generating a rock salt-type oxide and Li<sub>2</sub>O. After uptake of 2 Li per formula unit, all Fe<sup>3+</sup> are reduced to Fe<sup>2+</sup> and all octahedral sites are now occupied by Fe<sup>2+</sup>/Mn<sup>2+</sup>, whereas the tetrahedral sites are empty. The occupancy of all octahedral sites by the TM cations corresponds to a NaCl-type monoxide, which is the only crystalline phase that could be identified in the XRD patterns. Upon increasing the number of inserted Li, Fe<sup>2+</sup>/Mn<sup>2+</sup> are successively converted to metallic Fe and Mn nanoparticles that are embedded in a Li<sub>2</sub>O matrix. During the charge process, the

spinel phase is not recovered, but divalent Fe oxide is formed, which was evidenced by <sup>57</sup>Fe Mössbauer spectra.

During Li uptake/release, new species are generated with high chemical reactivity and sensitivity against oxygen and water/moisture. Investigating battery cells in operation (operando) enables the detection of the electronic and structural changes occurring during Li uptake and removal without the risk of contamination or formation of unwanted chemical species caused by contact with air and/or moisture.<sup>47–58</sup>

The present operando XAS and XRD study of the charge and discharge mechanisms of nanosized CoFe<sub>2</sub>O<sub>4</sub> during Li uptake/removal sheds light on the step-by-step long- and short-range structural order as well as on changes of the electronic states of the absorber atoms.<sup>66</sup> On the basis of the operando investigations and literature data, we postulate a general reaction pathway for Li uptake and release for spinel materials of general formula MFe<sub>2</sub>O<sub>4</sub>.

## 2. EXPERIMENTAL SECTION

CoFe<sub>2</sub>O<sub>4</sub> nanoparticles were synthesized by calcination of a precipitate prepared by mixing 5 mmol of Co(NO<sub>3</sub>)<sub>2</sub>·6H<sub>2</sub>O (97%, Merck), 10 mmol of Fe(NO<sub>3</sub>)<sub>3</sub>·9H<sub>2</sub>O (98%, Riedel-de Haen), and 15 mmol of citric acid (99%, Merck) in a Fritsch Pulverisette ball mill for 2 h with 15 mm agate balls at 500 rpm in air. The viscous product was decomposed at 400 °C in a preheated oven for 3 h.

XRD patterns were recorded in reflection mode with an X'Pert Pro PANalytical equipped with a PIXcel detector using Cu K $\alpha$  radiation. EDX spectra were collected in a Philips ESEM XL 30 with an EDAX New XL-30 detecting unit. TEM investigations were performed in a Tecnai F30 G<sup>2</sup>-STwin microscope operated at 300 kV with a field emission gun cathode and a Si/Li detector (EDAX). For TEM preparation, CoFe<sub>2</sub>O<sub>4</sub> nanoparticles were suspended in *n*-butanol and dropped on a holey-carbon copper grid.

For electrochemical characterization, 80 wt % CoFe<sub>2</sub>O<sub>4</sub> powder was mixed with 10 wt % SUPER C65 carbon (Timcal, Switzerland) and 10 wt % PVDF (Solvay, Germany). The mixture was dissolved with NMP (*N*-methyl-2-pyrrolidone), deposited on copper foil, dried overnight at room temperature, and sintered at 80 °C for 24 h in a vacuum drying chamber. Afterward, 10 mm discs were cut with about 2 mg of active material and applied as the cathode in a Swagelok-type test cell, using lithium metal as the anode, glass fiber filter disks (Whatman, United Kingdom) as the separator, and a solution of 1 M LiPF<sub>6</sub> in an ethylene carbonate/dimethyl carbonate mixture (Merck, Germany) as the electrolyte. Test cells were discharged/charged at a C/10 rate, performed with a Materials Mates 510 DC potentiostat/galvanostat. A C/10 rate equates to the current for uptake/release of 8 Li per formula unit within 10 h, which corresponds to 914 mA/g.

For operando investigations, a custom-built cell (Figure 1) consisting of two aluminum plates with rectangular apertures (14 × 3 mm) in the center and two sheets of Kapton foil windows glued on both sides was used. The active anode material was mixed with carbon and PVDF (as described above). The mixture was suspended in NMP,

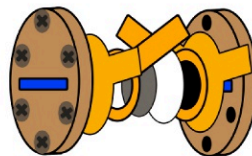


**Figure 1.** Schematic illustration of the in situ cell for XRD and XAS investigations. Design from left to right: aluminum plate, Kapton foil, copper current collector, lithium, separator, copper foil with active material, Kapton foil, and aluminum plate.



deposited on a thin Cu foil, and dried. Li metal as the counter electrode was attached on Cu foil. A microporous polyethylene/polypropylene membrane (Celgard 2325) was used as the separator, and 1 M LiPF<sub>6</sub> in an ethylene carbonate/dimethyl carbonate mixture was used as the electrolyte. The cells were assembled in an argon-filled glovebox (<1 ppm of O<sub>2</sub>, <1 ppm of H<sub>2</sub>O) and transferred to the beamline in a plastic bag. Galvanostatic lithiation/delithiation was realized with a Biologic SP-300 at a C/15 rate in a voltage range from 3.0 to 0.1 V.

For operando XRD, the PDIFF beamline at ANKA/Karlsruhe was operated at 16 keV with a Princeton CCD detector. Powder patterns were collected within 5 min. Copper diffraction reflections were masked, and 2D patterns were transformed with Area Diffraction Machine.<sup>67</sup>

XAS measurements were carried out at the KMC-2 beamline/BESSY II at Helmholtz-Zentrum Berlin in transmission mode. To enable comparison of the data, Fe and Co foils were always measured between the second and third ionization chambers. Spectra were background corrected, normalized, *k*<sup>2</sup>-weighted, and Fourier transformed with the Athena Software package.<sup>68</sup>

### 3. RESULTS

**3.1. Characterization of the Pristine Material.** Figure 2 presents the X-ray powder pattern of the as-prepared CoFe<sub>2</sub>O<sub>4</sub>

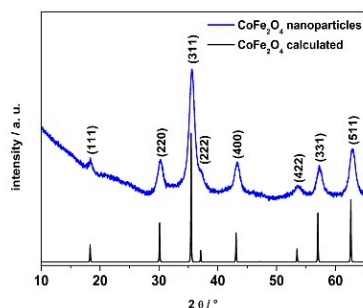


Figure 2. XRD powder pattern of the as-prepared CoFe<sub>2</sub>O<sub>4</sub> particles (blue) and calculated powder pattern (black).

nanoparticles. All reflections can be indexed on the basis of the cubic spinel phase (space group *Fd3m*, *a* = 8.360(2) Å). The broadened reflections indicate crystallites in the nanometer range, and an analysis applying the fundamental parameter approach implemented in TOPAS (Supporting Information, Figure S1)<sup>69</sup> yields a volume-weighted average size of 5.5(4) nm. The EDX analysis of the K-lines yields a Fe/Co ratio of 2:1, as expected (Supporting Information, Table S1). The root-mean-square deviation is about 0.36 atom % for Co and 0.37 atom % for Fe estimated from measurements at different positions of the sample.

A TEM image (Figure 3, bottom left) of pristine CoFe<sub>2</sub>O<sub>4</sub> nanoparticles demonstrates that the particle size ranges from 6 to 12 nm. Nanoprobe EDX analysis gave no indication of chemical inhomogeneity, and the Fe/Co ratio of 2:1 was verified. A representative electron diffraction pattern (Figure 3, top left) can be indexed on the basis of the cubic spinel-type structure (space group *Fd3m*, *d(hkl)* exp./calc. in Å: *d*(220) = 2.95/2.965, *d*(311) = 2.52/2.529, *d*(400) = 2.12/2.097, *d*(333/511) = 1.61/1.614, and *d*(440) = 1.48/1.483). The diffraction pattern of the as-prepared CoFe<sub>2</sub>O<sub>4</sub> particles was simulated using the JEMS program package<sup>70,71</sup> (Figure 3, top right).

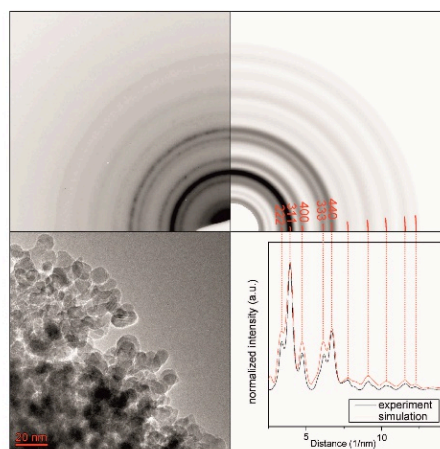
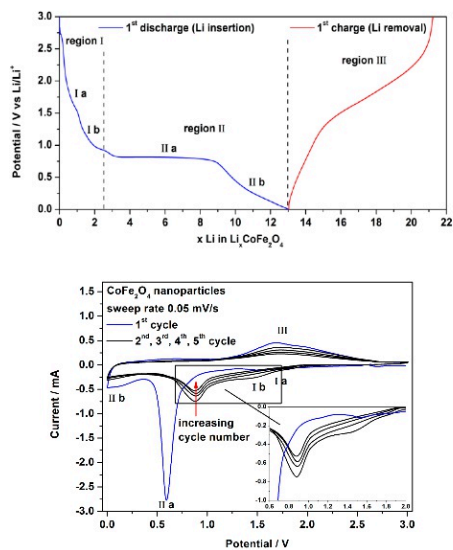


Figure 3. SAED pattern (top left) and corresponding simulation (top right) of the as-prepared CoFe<sub>2</sub>O<sub>4</sub> nanoparticles, as shown in a TEM bright-field image (bottom left). Comparison of experimental and simulated rotational average profiles (bottom right).

Background-subtracted rotational average profiles were created using a plug-in script (DiffTool) of Digital Micrograph software (Gatan). The rotational average profiles represent the circularly integrated intensity within a SAED pattern (Figure 3, bottom right) in dependence on reciprocal spacing. All reflections of the simulated diffraction pattern as well as the rotational average profile correspond to *d* values, as do the intensities to the reflections of the corresponding experimental data. A HRTEM image of CoFe<sub>2</sub>O<sub>4</sub> nanoparticles indicates that the particles are covered by a thin amorphous layer (Supporting Information, Figure S2).

**3.2. Electrochemical Performance.** Galvanostatic cycling (Figure 4, top) was done at a C/10 rate. The potential profile during discharge (Li uptake) is separated into two main regions, denoted I + II, and the charge process (Li removal) consists of one region (region III). In region I, the cell potential drops very fast to 1.5 V (Figure 4, region Ia), followed by a quasi-plateau at about 1.0 V with a length of 1.4 Li (160 mAh g<sup>-1</sup>). An even longer plateau appears at 0.8 V, corresponding to an uptake of 5.6 Li (638 mAh g<sup>-1</sup>) per formula unit (Figure 4, region IIa). At the end of the discharge process, the potential decreased to 0.01 V (Figure 4, top, region IIb). The capacity of the whole discharge process amounts to 1485 mAh g<sup>-1</sup> (theoretical capacity: 914 mAh g<sup>-1</sup>), corresponding to an uptake of 13 Li per formula unit (114 mAh g<sup>-1</sup> = 1 Li). The phenomenon of obtaining a higher capacity than the theoretical one has also been reported in the literature for CoFe<sub>2</sub>O<sub>4</sub>.<sup>29–46</sup> During the charge process, no clear plateau occurs. At about 1.8 V, a quasi-plateau is observed with a length corresponding to the release of 5 Li (563 mAh g<sup>-1</sup>), i.e., the reversible capacity amounts to 1027 mAh g<sup>-1</sup>. The irreversible capacity loss is 458 mAh g<sup>-1</sup> (30%). Such an initial capacity loss is mainly caused by irreversible reactions of the electrolyte, like the formation of a solid electrolyte interphase (SEI).<sup>72</sup> The phenomenon of extra reversible capacity (higher than the theoretical one) can be based either on charge storage at interfaces of nanoparticles<sup>73,74</sup> or partially reversible electrolyte decomposi-



**Figure 4.** Potential profile during the first discharge and charge cycle of  $\text{CoFe}_2\text{O}_4$  (top). CV of  $\text{CoFe}_2\text{O}_4$  in a potential range from 0 to 3 V with a sweep rate of 0.05 mV/s (bottom). The inset shows the cathodic sweep in detail.

tion.<sup>75–78</sup> Further cycles are shown in Supporting Information Figure S3.

In the CV curve (Figure 4, bottom), the first cycle is different from the subsequent ones. During the first discharge, the long plateau observed in the galvanostatic discharge (Figure 4, region IIa) is visible as an intense signal at 0.6 V (Figure 4, IIa) in the CV curve, whereas the two small plateaus in region I (Figure 4) cause only very low peak intensity in the CV curve. During the charge process, one broad signal is observed at 1.7 V that belongs to the potential increase in region III in Figure 4. The intense peak at 0.6 V disappeared after the first cycle, and two new events are observed at 1.6 and 0.8 V. The anodic peak at 1.7 V shifts slightly to 1.8 V. This is clear evidence that strong structural and electronic changes are taking place during the first cycle and that new phases are formed at the end of the first cycle. The CV curve observed here is similar to that presented in the literature for  $\text{CoFe}_2\text{O}_4$  powders.<sup>79,80</sup> Galvanostatic cycling and CV evidence complex changes of the material during Li uptake and removal, which cannot be interpreted straightforwardly without results obtained via in situ/operando investigations of Li uptake/release.

**3.3. Operando XRD.** Operando X-ray diffraction patterns recorded during the initial uptake of 2 Li per formula unit are presented in Figure 5. The potential curve of the in situ cell is presented in Figure 5 (bottom left) and is identical with that of region I in Figure 4 (top). First (region Ia), a fast drop of the potential to 1.5 V occurs (Figure 5, bottom left). During uptake of the first 0.5 Li per formula unit, all reflections shift to smaller  $2\theta$  angles (Figure 5, top). The value of the  $a$  axis of pristine  $\text{CoFe}_2\text{O}_4$  nanoparticles refined from the synchrotron XRD data is 8.372(2) Å (laboratory data: 8.360(2) Å). The Li uptake leads to a linear expansion of the  $a$  axis from 8.372(2) to 8.427(3) Å (Figure 5, bottom right), and the unit cell volume is

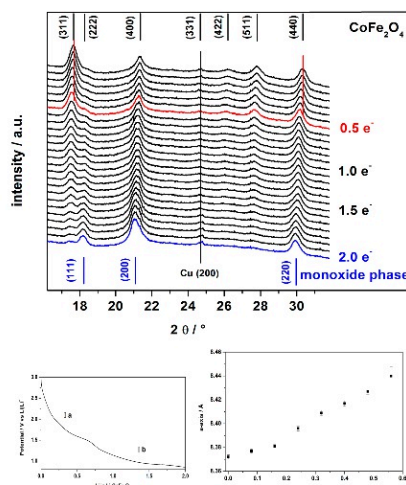


**Figure 5.** Operando XRD of  $\text{CoFe}_2\text{O}_4$  during Li uptake of 2 Li per formula unit (top), cell potential of region I during Li uptake (bottom, left), and refined lattice parameter  $a$  during insertion of the first 0.6 Li with error bars (bottom, right). The Cu (200) reflection at  $24.3^\circ 2\theta$  is caused by the setup of the in situ cell described in Section 2.

enlarged by about 2%, suggesting a 3D lithium ion insertion reaction. Cycling in the potential range from 1.6 to 3 V shows strong capacity fading (about 50%) after the first cycle (Supporting Information, Figure S4). Hence, the insertion process is only partially reversible, and one may assume that a small amount of Li can be reversibly incorporated in vacancies and/or defects at the surface of the  $\text{CoFe}_2\text{O}_4$  nanoparticles. A similar observation was made for  $\text{MnFe}_2\text{O}_4$ ,<sup>64</sup>  $\text{MgFe}_2\text{O}_4$ ,<sup>65</sup> and also for  $\text{CoFe}_2\text{O}_4$  nanospheres, where a shift of all reflections during the first discharge (at 1.2 V) was reported.<sup>37</sup> For  $\text{CoFe}_2\text{O}_4$  bulk material, an expansion of the unit cell during wet chemical Li uptake was also reported in combination with the poor reversibility of the Li uptake/release reaction.<sup>81</sup>

In region Ib (after uptake of 0.5 Li per formula unit), no further shift in the reflections can be observed. However, insertion of more Li leads to a significant drop in the intensity of the (311) and (511) reflections of the spinel phase while reflections of a new phase simultaneously develop, as can be seen by the occurrence of intensities adjacent to the (222), (400), and (440) reflections of the spinel phase. With increasing Li content, these new reflections exhibit a significant increase in intensity. Similar to  $\text{Mn}_3\text{O}_4$ ,<sup>58</sup>  $\text{ZnFe}_2\text{O}_4$ ,<sup>63</sup>  $\text{MnFe}_2\text{O}_4$ ,<sup>64</sup> and  $\text{MgFe}_2\text{O}_4$ ,<sup>65</sup> we propose that the spinel structure is successively transformed to a rock salt-type structure by movement of  $\text{Co}^{2+}$  and  $\text{Fe}^{3+}$  ions from tetrahedral sites to neighboring octahedral sites while  $\text{Fe}^{3+}$  ions are simultaneously reduced to  $\text{Fe}^{2+}$  (see below). The formation of a NaCl-type structure is accompanied by a change of the space group from  $Fd\bar{3}m$  to  $Fm\bar{3}m$ , and the unit cell parameter is about half of the original cell. After uptake of 2 Li per formula unit, the reflections of the spinel phase cannot be detected anymore, whereas reflections of the oxidic rock salt consisting of either both cations or phase-separated oxides dominate the XRD pattern. We note that under thermodynamic equilibrium



conditions  $T > 900$  °C is required for formation of a solid solution  $\text{Fe}_{1-x}\text{Co}_x\text{O}$ .<sup>82</sup> The  $a$ -axis parameter of the newly formed oxide was refined to 4.247(3) Å with a particle size of about 5 nm (Supporting Information Figure S5). Nearly stoichiometric FeO has a slightly larger  $a$  axis at 4.326(2) Å.<sup>83</sup> For the rock salt structure of CoO with a particle size of 22 nm, the  $a$  axis amounts to 4.260(1) Å.<sup>84</sup> Hence, the refined value for the  $a$  axis is near the values of the two monoxides. Keeping in mind that the octahedral positions are randomly occupied by  $\text{Co}^{2+}/\text{Fe}^{2+}$ , the formation of two separated monoxides ( $\text{Co}_{1-x}\text{O}$ ,  $\text{Fe}_{1-x}\text{O}$ ) does not seem to be reasonable. The XRD pattern was refined with only one monoxide phase. In the case of the formation of two monoxides with two different lattice parameters, an asymmetry of the reflections would occur at larger scattering angles, which does not seem to be the case here. Hence, the most probable assumption is the development of a mixed monoxide. Whether the monoxide is non-stoichiometric cannot be decided on the basis of the XRD experiments.

After conversion of 2 Li per formula unit, an extended plateau at 0.8 V has been observed in the galvanostatic discharge curve (Figure 4, top, region IIa), which is also seen in the potential recorded with the in situ cell (Figure 6, bottom).

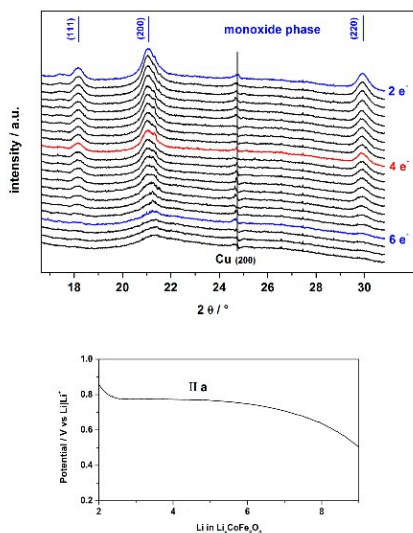


**Figure 6.** Operando XRD of  $\text{CoFe}_2\text{O}_4$  during Li uptake between 2 and 6.5 Li per formula unit (top) and change of the cell potential (bottom).

The slightly different potential profile may be caused by the different design of the in situ cell (without spring). During uptake of more than 2 Li per formula unit, the intensity of the reflections of the monoxide phase decreases and the FWHM increases due to the decrease of the sizes of coherently scattering domains (Figure 6). These observations indicate that the intermediately formed mixed monoxide is transformed into an amorphous phase. After uptake of 6 Li, no reflections could be detected, demonstrating that the crystalline domains are too small to be detected by XRD. In further cycles, no crystalline

phases exhibiting long-range order are formed. The presence of nanocrystallites that are too small to be detected in XRD patterns cannot be safely excluded. We note that the formation of an amorphous/nanocrystalline product was also observed in ex situ XRD experiments after discharge to 0.01 V.<sup>34,37</sup>

**3.4. Operando XAS.** As discussed above, the spinel is not recovered after the first cycle, thus requiring application of XAS as a powerful method to provide information about the oxidation state and detailed information about changes of the local environment of atoms on a short-range scale. The K absorption edges of Co and Fe have an energy difference of only about 0.6 keV, which allows XAS measurements to be made in just one cell. The potential curve recorded with the XAS in situ cell (Figure 7) shows the same behavior as that

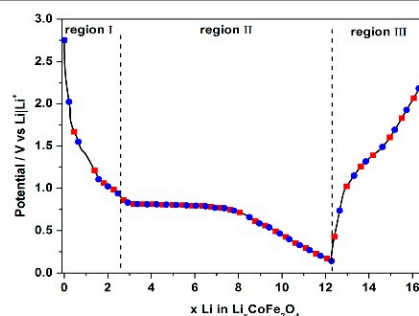


**Figure 7.** Cell potential (black line) during operando XAS investigation. Blue circles mark XAS scans at the Co K-edge, and red squares, at the Fe K-edge.

obtained with a Swagelok cell (Figure 4, top). In regions I + II, the material was discharged at a C/25 rate ( $I = 160$   $\mu\text{A}$ ), and for region III (charge process),  $I = 220$   $\mu\text{A}$  was selected (C/18 rate; Figure 7). A capacity loss during the first cycle occurred, as described in Section 3.1. Blue circles in Figure 7 mark XAS scans at the Co K-edge, and red squares, the scans at the Fe K-edge.

The first XAS scans of both K-edges are shown in Figure 8 (in each case, thick blue line). The edge energy of the Co K-edge was 7721 eV, and the pre-edge peak with a small intensity is located at 7710 eV, determined by the maximum of the first derivation (note that XAS spectra of pristine  $\text{CoFe}_2\text{O}_4$  are also shown in Figure 10). A Co K-edge energy of 7720 eV was reported for  $\text{CoFe}_2\text{O}_4$  nanoparticles (size about 5 nm), which was accompanied by a very small pre-edge peak at 7710 eV.<sup>85</sup> The edge energy of the Fe K-edge for the pristine material is 7126 eV, and the pre-edge feature is visible at 7114 eV, very similar to data reported in the literature.<sup>86</sup>

The pre-edge peak arises from the  $1s \rightarrow 3d$  dipole transition, which is forbidden for absorbers in a centrosymmetric environment. However, due to the absence of inversion symmetry in a tetrahedral environment, the mixing of 3d and 4p states leads to some p character of the empty energy levels and therefore pre-edge features occur in XAS spectra. Both the Fe and Co K-edges show a pre-edge feature, suggesting that both  $\text{Fe}^{3+}$  and  $\text{Co}^{2+}$  partially occupy the tetrahedral sites in the spinel structure. It has been shown in the literature that  $\text{CoFe}_2\text{O}_4$  nanoparticles adopt a partially inverse spinel structure that can be described as  $(\text{Co}_{1-2i}\text{Fe}_{2i})_A[\text{Co}_{2i}\text{Fe}_{2(1-i)}]_B\text{O}_4$  (A, B

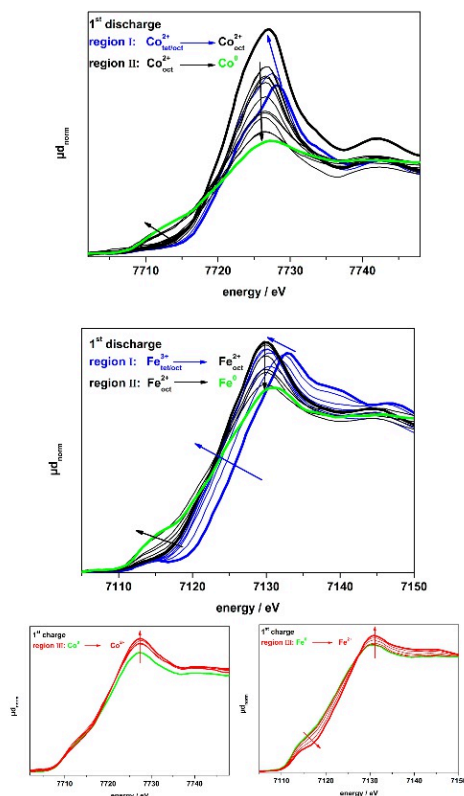


**Figure 8.** Scans at the Co K-edge (top) and the Fe K-edge (middle) during the discharge process. Scans of the charge process are presented at the bottom: Co K-edge (left) and Fe K-edge (right). Regions are marked in different colors, and arrows illustrate the shift.

= tetrahedral and octahedral sites, respectively) with  $\lambda$  between 0 and about 0.34.<sup>87,88</sup>

In region I, the potential drops fast to 1.5 V, and a plateau that is not well-resolved is reached at about 1.1 V. The Co K-edge does not exhibit a pronounced energy shift in this region (Figure 8, top), suggesting that there is no increase in the charge density (lower oxidation state) during Li uptake, whereas the Fe K-edge shows a continuous shift to lower edge energy, i.e., the electrons are transferred to Fe<sup>3+</sup> during this reaction step (Figure 8, middle).

The intense absorption above the Co K-edge (Figure 8, top) is assigned to a transition of the 1s electron to an unoccupied 4p bound state ( $t_{1g}$  symmetry). This transition is dipole-allowed for absorber atoms in tetrahedral and octahedral environments. During formation of the intermediate NaCl-type structure, the intensity of the 1s  $\rightarrow$  4p transition increases for the Co K-edge. For further discharge (more than 2 Li are inserted), the intensity of this spectral feature progressively decreases, which can be explained by the loss of p character of the 1s  $\rightarrow$  4p transition as a consequence of the formation of metallic Co nanoparticles. For the Fe–K edge, a significant shift to lower

energy of the 1s  $\rightarrow$  4p resonance above the absorption edge is observed followed by a decrease of the intensity with increasing Li content. This observation can be explained with the successive reduction of Fe<sup>3+</sup> to Fe<sup>2+</sup> followed by formation of metallic Fe particles (Figure 8, middle).

At the end of region I, about 2 Li per formula unit are inserted and the pre-edge features in the spectra disappeared, indicating that both ions are now in an environment with inversion symmetry (octahedral sites). These scans, marked as thick black lines, also show the largest intensity of the 1s  $\rightarrow$  4p transition (Figure 8, top: Co K-edge, middle: Fe K-edge). This result is in perfect agreement with the formation of the rock salt structure observed during operando XRD (Section 3.3), where Co<sup>2+</sup> and Fe<sup>2+</sup> are in a centrosymmetric octahedral oxygen environment. Fourier transformed XAS data (FT( $\chi(k)$ )) for Co is presented in Figure 9 (left). For pristine CoFe<sub>2</sub>O<sub>4</sub> (blue

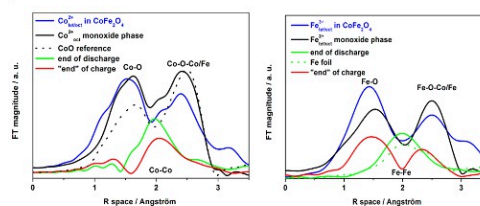


**Figure 9.** FT-EXAFS data during first discharge/charge cycle: Co (left) and Fe (right).

line), the dominating Co–O distance is located at about 1.5 Å, with a shoulder occurring at 1.4 Å, and the Co–O–Co/Fe shells are at about 2.3 and 2.4 Å (note that the values are not phase-shift-corrected). The first shell of the Fe absorber has its maximum at ca. 1.5 Å (Figure 9, right), representing the Fe–O bond length, with no visible shoulder at shorter distance as observed for Co, and the Fe–O–Co/Fe distances are located at about 2.5 Å. For both elements, the second maximum is broad due to overlapping contributions from Co/Fe on octahedral (longer distance) and tetrahedral sites (shorter distance). At the end of region I, the Fe–O and Co–O distances slightly increase (Figure 9, broad black line) due to the formation of a rock salt-like structure, as observed in the operando XRD investigations. The intensity of the second maximum increases and the peak becomes sharper for both elements because all ions are now on octahedral sites.

In region II, the rock salt structure is transformed into an amorphous product. The Fe and Co K-edges show no shift to lower energies, but a rotation around a quasi-isosbestic point is visible (Figure 8). The pre-edge area shifts to lower energies, whereas the intensity of the K-edge maximum is reduced. The Fe<sup>2+</sup> and Co<sup>2+</sup> cations are reduced simultaneously to the metallic state, and at the end of the discharge process, the XAS spectra of Co and Fe are very similar to those of elemental Co and Fe foils (Supporting Information, Figure S6). In the EXAFS region, no significant modulation is visible due to the amorphous character of the product. In the FT( $\chi(k)$ ) spectra (Figure 9), the intensity of the Co–O/Fe–O shells decreases and finally vanishes, whereas the M–M shells start to develop, exhibiting a pronounced intensity at the end of the discharge process (Figure 9, compare the black and green lines).

The charge process (region III) without a well-resolved plateau at 1.6 V is characterized by a shift of the Fe pre-edge



feature to higher energies and an increase of the intensity of the  $1s \rightarrow 4p$  transition in the XANES region (Figure 8, bottom right). For Co, the shift of the absorption edge as well as changes in the XANES region are less pronounced (Figure 8, bottom left). The alteration in the spectra can be explained by the oxidation of Fe and Co to  $\text{Fe}^{2+}$  and  $\text{Co}^{2+}$ , respectively. Because the Fe K-edge exhibits no pronounced shift to higher energies during the charge process at this stage, we exclude the formation of  $\text{Fe}^{3+}$ . In FT( $\chi(k)$ ) spectra, the intensity of the Fe–Fe and Co–Co shells drops (Figure 9 green line), and for Fe (Figure 9, red line), the signals of Fe–O and Fe–O–Fe/Co develop again. The results strongly suggest that Fe is oxidized to  $\text{Fe}^{2+}$ , whereas Co is only partially oxidized to  $\text{Co}^{2+}$ . Fe–O and Fe–O–Co/Fe shells occur at nearly the same distance as that observed after uptake of 2 Li per formula unit (compare the red and black curves in Figure 9). The evolution of the potential curve of the in situ cell and the absence of the Co–O and Co–O–Co/Fe shells in the FT( $\chi(k)$ ) data indicate that the charge process is not finished during the operando XAS investigations.

**3.5. Ex Situ XAS.** The cells used for the operando XAS studies were not equipped with a spring to guarantee that perfect contact is made with the active material and to compensate for the volume expansion that is expected for conversion materials. Hence, ex situ XAS investigations were performed at the KMC-2/BESSYII beamline to support the results presented in Section 3.4.  $\text{CoFe}_2\text{O}_4$  was prepared on copper foil as described in Section 2. After one, two, and three discharge/charge cycles, the Swagelok cells were opened in an argon glovebox and the active material was transferred into in situ cells. XAS scans of pristine  $\text{CoFe}_2\text{O}_4$  after the first discharge and after one, two, and three cycles at the Co and Fe K-edges are presented in Figure 10. After complete discharge, Co and Fe are reduced to the metallic state, as evidenced by the similarity of the spectra with those of Fe/Co metal foils (Figure 10, continuous and dashed black lines). After one, two, and three complete cycles, the Fe K-edge is located at the same energy as that for pristine  $\text{CoFe}_2\text{O}_4$  (maximum of the first derivation). Hence,  $\text{Fe}^{3+}$  is first reduced to elemental  $\text{Fe}^0$  and then oxidized to  $\text{Fe}^{3+}$  during the charge process (Figure 10, top). The energy position of the Co K-edge after one, two, and three cycles is only approximately similar to that of pristine  $\text{CoFe}_2\text{O}_4$  nanoparticles, i.e.,  $\text{Co}^{2+}$  is reduced to Co metal during discharge and is at least partially oxidized to  $\text{Co}^{2+}$  during the charge process. In contrast to the results for Fe, the spectra at the Co K-edge exhibit differences in intensity and shape after each cycle. The spectrum recorded after one cycle (Figure 10, bottom, red line) is more similar to the pristine material, whereas the spectrum obtained after three cycles (Figure 10, bottom, brown line) shows a lower intensity of the  $1s \rightarrow 4p$  transition and the shape of the spectra more closely resembles that of metallic Co. These observations suggest that at least part of the capacity loss during cycling is caused by an inability to reoxidize metallic Co, whereas Fe is reoxidized to  $\text{Fe}^{3+}$  after each charge process. A capacity loss was also observed by some groups for  $\text{CoFe}_2\text{O}_4$  during the first 10–20 cycles.<sup>32,33,44–46</sup> Whether the fading of the capacity in these cases is at least partially due to the inability to reoxidize metallic Co cannot be unequivocally answered. The decreasing ability of Co nanoparticles to be oxidized during repeated charge cannot be explained in a straightforward manner because CoO can be reasonably cycled against Li.<sup>16,89,90</sup> No straightforward explanation can be given for this observation from our study;

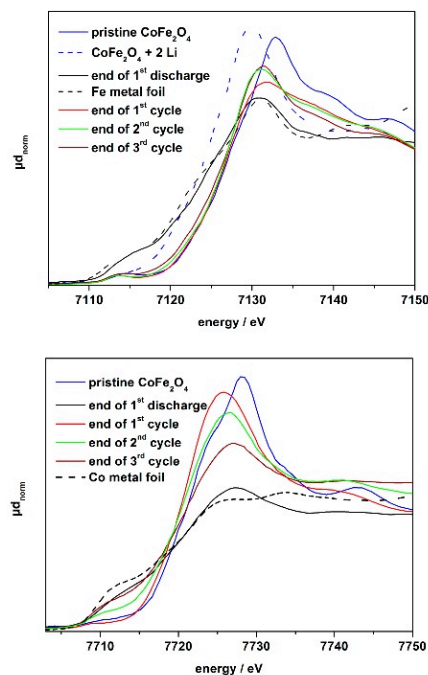


**Figure 10.** XAS scans at the Fe K-edge (top) and Co K-edge (bottom) of the pristine material after the first discharge and after one, two, and three cycles along with spectra of Fe/Co metal foils for comparison.

therefore, we can only speculate about the reason. One possibility is that the metallic Co nanoparticles have a poorer contact with the  $\text{Li}_2\text{O}$  matrix compared to that with the Fe nanoparticles, leading to hindered electron transfer. This assumption is supported by the fact that composites of  $\text{CoFe}_2\text{O}_4$ /graphene overcome the problem of capacity fading via better contact between the  $\text{Li}_2\text{O}$  matrix and metallic nanoparticles.<sup>39–42</sup>

#### 4. DISCUSSION

On the basis of available data for  $\text{MFe}_2\text{O}_4$  ( $\text{M} = \text{Mg}, \text{Mn}, \text{Fe}, \text{Co}, \text{Ni}, \text{Cu}$ ) nanoparticles, which are partially inverse spinels with general formula  $(\text{M}_{1-2j}\text{Fe}_{2j})_A[\text{M}_{2j}\text{Fe}_{2(1+j)}]_B\text{O}_4$ ,<sup>64,65,73,87,88</sup> some general conclusions concerning the reaction mechanism can be drawn. The tetrahedral 8a and the octahedral 16d sites are fully occupied by  $\text{M}^{2+}$  and  $\text{Fe}^{3+}$  cations, whereas crystallographic positions 8b, 16c, and 48f are empty. The CV curves of  $\text{MFe}_2\text{O}_4$  samples ( $\text{M} = \text{Mn}, \text{Fe}, \text{Co}, \text{Ni}, \text{Cu}$ ) are, in general, very similar, which may indicate a common mechanism for these spinels. In Table 1, the potential positions of the anodic and cathodic peaks observed during the first and second cycles of Li uptake/release for  $\text{MFe}_2\text{O}_4$  ( $\text{M} = \text{Mn}, \text{Fe}, \text{Co}, \text{Ni}, \text{Cu}$ ) spinels are summarized. In all investigations, a difference between the cathodic peaks of the first and subsequent cycles was observed. This finding indicates that all materials are transformed into new products during the first discharge/charge cycle. The fact that the cathodic peaks occur at different voltages in the second cycle compared to that in the

**Table 1. Potential Positions of Cathodic and Anodic Peaks during the First and Second Cycles of Different Spinel-Type Materials Observed in CV Curves**

spinel type	first cycle		second cycle		ref
	cathodic peaks	anodic peaks	cathodic peaks	anodic peaks	
MnFe <sub>2</sub> O <sub>4</sub>	0.6 V	1.7 V	1.5 V; 0.8 V	1.8 V	22
FeFe <sub>2</sub> O <sub>4</sub>	0.5 V	1.7 V	1.5 V; 0.9 V	1.7 V	91
CuFe <sub>2</sub> O <sub>4</sub>	0.6 V	1.7 V	1.5 V; 0.9 V	1.7 V	23
NiFe <sub>2</sub> O <sub>4</sub>	0.4 V	1.7 V	1.5 V; 0.8 V	1.7 V	92
CoFe <sub>2</sub> O <sub>4</sub>	0.6 V	1.7 V	1.6 V; 0.8 V	1.8 V	Section 3.2

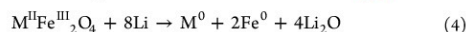
first cycle suggests that the reaction mechanism during the first cycle is different from the second one.

In region Ia of the galvanostatic discharge curve (Figure 4, top), a slight expansion of the unit cell parameter is observed in XRD patterns (Figure 5). XRD powder patterns of CoFe<sub>2</sub>O<sub>4</sub> recorded after 20 cycles in a potential range of 1.6 to 3 V (uptake of ca. 0.5 Li per formula unit, region Ia) are presented in Supporting Information Figure S7. Most of the material still consists of the CoFe<sub>2</sub>O<sub>4</sub> spinel. However, an asymmetry of the reflections at 43.5 and 62° 2θ suggests that a small amount of the spinel is already transformed to the monoxide phase. This finding can be regarded as a hint that no reversible intercalation occurs at the early stages of Li insertion but, rather, that there is a transformation to the monoxide accompanied by Li insertion into an amorphous layer covering the spinel nanoparticles. The reflections of the very small domains of the monoxide cannot be detected in X-ray powder patterns and are seen only as asymmetry on the low 2θ side of the reflections of the spinel. Hence, the expansion of the lattice parameter of the spinel phase is more likely to be due to tensile strain exerted by the monoxide domains than by intercalation. This scenario is supported by structural considerations. Independent of the empty sites in the spinel structure, the introduction of Li on one of these sites leads to very short Li–M/Fe distances, which are strongly repulsive. The size of coherently scattering domains of the spinel exhibits no changes within experimental accuracy during Li uptake up to ca. 0.5 Li/CoFe<sub>2</sub>O<sub>4</sub>. Moreover, the normalized intensity of the (311) reflection remains constant during the Li uptake process, suggesting that the first 0.5 Li/CoFe<sub>2</sub>O<sub>4</sub> are at least partially consumed by an amorphous oxidic layer and grain boundaries on the surface of the nanoparticles. This amorphous layer is visible in the HRTEM image shown in Supporting Information Figure S2. Whether Li<sub>2</sub>O is formed during this reaction cannot be decided on the basis of analytic data presented here. The reactions occurring during Li uptake of 0.5 Li/CoFe<sub>2</sub>O<sub>4</sub> can be summarized as follows: Li is partially consumed by amorphous material on the surface of the nanoparticles, which is consistent with the investigations on MnFe<sub>2</sub>O<sub>4</sub> and MgFe<sub>2</sub>O<sub>4</sub>, where <sup>7</sup>Li MAS NMR showed a strong shift of the Li signal, indicating formation of Li–Fe–O connections.<sup>64,65</sup> Repeated cycling at higher potentials is not reversible, and small amounts of the monoxide phase are formed.

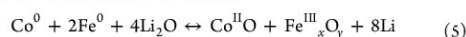
In the next reaction step (region Ib), where the potential is further reduced to 0.8 V (Figure 4 top), formation of a disordered oxide exhibiting a NaCl-type structure takes places,

as evidenced by operando XRD and XAS (Figures 5 and 8). At this stage of the reaction, the 2 Li atoms inserted per formula unit reduced Fe<sup>3+</sup> to Fe<sup>2+</sup>. Simultaneously, all cations located on the tetrahedral site moved to neighboring octahedral sites. The driving force for this movement is most likely a strong repulsive interaction between Li entering the spinel structure and Co/Fe ions residing on the tetrahedral site. The formation of the NaCl-type structure is accompanied by an increase of the Fe/Co–O bond length (Section 3.3). During conversion of CoFe<sub>2</sub>O<sub>4</sub>, three formula units of monoxide(s) are generated together with Li<sub>2</sub>O. The occurrence of the latter was recently proved for MnFe<sub>2</sub>O<sub>4</sub> and MgFe<sub>2</sub>O<sub>4</sub>.<sup>64,65</sup> Similar intermediate rock salt phases were also reported for ZnFe<sub>2</sub>O<sub>4</sub> and Mn<sub>3</sub>O<sub>4</sub>.<sup>63,58</sup> The mechanism during uptake of small amounts of Li is also affected by the size of the particles. This was demonstrated for Co<sub>3</sub>O<sub>4</sub>, where two different mechanisms were proposed depending on the particle size. For larger particles, the formation of Li<sub>x</sub>Co<sub>3</sub>O<sub>4</sub> is favored, whereas for nanosized crystallites, CoO is formed.<sup>33</sup>

Further increasing Li to 8 per formula unit leads to a successive reduction of Co<sup>2+</sup>/Fe<sup>2+</sup> to metallic nanoparticles embedded in an amorphous Li<sub>2</sub>O matrix (see, also, refs 32, 40, 41, 45, and 46). Hence, a reaction mechanism for Li uptake may be formulated for MFe<sub>2</sub>O<sub>4</sub> (M = Mn, Fe, Co, Ni, Cu) materials, in agreement with<sup>31,32,40,41,44–46,64,91</sup> eq 4



During the charge process, the formation of the spinel phase can be excluded (Section 3.3). Both Fe and Co nanoparticles may be oxidized to divalent or trivalent oxides. Fourier transformed XAS data derived from operando XAS experiments show a decrease of the intensity of the metal–metal shell (Figure 9) and the evolution of M/Fe–O shells (Figure 9). During Li extraction, Fe<sup>0</sup> is first oxidized to Fe<sup>2+</sup> followed by partial oxidation of Co<sup>0</sup> to Co<sup>2+</sup>. Ex situ XAS demonstrated that Fe<sup>3+</sup> is formed at the end of the charge process (Figure 10). In summary, the first charge process and the following cycles can be formulated according to eq 5



Due to the amorphous character of the charge products, one can only speculate about the local structure of the oxides. However, the occurrence of Fe/Co–O shells in the FT(χ(k)) data (see Section 3.4) exhibiting interatomic distances very similar to those of the monoxide points to the formation of NaCl-like phases. The small pre-edge peak at the Fe K-edge spectra after the first, second, and third cycles is a hint that there is a local environment around Fe ions with higher and lower symmetry (Figure 10). The capacity loss observed during cycling of the material is at least partially caused by the fact that it is impossible to reoxidize Co, i.e., metallic Co nanoparticles remain in the Li<sub>2</sub>O matrix. Similar charge/discharge mechanisms after the first discharge were postulated for MFe<sub>2</sub>O<sub>4</sub> (M = Mn, Ni, Cu).<sup>31,64,91</sup>

## 5. CONCLUSIONS

The Li uptake and release of nanosized CoFe<sub>2</sub>O<sub>4</sub> as an anode material have been studied by applying operando synchrotron XRD and XAS, providing insight into the individual reaction mechanisms occurring during the conversion reaction. XRD results demonstrate an electrochemically induced structural transformation of the initial spinel structure into a disordered



NaCl-type structure in the region from 2.75 to 1 V. The movement of the cations residing on the tetrahedral site to empty octahedral sites to generate the NaCl-type structure is evidenced by XRD patterns and XAS spectra. The uptake of the first 2 Li fully reduces  $\text{Fe}^{3+}$  to  $\text{Fe}^{2+}$ . Further increasing the amount of Li/ $\text{CoFe}_2\text{O}_4$  leads to successive reduction of the cations to the metallic state during the lower voltage region, as evidenced by the XAS data. The nanosized metallic Co/Fe particles occur in the  $\text{FT}(\chi(k))$  data at the end of the large plateau at 0.6 V.

The first few discharge/charge cycles seem to be at least partially reversible, whereas the metallic Co particles become inactive with increasing cycle number. All reaction steps are accompanied by diffusion of the involved ions: at the early stages, Li enters the spinel followed by diffusion of  $\text{Li}^+$  and  $\text{O}^{2-}$  to form  $\text{Li}_2\text{O}$  and the monoxide; toward the end of the Li uptake,  $\text{Co}^{2+}/\text{Fe}^{2+}$  or  $\text{O}^{2-}$  must diffuse out of the monoxide until Co/Fe clusters/nanoparticles can nucleate. It seems to be of interest to use  $\text{CoFe}_2\text{O}_4$  as an anode material at elevated temperatures because diffusion is accelerated at higher temperature. However, such application requires suitable stable electrolytes. Finally, the combination of different analytic techniques (XAS and XRD during galvanostatic cycling) allows for the direct detection of the individual structural and electronic alterations related to the electrochemical Li uptake/release.

#### ■ ASSOCIATED CONTENT

##### Supporting Information

The Supporting Information is available free of charge on the ACS Publications website at DOI: 10.1021/acs.chemmater.5b01754.

Rietveld refinement and EDX results of pristine  $\text{CoFe}_2\text{O}_4$ ; potential profile during cycling in a potential range from 3 V to 10 mV and from 1.6 to 3.0 V; a HRTEM image of the nanoparticles, including amorphous surface of the particles; and XRD powder pattern after cycling in a potential range from 1.6 to 3.0 V (PDF)

#### ■ AUTHOR INFORMATION

##### Corresponding Author

\*E-mail: [wbsensch@ac.uni-kiel.de](mailto:wbsensch@ac.uni-kiel.de).

##### Notes

The authors declare no competing financial interest.

#### ■ ACKNOWLEDGMENTS

We are grateful to the Deutsche Forschungsgemeinschaft (DFG) and to the German Federal Ministry of Education and Research for financial support. Synchrotron radiation beamtime allocation by ANKA (Karlsruhe) and HZB (BESSY, Berlin) is acknowledged with thanks.

#### ■ REFERENCES

- Armand, M.; Tarascon, J.-M. Building better batteries. *Nature* **2008**, *451*, 652–657.
- Choi, N.-S.; Chen, Z.; Freunberger, S. A.; Ji, X.; Sun, Y.-K.; Amine, K.; Yushin, G.; Nazar, L. F.; Cho, J.; Bruce, P. G. Challenges Facing Lithium Batteries and Electrical Double-Layer Capacitors. *Angew. Chem., Int. Ed.* **2012**, *51*, 9994–10024.
- Scrosati, B. Challenge of portable power. *Nature* **1995**, *373*, 557–558.
- Tarascon, J.-M.; Armand, M. Issues and challenges facing rechargeable lithium batteries. *Nature* **2001**, *414*, 359–367.
- Goodenough, J. B. Rechargeable batteries: challenges old and new. *J. Solid State Electrochem.* **2012**, *16*, 2019–2029.
- Etacheri, V.; Marom, R.; Elazari, R.; Salitra, G.; Aurbach, D. Challenges in the development of advanced Li-ion batteries: a review. *Energy Environ. Sci.* **2011**, *4*, 3243–3262.
- Whittingham, M. S. Lithium Batteries and Cathode Materials. *Chem. Rev.* **2004**, *104*, 4271–4301.
- Whittingham, M. S. Ultimate Limits to Intercalation Reactions for Lithium Batteries. *Chem. Rev.* **2014**, *114*, 11414–11443.
- Takamatsu, D.; Koyama, Y.; Orikasa, Y.; Mori, S.; Nakatsutsumi, T.; Hirano, T.; Tanida, H.; Arai, H.; Uchimoto, Y.; Ogumi, Z. First In situ Observation of the  $\text{LiCoO}_2$  Electrode/Electrolyte Interface by Total-Reflection X-ray Absorption Spectroscopy. *Angew. Chem.* **2012**, *124*, 11765–11769.
- Aurbach, D.; Ein-Eli, Y. The Study of Li-Graphite Intercalation Process in Several Electrolyte Systems Using In situ X-Ray Diffraction. *J. Electrochem. Soc.* **1995**, *142*, 1746–1752.
- Kaus, M.; Issac, I.; Heinzmann, R.; Doyle, S.; Mangold, S.; Hahn, H.; Chakravadhanula, V. S. K.; Kubel, C.; Ehrenberg, H.; Indris, S. Electrochemical Delithiation/Relithiation of  $\text{LiCoPO}_4$ : A Two-Step Reaction Mechanism Investigated by in Situ X-ray Diffraction, in Situ X-ray Absorption Spectroscopy, and ex Situ  $^7\text{Li}/^{31}\text{P}$  NMR Spectroscopy. *J. Phys. Chem. C* **2014**, *118*, 17279–17290.
- Bramnik, N. N.; Bramnik, K. G.; Baecht, C.; Ehrenberg, H. Study of the effect of different synthesis routes on Li extraction-insertion from  $\text{LiCoPO}_4$ . *J. Power Sources* **2005**, *145*, 74–81.
- Murphy, D. W.; Christian, P. A. Solid State Electrodes for High Energy Batteries. *Science* **1979**, *205*, 651–656.
- Nazar, L. F.; Goward, G.; Leroux, F.; Duncan, M.; Huang, H.; Kerr, T.; Gaubicher, J. Nanostructured materials for energy storage. *Int. J. Inorg. Mater.* **2001**, *3*, 191–200.
- Bruce, P.; Scrosati, B.; Tarascon, J.-M. Nanomaterials for rechargeable lithium batteries. *Angew. Chem.* **2008**, *120*, 2972–2989.
- Poizot, P.; Laruelle, S.; Grugeon, S.; Dupont, L.; Tarascon, J.-M. Nano-sized transition-metal oxides as negative-electrode materials for lithium-ion batteries. *Nature* **2000**, *407*, 496–499.
- Reddy, M. V.; Subba Rao, G. V.; Chowdari, B. V. R. Metal Oxides and Oxysalts as Anode Materials for Li Ion Batteries. *Chem. Rev.* **2013**, *113*, 5364–5457.
- Rui, X.; Tan, H.; Yan, Q. Nanostructured metal sulfides for energy storage. *Nanoscale* **2014**, *6*, 9889–9924.
- Cabana, J.; Monconduit, L.; Larcher, D.; Palacin, M. R. Beyond Intercalation-Based Li-Ion Batteries: State of the Art and Challenges of Electrode Materials Reacting Through Conversion Reactions. *Adv. Mater.* **2010**, *22*, E170–E192.
- Bruce, P. G.; Freunberger, S. A.; Hardwick, L. J.; Tarascon, J.-M. Li-O<sub>2</sub> and Li-S batteries with high energy storage. *Nat. Mater.* **2011**, *11*, 19–29.
- Wang, F.; Robert, R.; Chernova, N. A.; Pereira, N.; Omenya, F.; Badway, F.; Hua, X.; Ruotolo, M.; Zhang, R.; Wu, L.; Volkov, V.; Su, D.; Key, B.; Whittingham, M. S.; Grey, C. P.; Amatucci, G. G.; Zhu, Y.; Graetz, J. Conversion Reaction Mechanisms in Lithium Ion Batteries: Study of Binary Metal Fluoride Electrodes. *J. Am. Chem. Soc.* **2011**, *133*, 18828–18836.
- Badway, F.; Cosandey, F.; Pereira, N.; Amatucci, G. G. Carbon Metal Fluoride Nanocomposites: High-Capacity Reversible Metal Fluoride Conversion Materials as Rechargeable Positive Electrodes for Li Batteries. *J. Electrochem. Soc.* **2003**, *150*, 1318–1327.
- Bervas, M.; Badway, F.; Klein, L. C.; Amatucci, G. G. Bismuth Fluoride Nanocomposite as a Positive Electrode Material for Rechargeable Lithium Batteries. *Electrochem. Solid-State Lett.* **2005**, *8*, 179–183.
- Pralong, V.; Souza, D. C. S.; Leung, K. T.; Nazar, L. F. Reversible lithium uptake by  $\text{CoP}_3$  at low potential: role of the anion. *Electrochem. Commun.* **2002**, *4*, 516–520.
- Boyanov, S.; Bernardi, J.; Gillot, F.; Dupont, L.; Womes, M.; Tarascon, J. M.; Monconduit, L.; Doublet, M. L. FeP: Another Attractive Anode for the Li-Ion Battery Enlisting a Reversible Two-

- Step Insertion/Conversion Process. *Chem. Mater.* **2006**, *18*, 3531–3538.
- (26) Nishijima, M.; Tadokoro, N.; Takeda, Y.; Imanishi, N.; Yamamoto, O. Li Deintercalation-Intercalation Reaction and Structural Change in Lithium Transition Metal Nitride  $\text{Li}_7\text{MnN}_4$ . *J. Electrochem. Soc.* **1994**, *141*, 2966–2971.
- (27) Rowsell, J. L. C.; Pralong, V.; Nazar, L. F. Layered Lithium Ion Nitride: A Promising Anode Material for Li-Ion Batteries. *J. Am. Chem. Soc.* **2001**, *123*, 8598–8599.
- (28) Sun, Q.; Fu, Z.-W. Vanadium nitride as a novel thin film anode material for rechargeable lithium batteries. *Electrochim. Acta* **2008**, *54*, 403–409.
- (29) Courtel, F. M.; Duncan, H.; Abu-Lebdeh, Y.; Davidson, I. J. High capacity anode materials for Li-ion batteries based on spinel metal oxides  $\text{AMn}_2\text{O}_4$  (A = Co, Ni and Zn). *J. Mater. Chem.* **2011**, *21*, 10206–10218.
- (30) Xiao, Y.; Zai, J.; Tao, L.; Li, B.; Han, Q.; Yu, C.; Qian, X.  $\text{MnFe}_2\text{O}_4$ -graphene nanocomposites with enhanced performances as anode materials for Li-ion batteries. *Phys. Chem. Chem. Phys.* **2013**, *15*, 3939–3945.
- (31) Xing, Z.; Ju, Z.; Yang, J.; Xu, H.; Qian, Y. One-step solid state reaction to selectively fabricate cubic and tetragonal  $\text{CuFe}_2\text{O}_4$  anode material for high power lithium ion batteries. *Electrochim. Acta* **2013**, *102*, 51–57.
- (32) Lavela, P.; Tirado, J. L.  $\text{CoFe}_2\text{O}_4$  and  $\text{NiFe}_2\text{O}_4$  synthesized by sol-gel procedures for their use as anode materials for Li ion batteries. *J. Power Sources* **2007**, *172*, 379–387.
- (33) Lavela, P.; Tirado, J. L.; Womes, M.; Jumas, J. C. Elucidation of Capacity Fading on  $\text{CoFe}_2\text{O}_4$  Conversion Electrodes for Lithium Batteries Based on  $^{57}\text{Fe}$  Mössbauer Spectroscopy. *J. Electrochem. Soc.* **2009**, *156*, A589–A594.
- (34) NuLi, Y.-N.; Qin, Q.-Z. Nanocrystalline transition metal ferrite thin films prepared by an electrochemical route for Li-ion batteries. *J. Power Sources* **2005**, *142*, 292–297.
- (35) Yao, X.; Kong, J.; Tang, X.; Zhou, D.; Zhao, C.; Zhou, R.; Lu, X. Facile synthesis of porous  $\text{CoFe}_2\text{O}_4$  nanosheets for lithium-ion batteries anodes with enhanced rate capability and cycling stability. *RSC Adv.* **2014**, *4*, 27488–27492.
- (36) Yoon, S. Facile microwave synthesis of  $\text{CoFe}_2\text{O}_4$  spheres and their application as an anode for lithium ion batteries. *J. Appl. Electrochem.* **2014**, *44*, 1069–1074.
- (37) Wang, Y.; Su, D.; Ung, A.; Ahn, J.-H.; Wang, G. Hollow  $\text{CoFe}_2\text{O}_4$  nanospheres as a high capacity anode material for lithium ion batteries. *Nanotechnology* **2012**, *23*, 55402.
- (38) Wang, N.; Xu, H.; Chen, L.; Gu, X.; Yang, J.; Qian, Y. A general approach for  $\text{MFe}_2\text{O}_4$  (M = Zn, Co, Ni) nanorods and their high performance as anode materials for lithium ion batteries. *J. Power Sources* **2014**, *247*, 163–169.
- (39) Zhang, Z.; Wang, Y.; Zhang, M.; Tan, Q.; Lv, X.; Zhong, Z.; Su, F. Mesoporous  $\text{CoFe}_2\text{O}_4$  nanospheres cross-linked by carbon nanotubes as high-performance anodes for lithium-ion batteries. *J. Mater. Chem. A* **2013**, *1*, 7444–7450.
- (40) Li, S.; Wang, B.; Liu, J.; Yu, M. In situ one-step synthesis of  $\text{CoFe}_2\text{O}_4$ /graphene nanocomposites as high-performance anode for lithium-ion batteries. *Electrochim. Acta* **2014**, *129*, 33–39.
- (41) Xiao, Y.; Li, X.; Zai, J.; Wang, K.; Gong, Y.; Li, B.; Han, Q.; Qian, X.  $\text{CoFe}_2\text{O}_4$ -Graphene Nanocomposites Synthesized through An Ultrasonic Method with Enhanced Performance as Anode Materials for Li-Ion Batteries. *Nano-Micro Lett.* **2014**, *6*, 307.
- (42) Xia, H.; Zhu, D.; Fu, Y.; Wang, X.  $\text{CoFe}_2\text{O}_4$ -graphene nanocomposite as a high-capacity anode material for lithium-ion batteries. *Electrochim. Acta* **2012**, *83*, 166–174.
- (43) Jin, Y.-H.; Seo, S.-D.; Shim, H.-W.; Park, K.-S.; Kim, D.-W. Synthesis of core/shell spinel ferrite/carbon nanoparticles with enhanced cycling stability for lithium ion battery anodes. *Nanotechnology* **2012**, *23*, 125402–125408.
- (44) Li, Z. H.; Zhao, T. P.; Zhan, X. Y.; Gao, D. S.; Xiao, Q. Z.; Lei, G. T. High capacity three-dimensional ordered macroporous  $\text{CoFe}_2\text{O}_4$  as anode material for lithium ion batteries. *Electrochim. Acta* **2010**, *55*, 4594–4598.
- (45) Vidal-Abarca, C.; Lavela, P.; Tirado, J. L. On the role of faradaic and capacitive contributions in the electrochemical performance of  $\text{CoFe}_2\text{O}_4$  as conversion anode for Li-ion cells. *Solid State Ionics* **2010**, *181*, 616–622.
- (46) Chu, Y.-Q.; Fu, Z.-W.; Qin, Q.-Z. Cobalt ferrite thin film as anode material for lithium ion batteries. *Electrochim. Acta* **2004**, *49*, 4915–4921.
- (47) Reimers, J. N.; Dahn, J. R. Electrochemical and In Situ X-ray Diffraction Studies of Lithium Intercalation in  $\text{Li}_x\text{CoO}_2$ . *J. Electrochem. Soc.* **1992**, *139*, 2091–2097.
- (48) Morcrette, M.; Chabre, Y.; Vaughan, G.; Amatucci, G.; Leriche, J.-B.; Patoux, S.; Masquelier, C.; Tarascon, J.-M. In situ X-ray diffraction techniques as a powerful tool to study battery electrode materials. *Electrochim. Acta* **2002**, *47*, 3137–3149.
- (49) Bensch, W.; Ophey, J.; Hain, H.; Gesswein, H.; Chen, D.; Mönig, R.; Gruber, P. A.; Indris, S. Chemical and electrochemical insertion of Li into the spinel structure of  $\text{CuCr}_2\text{Se}_4$ , ex situ and in situ observations by X-ray diffraction and scanning electron microscopy. *Phys. Chem. Chem. Phys.* **2012**, *14*, 7509–7516.
- (50) Bensch, W.; Bredow, T.; Ebert, H.; Heitjans, P.; Indris, S.; Mankovsky, S.; Wilkening, M. Li intercalation and anion/cation substitution of transition metal chalcogenides: Effects on crystal structure, microstructure, magnetic properties and  $\text{Li}^+$  ion mobility. *Prog. Solid State Chem.* **2009**, *37*, 206–225.
- (51) Wontcheu, J.; Behrens, M.; Bensch, W.; Indris, S.; Wilkening, M.; Heitjans, P. A study of Li intercalation into  $\text{Cr}_3\text{Ti}_2\text{Se}_8$  using electrochemistry, in-situ energy dispersive X-ray diffractometry and NMR spectroscopy. *Solid State Ionics* **2007**, *178*, 759–768.
- (52) Behrens, M.; Riemenschneider, O.; Bensch, W.; Indris, S.; Wilkening, M.; Heitjans, P. Lithium Intercalation into Monodimic  $\text{Cr}_x\text{Ti}_y\text{Se}_z$ : Synthesis, Structural Phase Transition, and Properties of  $\text{Li}_x\text{Cr}_y\text{Ti}_z\text{Se}_8$  ( $x = 0.1–2.8$ ). *Chem. Mater.* **2006**, *18*, 1569–1576.
- (53) Behrens, M.; Kiebach, R.; Ophey, J.; Riemenschneider, O.; Bensch, W. The Reaction Mechanism of a Complex Intercalation System: In Situ X-ray Diffraction Studies of the Chemical and Electrochemical Lithium Intercalation in  $\text{Cr}_4\text{TiSe}_8$ . *Chem. - Eur. J.* **2006**, *12*, 6348–6355.
- (54) Behrens, M.; Wontcheu, J.; Kiebach, R.; Bensch, W. Tuning the Magnetic Properties of  $\text{Li}_x\text{CrTi}_{0.25}\text{Se}_2$  ( $0.03 \leq x \leq 0.7$ ) by Directed Deintercalation of Lithium. *Chem. - Eur. J.* **2008**, *14*, 5021–5029.
- (55) Terada, Y.; Yasaka, K.; Nishikawa, F.; Konishi, T.; Yoshio, M.; Nakai, I. In Situ XAFS Analysis of  $\text{Li}(\text{Mn}, \text{M})_2\text{O}_4$  (M = Cr, Co, Ni) 5 V Cathode Materials for Lithium-Ion Secondary Batteries. *J. Solid State Chem.* **2001**, *156*, 286–291.
- (56) Leriche, J. B.; Hamelet, S.; Shu, J.; Morcrette, M.; Masquelier, C.; Ouvrard, G.; Zerrouki, M.; Soudan, P.; Belin, S.; Elkaïm, E.; Baudelet, F. An Electrochemical Cell for Operando Study of Lithium Batteries Using Synchrotron Radiation. *J. Electrochem. Soc.* **2010**, *157*, 606–610.
- (57) Nelson, J.; Misra, S.; Yang, Y.; Jackson, A.; Liu, Y.; Wang, H.; Dai, H.; Andrews, J. C.; Cui, Y.; Toney, M. F. In Operando X-ray Diffraction and Transmission X-ray Microscopy of Lithium Sulfur Batteries. *J. Am. Chem. Soc.* **2012**, *134*, 6337–6343.
- (58) Lowe, M. A.; Gao, J.; Abruna, H. D. In operando X-ray studies of the conversion reaction in  $\text{Mn}_3\text{O}_4$  lithium battery anodes. *J. Mater. Chem. A* **2013**, *1*, 2094–2103.
- (59) Liu, X.; Wang, D.; Liu, G.; Srinivasan, V.; Liu, Z.; Hussain, Z.; Yang, W. Distinct charge dynamics in battery electrodes revealed by in situ and operando soft X-ray spectroscopy. *Nat. Commun.* **2013**, *4*, 2568–2576.
- (60) Marino, C.; Fraisse, B.; Womes, M.; Villeveille, C.; Monconduit, L.; Stievano, L. At the Heart of Conversion Reaction: An Operando X-ray Absorption Spectroscopy Investigation of  $\text{NiSb}_2$ , a Negative Electrode Material for Li-ion Batteries. *J. Phys. Chem. C* **2014**, *118*, 27772–27780.
- (61) Boesenberg, U.; Marcus, M. A.; Shukla, A. K.; Yi, T.; McDermott, E.; Teh, P. F.; Srinivasan, M.; Moewes, A.; Cabana, J.



- Asymmetric pathways in the electrochemical conversion reaction of NiO as battery electrode with high storage capacity. *Sci. Rep.* **2014**, *4*, 7133–7242.
- (62) Chen, C.-H.; Pan, C.-J.; Su, W.-N.; Rick, J.; Wang, C.-J.; Venkateswarlu, M.; Lee, J.-F.; Hwang, B.-J. Operando X-ray diffraction and X-ray absorption studies of the structural transformation upon cycling excess Li layered oxide  $\text{Li}[\text{Li}_{1/18}\text{Co}_{1/6}\text{Ni}_{1/3}\text{Mn}_{4/9}]\text{O}_2$  in Li ion batteries. *J. Mater. Chem. A* **2015**, *3*, 8613–8626.
- (63) Bresser, D.; Paillard, E.; Kloepsch, R.; Krueger, S.; Fiedler, M.; Schmitz, R.; Baither, D.; Winter, M.; Passerini, S. Carbon Coated  $\text{ZnFe}_2\text{O}_4$  Nanoparticles for Advanced Lithium-Ion Anodes. *Adv. Energy Mater.* **2013**, *3*, 513–523.
- (64) Permien, S.; Hain, H.; Scheuermann, M.; Mangold, S.; Mereacre, V.; Powell, A. K.; Indris, S.; Schürmann, U.; Kienle, L.; Duppel, V.; Harm, S.; Bensch, W. Electrochemical Insertion of Li into nanocrystalline  $\text{MnFe}_2\text{O}_4$ : a study of the reaction mechanism. *RSC Adv.* **2013**, *3*, 23001–23014.
- (65) Permien, S.; Indris, S.; Scheuermann, M.; Schürmann, U.; Mereacre, V.; Powell, A. K.; Kienle, L.; Bensch, W. Is there a universal reaction mechanism of Li insertion into oxide spinels: a case study using  $\text{MgFe}_2\text{O}_4$ . *J. Mater. Chem. A* **2015**, *3*, 1549–1561.
- (66) Balasubramanian, M.; Sun, X.; Yang, X. Q.; McBreen, J. In situ X-ray diffraction and X-ray absorption studies of high-rate lithium-ion batteries. *J. Power Sources* **2001**, *92*, 1–8.
- (67) *Area Diffraction Machine*, version 2 Beta248, 2007.
- (68) *Athena*, version 0.8.056, 2012.
- (69) Coelho, A. A. *TOPAS-Academic*, version 4.0; Coelho Software: Brisbane.
- (70) Stadelmann, P. A. EMS – a software package for electron diffraction analysis and HREM image simulation in materials science. *Ultramicroscopy* **1987**, *21*, 131–145.
- (71) Patil, V. G.; Shirsath, S. E.; More, S. D.; Shukla, S. J.; Jadhav, K. M. Effect of zinc substitution on structural and elastic properties of cobalt ferrite. *J. Alloys Compd.* **2009**, *488*, 199–203.
- (72) Gachot, G.; Grugeon, S.; Armand, M.; Pilard, S.; Guenot, P.; Tarascon, J.-M.; Laruelle, S. Deciphering the multi-step degradation mechanisms of carbonate-based electrolyte in Li batteries. *J. Power Sources* **2008**, *178*, 409–421.
- (73) Bekeert, E.; Balaya, P.; Murugavel, S.; Maier, J.; Menetrier, M.; Li, M. A. S. NMR Investigation on Electrochemical Lithiation of  $\text{RuO}_2$ : Evidence for an Interfacial Storage Mechanism. *Chem. Mater.* **2009**, *21*, 856–861.
- (74) Maier, J. Nanoionics: ion transport and electrochemical storage in confined systems. *Nat. Mater.* **2005**, *4*, 805–815.
- (75) Ponrouch, A.; Taberna, P.-L.; Simon, P.; Palacin, M. R. On the origin of the extra capacity at low potential in materials for Li batteries reacting through conversion reactions. *Electrochim. Acta* **2012**, *61*, 13–18.
- (76) Laruelle, S.; Grugeon, S.; Poizat, P.; Dolle, M.; Dupont, L.; Tarascon, J. M. On the Origin of the Extra Electrochemical Capacity Displayed by MO/Li Cells at Low Potential. *J. Electrochem. Soc.* **2002**, *149*, A627–A634.
- (77) Dedryvere, R.; Laruelle, S.; Grugeon, S.; Poizat, P.; Gonbeau, D.; Tarascon, J. M. Contribution of X-ray Photoelectron Spectroscopy to the Study of the Electrochemical Reactivity of CoO toward Lithium. *Chem. Mater.* **2004**, *16*, 1056–1061.
- (78) Gireaud, L.; Grugeon, S.; Pilard, S.; Guenot, P.; Tarascon, J. M.; Laruelle, S. Mass Spectrometry Investigations on Electrolyte Degradation Products for the Development of Nanocomposite Electrodes in Lithium Ion Batteries. *Anal. Chem.* **2006**, *78*, 3688–3698.
- (79) Ko, Y. N.; Park, S. B.; Lee, J.-H.; Kang, Y. C. Comparison of the electrochemical properties of yolk-shell and dense structured  $\text{CoFe}_2\text{O}_4$  powders prepared by a spray pyrolysis process. *RSC Adv.* **2014**, *4*, 40188–40192.
- (80) Ding, Z.; Yao, B.; Feng, J.; Zhang, J. A facile nitrogen-doped carbon encapsulation of  $\text{CoFe}_2\text{O}_4$  nanocrystalline for enhanced performance of lithium ion battery anodes. *J. Solid State Electrochem.* **2014**, *18*, 19–27.
- (81) Chen, C. J.; Greenblatt, M.; Waszczak, J. V. Lithium Insertion into Spinel Ferrites. *Solid State Ionics* **1986**, *18-19*, 838–846.
- (82) Schmidt, P. How to Get Ternary Solid Solutions  $\text{Fe}_{1-x}\text{M}_x\text{O}$  (M = Co, Ni)? A Thermodynamic Concept. *Eur. J. Inorg. Chem.* **2008**, *2008*, 2847–2855.
- (83) Fjellvag, H.; Gronvold, F.; Stolen, S.; Hauback, B. On the Crystallographic and Magnetic Structures of Nearly Stoichiometric Iron Monoxide. *J. Solid State Chem.* **1996**, *124*, 52–57.
- (84) Liu, J. F.; Yin, S.; Wu, H. P.; Zeng, Y. W.; Hu, X. R.; Wang, Y. W.; Lv, G. L.; Jiang, J. Z. Wurtzite-to-Rocksalt Structural Transformation in Nanocrystalline CoO. *J. Phys. Chem. B* **2006**, *110*, 21588–21592.
- (85) Artus, M.; Tahar, L. B.; Herbst, F.; Smiri, L.; Villain, F.; Yaacoub, N.; Greneche, J.-M.; Ammar, S.; Fievet, F. Size-dependent magnetic properties of  $\text{CoFe}_2\text{O}_4$  nanoparticles prepared in polyol. *J. Phys.: Condens. Matter* **2011**, *23*, S06001.
- (86) Aquilanti, G.; Cognigni, A.; Anis-ur-Rehman, M. Cation Distribution in Zn Doped Cobalt Nanoferrites Determined by X-ray Absorption Spectroscopy. *J. Supercond. Novel Magn.* **2011**, *24*, 659–663.
- (87) Peddis, D.; Mansilla, M. V.; Morup, S.; Cannas, C.; Musinu, A.; Piccaluga, G.; D'Orazio, F.; Lucari, F.; Fiorani, D. Spin-Canting and Magnetic Anisotropy in Ultrasmall  $\text{CoFe}_2\text{O}_4$  Nanoparticles. *J. Phys. Chem. B* **2008**, *112*, 8507–8513.
- (88) Liu, C.; Zou, B.; Rondinone, A. J.; Zhang, Z. J. Chemical Control of Superparamagnetic Properties of Magnesium and Cobalt Spinel Ferrite Nanoparticles through Atomic Level Magnetic Couplings. *J. Am. Chem. Soc.* **2000**, *122*, 6263–6267.
- (89) Peng, C.; Chen, B.; Qin, Y.; Yang, S.; Li, C.; Zuo, Y.; Liu, S.; Yang, J. Facile Ultrasonic Synthesis of CoO Quantum Dot/Graphene Nanosheet Composites with High Lithium Storage Capacity. *ACS Nano* **2012**, *6*, 1074–1081.
- (90) Sun, Y.; Hu, X.; Luo, W.; Huang, Y. Self-assembled mesoporous CoO nanodisks as a long-life anode material for lithium-ion batteries. *J. Mater. Chem.* **2012**, *22*, 13826–13831.
- (91) Jin, S.; Deng, H.; Long, D.; Liu, X.; Zhan, L.; Liang, X.; Qiao, W.; Ling, L. Facile synthesis of hierarchically structured  $\text{Fe}_3\text{O}_4$ /carbon micro-flowers and their application to lithium ion battery anodes. *J. Power Sources* **2011**, *196*, 3887–3893.
- (92) Zhao, H.; Zheng, Z.; Wong, K. W.; Wang, S.; Huang, B.; Li, D. Fabrication and electrochemical performance of nickel ferrite nanoparticles as anode material in lithium ion batteries. *Electrochem. Commun.* **2007**, *9*, 2606–2610.
- (93) Larcher, D.; Sudant, G.; Leriche, J.-B.; Chabre, Y.; Tarascon, J.-M. The Electrochemical Reduction of  $\text{Co}_3\text{O}_4$  in a Lithium Cell. *J. Electrochem. Soc.* **2002**, *149*, A234–A241.



### 3.4 Elucidation of the Conversion Reaction of CoMnFeO<sub>4</sub> Nanoparticles in Lithium Ion Battery Anode via Operando Studies

CoMnFeO<sub>4</sub> nanoparticles were synthesized by a new and simple synthesis route. The as-prepared material was characterized with XRD, EDX, SEM and TEM. Electrochemical Li uptake and release as well as *operando* XAS/XRD investigations are reported for the first time for such a tri-metallic oxide. The material exhibits promising capacity stability over many cycles accompanied by a high capacity at different currents. For the first time the whole powder pattern modelling (WPPM) approach was used to analyse *operando* XRD data giving unique insights into alterations of the lognormal domain size distribution during Li uptake and of the particle morphologies during the chemical reaction. *Operando* XAS studies at the Mn, Fe and Co K-edges displayed the sequence of changes of the oxidations states and of the local environments of the different transition metals, which are related to the potential steps in galvanostatic cycling. The pathway of the discharging reaction starts with insertion of ~0.5 Li into the amorphous oxide on the surface of the nanoparticles. After uptake of 2.5 Li per formula unit a (distorted) rock salt structure is formed. Further Li uptake leads to successive formation of amorphous Mn, Fe and Co metal nanoparticles embedded in a Li<sub>2</sub>O matrix. The XAS data demonstrate that first Mn<sup>3+</sup> is reduced followed by Fe<sup>3+</sup>. After the charge process metallic Mn, Fe and Co are oxidized to Mn<sup>2+</sup>, Fe<sup>3+</sup> and Co<sup>2+</sup>, i.e. Mn adopts the oxidation state +2 explaining the partial capacity loss reported for Mn(III) containing spinels. Further cycling and TEM investigations showed stable redox reactions over many cycles and no phase separation could be detected.

Reprinted with permission from Stefan Permien, Sylvio Indris, Anna-Lena Hansen, Marco Scheuermann, Dirk Zahn, Ulrich Schürmann, Gero Neubüser, Lorenz Kienle, Eugen Yegudin, Wolfgang Bensch, *ACS Applied Materials & Interfaces*, **2016**, *8*, 15320-15332.

DOI: 10.1021/acsami.6b03185. Copyright 2016 American Chemical Society.

## Elucidation of the Conversion Reaction of $\text{CoMnFeO}_4$ Nanoparticles in Lithium Ion Battery Anode via Operando Studies

Stefan Permien,<sup>†</sup> Sylvio Indris,<sup>‡</sup> Anna-Lena Hansen,<sup>†</sup> Marco Scheuermann,<sup>‡</sup> Dirk Zahn,<sup>||</sup> Ulrich Schürmann,<sup>§</sup> Gero Neubüser,<sup>§</sup> Lorenz Kienle,<sup>§</sup> Eugen Yegudin,<sup>†</sup> and Wolfgang Bensch<sup>\*,†</sup>

<sup>†</sup>Institute of Inorganic Chemistry, University of Kiel, Max-Eyth-Straße 2, 24118 Kiel, Germany

<sup>‡</sup>Institute for Applied Materials, Karlsruhe Institute of Technology, P.O. Box 3640, 76021 Karlsruhe, Germany

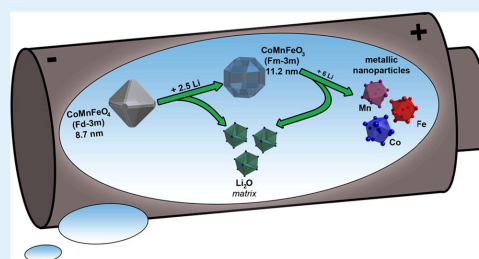
<sup>§</sup>Institute for Materials Science, University of Kiel, Kaiserstraße 2, 24143 Kiel, Germany

<sup>||</sup>Chair for theoretical Chemistry/Computer Chemistry Centrum, Friedrich-Alexander University Erlangen-Nürnberg, Nagelsbachstraße 25, 91052 Erlangen, Germany

### Supporting Information

**ABSTRACT:** Conversion reactions deliver much higher capacities than intercalation/deintercalation reactions of commercial Li ion batteries. However, the complex reaction pathways of conversion reactions occurring during Li uptake and release are not entirely understood, especially the irreversible capacity loss of Mn(III)-containing oxides. Here, we report for the first time on the electrochemical Li uptake and release of  $\text{Co}^{\text{II}}\text{Mn}^{\text{III}}\text{Fe}^{\text{III}}\text{O}_4$  spinel nanoparticles and the conversion reaction mechanisms elucidated by combined operando X-ray diffraction, operando and ex-situ X-ray absorption spectroscopy, transmission electron microscopy, <sup>7</sup>Li NMR, and molecular dynamics simulation. The combination of these techniques enabled uncovering the pronounced electronic changes and structural alterations on different length scales in a unique way. The spinel nanoparticles undergo a successive phase transition into a mixed monoxide caused by a movement of the reduced cations from tetrahedral to octahedral positions. While the redox reactions  $\text{Fe}^{3+} \leftrightarrow \text{Fe}^0$  and  $\text{Co}^{2+} \leftrightarrow \text{Co}^0$  occur for many charge/discharge cycles, metallic Mn nanoparticles formed during the first discharge can only be oxidized to  $\text{Mn}^{2+}$  during charge. This finding explains the partial capacity loss reported for Mn(III)-based spinels. Furthermore, the results of the investigations evidence that the reaction mechanisms on the nanoscale are very different from pathways of microcrystalline materials.

**KEYWORDS:** lithium ion battery, spinel oxide, conversion, operando XRD, operando XAS, anode



### 1. INTRODUCTION

Massive efforts are under way to develop new rechargeable batteries and to identify new electrode materials, because there is a pronounced need for compact sources for portable electricity, transportation, and energy storage of renewables such as solar and wind power.<sup>1,2</sup> The commercialized rechargeable Li batteries are characterized by a specific capacity between  $\sim 120$  and  $180 \text{ mAh g}^{-1}$ , and it seems that there is an upper capacity limit for systems where one Li per formula unit is intercalated/deintercalated.<sup>3</sup> Hence, intense research is going on to identify new materials for lithium ion batteries (LIBs),<sup>1,4</sup> and a large variety of materials including layered transition metal oxides, phosphates with olivine structure, or spinels are investigated.<sup>5–7</sup> To improve the performance of LIBs based on intercalation/deintercalation reactions, ex situ and in situ/operando studies were performed with a large variety of analytic tools.<sup>1,8–13</sup> Reasonably good understanding of the reaction mechanisms occurring during discharge/charge in commer-

cially used electrode materials helped to improve the performance of LIBs.

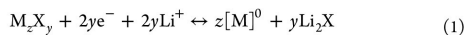
However, as mentioned above, the capacity is limited, and therefore, to overcome such limitation, conversion reactions were investigated in the past. Nowadays, they are more intensively studied. During a conversion reaction many more Li atoms can be transferred between the cathode and anode thus leading to capacities that are 2–5 times larger than for, for example, commercially used  $\text{LiCoO}_2/\text{graphite}$ .<sup>14,15</sup> Transition metal (TM) oxides, sulfides, nitrides, fluorides, or phosphides  $\text{M}_2\text{X}_4$  ( $\text{M} = \text{Mn}, \text{Fe}, \text{Co}, \text{Ni}, \text{Cu}, \text{Zn}, \dots$ ;  $\text{X} = \text{O}, \text{S}, \text{N}, \text{F}, \text{P}$ ) were investigated as electrode materials, and during discharge (Li uptake) the cations are reduced to metal nanoparticles embedded in a  $\text{Li}_x\text{X}_b$  salt matrix.<sup>15–18</sup> During charging (Li

Received: March 15, 2016

Accepted: May 24, 2016

Published: May 24, 2016

release), it is postulated that binary compounds  $M_xX_y$  are formed and Li is recovered as described in eq 1:



(M = transition metal, X = O, S)

This type of reaction is more complex than presented in eq 1 with occurrence of several intermediate phases for distinct materials.<sup>19–23</sup> Operando/in situ investigations demonstrated that the reactions proceed via different steps.<sup>24–26</sup> One advantage of operando/in situ experiments is that unwanted side reactions with air or moisture and undesirable altering products are avoided. Using X-ray powder diffraction (XRD) the long-range order of the material as well as new phases can be identified during discharge/charge processes. Combining XRD with X-ray absorption spectroscopy (XAS), structural alterations and changes of the electronic structure as well as local environments of the transition metals (irrespective of whether the material is crystalline, amorphous, or nanocrystalline) can be monitored simultaneously. Recently, we investigated the reaction mechanisms of Li uptake and release using  $MnFe_2O_4$ ,  $CoFe_2O_4$ , and  $MgFe_2O_4$  nanoparticles as electrode materials.<sup>21–23</sup> The reaction proceeds in distinct steps: (i) consumption of a small amount of Li by reaction with amorphous oxides on the particle surface; (ii) formation of a monoxide with NaCl-type structure after uptake of  $\sim 2$  Li per formula unit; (iii) reduction of TM cations to the metallic state and simultaneous formation of  $Li_2O$ ; (iv) formation of the metal oxides for M = Mn, Fe, Co during the charge process.

Spinel oxides containing one ( $Co_3O_4$ ,<sup>27</sup>  $Mn_3O_4$ ,<sup>28</sup>  $Fe_3O_4$ ,<sup>29</sup>) or two ( $CoFe_2O_4$ ,<sup>30,31</sup>  $NiFe_2O_4$ ,<sup>32</sup>  $MnFe_2O_4$ ,<sup>33</sup>  $ZnFe_2O_4$ ,<sup>34</sup>  $ZnMn_2O_4$ ,<sup>35</sup>) transition metals used as anode materials exhibit high specific capacities of  $\sim 1100$ – $1400$  mAh  $g^{-1}$  (first discharge), because eight Li can be converted per formula unit. Zn-containing TM oxides enable even storage of one additional Li per formula unit by formation of a LiZn alloy. It was demonstrated that special morphologies of the oxide particles and/or composites with graphene or carbon nanotubes led to stable capacities of 800 to 1000 mAh  $g^{-1}$ , for example, in the 100th cycle.<sup>36,37</sup>

While several mono- and bimetallic spinel oxides were investigated as electrode materials in LIBs, comparable experiments on trimetallic spinels are scarce. Lavela et al.<sup>38</sup> synthesized  $NiFeMnO_4$  by a reverse micelle method, and the capacity after 20 cycles was  $\sim 900$  mAh  $g^{-1}$  being competitive with the performance of mono- and bimetallic spinels.  $CoMn_2O_4$ ,<sup>39,40</sup> and  $CoFe_2O_4$ ,<sup>30,31,41</sup> spinels were reported as high-capacity anode materials, but Li uptake into  $CoMnFeO_4$  has not been investigated, yet.  $CoMnFeO_4$  was synthesized as thin films<sup>42,43</sup> and as powders for determination of the cation distribution and magnetic and catalytic properties.<sup>44,45</sup> Here we report for the first time on the electrochemical performance of  $CoMnFeO_4$  nanoparticles as anode material. Furthermore, we investigate the reaction mechanism during Li insertion into the quaternary spinel by operando synchrotron-based XRD and XAS allowing monitoring the individual structural and electronic events occurring during the reaction. The XRD/XAS experiments are complemented by ex situ  $^7Li$  magic-angle spinning (MAS) NMR and transmission electron microscopy (TEM) investigations. To the best of our knowledge, operando studies on quaternary spinels were never reported before. The elucidation of an exact reaction mechanism helps to understand

the behavior of the constituents of the anode material thus enabling optimization for potential application in LIBs.

## 2. RESULTS

**2.1. Structural Characterization.** The XRD powder pattern of  $CoFeMnO_4$  is presented in Figure 1, top. The

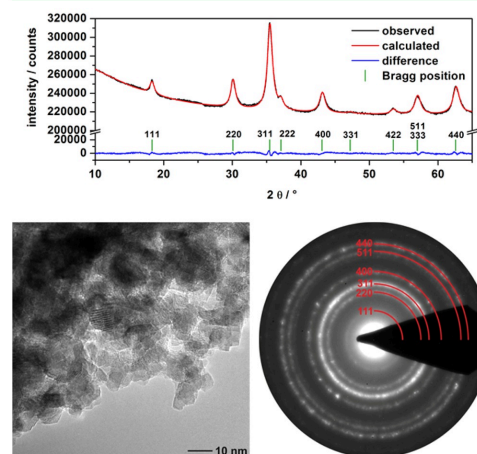


**Figure 1.** (top) XRD powder pattern of  $CoFeMnO_4$  nanoparticles (black), Pawley Fit (red), and difference curve (blue). (bottom) HRTEM image (left) and SAED pattern (right).

position of the Bragg reflections and their relative intensities match very well with the cubic spinel, space group  $Fd\bar{3}m$ . The refinements of the pattern revealed that the observed broadening of the reflections are caused predominantly by particle size effects. The volume-weighted average particle size was determined to be 8.5(2) nm, and the lattice parameter  $a$  was refined to 8.387(2) Å. The value for  $a$  is slightly shorter than that reported in ref 46 ( $a = 8.402$  Å) and ref 44 ( $a = 8.41$  Å for 42 nm particles), indicating that the synthesis conditions affect the lattice parameters.

Scanning electron microscope (SEM) pictures show large particles composed of agglomerated smaller particles (Figure S1). Energy-dispersive X-ray (EDX) analysis confirmed the presence of Co, Fe, Mn, and O (Mn: 37.8 atom %, Fe: 30.9 atom %, and Co: 32.3 atom %). The slight deviation of the theoretical value for Fe can be explained by an overlap of the Fe  $K\alpha$  line with the Mn  $K\beta$  emission and an overlap of the Fe  $K\beta$  line with the Co  $K\alpha$  line (Figure S1). Because the deviation is only  $\sim 3$  atom % the sample is named  $CoFeMnO_4$  in the manuscript.

The high-resolution transmission electron microscopy (HRTEM) image of  $CoFeMnO_4$  nanoparticles shows a particle size distribution with average sizes of  $\sim 8$  nm (Figure 1, bottom). A statistical analysis was hindered by the fact that the particles formed aggregates. The representative selected area electron diffraction (SAED) pattern (Figure 1, bottom) can be unambiguously assigned to the cubic spinel without impurity phases (Table S2). A closer view demonstrates that crystalline cores are covered by a thin noncrystalline surface layer (magnification: Figure S2).



The  $\text{CoMnFeO}_4$  nanoparticles were further chemically analyzed in the TEM demonstrating a homogeneous dispersion of Co, Fe, and Mn (Figure 2, top). The intensity distributions

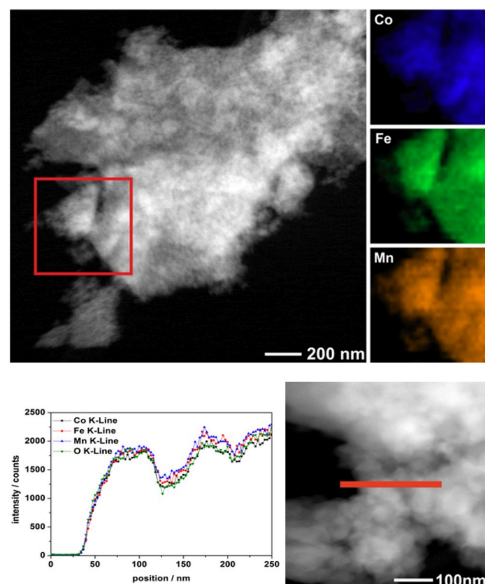


Figure 2. (top) STEM image (top left), EDX mapping at the area marked with a red square (top right). EDX line scan (bottom left) of pristine  $\text{CoMnFeO}_4$  particles (bottom right). Dark-field STEM image (right) with line scan position marked by the red bar.

in the elemental maps are very similar, and EDX point measurements yielded a TM ratio close to 1:1:1 (Figure 2, top). These results were confirmed by an EDX line scan performed on a neighboring particle (see Figure 2, bottom) evidencing the coincidence with the X-ray intensities for Fe, Co, and Mn (see Figure 2, left) and rendering the homogeneous dispersion of the elements.

**2.2. Electrochemical Performance of Nanosized  $\text{CoFeMnO}_4$ .** The electrochemical performance of the  $\text{CoFeMnO}_4$  nanoparticles in a potential range from 0.1 to 3 V is shown in Figure 3. During the first discharge process, a not well-resolved plateau at  $\sim 1.2$  V is visible followed by a long plateau located at 0.8 V (Figure 3a). The overall capacity of the first discharge process of  $1448 \text{ mAh g}^{-1}$  corresponds to an uptake of  $\sim 12.7$  Li per formula unit (f.u.).

Capacities larger than the theoretically expected one ( $917 \text{ mAh g}^{-1}$ ) are characteristic for nanosized spinel oxides<sup>27,29–38,41</sup> caused by irreversible reactions of the electrode materials with the electrolyte and formation of the solid electrolyte interphase (SEI). These unwanted processes are responsible for irreversible capacity loss during charge processes, for which a sloping plateau at  $\sim 1.7$  V is observed (Figure 3a). The reversible capacity of the first cycle of  $968 \text{ mAh g}^{-1}$  (capacity loss:  $480 \text{ mAh g}^{-1}$ ) is in the range reported for other spinel oxides  $\text{M}^{\text{II}}\text{M}^{\text{III}}_2\text{O}_4$  ( $\text{M}^{\text{II}} = \text{Co, Fe, Ni, Mn, Zn}$ ;  $\text{M}^{\text{III}} = \text{Co, Mn, Fe}$ ).<sup>27–41</sup> The slightly larger capacity than the theoretically expected one may be explained by reversible

reactions with the electrolyte and/or capacitive effects at the surface of the nanoparticles.<sup>47–49</sup>

Cyclic voltammetry (CV) exhibits two anodic peaks during the first discharge (Figure 3b), of which a less intense one occurs at 1.0 V (Figure 3b, inset), and a very intense signal is located at 0.5 V. During the charge process a broad cathodic peak ranging from 1.5 to 2.0 V is observed, which consists of more than one event. The discharge process of the second and following cycles are different from the first one, and only a weak anodic event occurs at 1.2 V; a second more intense signal occurs at 0.8 V (Figure 3b). With increasing cycle number the events slightly shift to lower cell potentials. The voltage profile during the first discharge process is completely different from the following as can be seen for cycling with constant current and CV (compare Figure 3a,b). Obviously, during the first charge process new phases are formed exhibiting different electronic and structural characteristics.

In Figure 3c the charge and discharge capacity as a function of the cycle number at C/10 rate is displayed. The capacity remains stable during the first 12 cycles, while a slight decrease is observed in subsequent cycles, and after 50 cycles the capacity is still  $717 \text{ mAh g}^{-1}$ , that is, 74% of the first cycle. A comparison with literature data demonstrates that the cycle stability of the  $\text{CoFeMnO}_4$  nanoparticles are better or at least competitive with other transition metal oxides like  $\text{NiFe}_2\text{O}_4$  nanoparticles<sup>32</sup> ( $345 \text{ mAh g}^{-1}$ , after 40th cycle),  $\text{Mn}_3\text{O}_4$ <sup>28</sup> ( $720 \text{ mAh g}^{-1}$ , after 40th cycle),  $\text{CoFe}_2\text{O}_4$ <sup>30</sup> ( $730 \text{ mAh g}^{-1}$ , after 50 cycles),  $\text{ZnFe}_2\text{O}_4/\text{C}$ <sup>34</sup> ( $713 \text{ mAh g}^{-1}$ , after 50 cycles), and  $\text{NiMnFeO}_4$ <sup>38</sup> ( $750 \text{ mAh g}^{-1}$ , after 50 cycles). We note that optimization of the particle morphology as well as addition of suitable additives like carbon species should lead to an even better performance of the material.

Figure 3d illustrates the capacity at different C-rates from C/10 to 1.4 C. For C/10, C/5, C/2, 1, and 1.4 C rates the capacity is 1011, 853, 661, 495, and  $375 \text{ mAh g}^{-1}$ , respectively, being larger than for graphite even at high currents. After it cycles at high current density the material is at least partially destroyed, and cycle stability is lost as can be seen in Figure 3d for the C/10 data measured after cycling at 1.4 C.

**2.3. Operando XRD.** The refinement of the powder pattern of the pristine material yielded  $a = 8.388(2) \text{ \AA}$  and a volume-weighted particle size  $d = 8.7(1) \text{ nm}$ . The differences of the values between *in house* diffraction experiments and the synchrotron-based investigation are marginal (0.1%).

The evolution of the potential of the *in situ* cell during first discharge is similar to that recorded for the Swagelock cell (Figure 4, bottom left). According to the potential profile three regions can be distinguished: (a) region I: uptake of the first 2.5 Li per formula unit, (b) region II: uptake of  $>2.5$  Li until end of discharge, (c) region III: charge process. The operando XRD patterns recorded during region I are presented in Figure 4 (top). At the beginning of Li uptake (ca. 0.5 Li per f.u., region Ia) a slight shift of all reflections occurred due to an expansion of the  $a$  axis of  $\sim 0.2\%$  (Figure 4, bottom right). The integrated intensity of all reflections of the powder patterns collected up to 0.5 Li exhibit no change evidencing that the crystalline material is not converted into a new product at this stage. The ( $hkl$ )-dependent domain sizes yield octahedral crystal morphology for the pristine material being in good accordance with TEM image (Figure S2). The morphology is preserved until  $\sim 0.5$  Li/f.u. (Figure 4 top, red line), while a truncation of the octahedra occurs for  $>0.5$  Li/f.u. yielding a more spherical

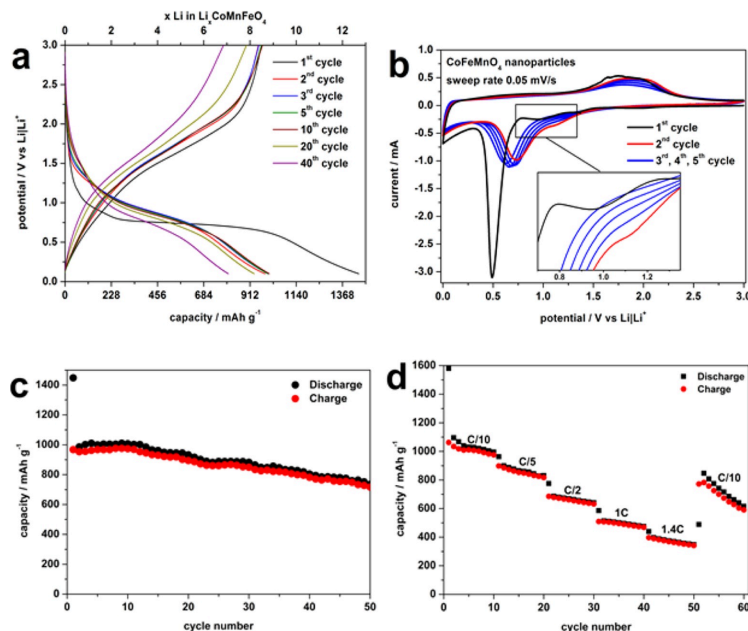


**Figure 3.** Electrochemical performance of CoFeMnO<sub>4</sub> nanoparticles. (a) Potential vs capacity of the first three cycles and of cycles 5, 10, 20, and 40. (b) CV of the first five cycles at a sweep rate of 0.05 mV/s. (c) Capacity of the first 50 cycles at a C/10 rate. (d) Cycle stability at different cycling rates.

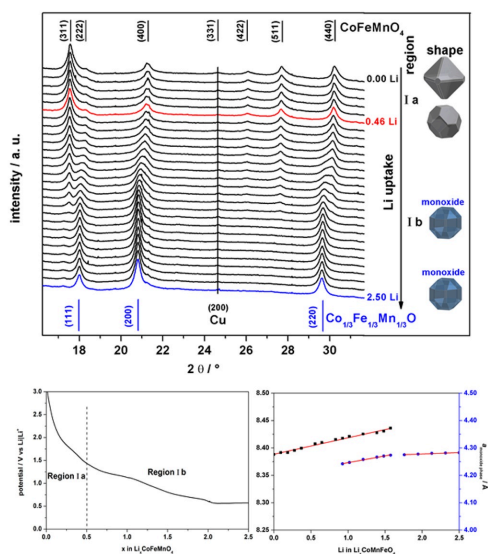


**Figure 4.** Operando XRD of region I during uptake of the first 2.5 Li per formula unit (top), potential process of region I (bottom left), and expansion of the *a* axes during Li uptake for spinel phase as well as monoxide phase (bottom right).

shape. An analogous spherical morphology is found for the monoxide phase (Figure 4).

Increasing the Li content beyond 0.5 Li/f.u., the (311) and (511) reflections start to lose intensity, while at the position of the (222) reflection an intensity gain can be observed. Simultaneously, the (400) and (440) reflections are broadened indicating an overlap of reflections, that is, new Bragg reflections appeared, which are assigned to a monoxide adopting space group *Fm* $\bar{3}$ *m* with *a* = 4.239(3) Å (for uptake of ~0.6 Li). A linear expansion of the *a* axis of the spinel phase occurs until the refinement of the lattice parameter is not reliable anymore, due to low intensity of the reflections. Simultaneously, the lattice parameter of the monoxide phase is increasing continuously up to 2 Li per f.u., and afterward it remains constant. The reflections of the starting material disappeared, and the powder pattern can be refined with only one phase, that is, a monoxide with a NaCl-type structure Co<sub>1/3</sub>Fe<sub>1/3</sub>Mn<sub>1/3</sub>O; *a* = 4.275(1). The NaCl-type structure can only be realized by the movement of ions located on tetrahedral sites to neighboring empty octahedral sites and simultaneous reduction of M<sup>III</sup> cations to M<sup>II</sup> (see Section 2.4). A challenging question is whether phase separation and formation of FeO, CoO, and MnO particles occurred. Such a phase separation requires a directed movement and reduction of M<sup>III</sup> located on tetrahedral sites to those empty octahedral sites having M<sup>II</sup> in octahedral site as direct neighbor; that is, Fe<sup>III</sup>/Mn<sup>III</sup> are reduced and jump to those empty octahedral sites where Fe<sup>II</sup>/Mn<sup>II</sup> are the next nearest neighbor. Because the tetrahedral sites are statistically occupied by the trivalent ions such a concerted



mechanism/movement seems not to be plausible under the experimental conditions.

In addition, the presence of three separated oxides would lead to much broader reflections in the powder patterns because the coherently scattering domains of the individual oxides are much smaller than those of a mixed monoxide. Additionally, cubic MnO exhibits a larger lattice parameter compared to  $\text{Fe}_{1-x}\text{O}$  and CoO leading to an asymmetric shape of the reflections (simulated powder pattern: Figure S3). On the basis of the present results and those reported in the literature it is most likely that Li uptake gradually forces the formation of a mixed monoxide.<sup>43,45–47</sup> Between 2.0 and 2.5 Li/f.u. a further growth of the particles was not observed.

Analysis of log-normal domain size distribution revealed a decrease of small spinel crystallites in favor of the newly formed monoxide during the chemical reaction. A comparison of the spinel (0 Li) and the monoxide after uptake of  $\sim 2.5$  Li clearly displays the loss of smaller particles and a shift in the distribution toward larger crystallites (Figure S4, volume weighted particle size  $d = 11.2(1)$  nm).

The continuing uptake of Li (long plateau at 0.6 V, region IIa) leads to a successive decrease of the reflection intensities and a continuous broadening of the reflections; that is, either the intermediate phase is converted to an amorphous product or the coherent scattering domains are too small to be detected by XRD (Figure 5). No reflections are observed after uptake of 8 Li/f.u. suggesting that all metal ions are reduced to the metallic state and the metallic particles are too small to be detected by XRD (Figure 5, red pattern). Accommodation of additional Li in region IIb can be explained by reversible/irreversible reactions with the electrolyte and/or surface charge transfer mechanism (discussed in Section 2.2). The diffraction

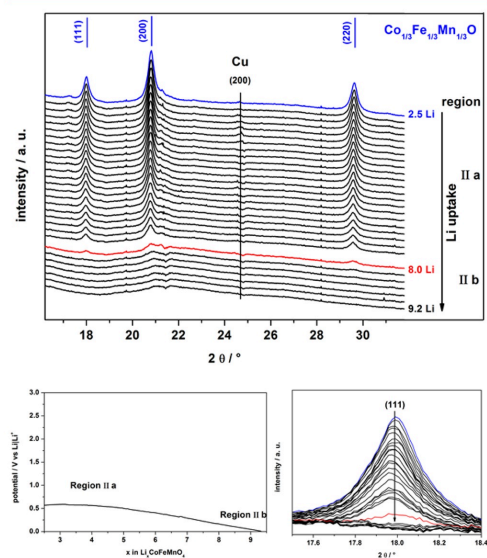
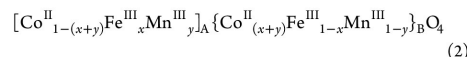


**Figure 5.** Operando XRD patterns recorded in region II during uptake of more than two Li until end of discharge (top), voltage profile of region II (bottom left), and magnified view of the region of the 111 reflection (bottom right).

patterns collected during the charge process and after the first cycle (not presented here) give evidence that the particles are either amorphous or that the crystalline domains are smaller than the coherence length of the X-rays.

**2.4. Operando X-ray Absorption Spectroscopy.** The small energy differences of the Mn, Fe and Co, K absorption edges allow quick XAS measurements with just one cell, reducing the risk of varying data, which may occur if individual cells are used for every absorption edge. The spectra of the pristine material at all three K edges show a pre-edge peak (Figure 6 thick blue line) delivering information about the local structure of the absorber atom. Pre-edge features are a result of  $1s \rightarrow 3d/4p$  (hybridized orbitals) transitions, which may appear with large intensity in a non-centrosymmetric environment. For the centrosymmetric octahedral (B) environment the pre-edge signal is very weak and a result of mainly quadrupole transitions of very low intensity.

The occurrence of  $1s \rightarrow 3d/4p$  transitions for all three metal ions is a clear hint that they are at least partially located on tetrahedral sites.<sup>50,51</sup> The energy of the Mn K-edge at 6550 eV (determined by the maximum of the first derivative) is identical with that of  $\alpha\text{-Mn}^{\text{III}}\text{O}_2$ ,<sup>52</sup> evidencing that Mn in  $\text{CoFeMnO}_4$  nanoparticles is in the expected oxidation state  $\text{Mn}^{\text{III}}$ . For the Fe K-edge a value of 7125 eV is obtained in agreement with the value for  $\text{Fe}^{\text{III}}$  in  $\text{MFe}_2\text{O}_4$  ( $M = \text{Ni}, \text{Co}, \text{Mn}$ ).<sup>51</sup> The Co K-edge energy at 7716 eV is in line with that of  $\text{Co}^{\text{II}}$  in  $\text{CoFe}_2\text{O}_4$ .<sup>33</sup> Summarizing, the expected oxidation states could be confirmed by XAS for pristine  $\text{CoFeMnO}_4$ . Hence, the chemical formula can be presented as



(A: tetrahedral sites and B = octahedral sites).

In Figure 7, the potential curve of the operando XAS cell is shown, displaying processes similar to the first cycle discussed in Section 2.2. Below the potential curve the energy position of the Mn K-, Fe K-, and Co K-edges are displayed. In region I, the position of the Co K-edge is only slightly affected by Li uptake, while both the Fe K-edge and Mn K-edge exhibit a strong shift to lower energy. We note that in region I  $\text{Mn}^{\text{III}}$  is reduced first, and at later stage reduction of  $\text{Fe}^{\text{III}}$  starts (Figure 7).

After uptake of  $\sim 2.5$  Li per f.u. the Mn K-edge energy at 6545 eV is identical with that of MnO (Figure 6, top).<sup>54</sup> Also a strong shift of the Fe K-edge occurred, that is,  $\text{Fe}^{\text{III}}$  is reduced to  $\text{Fe}^{\text{II}}$  (Figure 6), as also observed during Li uptake into  $\text{Fe}_2\text{O}_3$ .<sup>55</sup>

Not only shifts of the absorption edges are obvious but also their shapes are altered during Li uptake. The pre-edge features for all three elements disappeared when  $\sim 2.5$  Li/f.u. are inserted because the ions moved from the tetrahedral to neighbored octahedral sites. At this stage of discharge, X-ray absorption near edge structure (XANES) spectra of all three elements display the largest intensity of the  $1s \rightarrow 4p$  transition (Figure 6, thick blue line). In region II (during the long plateau at  $\sim 0.6$  V), the intermediately formed monoxide is transformed to an amorphous respectively nanocrystalline product (Section 2.3).  $\text{Co}^{\text{II}}$ ,  $\text{Mn}^{\text{II}}$ , and  $\text{Fe}^{\text{II}}$  are reduced to the metallic state during the long plateau in region II (Figure 7). In the spectra of all three metals a rotation around isosbestic points is visible at 6545 eV for Mn, at 7123 eV for Fe, and at 7718 eV for Co (Figure 6) giving evidence that the three metals are transformed in a one-step reaction without formation of

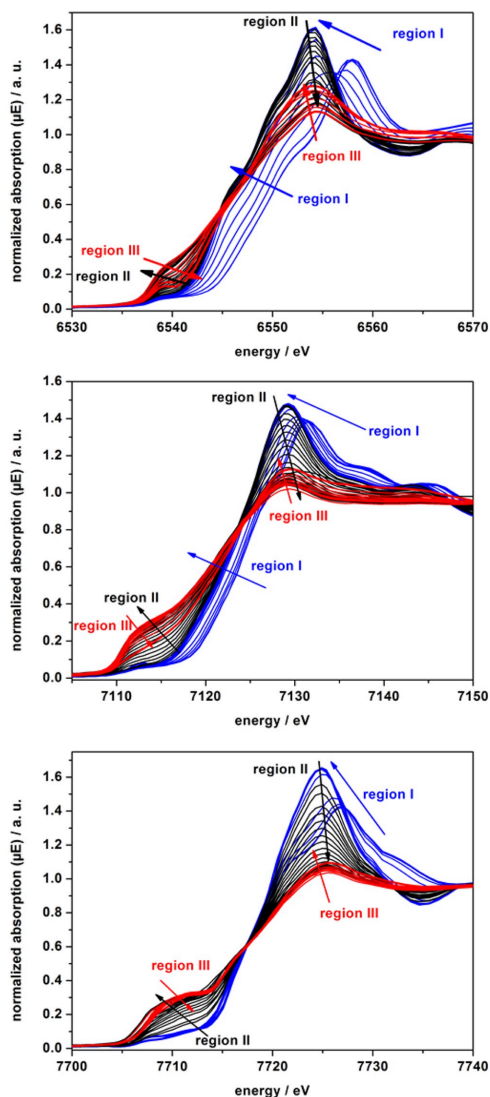


Figure 6. Operando XANES spectra at Mn (top), Fe (middle), and Co K-edge (bottom) during uptake of the first 2.5 Li per f.u. (region I, blue lines), during uptake of more than 2.5 Li (region II, black lines), and during charge process (region III, red lines).

intermediates. At the end of region II (end of discharge process), the spectra of all three elements resemble those of metallic reference foils, that is, the metallic states of Mn, Fe, and Co are reached. Similar observations were made for the Li uptake by  $\text{NiCo}_2\text{O}_4$ . But this material contains  $\text{Co}^{\text{III}}$ , which is reduced in the first step followed by simultaneous reduction of  $\text{Ni}^{\text{II}}$  and  $\text{Co}^{\text{II}}$  to the metallic state.<sup>56</sup>

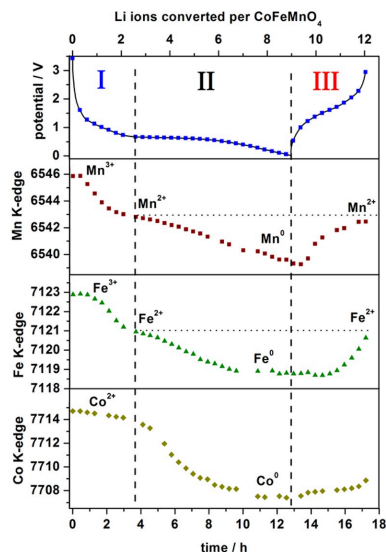


Figure 7. Potential curve of the in situ cell (top) and K-edge position of Mn, Fe, and Co (from top).

The charge process is accompanied by a strong shift of the Mn K-edge to higher energy, that is,  $\text{Mn}^0$  is oxidized, followed by oxidation of Fe. The beginning of oxidation of metallic Co is only partially visible at the end of the charge process (see Figures 6 and 7).

Fourier transformation (FT R-space) of the spectra of the pristine state and at the end of regions I, II, and III was performed to interpret the changes in the local environment of the ions (Figure 8; the normalized XAS spectra covering the pre-edge, XANES, and extended X-ray absorption fine structure region are displayed in Figure S5). For pristine  $\text{CoMnFeO}_4$  two signals are visible in the FT R-space plot for each element representing the M–O bonds (1.5 Å) and M–O–M paths (2.5 Å). The asymmetry of the shape of the first signal is caused by overlapping paths of the cations located on tetrahedral (shorter path) and octahedral sites (longer path) in the spinel structure. At the end of region I, the distance of all three elements to the first neighbor increases slightly caused by formation of the monoxide phase characterized by longer M–O bonds (M = Co, Fe, Mn). At the end of region II a new signal at 2 Å developed corresponding to interatomic distances for metallic Co, Fe, and Mn (Figure 8), while signals at 1.5 and 2.5 Å disappeared. During the first two scans of the charge process (region III) the K-edge positions of the elements are not shifting (Figure 6), suggesting a reversible additional storage mechanism affecting the capacity at the early stages of Li release.<sup>48,49</sup>

The FT R-space curves at the end of region III (charged state) are characterized by an intensity reduction of the M–M paths at ca. 2 Å for all three elements and the development of the two signals assigned to M–O and M–O–M scattering paths. The maxima of the Mn/Fe–O and Mn/Fe–O–M signals occur at nearly identical distances as in the monoxide intermediate phase. Furthermore, as can be seen in Figure 7 only 3.1 Li (capacity: 355  $\text{mAhg}^{-1}$ ) could be removed during

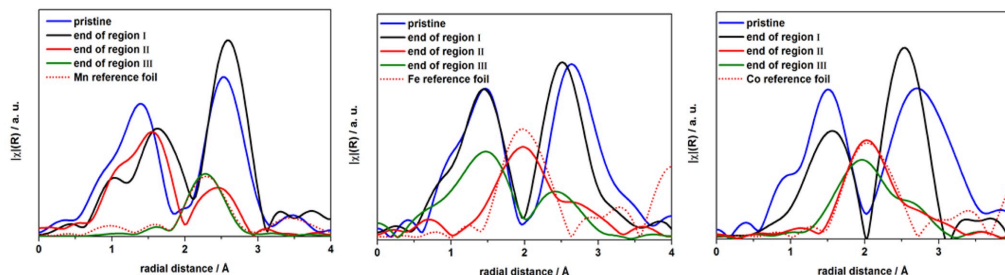


Figure 8. FT R-space spectra of Mn (left), Fe (middle), and Co (right). Note: no phase shift correction was applied.

charge demonstrating that the charge process was incomplete (see Section 2.2). Most probably, the setup of the in situ cell does not compensate the volume expansion during cycling, and parts of the active material may become inactive. Indeed the last spectra of the operando study evidence that the final oxidation states of the transition metal ions are not reached. Nevertheless, operando XAS during the charge process provides information in which sequence the transition metals are oxidized from the metallic state. The final oxidation state of the transition metals was determined by ex situ XANES spectra of a fully cycled sample (Figure S6). The XANES data evidence that metallic Mn is oxidized to  $\text{Mn}^{\text{II}}$  and remains in this oxidation state. This observation is in line with results obtained on  $\text{Mn}_3\text{O}_4$ , where during charge MnO is formed instead of  $\text{Mn}^{\text{III}}$ .<sup>20</sup> The XANES spectra at the Fe K-edge indicate that trivalent  $\text{Fe}^{\text{III}}$  is obtained after the first cycle. Co is also oxidized, and the K-edge absorption energy gives hints for the presence of  $\text{Co}^{\text{II}}$  after the first cycle. The results are in agreement with observations recently made for  $\text{CoFe}_2\text{O}_4$  nanoparticles.<sup>23</sup> The presence of weak pre-edge features in the K-edge spectra suggests a local symmetry without an inversion center.

**2.5. Ex Situ  $^7\text{Li}$  Magic-Angle Spinning Nuclear Magnetic Resonance.** The ex situ  $^7\text{Li}$  MAS NMR spectra of the lithiated  $\text{CoMnFeO}_4$  samples and of the sample obtained after one complete electrochemical cycle are displayed in Figure 9. The samples with small Li contents (0.3 Li, 0.6 Li, 1 Li) exhibit very broad spinning sideband patterns and very broad isotropic peaks. The intensity of the isotropic peaks is covering the range from +100 to -400 ppm. Such large  $^7\text{Li}$  NMR shift values occur only in samples with paramagnetic neighbors in the direct environment of the Li ions.<sup>57</sup> Thus, these large shifts reflect the presence of Li–O–(Fe/Mn/Co) bonds. The extremely broad contributions in the patterns obtained in spite of the very fast MAS spinning (60 kHz) show that the Li ions experience a large variety of local environments, that is, many different compositions and arrangements of the transition metal neighbors (Co, Mn, Fe). This is consistent with a random arrangement of the different transition metal elements in the amorphous phase on the surface of the nanoparticles. After conversion of two Li ions, the spinning sideband pattern in the  $^7\text{Li}$  NMR spectrum shows a clear narrowing and a major isotropic peak close to 0 ppm with strongly reduced width. This reveals the formation of a Li-containing phase without transition metal neighbors around the Li, and thus this peak can be assigned to the  $\text{Li}_2\text{O}$  phase that is formed together with the  $\text{Co}_{1/3}\text{Fe}_{1/3}\text{Mn}_{1/3}\text{O}$  rock salt phase. Additionally, in this spectrum broad contributions covering the range from +200 to -100 ppm are visible (marked with arrows in Figure 9). These

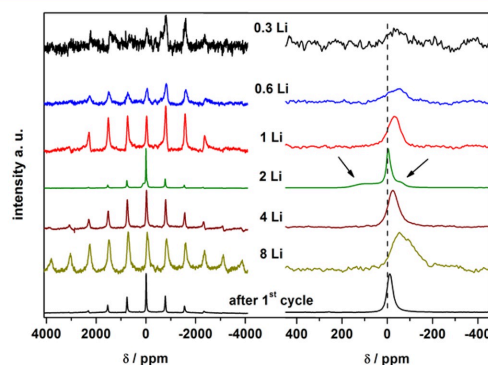
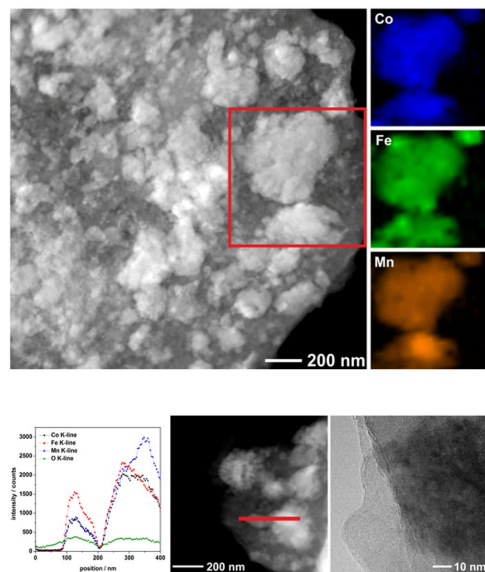


Figure 9.  $^7\text{Li}$  MAS NMR spectra of  $\text{CoFeMnO}_4$  nanoparticles after uptake of 0.3, 0.6, 1, 2, 4, 8 Li per formula unit and after the first cycle. (left) Full spinning sideband patterns. (right) Magnified view of the region of the isotropic peaks.

are caused either by residuals of the spinel phase or small amounts of Li in the rock salt phase. Further increasing of the Li content, the width of the spinning sideband pattern increases again, and the isotropic peaks also show a strong broadening. This behavior is consistent with our earlier observations on  $\text{MnFe}_2\text{O}_4$ <sup>21</sup> and  $\text{MgFe}_2\text{O}_4$ ,<sup>22</sup> and it is caused by the increasing amount and size of Mn, Fe, and Co metal particles. The spectrum of the sample obtained after one full cycle shows again a quite narrow peak and a rather narrow spinning sideband pattern. This spectrum confirms that the overall reaction is not reversible; that is, the transition metal particles are converted back to oxides, but the initial spinel phase is not reformed.

**2.6. Ex Situ Transmission Electron Microscopy of Lithium-Containing Samples.** TEM investigations were performed on  $\text{CoMnFeO}_4$  nanoparticles that were discharged to 10 mV and cycled (0.1–3.0 V, charged state) three times (potential profiles are shown in Figure S7). Figure 10 (top, left) shows a dark-field STEM image of a completely discharged sample. The Co-, Mn-, and Fe-containing particles (with strong Z-contrast) are randomly dispersed in an amorphous matrix. STEM-EDX mapping (Figure 10, top right) performed on a single particle reveals that iron, cobalt, and manganese are not homogeneously dispersed (cf. Mn-rich and Fe-poor area marked in Figure 10, top right) within the metal oxide; however, phase separation of single metal (oxide) nanoparticles





**Figure 10.** Dark-field STEM image (top left), EDX mapping at the area marked with a red square. EDX line scan (bottom left) of CoMnFeO<sub>4</sub> particles after cycling three times between 3.0 and 0.1 V. Dark-field STEM image (bottom middle) with line scan marked by the red bar. HRTEM micrograph at the edge of an amorphous particle with SEI on the left side (bottom, right).

is not observed. Very recently a local segregation of chemical elements on the nanometer scale was reported, which significantly improved the electrochemical performance.<sup>58</sup> Whether the inhomogeneous distribution of the metals is

beneficial for the electrochemical performance of the material cannot be answered on the basis of the present data.

After three cycles an EDX line scan (Figure 10, bottom left) over two particles (see Figure 10 middle, red bar) demonstrates the equal distribution of oxygen and metals content in both particles. On the left side of the measuring area an oxygen excess arising from the SEI is visible. At high resolution the amorphous SEI covering the surface of a particle is visible (see Figure 10, bottom right). After the cycles, the metal-containing particles lose their crystalline character. HRTEM and SAED investigations revealed that the product is amorphous, also visible by FFT transformation of the image (Figure S8; Moreover, carbon could be found due to the sample preparation and its presence in the SEI).

**2.7. Molecular Dynamics Simulation of Li Ion Intercalation and Mobility in Fe<sub>3</sub>O<sub>4</sub>.** To explore the early stage of Li intercalation into the spinel structure of M<sub>3</sub>O<sub>4</sub> we performed molecular dynamics simulations on an Fe<sub>3</sub>O<sub>4</sub> nanocube initially prepared as an ideal crystal. Upon relaxation at 300 K the nanocube evolved into a slightly more rounded shape, exhibiting partial amorphous arrangements at its edges and corners, which is in good agreement with amorphous surface visible in TEM. Subsequently five Li<sup>+</sup> were incorporated into neighboring 8b and 48f tetrahedral sites, and relaxation was explored (i) without charge compensation and (ii) with charge compensation by reducing an adjacent Fe<sup>III</sup> ion. In both cases, structural relaxation of the defect involves only local rearrangements keeping the overall lattice intact. At 300 K the average distance of Li–O contacts was found as 2.2 Å, while the Fe<sup>II</sup>–O and Fe<sup>III</sup>–O nearest neighbor distances are 2.9 and 2.7 Å, respectively. In turn, the metal ions are shifted to expand the distance with respect to the tetrahedral sites from less than 2 Å (for empty tetrahedral sites) to ~2.7 Å (Li–Fe<sup>II</sup> contact after intercalation).

By filling of five neighboring tetrahedral sites, our starting model was prepared to locally mimic intercalation by one Li per Fe<sub>3</sub>O<sub>4</sub> f.u. However, in both setups (i) and (ii), that is, with and without charge Fe<sup>III</sup> reduction, we identified Li<sup>+</sup> diffusion steps

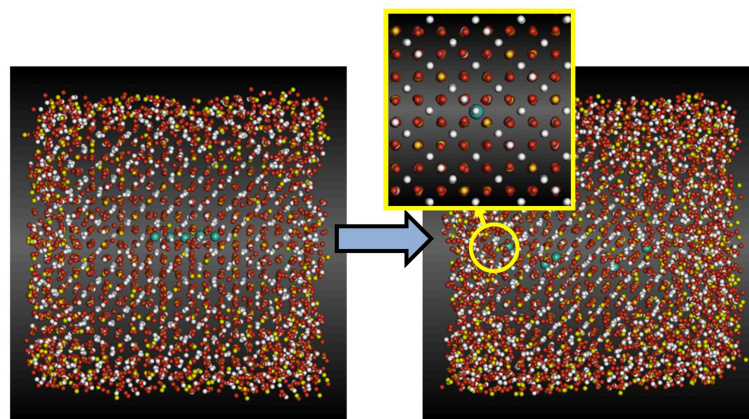


**Figure 11.** Snapshots from molecular dynamics runs of a Fe<sub>3</sub>O<sub>4</sub> nanocube intercalated by five Li ions (left). Relaxation occurs in two steps: rapid separation of the Li ions, by at least one vacant tetrahedral site, and much slower Li<sup>+</sup> diffusion within the nanoparticle. (inset) A single Li intercalation site after model quenching to 0 K. Colors: Fe<sup>III</sup> (white), Fe<sup>II</sup> (yellow), O (red), Li (cyan).

leading to larger Li–Li separation after ~100 ps. Upon Li separation by at least one vacant tetrahedral site, ion mobility decreased, and diffusion steps were observed on the 1 ns scale (Figure 11). Our simulations hence suggest that intercalation by 0.5 Li per  $\text{Fe}_3\text{O}_4$  f.u. constitutes a limiting scenario. Full intercalation of all tetrahedral sites would hinder the beforehand described relaxation of Li–Fe and Li–O distances and result in a sharp increase in potential energy.

### 3. DISCUSSION

$\text{CoMnFeO}_4$  nanoparticles crystallize as a partially inverse spinel with formula  $[\text{Co}^{II}_{1-(x+y)}\text{Fe}^{III}_x\text{Mn}^{III}_y]_A[\text{Co}^{II}_{(x+y)}\text{Fe}^{III}_{1-2x}\text{Mn}^{III}_{1-y}]_B\text{O}_4$ . XANES spectra of the pristine nanoparticles confirm the presence of  $\text{Fe}^{III}$ ,  $\text{Mn}^{III}$ , and  $\text{Co}^{II}$ . In the spinel structure, two different tetrahedral sites (8b and 48f) and one octahedral site (16d) are empty. If  $\text{Li}^+$  enters the structure either on 8b or 48f the Fe/Mn/Co–Li distances are shorter than 2 Å leading to strong repulsive interactions if the structure is assumed as a stiff lattice. An alternative scenario is the uptake of  $\text{Li}^+$  on one of these sites followed by a movement of the M cations located on 8a to empty 16d sites accompanied by reduction of  $\text{M}^{III}$  and a jump of Li ions to 16d sites. Obviously, all octahedral sites are occupied after uptake of 1 Li per formula unit, and a NaCl-like structure should be generated. We note that this scenario was postulated for the Li uptake by  $\text{Fe}_3\text{O}_4$ .<sup>59</sup>

Molecular dynamics (MD) simulation showed this scenario can be excluded for nanoparticles:  $\text{Li}^+$  ions intercalated on tetrahedral sites (8b and 48f) clearly favor this position and only temporarily visit empty octahedral 16d sites when diffusing from one tetrahedral site to another.

Strong repulsive interactions are compensated by a shift of metal ions to expand the distance with respect to the tetrahedral sites from less than 2 Å to ~2.7 Å (Li–Fe<sup>II</sup> contact after intercalation). Hence, the MD simulation suggests that up to 0.5 Li may be incorporated into the structure. This is in agreement with the operando XRD investigations (Section 2.3). In the beginning the integrated and normalized reflection areas of the powder patterns exhibit no variation up to 0.5 Li/ $\text{CoFeMnO}_4$  indicating that the spinel phase is not converted into a new product. The unit cell expansion of the spinel phase is only 0.2%, which is in agreement with the marginal enlargement observed in the MD simulation. The  $^7\text{Li}$  MAS NMR spectra after uptake of 0.3 and 0.6 Li exhibit large shifts indicating the presence of Li–O–M (M = Fe, Co, Mn) bonds, which is in agreement with Li ions being either inserted into the spinel structure or on the surface of the particles. In the operando XANES spectra a slight shift of the Mn K-edge energy is observed indicating that  $\text{Mn}^{III}$  ions are reduced first. Summarizing these results, a possible scenario is an uptake of small amounts of Li into the spinel structure being accompanied by reduction of some  $\text{Mn}^{III}$  ions and expansion of tetrahedral sites, while direct neighbored empty tetrahedral sites are contracted (Section 2.7). This reaction step seems to be partially reversible as demonstrated by repeated cycling between 1.3 and 3.0 V (Figure S9).

For Li contents beyond 0.5/ $\text{CoFeMnO}_4$  an abrupt rise in potential energy is observed in the MD simulation. This increase is induced by the beginning of the transformation of crystalline spinel phase into a NaCl-type oxide as evidenced by XRD. During further Li uptake the  $\text{M}^{III}$  ions are successively reduced, and the  $\text{M}^{II}$  ions on the tetrahedral site move to empty octahedra. Where are the  $\text{Li}^+$  ions located? One may assume

that  $\text{Li}^+$  ions also occupy empty octahedral site. But the observation that up to 1.5 Li/f.u. two crystalline phases coexist (XRD), while at this Li content all 16c/16d sites are occupied, requiring an explanation. A narrowing of the  $^7\text{Li}$  NMR signal for the sample containing one Li/ $\text{CoFeMnO}_4$  suggests formation of  $\text{Li}_2\text{O}$  with only weak or no Li–O–M bridges. On the basis of this finding we conclude that  $\text{Li}^+$  does not occupy octahedral sites, but rather  $\text{Li}_2\text{O}$  is formed. We note that the reaction proposed here is not in accordance with that reported for microcrystalline spinel materials.<sup>59–62</sup> The XANES spectra clearly demonstrate that  $\text{Mn}^{III}$  is reduced first to  $\text{Mn}^{II}$  followed by simultaneous reduction of remaining  $\text{Mn}^{III}$  and  $\text{Fe}^{III}$  to  $\text{Mn}^{II}/\text{Fe}^{II}$ . The reduction of the trivalent ions is finished at the end of region I in the galvanostatic discharge curve. All metal ions are now in the centrosymmetric octahedral environment as evidenced by the disappearance of the pre-edge features in the XANES spectra. According to operando XRD data the spinel structure is now completely converted to the NaCl-type structure (Section 2.3). Occupation of all 16c/16d site leaves behind a network of empty tetrahedral sites, resembling that observed for  $\text{Li}_2\text{O}$  (Li is tetrahedrally surrounded by oxygen atoms). In the  $^7\text{Li}$  MAS NMR spectrum a narrow line is observed, which is typical for  $\text{Li}_2\text{O}$ . The observation of formation of a monoxide as an intermediate during discharge is not unique and was also reported or postulated for a number of spinel materials.<sup>19–22</sup> But compared to these studies we are able to present evidence for  $\text{Li}_2\text{O}$  formation during discharge, the stepwise reduction of  $\text{M}^{III}$  to  $\text{M}^{II}$ , and the successive transformation of the spinel into a NaCl-type structure. The elaborate evaluation of operando XRD demonstrates the successive morphology change and alteration of crystallite size distribution of the nanoparticles. Interestingly, the size of coherently scattering domains of the monoxide after uptake of ~2.5 Li clearly displays a shift in the log-normal size distribution toward larger crystallites (Section 2.3).

Further discharge (cf. long plateau at 0.8 V in galvanostatic cycling, the intense peak in the CV (Figure 3)) leads to simultaneous reduction of all  $\text{M}^{II}$  ions to the metallic state (Section 2.3); that is, no further intermediates are formed. The TEM/EDX investigations of particles formed after three cycles evidence that the nanoparticles contain Co, Mn, Fe, and O; thus, a phase separation can be safely excluded. From thermodynamics the occurrence of the monoxide containing all three cations is surprising and may be explained by the nanosized nature of the spinel particles.

After the first charge process no long-range ordered crystalline materials is formed as evidenced by XRD. But one cannot exclude formation of nanocrystallites being smaller than the coherence length of the X-rays. The results of the XAS experiments demonstrate that metallic Mn is oxidized first, followed by Fe and then Co. Oxidation of metallic Fe to  $\text{Fe}^{III}$  during charge could be definitely answered by accompanying *in situ* XAS investigation (Figure S6). Because Mn nanoparticles can only be oxidized to  $\text{Mn}^{2+}$  the partial capacity loss reported for Mn(III)-based spinels can be explained with this finding.<sup>48</sup>

### 4. CONCLUSION

Phase-pure  $\text{CoMnFeO}_4$  nanoparticles were synthesized via a new synthesis route and investigated for the first time with respect to the electrochemical performance. The material exhibits excellent cycling stability (717 mAh  $\text{g}^{-1}$ , i.e., 74% after 50 cycles) outperforming many other binary and ternary oxides.



For the first time an oxidic spinel consisting of three transition metal cations was investigated by a combination of operando XRD, operando and ex-situ XAS, HRTEM/EDX,  $^7\text{Li}$  MAS NMR, and MD simulation allowing formulation of a very detailed picture of the complex reactions occurring during Li uptake and release. On the basis of all results we safely exclude intercalation of larger quantities of Li in contrast to what was reported for microcrystalline particles.<sup>19,59,62</sup> The spinel phase is successively transformed to rock salt structured  $\text{Co}_{1/3}\text{Mn}_{1/3}\text{Fe}_{1/3}\text{O}$ , which is accompanied by formation of  $\text{Li}_2\text{O}$ . We also investigated for the first time the change of the log-normal domain size distribution and of the particle morphologies. At the end of discharge metallic Co, Fe, and Mn nanoparticles are embedded in a  $\text{Li}_2\text{O}$  matrix. During cycling of the material, metallic nanoparticles and oxidized species are reversibly formed. The oxidized samples most probably consist of oxide(s), while only the local structure of the oxide(s) is known. In summary,  $\text{CoMnFeO}_4$  nanoparticles are a highly promising new anode material both from a fundamental and application point of view. Addition of graphene or carbon coating and/or special morphology will improve the cycling stability and is a topic of further investigations.

## 5. METHODS

**Synthesis.**  $\text{CoFeMnO}_4$  nanoparticles were synthesized by dissolving  $\text{Co}(\text{NO}_3)_2 \cdot 6\text{H}_2\text{O}$  (97%, Merck Millipore),  $\text{Fe}(\text{NO}_3)_3 \cdot 9\text{H}_2\text{O}$  (98%, Riedel-de Haen), and  $\text{Mn}(\text{NO}_3)_2 \cdot 4\text{H}_2\text{O}$  (98%, Grüssing) in 20 mL of deionized water. Nitric acid (5 mL, 65%, p.A., Grüssing) was added to the solution by stirring at room temperature. Afterward 10 mL of ethylene glycol (99%, Merck Millipore) was added, and the mixture was heated at 80 °C until a viscous gel formed. Afterward the gel was dried at 120 °C for 24 h. The solid was ground in an agate mortar and heated at 400 °C in a preheated oven in air for 3 h. The synthesis presented here is similar to that of  $\text{NiFeMnO}_4$  nanoparticles reported in ref 63.

**Materials Characterizations.** XRD patterns were recorded with an X'pert PRO diffractometer (PANalytical) equipped with a PIXcel detector using  $\text{Cu K}\alpha$  radiation. The refinement of the powder pattern was performed employing the fundamental parameter approach in combination with a Pawley fit using Topas Academic.<sup>64</sup> EDX spectra were collected in a Philips ESEM XL 30 with an EDAX New XL-30 Detecting Unit. An acceleration voltage of 20 kV was used to detect the K-lines. TEM investigations were performed with a Tecnai F30 G2-STwin microscope at 300 kV with a field emission gun cathode and a Si/Li detector (Thermo Fisher, NSS). For TEM investigations  $\text{CoFeMnO}_4$  nanoparticles were suspended in *n*-butanol and treated in ultrasonic bath to induce particle separation. Afterward the dispersion was dropped onto a holey-carbon copper grid.

**Electrochemical Measurements.** Electrochemical tests were performed in Swagelok cells. The cells were prepared by mixing 70 wt % active material with 20 wt % SUPER C65 Carbon (Timcal, Switzerland) and 10 wt % sodium carboxy methylcellulose (Sigma-Aldrich, Germany). The mixture was dispersed in deionized water, deposited on dendritic copper foil (Schlenk, Germany), and dried overnight at room temperature and at 80 °C for 24 h. Afterward 10 mm discs were cut with ~1 mg of active material. Lithium metal was used as counter electrode, glass microfiber filters (Whatman, United Kingdom) as the separator, and a solution of 1 M  $\text{LiPF}_6$  in an ethylene carbonate/dimethyl carbonate mixture (Merck, Germany) as electrolyte. The cells were assembled in an argon-filled glovebox (<1 ppm of  $\text{O}_2$ , <1 ppm of  $\text{H}_2\text{O}$ ) and were discharged/charged with a MMates 510 DC galvanostat.

**Operando X-ray Diffraction and X-ray Absorption Spectroscopy.** For operando XRD and XAS investigations a custom-built cell (40 × 40 × 15 mm) consisting of two aluminum plates with rectangular apertures (14 × 3 mm) in the center and two sheets of

Kapton foil windows glued on both sides was used. 80 wt % active material was mixed with 10 wt % SUPER C65 Carbon (Timcal, Switzerland) and 10 wt % polyvinylidene fluoride (Solvay, Germany). The mixture was suspended in *N*-methyl-2-pyrrolidone, deposited on 8  $\mu\text{m}$  Cu foil, and dried. Li metal as counter electrode was attached to a Cu foil. A microporous polyethylene/polypropylene membrane (Celgard 2325) was used as separator, and 1 M  $\text{LiPF}_6$  in an ethylene carbonate/dimethyl carbonate mixture was used as electrolyte. For operando XRD, the PDIFF beamline at synchrotron source ANKA (Karlsruhe, Germany) was operated at 16 keV ( $\lambda = 0.774901 \text{ \AA}$ ) with a Princeton CCD detector. Powder patterns were collected within 3 min. Reflections of copper were masked, and two-dimensional patterns were transformed with Area Diffraction Machine.<sup>65</sup> To determine the line profile of the instrument, a  $\text{LaB}_6$  standard material (NIST 660a) was measured under the same conditions. The operando XRD patterns were analyzed using Whole Powder Pattern Modeling macros implemented in TOPAS Academic 5.0.<sup>64,66</sup> The log-normal size distribution of the coherently scattering domains (modeled as spheres) are displayed in the Supporting Information (Figure S4). Additionally, the anisotropic [(*hkl*)-dependent] crystallite sizes were determined in combination with a Pawley Fit.<sup>67</sup> These results were utilized to model the crystallite morphologies.

Operando XAS analysis was performed at XAS beamline at ANKA applying repeated quick XAS scans at the Mn, Fe, and Co K-edges. The energy was calibrated with Fe foil before the experiment. Additional Mn, Fe, and Co reference foils were measured simultaneously between the second and third ionization chambers. Spectra were background-corrected, normalized,  $k^2$ -weighted, and Fourier transformed with the Athena Software package.<sup>68</sup> In situ cells were discharged/charged at a C/12 rate with a Biologic VSP 300 potentiostat/galvanostat. (C/12 rate corresponds to 12 h for the charge and discharge process, and the calculation is based on the theoretical capacity of 917 mAh  $\text{g}^{-1}$  corresponding to a current density of 77 mA  $\text{g}^{-1}$ ).

**Ex Situ Investigation by  $^7\text{Li}$  Nuclear Magnetic Resonance and Transmission Electron Microscopy.** For ex situ  $^7\text{Li}$  NMR investigations nanoparticles were mixed with SUPER C65 carbon and PVDF (80/10/10 wt %). Approximately 25 mg were pressed into 8 mm pellets and assembled in a Swagelok cell. The test cells were prepared with electrolyte, separator, and lithium as described above. After it reached the desired (overall) composition  $\text{Li}_x\text{CoFeMnO}_4$ , the discharge process was stopped, and the cells were opened in an argon-filled glovebox.  $^7\text{Li}$  MAS NMR spectroscopy was performed at room temperature on a Bruker Avance 200 MHz spectrometer at a magnetic field of 4.7 T corresponding to a Larmor frequency of  $\nu_L = 77.8 \text{ MHz}$ . A spinning speed of 60 kHz was applied using 1.3 mm rotors in a dry nitrogen atmosphere. An aqueous 1 M  $\text{LiCl}$  solution served as  $^7\text{Li}$  reference (0 ppm). The typical value for the recycling delay was 1 s.  $^7\text{Li}$  MAS NMR experiments were implemented with a rotor-synchronized Hahn-echo sequence ( $\pi/2 - \tau - \pi - \tau$ -acquisition) and a typical  $\pi/2$  pulse length of 2  $\mu\text{s}$ . For ex situ TEM investigations an in situ preparation method was used as described by Lin et al.<sup>69</sup> Instead of using coin cells we used Swagelok cells.

**Molecular Dynamics Simulations.** Molecular dynamics simulations were performed on a magnetite nanocube model using a 5 × 5 × 5 supercell as a starting point. The interatomic potentials were calculated on the basis of the 12–6 interaction model of Zhao et al. using explicit Coulomb summation.<sup>70</sup> Constant-temperature molecular dynamics simulations with a time step of 1 fs were performed at a variety of different temperature conditions ( $T = 300, 600, \text{ and } 900 \text{ K}$ ) to explore nanoparticle relaxation, which typically converged after less than 0.1 ns. After intercalation of five  $\text{Li}^+$  ions structural relaxation (using  $T = 300 \text{ K}$ ) and  $\text{Li}^+$  mobility were investigated at  $T = 600$  and 900 K from independent simulation runs each comprising 5 ns, respectively.

## ■ ASSOCIATED CONTENT

### ● Supporting Information

The Supporting Information is available free of charge on the ACS Publications website at DOI: 10.1021/acsami.6b03185.

SEM image of the as-prepared sample with corresponding EDX spectrum, EDX results, details of TEM investigations, detailed view on powder pattern after uptake of 2.5 Li per f.u., log-normal size distribution of as-prepared and sample after uptake of 2.5 Li per f.u., XAS spectra of CoMnFeO<sub>4</sub> and at the end of regions I, II, and III, ex situ XANES spectra, preparation of lithiated TEM samples, FFT TEM image, repeated cycling at high potentials (1.3–3.0 V) (PDF)

## ■ AUTHOR INFORMATION

### Corresponding Author

\*E-mail: wbensch@ac.uni-kiel.de.

### Author Contributions

The manuscript was written through contributions of all authors. All authors have given approval to the final version of the manuscript.

### Notes

The authors declare no competing financial interest.

## ■ ACKNOWLEDGMENTS

We are grateful to the Deutsche Forschungsgemeinschaft and to the German Federal Ministry of Education and Research for financial support. Beamtime allocation by ANKA (Karlsruhe) is thankfully acknowledged. We are also very thankful to Dr. S. Doyle and Dr. S. Mangold for their great support during experiments at ANKA PDIFF and XAS beamlines.

## ■ ABBREVIATIONS

LIB, lithium ion battery  
f.u., formula unit  
MD, molecular dynamics

## ■ REFERENCES

- Goodenough, J. B.; Park, K.-S. The Li-Ion Rechargeable Battery: A Perspective. *J. Am. Chem. Soc.* **2013**, *135*, 1167–1176.
- Panwar, N. L.; Kaushik, S. C.; Kothari, S. Role of Renewable Energy Sources in Environmental Protection: A Review. *Renewable Sustainable Energy Rev.* **2011**, *15*, 1513–1524.
- Whittingham, M. S. Ultimate Limits to Intercalation Reactions for Lithium Batteries. *Chem. Rev.* **2014**, *114*, 11414–11443.
- Scrosati, B.; Garche, J. Lithium Batteries: Status, Prospects and Future. *J. Power Sources* **2010**, *195*, 2419–2430.
- Wagemaker, M.; Mulder, F. M. Properties and Promises of Nanosized Insertion Materials for Li-Ion Batteries. *Acc. Chem. Res.* **2013**, *46*, 1206–1215.
- Kaus, M.; Issac, I.; Heinzmann, R.; Doyle, S.; Mangold, S.; Hahn, H.; Chakravadhanula, V. S. K.; Kübel, C.; Ehrenberg, H.; Indris, S. Electrochemical Delithiation/Relithiation of LiCoPO<sub>4</sub>: A Two-Step Reaction Mechanism Investigated by *in Situ* X-Ray Diffraction, *in Situ* X-Ray Absorption Spectroscopy, and *ex Situ* <sup>7</sup>Li/<sup>31</sup>P NMR Spectroscopy. *J. Phys. Chem. C* **2014**, *118*, 17279–17290.
- Bezza, I.; Kaus, M.; Heinzmann, R.; Yavuz, M.; Knapp, M.; Mangold, S.; Doyle, S.; Grey, C. P.; Ehrenberg, H.; Indris, S.; Saadoun, I. Mechanism of the Delithiation/Lithiation Process in LiFe<sub>0.4</sub>Mn<sub>0.6</sub>PO<sub>4</sub>: *in Situ* and *Ex Situ* Investigations on Long-Range and Local Structures. *J. Phys. Chem. C* **2015**, *119*, 9016–9024.
- Liu, H.; Strohbridge, F. C.; Borkiewicz, O. J.; Wiaderek, K. M.; Chapman, K. W.; Chupas, P. J.; Grey, C. P. Capturing Metastable Structures during High-Rate Cycling of LiFePO<sub>4</sub> Nanoparticle Electrodes. *Science* **2014**, *344*, 1252817–1252817.
- Zhang, X.; van Hulzen, M.; Singh, D. P.; Brownrigg, A.; Wright, J. P.; van Dijk, N. H.; Wagemaker, M. Direct View on the Phase Evolution in Individual LiFePO<sub>4</sub> Nanoparticles during Li-Ion Battery Cycling. *Nat. Commun.* **2015**, *6*, 8333.
- Zhang, X.; van Hulzen, M.; Singh, D. P.; Brownrigg, A.; Wright, J. P.; van Dijk, N. H.; Wagemaker, M. Rate-Induced Solubility and Suppression of the First-Order Phase Transition in Olivine LiFePO<sub>4</sub>. *Nano Lett.* **2014**, *14*, 2279–2285.
- Chueh, W. C.; El Gabaly, F.; Sugar, J. D.; Bartelt, N. C.; McDaniel, A. H.; Fenton, K. R.; Zavadil, K. R.; Tyliczszak, T.; Lai, W.; McCarty, K. F. Intercalation Pathway in Many-Particle LiFePO<sub>4</sub> Electrode Revealed by Nanoscale State-of-Charge Mapping. *Nano Lett.* **2013**, *13*, 866–872.
- Etacheri, V.; Marom, R.; Elazari, R.; Salitra, G.; Aurbach, D. Challenges in the Development of Advanced Li-Ion Batteries: A Review. *Energy Environ. Sci.* **2011**, *4*, 3243–3262.
- Li, D.; Zhou, H. Two-Phase Transition of Li-Intercalation Compounds in Li-Ion Batteries. *Mater. Today* **2014**, *17*, 451–463.
- Tarascon, J.-M.; Laruelle, S.; Grugeon, S.; Dupont, L.; Poizot, P. Nano-Sized Transition-Metal Oxides as Negative-Electrode Materials for LiB. *Nature* **2000**, *407*, 496–499.
- Reddy, M. V.; Subba Rao, G. V.; Chowdari, B. V. R. Metal Oxides and Oxyalts as Anode Materials for LiB. *Chem. Rev.* **2013**, *113*, 5364–5457.
- Cabana, J.; Monconduit, L.; Larcher, D.; Palacin, M. R. Beyond Intercalation-Based Li-Ion Batteries: The State of the Art and Challenges of Electrode Materials Reacting Through Conversion Reactions. *Adv. Mater.* **2010**, *22*, E170–E192.
- Rui, X.; Tan, H.; Yan, Q. Nanostructured Metal Sulfides for Energy Storage. *Nanoscale* **2014**, *6*, 9889–9924.
- Wang, F.; Robert, R.; Chernova, N. A.; Pereira, N.; Omenya, F.; Badway, F.; Hua, X.; Ruotolo, M.; Zhang, R.; Wu, L.; Volkov, V.; Su, D.; Key, B.; Whittingham, M. S.; Grey, C. P.; Amatucci, G. G.; Zhu, Y.; Graetz, J. Conversion Reaction Mechanisms in Lithium Ion Batteries: Study of the Binary Metal Fluoride Electrodes. *J. Am. Chem. Soc.* **2011**, *133*, 18828–18836.
- Bresser, D.; Paillard, E.; Kloepsch, R.; Krueger, S.; Fiedler, M.; Schmitz, R.; Baither, D.; Winter, M.; Passerini, S. Carbon Coated ZnFe<sub>2</sub>O<sub>4</sub> Nanoparticles for Advanced Lithium-Ion Anodes. *Adv. Energy Mater.* **2013**, *3*, 513–523.
- Lowe, M. A.; Gao, J.; Abruña, H. D. *In Operando* X-Ray Studies of the Conversion Reaction in Mn<sub>2</sub>O<sub>4</sub> Lithium Battery Anodes. *J. Mater. Chem. A* **2013**, *1*, 2094–2103.
- Permien, S.; Hain, H.; Scheuermann, M.; Mangold, S.; Mereacre, V.; Powell, A. K.; Indris, S.; Schürmann, U.; Kienle, L.; Duppel, V.; Harm, S.; Bensch, W. Electrochemical Insertion of Li into Nanocrystalline MnFe<sub>2</sub>O<sub>4</sub>: A Study of the Reaction Mechanism. *RSC Adv.* **2013**, *3*, 23001–23014.
- Permien, S.; Indris, S.; Scheuermann, M.; Schürmann, U.; Mereacre, V.; Powell, A. K.; Kienle, L.; Bensch, W. Is There a Universal Reaction Mechanism of Li Insertion into Oxidic Spinel: A Case Study Using MgFe<sub>2</sub>O<sub>4</sub>. *J. Mater. Chem. A* **2015**, *3*, 1549–1561.
- Permien, S.; Indris, S.; Schürmann, U.; Kienle, L.; Zander, S.; Doyle, S.; Bensch, W. What Happens Structurally and Electronically during the Li Conversion Reaction of CoFe<sub>2</sub>O<sub>4</sub> Nanoparticles: An *Operando* XAS and XRD Investigation. *Chem. Mater.* **2016**, *28*, 434–444.
- Liu, X.; Wang, D.; Liu, G.; Srinivasan, V.; Liu, Z.; Hussain, Z.; Yang, W. Distinct Charge Dynamics in Battery Electrodes Revealed by *in Situ* and *Operando* Soft X-Ray Spectroscopy. *Nat. Commun.* **2013**, *4*, 2568.
- Marino, C.; Fraise, B.; Womes, M.; Villevieille, C.; Monconduit, L.; Stievano, L. At the Heart of a Conversion Reaction An *Operando* X-ray Absorption Spectroscopy Investigation of NiSb<sub>2</sub>, a Negative Electrode Material for Li-Ion Batteries. *J. Phys. Chem. C* **2014**, *118*, 27772–27780.



- (26) Boesenberg, U.; Marcus, M. A.; Shukla, A. K.; Yi, T.; McDermott, E.; Teh, P. F.; Srinivasan, M.; Moewes, A.; Cabana, J. Asymmetric Pathways in the Electrochemical Conversion Reaction of NiO as Battery Electrode with High Storage Capacity. *Sci. Rep.* **2014**, *4*, 7133.
- (27) Wu, Z.-S.; Ren, W.; Wen, L.; Gao, L.; Zhao, J.; Chen, Z.; Zhou, G.; Li, F.; Cheng, H.-M. Graphene Anchored with Co<sub>3</sub>O<sub>4</sub> Nanoparticles as Anode of Lithium Ion Batteries with Enhanced Reversible Capacity and Cyclic Performance. *ACS Nano* **2010**, *4*, 3187–3194.
- (28) Gao, J.; Lowe, M. A.; Abruña, H. D. Spongelike Nanosized Mn<sub>3</sub>O<sub>4</sub> as a High-Capacity Anode Material for Rechargeable Lithium Batteries. *Chem. Mater.* **2011**, *23*, 3223–3227.
- (29) Zhou, G.; Wang, D.-W.; Li, F.; Zhang, L.; Li, N.; Wu, Z.-S.; Wen, L.; Lu, G. Q.; Cheng, H.-M. Graphene-Wrapped Fe<sub>3</sub>O<sub>4</sub> Anode Material with Improved Reversible Capacity and Cyclic Stability for Lithium Ion Batteries. *Chem. Mater.* **2010**, *22*, 5306–5313.
- (30) Yoon, S. Facile Microwave Synthesis of CoFe<sub>2</sub>O<sub>4</sub> Spheres and Their Application as an Anode for Lithium-Ion Batteries. *J. Appl. Electrochem.* **2014**, *44*, 1069–1074.
- (31) Yao, X.; Kong, J.; Tang, X.; Zhou, D.; Zhao, C.; Zhou, R.; Lu, X. Facile Synthesis of Porous CoFe<sub>2</sub>O<sub>4</sub> Nanosheets for Lithium-Ion Battery Anodes with Enhanced Rate Capability and Cycling Stability. *RSC Adv.* **2014**, *4*, 27488–27492.
- (32) Cherian, C. T.; Sundaramurthy, J.; Reddy, M. V.; Suresh Kumar, P.; Mani, K.; Pliszka, D.; Sow, C. H.; Ramakrishna, S.; Chowdari, B. V. R. Morphologically Robust NiFe<sub>2</sub>O<sub>4</sub> Nanofibers as High Capacity Li-Ion Battery Anode Material. *ACS Appl. Mater. Interfaces* **2013**, *5*, 9957–9963.
- (33) Xiao, Y.; Zai, J.; Tao, L.; Li, B.; Han, Q.; Yu, C.; Qian, X. MnFe<sub>2</sub>O<sub>4</sub>-graphene Nanocomposites with Enhanced Performances as Anode Materials for Li-Ion Batteries. *Phys. Chem. Chem. Phys.* **2013**, *15*, 3939–3945.
- (34) Lin, L.; Pan, Q. ZnFe<sub>2</sub>O<sub>4</sub>@C/graphene Nanocomposites as Excellent Anode Materials for Lithium Batteries. *J. Mater. Chem. A* **2015**, *3*, 1724–1729.
- (35) Wang, G.; Chen, R.; Zhou, Y.; Wang, H.; Bai, J. One-Pot Template-Free Fabrication of ZnMn<sub>2</sub>O<sub>4</sub> Hollow Microspheres as High-Performance Lithium-Ion Battery Anodes. *J. Nanopart. Res.* **2014**, *16*, 2300.
- (36) Zhang, Z.; Wang, Y.; Zhang, M.; Tan, Q.; Lv, X.; Zhong, Z.; Su, F. Mesoporous CoFe<sub>2</sub>O<sub>4</sub> Nanospheres Cross-Linked by Carbon Nanotubes as High-Performance Anodes for Lithium-Ion Batteries. *J. Mater. Chem. A* **2013**, *1*, 7444–7450.
- (37) Wang, N.; Xu, H.; Chen, L.; Gu, X.; Yang, J.; Qian, Y. A General Approach for MFe<sub>2</sub>O<sub>4</sub> (M = Zn, Co, Ni) Nanorods and Their High Performance as Anode Materials for Lithium Ion Batteries. *J. Power Sources* **2014**, *247*, 163–169.
- (38) Lavela, P.; Kyeremateng, N. A.; Tirado, J. L. NiMn<sub>2-x</sub>Fe<sub>x</sub>O<sub>4</sub> Prepared by a Reverse Micelles Method as Conversion Anode Materials for Li-Ion Batteries. *Mater. Chem. Phys.* **2010**, *124*, 102–108.
- (39) Zhang, G.; Lou, X. W. D. General Synthesis of Multi-Shelled Mixed Metal Oxide Hollow Spheres with Superior Lithium Storage Properties. *Angew. Chem., Int. Ed.* **2014**, *53*, 9041–9044.
- (40) Zhou, L.; Zhao, D.; Lou, X. W. Double-Shelled CoMn<sub>2</sub>O<sub>4</sub> Hollow Microcubes as High-Capacity Anodes for Lithium-Ion Batteries. *Adv. Mater.* **2012**, *24*, 745–748.
- (41) Wu, L.; Xiao, Q.; Li, Z.; Lei, G.; Zhang, P.; Wang, L. CoFe<sub>2</sub>O<sub>4</sub>/C Composite Fibers as Anode Materials for Lithium-Ion Batteries with Stable and High Electrochemical Performance. *Solid State Ionics* **2012**, *215*, 24–28.
- (42) Lu, Z. M.; Li, Z. W.; Shen, J.; Meng, F. B.; Liu, H. Y.; Li, Y. X.; Li, C. Y. Magnetic and Structural Properties of Co<sub>0.8</sub>Mn<sub>x</sub>Fe<sub>2.2-x</sub>O<sub>4</sub> (x = 0.2, 0.4, 0.6, 0.8) Polycrystalline Powders Synthesized by Sol-Gel Process. *J. Appl. Phys.* **2009**, *105*, 519–520.
- (43) Oudhiri-Hassani, F.; Presmanes, L.; Barnabe, A.; Tailhades, P. Microstructural Characterization of CoMnFeO<sub>4</sub> Thin Films Deposited by Radio-Frequency Sputtering. *MATEC Web Conf.* **2013**, *5*, 04041.
- (44) Goyal, A.; Bansal, S.; Singh, J.; Singhal, S. Mn Substituted Cobalt Ferrites (CoMn<sub>x</sub>Fe<sub>2-x</sub>O<sub>4</sub> (x = 0.0, 0.2, 0.4, 0.6, 0.8, 1.0)) As Magnetically Separable Heterogeneous Nanocatalyst for Thereduction of Nitrophenols. *Appl. Surf. Sci.* **2015**, *324*, 877–889.
- (45) Jauhar, S.; Singhal, S.; Dhiman, M. Manganese Substituted Cobalt Ferrites as Efficient Catalysts for H<sub>2</sub>O<sub>2</sub> Assisted Degradation of Cationic and Anionic Dyes: Their Synthesis and Characterization. *Appl. Catal., A* **2014**, *486*, 210–218.
- (46) Chassaing, I.; Presmanes, L.; Tailhades, P.; Rousset, A. Submicron Mn<sub>x</sub>Co<sub>1-x</sub>Fe<sub>2-x</sub>O<sub>4</sub> Spinel Ferrites Cationic Distribution and Reactivity. *Solid State Ionics* **1992**, *58*, 261–267.
- (47) Laruelle, S.; Grugeon, S.; Poizot, P.; Dollé, M.; Dupont, L.; Tarascon, J.-M. On the Origin of the Extra Electrochemical Capacity Displayed by MO/Li Cells at Low Potential. *J. Electrochem. Soc.* **2002**, *149*, A627–A634.
- (48) Ponrouch, A.; Taberna, P.-L.; Simon, P.; Palacin, M. R. On the Origin of the Extra Capacity at Low Potential in Materials for Li Batteries Reacting through Conversion Reaction. *Electrochim. Acta* **2012**, *61*, 13–18.
- (49) Maier, J. Nanoionics: Ion Transport and Electrochemical Storage in Confined Systems. *Nat. Mater.* **2005**, *4*, 805–815.
- (50) Zhang, Z. J.; Wang, Z. L.; Chakoumakos, B. C.; Yin, J. S. Temperature Dependence of Cation Distribution and Oxidation State in Magnetic Mn-Fe Ferrite Nanocrystals. *J. Am. Chem. Soc.* **1998**, *120*, 1800–1804.
- (51) Carta, D.; Casula, M. F.; Falqui, A.; Loche, D.; Mountjoy, G.; Sangregorio, C.; Corrias, A. A Structural and Magnetic Investigation of the Inversion Degree in Ferrite Nanocrystals MFe<sub>2</sub>O<sub>4</sub> (M = Mn, Co, Ni). *J. Phys. Chem. C* **2009**, *113*, 8606–8615.
- (52) Aitchison, P.; Ammundsen, B.; Jones, D. J.; Burns, G.; Rozière, J. Cobalt Substitution in Lithium Manganate Spinels: Examination of Local Structure and Lithium Extraction by XAFS. *J. Mater. Chem.* **1999**, *9*, 3125–3130.
- (53) Artus, M.; Ben Tahar, L.; Herbst, F.; Smiri, L.; Villain, F.; Yaacoub, N.; Grenèche, J.-M.; Ammar, S.; Fiévet, F. Size-Dependent Magnetic Properties of CoFe<sub>2</sub>O<sub>4</sub> Nanoparticles Prepared in Polyol. *J. Phys.: Condens. Matter* **2011**, *23*, S06001.
- (54) Zhong, K.; Zhang, B.; Luo, S.; Wen, W.; Li, H.; Huang, X.; Chen, L. Investigation on Porous MnO Microsphere Anode for Lithium Ion Batteries. *J. Power Sources* **2011**, *196*, 6802–6808.
- (55) Jain, G.; Balasubramanian, M.; Xu, J. J. Structural Studies of Lithium Intercalation in a Nanocrystalline α-Fe<sub>2</sub>O<sub>3</sub> Compound. *Chem. Mater.* **2006**, *18*, 423–434.
- (56) Chadwick, A. V.; Savin, S. L. P.; Fiddy, S.; Alcantara, R.; FernandezLisbona, D.; Lavela, P.; Ortiz, G. F.; Tirado, J. L. Formation and Oxidation of Nanosized Metal Particles by Electrochemical Reaction of Li and Na with NiCo<sub>2</sub>O<sub>4</sub>: X-Ray Absorption Spectroscopic Study. *J. Phys. Chem. C* **2007**, *111*, 4636–4642.
- (57) Grey, C. P.; Dupré, N. NMR Studies of Cathode Materials for Lithium-Ion Rechargeable Batteries. *Chem. Rev.* **2004**, *104*, 4493–4512.
- (58) Lin, F.; Nordlund, D.; Li, Y.; Quan, M. K.; Cheng, L.; Weng, T.-C.; Liu, Y.; Xin, H. L.; Doeff, M. M. Metal Segregation in Hierarchically Structured Cathode Materials for High-Energy Lithium Batteries. *Nat. Energy* **2016**, *1*, 15004.
- (59) Thackeray, M. M.; David, W. I. F.; Goodenough, J. B. Structural Characterization of the Lithiaed Iron Oxides Li<sub>x</sub>Fe<sub>3-x</sub>O<sub>4</sub> and Li<sub>x</sub>Fe<sub>2-x</sub>O<sub>3</sub> (0 < x < 2). *Mater. Res. Bull.* **1982**, *17*, 785–793.
- (60) Chen, C.; Greenblatt, M.; Waszczak, J. Lithium Insertion into Spinel Ferrites. *Solid State Ionics* **1986**, *18–19*, 838–846.
- (61) Thackeray, M. M.; David, W. I. F.; Bruce, P. G.; Goodenough, J. B. Lithium Insertion into Manganese Spinels. *Mater. Res. Bull.* **1983**, *18*, 461–472.
- (62) Thackeray, M.; Baker, S.; Adendorff, K.; Goodenough, J. Lithium Insertion into Co<sub>3</sub>O<sub>4</sub>: A Preliminary Investigation. *Solid State Ionics* **1985**, *17*, 175–181.
- (63) Khosravi, I.; Yazdanbakhsh, M.; Goharshadi, E. K.; Youssefi, A. Preparation of Nanospinel NiMn<sub>x</sub>Fe<sub>2-x</sub>O<sub>4</sub> Using Sol-gel Method and Their Applications on Removal of Azo Dye from Aqueous Solutions. *Mater. Chem. Phys.* **2011**, *130*, 1156–1161.
- (64) Coelho, A. A. *Topas Academic*; Coelho Software, 2012.

(65) Lande, J. *Area Diffraction Machine*; 2013. Free and open-source software available online.

(66) Leoni, M.; Maggio, R.; Polizzi, S.; Scardi, P. X-Ray Diffraction Methodology for the Microstructural Analysis of Nanocrystalline Powders: Application to Cerium Oxide. *J. Am. Ceram. Soc.* **2004**, *87*, 1133–1140.

(67) Evans, J. S. O. Advanced Input Files & Parametric Quantitative Analysis Using Topas. *Mater. Sci. Forum* **2010**, *651*, 1–9.

(68) Ravel, B.; Newville, M. *ATHENA*, *ARTEMIS*, *HEPHAESTUS*: Data Analysis for X-Ray Absorption Spectroscopy Using *IFEFFIT*. *J. Synchrotron Radiat.* **2005**, *12*, 537–541.

(69) Lin, F.; Nordlund, D.; Weng, T.-C.; Zhu, Y.; Ban, C.; Richards, R. M.; Xin, H. L. Phase Evolution for Conversion Reaction Electrodes in Lithium-Ion Batteries. *Nat. Commun.* **2014**, *5*, 3358–3367.

(70) Zhao, L.; Liu, L.; Sun, H. Semi-Ionic Model for Metal Oxides and Their Interfaces with Organic Molecules. *J. Phys. Chem. C* **2007**, *111*, 10610–10617.



### 3.5 The role of reduced graphite oxide in transition metal oxide nanocomposites used as anode material: A case study on $\text{CoFe}_2\text{O}_4/\text{rGO}$

Spinel oxide nanoparticles were deposited on reduced graphite oxide (rGO), which is an efficient method to stabilize the capacity over many cycles. In this publication the excellent cycling stability for  $\text{CoFe}_2\text{O}_4/\text{rGO}$  is presented with the focus on the elucidation of the reaction mechanisms. Combining synchrotron radiation based *operando* X-ray diffraction (XRD) and X-ray absorption spectroscopy (XAS) allowed following the structural alterations on different length scales and monitoring changes of the electronic states of the metal ions during Li uptake and release. The results are supported by *ex situ* XAS and TEM. On the basis of all results a detailed reaction mechanism for Li uptake and release of  $\text{CoFe}_2\text{O}_4$  nanoparticles on rGO was formulated. The pathway of the discharging reaction starts with uptake of a small amount of Li on the surface of the nanoparticles and rGO respectively. After uptake of 2.5 Li per formula unit, rock salt structured monoxide  $\text{Co}_{1/3}\text{Fe}_{2/3}\text{O}$  is formed. Further Li uptake leads to successive formation of amorphous Co and Fe metal nanoparticles embedded in a  $\text{Li}_2\text{O}$  matrix. After the charge process metallic Co and Fe nanoparticles are oxidized to  $\text{Fe}^{3+}$  and  $\text{Co}^{2+}$ . This behaviour of the nanoparticles in  $\text{CoFe}_2\text{O}_4/\text{rGO}$  is similar to pure  $\text{CoFe}_2\text{O}_4$  nanoparticles. The reduced graphite oxide does not influence the reaction mechanism of the nanoparticles, but rGO seems to compensate the volume expansion occurring during the reactions thus improving the electronic conductivity between the formed species. The positive effect is visible during further cycling. The redox reactions  $\text{Co}^0 \leftrightarrow \text{Co}^{2+}$  and  $\text{Fe}^0 \leftrightarrow \text{Fe}^{3+}$  are stable over many cycles, in striking contrast to studies on  $\text{CoFe}_2\text{O}_4$  without rGO where metallic Co could not be oxidized during extended cycling. Even after many cycles Fe and Co are homogeneously dispersed over the rGO sheets, and a phase separation postulated on the basis of CV by other groups can be excluded. *Operando* Raman spectra show that rGO is not destroyed during cycling.

# The role of reduced graphite oxide in transition metal oxide nanocomposites used as Li anode material: An *operando* study on CoFe<sub>2</sub>O<sub>4</sub>/rGO

Stefan Permien<sup>a)</sup>, Sylvio Indris<sup>b)</sup>, Gero Neubüser<sup>c)</sup>, Andy Fiedler<sup>b)</sup>, Lorenz Kienle<sup>c)</sup>, Stefan Zander<sup>d)</sup>, Stephen Doyle<sup>e)</sup>, Björn Richter<sup>a)</sup>, Wolfgang Bensch<sup>\*a)</sup>

**Abstract:** A composite consisting of CoFe<sub>2</sub>O<sub>4</sub> spinel nanoparticles and reduced graphite oxide (rGO) was studied as anode material during Li uptake and release applying synchrotron *operando* X-ray diffraction (XRD) and *operando* X-ray absorption spectroscopy (XAS) yielding a comprehensive picture of the reaction mechanisms. At the early stages of Li uptake a monoxide is formed as intermediate phase containing Fe<sup>2+</sup> and Co<sup>2+</sup> ions, an observation which is in contrast to reaction pathways proposed in literature. At the fully discharged state metallic Co and Fe nanoparticles are embedded in an amorphous Li<sub>2</sub>O matrix. During charge metallic Co and Fe are simultaneously oxidized to Co<sup>2+</sup> resp. Fe<sup>3+</sup> thus enabling a high and stable capacity. Here we present evidences that the rGO acts as support for the nanoparticles and prevents the particles from contact loss. The *operando* investigations are complemented by TEM, Raman spectroscopy, galvanostatic cycling and cyclic voltammetry.

## Introduction

During the intense search for lithium ion batteries (LIBs) exhibiting larger capacities than commercially available cathode/anodes, so called conversion materials were identified as promising new electrode materials.<sup>[1–6]</sup> These materials are characterized by high specific capacities of about 800 mAh g<sup>-1</sup>

caused by cycling of more than 1 Li/formula unit. A promising group of compounds are oxidic spinels of the type AB<sub>2</sub>O<sub>4</sub> (A = Co, Fe, Mn, Ni, Zn; B = Fe, Co, Mn) with redox active cations.<sup>[7–19]</sup> During the first discharge the constituents of initially crystalline or nanocrystalline materials are fully reduced and nanosized or amorphous metallic nanoparticles are formed being embedded in a Li<sub>2</sub>O matrix.<sup>[7]</sup>

Despite the promising capacities the materials have several drawbacks like strong capacity fading and large volume changes during cycling.<sup>[20]</sup> Furthermore, the nanoparticles formed during discharge are characterized by a large surface area and SEI (solid electrolyte interphase) formation leads to unwanted consumption of Li and electrolyte making the materials less attractive. Often graphene, reduced graphite oxide (rGO) or other carbon materials are added to the active material leading often to much better cyclability.<sup>[21–32]</sup> It is assumed that graphene helps to keep electrical contact to the metallic nanoparticles in the matrix which was already demonstrated for CoFe<sub>2</sub>O<sub>4</sub>/rGO.<sup>[23,33–37]</sup> Hence, explanations for the benefits of the carbon materials are often given as synergistic effects without detailing the impact on the reaction mechanisms occurring during discharge and charge reactions.<sup>[38,39]</sup> It is well documented that the combination of *in situ*, *operando* and *ex situ* experiments performed during Li uptake and release yields a wealth of information about structural and electronic changes occurring during the chemical reactions.<sup>[40–49]</sup>

We investigated a CoFe<sub>2</sub>O<sub>4</sub>/rGO composite during Li uptake and release with *operando* X-ray diffraction (XRD), X-ray absorption spectroscopy (XAS) and *operando* Raman spectroscopy to gain insights into the complex mechanisms of the conversion reactions. The combination of these techniques enables detection of long-range and short-range structural changes as well as of the alteration of electronic properties. The characterization of the materials is further complemented by electrochemical studies, *ex situ* TEM and XAS yielding finally a comprehensive picture about the reaction mechanism.

## Results Characterisation of the pristine material

The X-ray powder patterns of as-prepared nanosized CoFe<sub>2</sub>O<sub>4</sub> and CoFe<sub>2</sub>O<sub>4</sub>/rGO were refined with the fundamental parameter approach implemented in the TOPAS software<sup>[50]</sup> (Figure 1). Both samples crystallize in the cubic spinel-type structure (*Fd*3̄*m*). A volume-weighted average domain size for both CoFe<sub>2</sub>O<sub>4</sub> and CoFe<sub>2</sub>O<sub>4</sub>/rGO of 5.8(1) nm was determined. The lattice

- [a] S. Permien, B. Richter, Prof. Dr. W. Bensch  
Institute of Inorganic Chemistry  
University of Kiel  
Max-Eyth-Str. 2, 24118 Kiel (Germany)  
E-mail: wbensch@ac.uni-kiel.de
- [b] Dr. S. Indris, Andy Fiedler  
Institute for Applied Materials - Energy Storage Systems  
Karlsruhe Institute of Technology  
P.O. Box 3640, 76021 Karlsruhe (Germany)
- [c] Gero Neubüser, Prof. Dr. L. Kienle  
Institute for Materials Science  
University of Kiel  
Kaiserstr. 2, 24143 Kiel (Germany)
- [d] Dr. S. Zander  
Helmholtz-Zentrum Berlin  
Helmholtz-Zentrum Berlin für Materialien und Energie  
Hahn-Meitner-Platz 1, 14109 Berlin (Germany)
- [e] Dr. S. Doyle  
ANKA Synchrotron Radiation Facility  
Karlsruhe Institute of Technology  
P.O. Box 3640, 76021 Karlsruhe (Germany)
- Supporting information for this article is given via a link at the end of the document

parameters  $a$  were refined as 8.355(2) Å for  $\text{CoFe}_2\text{O}_4$  and 8.386(2) Å for  $\text{CoFe}_2\text{O}_4/\text{rGO}$ . The EDX data measured the expected ratio of 1.0:2.0 for Co:Fe (ESI, Table S1). The elemental analysis of  $\text{CoFe}_2\text{O}_4/\text{rGO}$  yields a C content of 14 wt % (ESI, Table S2).

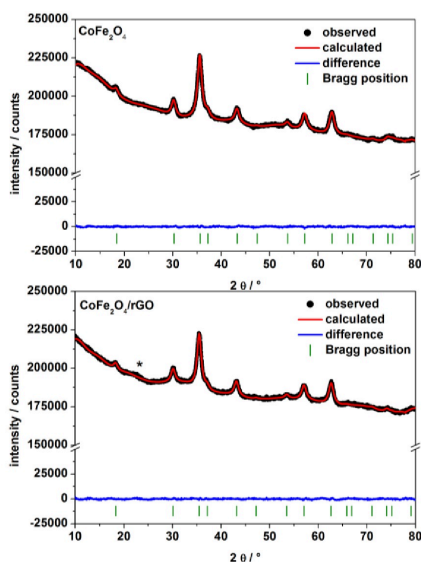


**Figure 1.** Rietveld refinement performed on as-prepared  $\text{CoFe}_2\text{O}_4$  (top) and  $\text{CoFe}_2\text{O}_4/\text{rGO}$  (bottom) with observed powder pattern (black), calculated pattern (red), difference curve (blue) and Bragg positions (green bars). The modulation of the background marked with "\*" can be attributed to graphene layer in the  $\text{CoFe}_2\text{O}_4/\text{rGO}$ .

High resolution transmission electron microscopy (HRTEM) images of  $\text{CoFe}_2\text{O}_4/\text{rGO}$  (Figure 2) display graphene layers.  $\text{CoFe}_2\text{O}_4$  nanoparticles are distributed on the reduced rGO but also next to the graphene layers. The EDX analyses yield a Fe:Co ratio of 2:1 and the SAED (selected area electron diffraction) pattern confirms the spinel-type crystal structure of the particles.

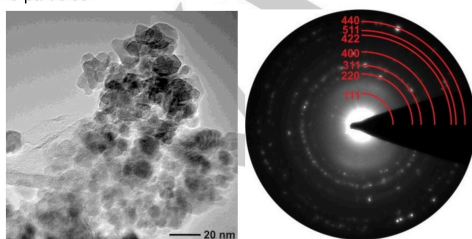


**Figure 2.** TEM micrograph of the  $\text{CoFe}_2\text{O}_4/\text{rGO}$  composite (left) and SAED pattern of the spinel (right).

The Raman spectra (Figure 3) of  $\text{CoFe}_2\text{O}_4/\text{rGO}$  nanoparticles display several bands of the cobalt ferrite spinel.<sup>[51]</sup> The D band of rGO caused by the breathing mode or  $\kappa$ -point phonons of  $A_{1g}$  symmetry is located at  $1346\text{ cm}^{-1}$ , while the G mode (first order of scattering of the  $E_{2g}$  photons) is observed at  $1594\text{ cm}^{-1}$  (see also ESI, Fig S1). These values are similar to pure rGO and those reported in literature for  $\text{MFe}_2\text{O}_4/\text{rGO}$  ( $M = \text{Co}$  and  $\text{Mn}$ ).<sup>[22,23,36,37]</sup>

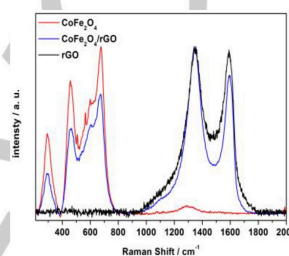


**Figure 3.** Raman spectra of  $\text{CoFe}_2\text{O}_4/\text{rGO}$  (blue), pure  $\text{CoFe}_2\text{O}_4$  (red) and rGO (black).

### Electrochemical performance

The theoretical capacity of  $\text{CoFe}_2\text{O}_4$  is  $914\text{ mAh g}^{-1}$  and for graphene  $744\text{ mAh g}^{-1}$  when Li ions are attached on both sides of the graphene layers.<sup>[52]</sup> On the basis of the C content the theoretical capacity of  $\text{CoFe}_2\text{O}_4/\text{rGO}$  is  $890\text{ mAh g}^{-1}$  ( $744\text{ mAh g}^{-1} \times 0.14 + 914\text{ mAh g}^{-1} \times 0.86 = 890\text{ mAh g}^{-1}$ ). The potential curve during the first discharge differs for the two materials (Figure 4 A): the potential drops faster to 0.8 V for pure  $\text{CoFe}_2\text{O}_4$  compared to  $\text{CoFe}_2\text{O}_4/\text{rGO}$  indicating different reaction mechanisms. After uptake of ca. 2.5 Li ( $\text{CoFe}_2\text{O}_4$ ) respectively 4 Li ( $\text{CoFe}_2\text{O}_4/\text{rGO}$ ) per formula unit a plateau is observed at 0.8 V. After conversion of 8 Li/f.u. the potential drops to 0.1 V for both materials ( $\sim 916\text{ mAh g}^{-1}$ ). The initial discharge capacities for both materials are significantly larger than the theoretical values, a phenomenon well documented in literature.<sup>[23,36,37,53–56]</sup> The potential curve during charging (Li release) is quite similar for both materials and reversible charge capacities for the first cycle are  $924\text{ mAh g}^{-1}$  ( $\text{CoFe}_2\text{O}_4$ ) and  $903\text{ mAh g}^{-1}$  ( $\text{CoFe}_2\text{O}_4/\text{rGO}$ ). Both values are slightly larger than theoretical values which is caused by reversible electrolyte decomposition and/or charge storage at the large surface of nanoparticles and graphene layers.<sup>[57–59]</sup> The formation of the SEI leads to the irreversible capacity loss.<sup>[60]</sup>

Figure 4 B displays the evolution of the capacities during repeated cycling in a potential range from 0.1 to 3.0 V (C/5 rate).  $\text{CoFe}_2\text{O}_4$  exhibits a higher capacity during the first 20 cycles than  $\text{CoFe}_2\text{O}_4/\text{rGO}$  in agreement with the smaller theoretical capacity of the latter. During cycling the two materials behave significantly different: for  $\text{CoFe}_2\text{O}_4$  a continuous decrease is

observed reaching  $< 400 \text{ mAh g}^{-1}$  after 90 cycles, while for  $\text{CoFe}_2\text{O}_4/\text{rGO}$  the capacity remains nearly stable after 10 cycles at about  $700 \text{ mAh g}^{-1}$ . Pure rGO (Fig. 4 B) shows also a strong capacity fading to less than  $400 \text{ mAh g}^{-1}$  after 90 cycles. Obviously, the composite  $\text{CoFe}_2\text{O}_4/\text{rGO}$  exhibits a much better cycling stability than  $\text{CoFe}_2\text{O}_4$ , which is in agreement with literature reports.<sup>[23,36,37,39]</sup>

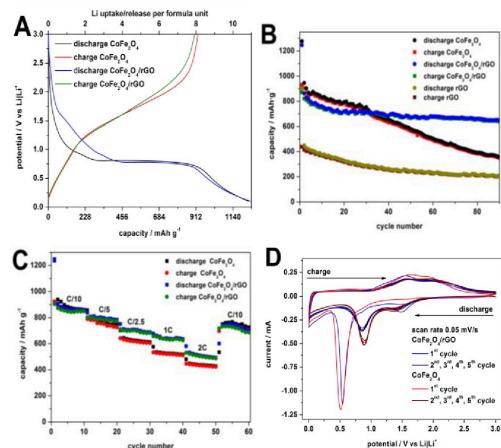


**Figure 4.** Electrochemical performance of  $\text{CoFe}_2\text{O}_4$  and  $\text{CoFe}_2\text{O}_4/\text{rGO}$ : First cycle measured from 0.1–3.0 V at a C/10 rate (A); 1  $\text{Li}/\text{CoFe}_2\text{O}_4 = 114 \text{ mAh/g}$ , 90 cycles measured from 0.1–3.0 V at a C/5 rate (B), 10 cycles each measured from 0.1–3.0 V at C/10, C/5, C/2.5, 1C, 2C and C/10 rate (C), CV in a potential range from 0–3 V at a scan rate of  $0.05 \text{ mVs}^{-1}$  (D).

Fast charging/discharging is important for electrodes, which is investigated by cycling at different C-rates (Fig. 4 C). For C/10 and C/5 the capacity of both materials is nearly identical, but at C/2, 1C and 2C rates the composite has a much better performance than  $\text{CoFe}_2\text{O}_4$ . Switching back to C/10 after 2C, the capacity at C/10 is slightly reduced but still at about  $800 \text{ mAh g}^{-1}$ . In summary, the addition of rGO increases the long-term cycling stability and enables faster discharge/charge capabilities with reasonably high capacities.

The cyclic voltammogram (CV) of  $\text{CoFe}_2\text{O}_4$  and  $\text{CoFe}_2\text{O}_4/\text{rGO}$  (Figure 4 D) exhibit weak signals at 1.4, 0.8 V and a strong peak at 0.6 V during first discharge, while during charging a very broad signal at 1.5 and 2.0 V is observed during all charging processes indicating an overlap of more than one signal due to more than one redox process. After the first cycle signals of the discharge process are now located at 1.3 and 0.9 V signalling the formation of new products. During further cycling these new products are reversibly charged/discharged. A comparison of the CV curves of  $\text{CoFe}_2\text{O}_4$  and  $\text{CoFe}_2\text{O}_4/\text{rGO}$  evidences similar signals and shapes.<sup>[36,56]</sup> The observations made in the CV diagrams indicate that the reaction mechanisms do not differ significantly for the two materials.

## Operando XRD

Rietveld refinement of the XRD patterns collected during first discharge of  $\text{CoFe}_2\text{O}_4/\text{rGO}$  (Figure 5) yields similar data as obtained with laboratory equipment (section 3.1,  $a$  axis =  $8.386(1) \text{ \AA}$ ,  $d_{\text{domain}} = 6.1(1) \text{ nm}$ ). During uptake/insertion of the first  $\sim 0.4 \text{ Li}$  per formula unit (first five scans) the intensity of the reflections is constant which is demonstrated for the (311) reflection (Figure 5, bottom left). Increasing the Li/f.u. leads to a decrease of the intensities of the (311) and (511) reflections (Figure 5) and adjacent to the (311) reflection develops (Figure 5, bottom left). After uptake of about 2.5 Li/f.u. only the new reflections are observed which can be assigned to a monoxide phase with NaCl-type structure (Figure 5, red powder pattern). The spinel is successively transformed starting from 0.5  $\text{Li}/\text{CoFe}_2\text{O}_4$  and is fully converted at about 2.5  $\text{Li}/\text{CoFe}_2\text{O}_4$ . The NaCl-type structure is easily formed in the spinel because the structural arrangement of empty and occupied octahedra corresponds to NaCl (space group:  $Fm\bar{3}m$ ). During Li uptake the cations on the tetrahedral sites move to empty octahedra, accompanied by simultaneous reduction of  $\text{Fe}^{3+}$  to  $\text{Fe}^{2+}$ . Simultaneously,  $\text{Li}_2\text{O}$  is formed with the  $\text{Li}^+$  ions being in a tetrahedral environment of  $\text{O}^{2-}$  anions. It is remarkable that the size of coherently scattering domains of the monoxide is identical with that of the starting material ( $d_{\text{domain}} = 6.1(1) \text{ nm}$ ).

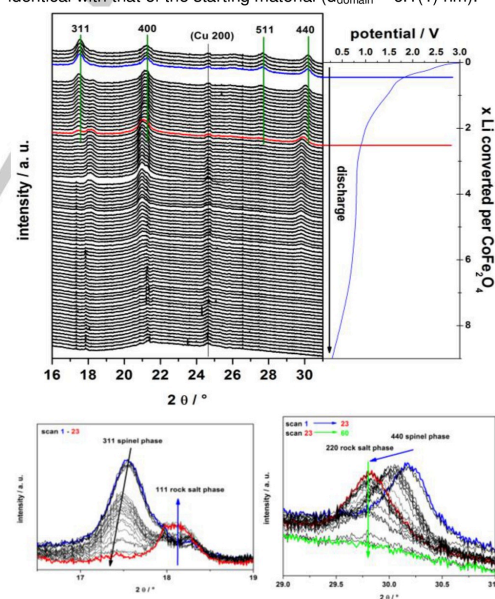


**Figure 5.** Operando XRD scans (top, left) during first discharge and potential of the *in situ* cell (top, right). After the first five scans, the following four scans are missing due to beamdump of the synchrotron source. Detailed view on 29



range 16.5–19° during scans 1–23 (uptake of 2 Li per formula unit, bottom left) and 29–31° during scans 1–60 (only every third scan is shown, bottom right)

The refined lattice parameter of the monoxide ( $a = 4.243(1)$  Å, ESI, Figure S2) does not allow deciding whether a mixed monoxide  $\text{Co}_x\text{Fe}_y\text{O}$  is formed or separated  $\text{Fe}_{1-x}\text{O}$  and  $\text{CoO}$  phases coexist (CoO:  $a = 4.240$  Å<sup>[61]</sup> and FeO:  $a = 4.2816$  Å<sup>[62]</sup>; note: the value depends on the Fe:O ratio). Thermodynamic data indicate that formation of  $\text{Co}_x\text{Fe}_y\text{O}$  requires high temperatures, *i.e.* on a first the presence of  $\text{Co}_x\text{Fe}_y\text{O}$  seems to be improbable.<sup>[63]</sup> But the symmetric shape of the reflections in X-ray powder patterns points towards a single phase (ESI, Figure S3). But a phase separation would require a concerted movement of  $\text{Co}^{2+}$  and  $\text{Fe}^{2+}$  ions to empty octahedra which have neighbored octahedra being occupied by  $\text{Co}^{2+}$  and  $\text{Fe}^{2+}$ , respectively, a scenario which seems not to be realistic. During the long plateau at 0.8 V the monoxide is successively converted as evidenced by the significant decrease of the reflection intensities and after uptake of further 7 Li/f.u. the material is fully converted into a nanosized phase or particles smaller than the coherence length of the X-rays. Very similar results were reported for several nanosized spinels.<sup>[64,46,47,65,48]</sup>

### Operando XAS

X-ray diffraction experiments give no information about the alteration of the electronic situation. *Operando* XAS was performed to gain insights into the variation of the local environment of the absorbers and the change of chemical states. The potential curve was recorded during the XAS experiments showing no pronounced difference to that obtained in the Swagelok cells (Figure 6).

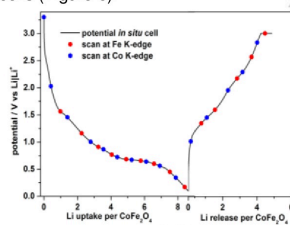


**Figure 6.** Cell potential (black line) during *operando* XAS investigation. Blue circles mark XAS scan at Co K-edge and red squares mark scans at Fe K-edge.

In the XAS spectrum of  $\text{CoFe}_2\text{O}_4/\text{rGO}$  (Figure 7) the Fe K-edge energy (7126 eV) and the pre-edge feature (7114 eV, thick blue line) agree with literature data for  $\text{Fe}^{3+}$ .<sup>[66,67]</sup> The Co K-edge at 7722 eV and the pre-edge feature (7709 eV) match with data for  $\text{Co}^{2+}$ .<sup>[68,69]</sup> The most intense signal is the  $1s \rightarrow 4p$  transition at about 7133 eV (Fe) and 7728 eV (Co). The pre-edge signal indicates that both cations are in a non-centrosymmetric environment because the  $1s \rightarrow 3d$  transition is dipole forbidden

in a centrosymmetric environment, and the allowed quadrupole transition exhibits a very low intensity. In the non-centrosymmetric tetrahedral environment mixing of 3d/4p states is allowed adding a partial p-character to the d-states. Hence, in  $\text{CoFe}_2\text{O}_4/\text{rGO}$   $\text{Co}^{2+}$  and  $\text{Fe}^{3+}$  ions partially occupy tetrahedral sites, *i.e.*  $\text{CoFe}_2\text{O}_4$  is a partial inverse spinel with formula  $(\text{Co}_{1-2\lambda}\text{Fe}_{2\lambda})_A[\text{Co}_{2\lambda}\text{Fe}_{2(1-\lambda)}]_B\text{O}_4$  (A: tetrahedral sites, B: octahedral sites) with  $\lambda$  representing the inversion parameter ranging from 0 (normal spinel) to about 0.34.<sup>[70]</sup>

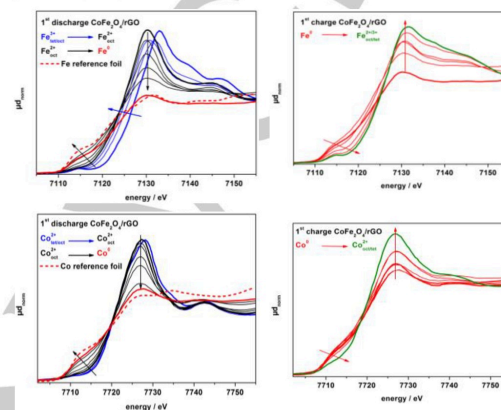


**Figure 7.** Scans at Fe K-edge (top) and Co K-edge (bottom) during discharge (left) and charge (right) process. Region I (blue) uptake of about 2 Li per formula unit, region II (black) discharge to 10 mV, region III (red) charge to 3 V. (only XANES region is presented to make the energy shift visible)

The Li uptake is accompanied by a strong shift of the Fe K-edge to lower energies (7124 eV) and disappearance of the pre-edge peak, while no shift is observed for the Co K-edge but the pre-edge feature disappears. The disappearance of the pre-edge signal indicates that  $\text{Co}^{2+}$  and  $\text{Fe}^{3+}$  are now in a centrosymmetric environment, *i.e.* they occupy formerly empty octahedra. The Fe K-edge shift demonstrates that  $\text{Fe}^{3+}$  is simultaneously reduced to  $\text{Fe}^{2+}$ . The intensity of the  $1s \rightarrow 4p$  transition decreases for  $\text{Li} > 2.5$  per formula unit due to formation of metallic Co and Fe, and at the end of the discharge process the spectra (Fig 8, thick red line) are very similar to those of metallic reference foils (Fig 8, red dashed line). The XAS curves of Fe and Co show a rotation around isosbestic points at 7124 eV for Fe and at 7720 eV for Co (Figure 7), *i.e.* no intermediate phase is formed and  $\text{Co}^{2+}/\text{Fe}^{2+}$  are directly reduced to the metallic state. Similar observations were made during the Li uptake by  $\text{NiCo}_2\text{O}_4$  and  $\text{Mn}_3\text{O}_4$ .<sup>[65,71]</sup>

The charge process (Li release) leads to pronounced increase of the intensity of the  $1s \rightarrow 4p$  transitions because metallic Co and Fe are simultaneously oxidized. XAS spectra of Co (Figure 7, bottom left) exhibit an isosbestic point at 7720 eV and no shift of the  $1s \rightarrow 4p$  transition demonstrating that  $\text{Co}^{2+}$  is formed. For the Fe K-edge spectra the  $1s \rightarrow 4p$  transition is located at 7125 eV which is between the values of  $\text{Fe}^{2+}$  and  $\text{Fe}^{3+}$ .

In the Fourier transformed XAS data,  $FT(\chi(k))$ , for Co (left) and Fe (right) (Figure 8) the first and second coordination shells around the absorber atoms (please note: the spectra are not phase-shift corrected) at about 1.5 Å with a shoulder at 1.4 Å for pristine  $\text{CoFe}_2\text{O}_4/\text{rGO}$  (Figure 8, blue) correspond to M-O distances of Fe/Co in tetrahedral and octahedral coordination. The shell at about 2.5 Å represents the M-M distance (M = Fe, Co, oxygen-bridged). After uptake of 2.5 Li/f.u. (Figure 8, black) the shoulder at 1.4 Å disappeared caused by movement of the cations to empty octahedra. After discharge to 0.1 V (Figure 8, red) the two signals disappeared and a new shell at about 2 Å is developed for Fe and Co corresponding to M-M bonds of Fe resp. Co metals (Figure 8, red dotted lines, reference foils). The oxidation of the metallic Fe/Co is seen by disappearance of the shell at 2 Å and the occurrence of the shells at 1.5 Å and 2.5 Å (Figure 8, green lines).

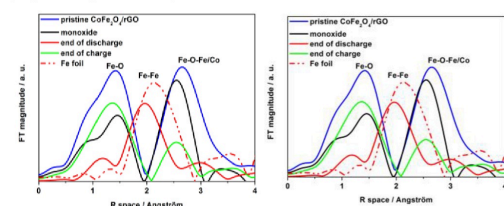


**Figure 8.** FT-EXAFS data of pristine  $\text{CoFe}_2\text{O}_4$  (blue), intermediate product (black), end of discharge (red), end of charge (green) and reference foil (dashed red line) of Fe (left) and Co (right).

### Ex situ XAS

Results of the *operando* XAS study suggested an oxidation state between the +2 and +3 for Fe. The charge curve (Figure 7) indicates that only about 4.5 Li/f.u. were extracted most probably caused by a pronounced volume change which could not be compensated by the construction of the *in situ* cell (without spring). *Ex situ* XAS spectra were recorded for the starting material, after first discharge and after several cycles (Figure 9). The spectra of all cycled materials exhibit no significant differences while the spectrum of pristine  $\text{CoFe}_2\text{O}_4/\text{rGO}$  displays more pronounced features due to a better crystallinity (see also section 3.3). The slight differences of the 1s  $\rightarrow$  4p transition are caused by the different crystallinity of the samples. The edge energies for Fe and Co indicate oxidation to  $\text{Fe}^{3+}$  resp. to  $\text{Co}^{2+}$  independent of the cycle number.

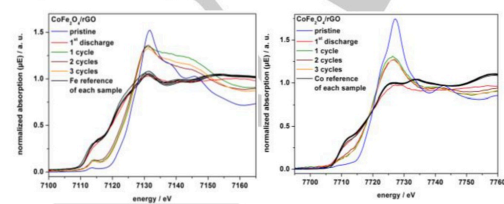


**Figure 9.** *Ex situ* XAS of pristine material, after 1<sup>st</sup> discharge and after 1, 2 and 3 full cycles measured at Fe K-edge (left) and Co K-edge (right). For each spectrum a reference spectrum is displayed to demonstrate the correct calibration of each spectrum.

### Ex situ TEM

Two samples have been investigated by TEM: sample A containing 2 Li per formula unit and sample B cycled ten times. Both samples present agglomerated nanoparticles holding good adhesion to the rGO after Li uptake and release (Figure 10 left). Sample A contains nanoparticles with sizes of 6-15 nm and show high crystallinity (Figure 10 middle). Electron diffraction (Figure 10 right) confirm the presence of a monoxide (space group:  $Fm\bar{3}m$ ) like observed with XRD (section 3.3). EDX measurements revealed a Fe:Co ratio of 1.92:1 which is close to its proposed chemical composition. An EDX-linescan of 100 nm (40 points) in one particle demonstrates a simultaneous increase and decrease of the Fe and Co content with an almost constant ratio of 2:1 for Fe:Co (Figure 10 bottom).

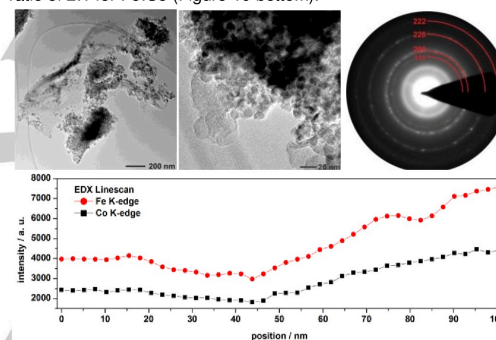


**Figure 10.** TEM image of  $\text{CoFe}_2\text{O}_4/\text{rGO}$  after uptake of 2 Li per formula unit. Overview (top, left) magnified image (top, middle) and the corresponding ED image (top, right). 100 nm EDX-linescan of Fe and Co content (bottom).

After cycling the sample ten times (sample B) the particle size increased to about 25 to 50 nm and they are nearly amorphous (ESI, Fig. S4). A dark-field STEM image (Figure 11 left) represents three agglomerations of cycled particles on rGO. STEM-EDX mapping demonstrates that Fe, Co and O are homogeneously distributed inside the agglomerate (Fig. 11 right) without visible gradients. C is distributed over the whole sample but the distribution does not coincide with any other element which confirms the presence of rGO. The Fe:Co ratio measured by EDX is 2.08:1 which is again close to the expected value.

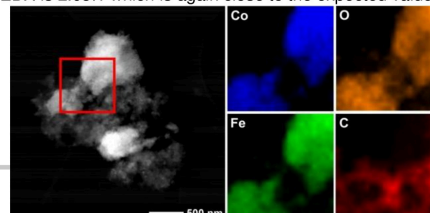


Figure 11: Dark-field STEM image (left), elemental maps (right) at the area marked with a red square of CoFe<sub>2</sub>O<sub>4</sub>/rGO after ten cycles.

## Discussion

The CoFe<sub>2</sub>O<sub>4</sub>/rGO composite exhibits a much better cycling stability and larger capacity at higher current density than CoFe<sub>2</sub>O<sub>4</sub> due to the synergistic effect between rGO and CoFe<sub>2</sub>O<sub>4</sub>. TEM investigations on a sample cycled ten times indicate good adhesion of the nanoparticles on the rGO sheets enabling an improvement of reversibility of discharge/charge cycles. The rGO sheets store only a small amount of Li ions on the surface without major impact on the reversible capacity.

For microcrystalline Fe<sub>3</sub>O<sub>4</sub> and Co<sub>3</sub>O<sub>4</sub> it was postulated that Li<sup>+</sup> ions enter the empty 8b sites followed by a cooperative movement of Li<sup>+</sup> (8b) and Fe<sup>3+</sup>/Co<sup>2+</sup> ions on the 8a sites to neighbouring empty octahedral 16c sites.<sup>[72,73]</sup> Obviously, all octahedra are fully occupied after uptake of 1 Li/f.u. resulting in a distorted NaCl-type structure. For larger Co<sub>3</sub>O<sub>4</sub> particles first an insertion compound Li<sub>x</sub>Co<sub>3</sub>O<sub>4</sub> was observed while for smaller particles the formation of CoO is favoured.<sup>[74]</sup> The mechanism for Li uptake elucidated on the basis of *operando* XRD and XAS is different:

- i) uptake of ca. 0.4 Li/f.u. occurs by an amorphous surface layer clearly suggested by the constant intensity of the reflections in the XRD patterns;
- ii) increasing the Li content to 2.5/f.u. leads to reduction of Fe<sup>3+</sup> to Fe<sup>2+</sup> and successive conversion of the spinel to a monoxide phase with all Fe<sup>2+</sup>/Co<sup>2+</sup> ions residing on octahedral sites (section 3.3) and a Co:Fe ratio of 1:2 (section 3.7) excluding a separation into two monoxides;
- iii) the uptake process is accompanied by generation of X-ray amorphous Li<sub>2</sub>O;
- iv) further Li uptake leads to successively reduction of the cations to the metals embedded in the Li<sub>2</sub>O matrix;
- v) during the charge process metallic Fe and Co are simultaneously oxidized (Fe<sup>3+</sup> and Co<sup>2+</sup>) but no long-range ordered crystalline particles are formed

*Operando* Raman spectra (ESI, Fig. S5) show a rapid increase of the fluorescence revealing the formation of metallic nanoparticles. But rGO is not affected during the chemical reaction. Compared to pure CoFe<sub>2</sub>O<sub>4</sub> where Fe is oxidized first,<sup>[48]</sup> the presence of rGO leads to a simultaneous oxidation of Co and Fe during many cycles, indicating a better conductivity and an improved contact to isolating Li<sub>2</sub>O. The capacity loss reported for CoFe<sub>2</sub>O<sub>4</sub> during the first few cycles is mainly caused by the inability of oxidation of Co.<sup>[48]</sup> The addition of rGO to CoFe<sub>2</sub>O<sub>4</sub> nanoparticles seems to facilitate oxidation thus retaining a relatively stable capacity over many cycles.

## Conclusions

The comprehensive investigation of the Li uptake and release by a CoFe<sub>2</sub>O<sub>4</sub>/rGO composite reveals a remarkable difference to previous studies on pure CoFe<sub>2</sub>O<sub>4</sub>: metallic Fe and Co nanoparticles embedded in the Li<sub>2</sub>O matrix can be oxidized simultaneously to Fe<sup>3+</sup>/Co<sup>2+</sup> during charging while for pure CoFe<sub>2</sub>O<sub>4</sub> oxidation/partial oxidation was only observed for few cycles. The presence of rGO in the composite keeps the nanoparticles in tight contact and prevents agglomeration of the highly reactive metal nanoparticles thus enabling reversible cycling. Moreover, the presence of rGO allows fast discharge/charge while retaining high capacities. All results suggest that rGO does not significantly influence the reaction mechanisms.

## Experimental Section

For the preparation of CoFe<sub>2</sub>O<sub>4</sub> nanoparticles 5 mmol Co(NO<sub>3</sub>)<sub>2</sub>·6H<sub>2</sub>O (97 %, Merck), 10 mmol Fe(NO<sub>3</sub>)<sub>3</sub>·9H<sub>2</sub>O (98 %, Riedel-de Haen) and 15 mmol citric acid (99 %, Merck) were ball milled for 2 h in a Fritsch Pulverisette with 15 mm agate balls at 500 rpm in air yielding a viscous product. The product was decomposed in air at 400 °C in a pre-heated oven for 3 h. Graphene oxide (GO) was synthesized via a modified Hummers method.<sup>[75–77]</sup> 0.200 g graphene oxide were suspended in 200 mL H<sub>2</sub>O in an ultrasonic bath (Elma Elmasonic 60 S, 37 kHz) for 1 h. Afterwards 0.500 g of CoFe<sub>2</sub>O<sub>4</sub> nanoparticles were added and sonicated for 1 h. 10 mL hydrazine was added drop-wise to the slurry which was sonicated for another 1 h. The product (CoFe<sub>2</sub>O<sub>4</sub>/rGO) was centrifuged, washed with water and dried at 80 °C.

XRD patterns were recorded in reflection mode with an X'PERT PRO (PANalytical) equipped with a PIXcel detector using Cu K<sub>α</sub> radiation. EDX spectra were collected in a Philips ESEM XL 30 with EDAX New XL-30 Detecting Unit. The carbon content was determined via elemental analysis with a Euro Vector EA3000 Elemental Analyser. Raman spectra were measured with a Horiba LaRam Evolution HR equipped with a 532 nm Nd:YAG solid state laser (10 mW). TEM investigations were performed in a Tecnai F30 G<sup>2</sup>-Stwin microscope operated at 300 kV with a field emission gun cathode and a Si/Li detector (Thermo Fisher, NSS). For TEM experiments CoFe<sub>2</sub>O<sub>4</sub>/rGO was suspended in *n*-butanol and dropped onto a holey-carbon copper grid.

The electrochemical characterisation was done with electrodes consisting of 70 wt% active material, 20 wt% SUPER C65 Carbon (Timcal, Switzerland) and 10 wt% sodium carboxymethyl cellulose (CMC WALOCEL™ CRT 2000, Dow Chemicals, Germany). 1.5 wt% CMC were dissolved in deionised water for 1 d. The active material and carbon were mixed in a ball mill for 30 min (Retsch MM 400, 15 Hz). Afterwards, the CMC solution was added and the mixture was homogenized for 15 min. The slurry was deposited onto a dendritic copper foil (Schlenk, Germany), dried overnight at room temperature and sintered at 80 °C for 24 h. 10 mm discs were cut and applied as cathode in a Swagelok type test cell with Li metal as anode. Glass fiber filter disks (Whatman, United Kingdom) were used as separator and a solution of 1M LiPF<sub>6</sub> in an ethylene carbonate/dimethyl carbonate mixture (Merck, Germany) as electrolyte. Galvanostatic tests were performed with a MTI BST8-MA. Cyclic voltammetry was performed with a Zahner XPot device. C/10 rate corresponds to 10 h for the charge and discharge processes, calculated on the theoretical capacity of 914 mAh g<sup>-1</sup>, corresponding to a current density of 91.4 mA g<sup>-1</sup>.

For *operando* investigations a custom built cell (40x40x15 mm) consisting of two Al plates with rectangular apertures (14x3 mm) in the



centre and two sheets of Kapton foil windows glued on both sides was used. CoFe<sub>2</sub>O<sub>4</sub>/rGO (80 wt%) was mixed with 10 wt% SUPER C65 Carbon (Timcal, Switzerland) and 10 wt% PVdF (Solvay, Germany). The mixture was dissolved in N-methyl-2-pyrrolidone (NMP) deposited on 8 μm Cu foil and dried in air. The Li metal counter electrode is attached to a Cu foil ring. A microporous polyethylene/polypropylene membrane (Celgard 2325) was used as separator and 1M LiPF<sub>6</sub> in EC/DMC (1:1) is used as electrolyte. The cells were assembled in an argon filled glove box (<1 ppm of O<sub>2</sub>, <1 ppm of H<sub>2</sub>O) and transferred to the beamline in a plastic bag. Galvanostatic Li uptake / release were carried out with a Biologic SP-300 device with a C/15 rate (60.9 mA g<sup>-1</sup>) in a voltage range from 3.0 to 0.1 V.

*Operando* XRD was done at the PDIFF beamline at ANKA (Karlsruhe Institute of Technology, 16 keV, λ = 0.77490 Å) with a Princeton CCD detector for data recording. All powder patterns were collected within 5 min, Cu reflections were masked and the 2D patterns were transformed with Area Diffraction Machine.<sup>[78]</sup>

*Operando* XAS measurements were carried out at the XANES station of the KMC-2 beamline at BESSY II (Helmholtz-Zentrum Berlin) in transmission mode. The collected spectra were background corrected, normalized, K<sup>2</sup>-weighted and Fourier transformed using the Athena Software package.<sup>[79]</sup> For *ex situ* XAS, electrode films were cycled in a Swagelok type test cell. The cells were opened in an argon filled glove box, glued between polyimide foil and transferred to the beamline in the *in situ* cells.

## Acknowledgements

We are grateful to the German Federal Ministry of Education and Research for financial support. Beam time allocation by ANKA (Karlsruhe) is thankfully acknowledged. We thank also HZB for allocation of synchrotron radiation beam time.

**Keywords:** nanoparticles • CoFe<sub>2</sub>O<sub>4</sub>/rGO • anode • *operando* • LiBs

- [1] H.-G. Wang, S. Yuan, D.-L. Ma, X.-B. Zhang, J.-M. Yan, *Energy Env. Sci* **2015**, *8*, 1660–1681.
- [2] N.-S. Choi, Z. Chen, S. A. Freunberger, X. Ji, Y.-K. Sun, K. Amine, G. Yushin, L. F. Nazar, J. Cho, P. G. Bruce, *Angew. Chem.* **2012**, *124*, 10134–10166.
- [3] X. Rui, H. Tan, Q. Yan, *Nanoscale* **2014**, *6*, 9889.
- [4] M. Armand, J.-M. Tarascon, *Nature* **2008**, *451*, 652–657.
- [5] J. B. Goodenough, K.-S. Park, *J. Am. Chem. Soc.* **2013**, *135*, 1167–1176.
- [6] V. Etacheri, R. Marom, R. Elazari, G. Salitra, D. Aurbach, *Energy Environ. Sci.* **2011**, *4*, 3243.
- [7] M. V. Reddy, G. V. S. Rao, B. V. R. Chowdari, *Chem. Rev.* **2013**, *113*, 5364–5457.
- [8] X. Wu, S. Li, B. Wang, J. Liu, M. Yu, *New J. Chem.* **2015**, *39*, 8416–8423.
- [9] F. M. Courtel, H. Duncan, Y. Abu-Lebdeh, I. J. Davidson, *J. Mater. Chem.* **2011**, *21*, 10206.
- [10] A. K. Rai, J. Gim, T. V. Thi, D. Ahn, S. J. Cho, J. Kim, *J. Phys. Chem. C* **2014**, *118*, 11234–11243.
- [11] W. Zhang, X. Hou, Z. Lin, L. Yao, X. Wang, Y. Gao, S. Hu, *J. Mater. Sci. Mater. Electron.* **2015**, *26*, 9535–9545.
- [12] X. Guo, X. Lu, X. Fang, Y. Mao, Z. Wang, L. Chen, X. Xu, H. Yang, Y. Liu, *Electrochem. Commun.* **2010**, *12*, 847–850.
- [13] Z. Xing, Z. Ju, J. Yang, H. Xu, Y. Qian, *Electrochim. Acta* **2013**, *102*, 51–57.
- [14] N. Wang, H. Xu, L. Chen, X. Gu, J. Yang, Y. Qian, *J. Power Sources* **2014**, *247*, 163–169.
- [15] G. Wang, R. Chen, Y. Zhou, H. Wang, J. Bai, *J. Nanoparticle Res.* **2014**, *16*, 1–9.
- [16] N. Wang, X. Ma, Y. Wang, J. Yang, Y. Qian, *J. Mater. Chem. A* **2015**, *3*, 9550–9555.
- [17] Y. Wang, M. Wang, G. Chen, C. Dong, Y. Wang, L.-Z. Fan, *Ionics* **2015**, *21*, 623–628.
- [18] L. F. Nazar, G. Goward, F. Leroux, M. Duncan, H. Huang, T. Kerr, J. Gaubicher, *Int. J. Inorg. Mater.* **2001**, *3*, 191–200.
- [19] P. G. Bruce, B. Scrosati, J.-M. Tarascon, *Angew. Chem.* **2008**, *120*, 2972–2989.
- [20] J. Cabana, L. Monconduit, D. Larcher, M. R. Palacin, *Adv. Mater.* **2010**, *22*, E170–E192.
- [21] F. Mueller, D. Bresser, E. Paillard, M. Winter, S. Passerini, *J. Power Sources* **2013**, *236*, 87–94.
- [22] Y. Xiao, J. Zai, L. Tao, B. Li, Q. Han, C. Yu, X. Qian, *Phys. Chem. Chem. Phys.* **2013**, *15*, 3939.
- [23] Y. Dong, Y.-S. Chui, X. Yang, R. Ma, J.-M. Lee, J. A. Zapien, *Chem. Electro. Chem.* **2015**, *2*, 1010–1018.
- [24] L. Ji, Z. Tan, T. R. Kuykendall, S. Aloni, S. Xun, E. Lin, V. Battaglia, Y. Zhang, *Phys. Chem. Chem. Phys.* **2011**, *13*, 7170.
- [25] Z.-S. Wu, W. Ren, L. Wen, L. Gao, J. Zhao, Z. Chen, G. Zhou, F. Li, H.-M. Cheng, *ACS Nano* **2010**, *4*, 3187–3194.
- [26] J.-Z. Wang, C. Zhong, D. Wexler, N. H. Idris, Z.-X. Wang, L.-Q. Chen, H.-K. Liu, *Chem. - Eur. J.* **2011**, *17*, 661–667.
- [27] Y. Chen, J. Zhu, B. Qu, B. Lu, Z. Xu, *Nano Energy* **2014**, *3*, 88–94.
- [28] G. Zhou, D.-W. Wang, F. Li, L. Zhang, N. Li, Z.-S. Wu, L. Wen, G. Q. (Max) Lu, H.-M. Cheng, *Chem. Mater.* **2010**, *22*, 5306–5313.
- [29] H. Kim, D.-H. Seo, S.-W. Kim, J. Kim, K. Kang, *Carbon* **2011**, *49*, 326–332.
- [30] M. Zhang, D. Lei, X. Yin, L. Chen, Q. Li, Y. Wang, T. Wang, *J. Mater. Chem.* **2010**, *20*, 5538.
- [31] H. Wang, L.-F. Cui, Y. Yang, H. Sanchez Casalongue, J. T. Robinson, Y. Liang, Y. Cui, H. Dai, *J. Am. Chem. Soc.* **2010**, *132*, 13978–13980.
- [32] X. Zhu, Y. Zhu, S. Murali, M. D. Stoller, R. S. Ruoff, *ACS Nano* **2011**, *5*, 3333–3338.
- [33] G. Zeng, N. Shi, M. Hess, X. Chen, W. Cheng, T. Fan, M. Niederberger, *ACS Nano* **2015**, *9*, 4227–4235.
- [34] P. R. Kumar, P. Kollu, C. Santhosh, K. Eswara Varaprasada Rao, D. K. Kim, A. N. Grace, *New J. Chem.* **2014**, *38*, 3654–3661.
- [35] S. Li, B. Wang, J. Liu, M. Yu, *Electrochim. Acta* **2014**, *129*, 33–39.
- [36] Y. Xiao, X. Li, J. Zai, K. Wang, Y. Gong, B. Li, Q. Han, X. Qian, *Nano-Micro Lett.* **2014**, *6*, 307–315.
- [37] H. Xia, D. Zhu, Y. Fu, X. Wang, *Electrochim. Acta* **2012**, *83*, 166–174.
- [38] R. Raccichini, A. Varzi, S. Passerini, B. Scrosati, *Nat. Mater.* **2014**, *14*, 271–279.
- [39] Z.-S. Wu, G. Zhou, L.-C. Yin, W. Ren, F. Li, H.-M. Cheng, *Nano Energy* **2012**, *1*, 107–131.
- [40] J. N. Reimers, J. R. Dahn, *J. Electrochem. Soc.* **1992**, *139*, 2091–2097.
- [41] H. Liu, F. C. Strobridge, O. J. Borkiewicz, K. M. Wiaderek, K. W. Chapman, P. J. Chupas, C. P. Grey, *Science* **2014**, *344*, 1252817–1252817.
- [42] X. Zhang, M. van Hulzen, D. P. Singh, A. Brownrigg, J. P. Wright, N. H. van Dijk, M. Wagemaker, *Nat. Commun.* **2015**, *6*, 8333.
- [43] H. Arai, K. Sato, Y. Orikasa, H. Murayama, I. Takahashi, Y. Koyama, Y. Uchimoto, Z. Ogumi, *J. Mater. Chem. A* **2013**, *1*, 10442–10449.
- [44] Q. Wu, Y. Liu, C. S. Johnson, Y. Li, D. W. Dees, W. Lu, *Chem. Mater.* **2014**, *26*, 4750–4756.
- [45] M. Herklotz, J. Weiß, E. Ahrens, M. Yavuz, L. Mereacre, N. Kiziltas-Yavuz, C. Dräger, H. Ehrenberg, J. Eckert, F. Fauth, L. Giebeler, M. Knapp, *J. Appl. Crystallogr.* **2016**, *49*, 340–349.
- [46] S. Permien, H. Hain, M. Scheuermann, S. Mangold, V. Mereacre, A. K. Powell, S. Indris, U. Schürmann, L. Kienle, V. Duppel, et al., *RSC Adv.* **2013**, *3*, 23001–23014.



- 1 [47] S. Permien, S. Indris, M. Scheuermann, U. Schürmann, V. Mereacre, A.  
2 K. Powell, L. Kienle, W. Bensch, *J Mater Chem A* **2015**, *3*, 1549–1561.
- 3 [48] S. Permien, S. Indris, U. Schürmann, L. Kienle, S. Zander, S. Doyle, W.  
4 Bensch, *Chem. Mater.* **2016**, *28*, 434–444.
- 5 [49] S. Permien, S. Indris, A.-L. Hansen, M. Scheuermann, D. Zahn, U.  
6 Schürmann, G. Neubüser, L. Kienle, E. Yegudin, W. Bensch, *ACS Appl.*  
7 *Mater. Interfaces* **2016**, *8*, 15320–15332.
- 8 [50] A. A. Coelho, *Topas Academic*, Coelho Software, **2012**.
- 9 [51] P. Chandramohan, M. P. Srinivasan, S. Velmurugan, S. V. Narasimhan,  
10 *J. Solid State Chem.* **2011**, *184*, 89–96.
- 11 [52] Dahn, *Science* **1995**, 590–593.
- 12 [53] Y.-Q. Chu, Z.-W. Fu, Q.-Z. Qin, *Electrochimica Acta* **2004**, *49*, 4915–  
13 4921.
- 14 [54] C. Vidal-Abarca, P. Lavela, J. L. Tirado, *Solid State Ion.* **2010**, *181*,  
15 616–622.
- 16 [55] P. Lavela, J. L. Tirado, *J. Power Sources* **2007**, *172*, 379–387.
- 17 [56] P. Lavela, J. L. Tirado, M. Womes, J. C. Jumas, *J. Electrochem. Soc.*  
18 **2009**, *156*, A589.
- 19 [57] J. Maier, *Nat. Mater.* **2005**, *4*, 805–815.
- 20 [58] A. Ponrouch, P.-L. Taberna, P. Simon, M. R. Palacin, *Electrochimica*  
21 *Acta* **2012**, *61*, 13–18.
- 22 [59] S. Laruelle, S. Grugeon, P. Poizat, M. Dollé, L. Dupont, J.-M. Tarascon,  
23 *J. Electrochem. Soc.* **2002**, *149*, A627.
- 24 [60] K. Xu, *Chem. Rev.* **2014**, *114*, 11503–11618.
- 25 [61] M. J. R. Redman, E. G. Steward, *Nature* **1962**, 867–867.
- 26 [62] E. R. Jette, F. Foote, *J. Chem. Phys.* **1933**, *1*, 29–36.
- 27 [63] P. Schmidt, *Eur. J. Inorg. Chem.* **2008**, *2008*, 2847–2855.
- 28 [64] D. Bresser, E. Paillard, R. Kloepsch, S. Krueger, M. Fiedler, R. Schmitz,  
29 D. Baither, M. Winter, S. Passerini, *Adv. Energy Mater.* **2013**, 513–523.
- 30 [65] M. A. Lowe, J. Gao, H. D. Abruña, *J Mater Chem A* **2013**, *1*, 2094–  
31 2103.
- 32 [66] G. Aquilanti, A. Cognigni, M. Anis-ur-Rehman, *J. Supercond. Nov.*  
33 *Magn.* **2011**, *24*, 659–663.
- 34 [67] C. Nordhei, A. L. Ramstad, D. G. Nicholson, *Phys Chem Chem Phys*  
35 **2008**, *10*, 1053–1066.
- 36 [68] S. Ammar, A. Helfen, N. Jouini, F. Fiévet, I. Rosenman, F. Villain, P.  
37 Molinié, M. Danot, *J. Mater. Chem.* **2001**, *11*, 186–192.
- 38 [69] M. Artus, L. Ben Tahar, F. Herbst, L. Smiri, F. Villain, N. Yaacoub, J.-M.  
39 Grenèche, S. Ammar, F. Fiévet, *J. Phys. Condens. Matter* **2011**, *23*,  
40 506001–506010.
- 41 [70] D. Peddis, M. V. Mansilla, S. Mörup, C. Cannas, A. Musinu, G.  
42 Piccaluga, F. D'Orazio, F. Lucari, D. Fiorani, *J. Phys. Chem. B* **2008**,  
43 *112*, 8507–8513.
- 44 [71] A. V. Chadwick, S. L. P. Savin, S. Fiddy, R. Alcantara, D.  
45 FernandezLisbona, P. Lavela, G. F. Ortiz, J. L. Tirado, *J. Phys. Chem.*  
46 *C* **2007**, *111*, 4636–4642.
- 47 [72] M. M. Thackeray, W. I. F. David, J. B. Goodenough, *Mater. Res. Bull.*  
48 **1982**, *17*, 785–793.
- 49 [73] M. Thackeray, S. Baker, K. Adendorff, J. Goodenough, *Solid State*  
50 *Ionics* **1985**, *17*, 175–181.
- 51 [74] D. Larcher, G. Sudant, J.-B. Leriche, Y. Chabre, J.-M. Tarascon, *J.*  
52 *Electrochem. Soc.* **2002**, *149*, A234.
- 53 [75] W. S. Hummers, R. E. Offeman, *J. Am. Chem. Soc.* **1958**, *80*, 1339–  
54 1339.
- 55 [76] M. Hirata, T. Gotou, S. Horiuchi, M. Fujiwara, M. Ohba, *Carbon* **2004**,  
56 *42*, 2929–2937.
- 57 [77] L. Zhang, J. Liang, Y. Huang, Y. Ma, Y. Wang, Y. Chen, *Carbon* **2009**,  
58 *47*, 3365–3368.
- 59 [78] J. Lande, *Area Diffraction Machine*, **2013**.
- 60 [79] B. Ravel, M. Newville, *J. Synchrotron Radiat.* **2005**, *12*, 537–541.

1 **Entry for the Table of Contents** (Please choose one layout)

2

3

4

5 Layout 2:

6

7

8 **FULL PAPER**

9

10

11

12

13

14

15

16

17

18

19

20

21

22

23

24

25

26

27

28

29

30

31

32

33

34

35

36

37

38

39

40

41

42

43

44

45

46

47

48

49

50

51

52

53

54

55

56

57

58

59

60

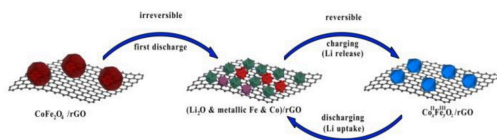
61

62

63

64

65



Schematic illustration of the reaction mechanism occurring during Li uptake and release of  $\text{CoFe}_2\text{O}_4$  nanoparticles on reduced graphite oxide.

Stefan Permien, Sylvio Indris, Gero Neubüser, Andy Fiedler, Lorenz Kienle, Stefan Zander, Stephen Doyle, Björn Richter, Wolfgang Bensch\*

Page No. – Page No.

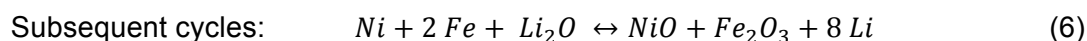
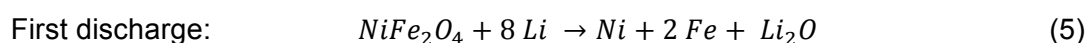
The role of reduced graphite oxide in transition metal oxide nanocomposites used as Li anode material: An *operando* study on  $\text{CoFe}_2\text{O}_4/\text{rGO}$

## 4 Further Projects (will be submitted soon)

### 4.1 The Lithiation and Delithiation Process of Nanocomposite Materials Consisting of NiFe<sub>2</sub>O<sub>4</sub> Nanoparticles and Carbon Nanotubes

#### 4.1.1 Short Introduction

NiFe<sub>2</sub>O<sub>4</sub> nanoparticles show high capacities for the first discharge and charge process.<sup>[121,174–176]</sup> Unfortunately for pure NiFe<sub>2</sub>O<sub>4</sub> nanoparticles strong capacity fading was observed during repeated cycling.<sup>[92,175–177]</sup> The main reason for this finding is the mechanical degradation due to the high volume change during Li uptake and release. Special morphologies like nanosheets, hollow spheres or nanorods compensate to a certain amount the volume expansion by a higher packing density.<sup>[178]</sup> Alternatives are carbon coatings or nanoparticles deposited on graphene nanosheets, which also improve the cycling stability compared to pure NiFe<sub>2</sub>O<sub>4</sub>.<sup>[90,179–182]</sup> Another approach is the usage of carbon nanotubes (CNTs) which cross-link the oxide nanoparticles.<sup>[91,183–188]</sup> It is assumed that CNTs form an interconnected network ensuring the electric conductivity and compensating the strong volume expansion. The reaction mechanisms occurring during Li uptake and release as well as the influence and role of the CNTs are not investigated in detail yet and as a consequence the role of CNTs is not fully understood. Furthermore, the intermediates and products during Li uptake and release of NiFe<sub>2</sub>O<sub>4</sub> are not proven. The following mechanisms were proposed on the basis of CV (eqn. 5+6).<sup>[175,179,180]</sup>



*In situ* XAS investigations on pure NiFe<sub>2</sub>O<sub>4</sub> nanoparticles evidence the formation of metallic Ni and Fe nanoparticles, but the discharge and charge reactions reported were incomplete and therefore the results remain unsatisfactory.<sup>[189]</sup> Moreover, the proposed mechanism is solely based on XAS which only provides information about the local structural environment of Ni and Fe and the electronic properties. A better cycling stability for CoFe<sub>2</sub>O<sub>4</sub>/CNT compared to bare CoFe<sub>2</sub>O<sub>4</sub> nanoparticles was already reported.<sup>[183]</sup>

For NiFe<sub>2</sub>O<sub>4</sub>/CNT here the first report on the electrochemical performance and reaction pathways is presented. In the course of the study NiFe<sub>2</sub>O<sub>4</sub> nanoparticles and NiFe<sub>2</sub>O<sub>4</sub>/CNT composite were synthesized and the electrochemical performance was investigated via galvanostatic cycling and CV. The electronic changes and structural alterations of NiFe<sub>2</sub>O<sub>4</sub>/CNT were investigated in detail using *operando* XAS and XRD. The experiments are complemented by *ex situ* XAS, TEM and <sup>7</sup>Li MAS NMR.

#### 4.1.2 Synthesis of NiFe<sub>2</sub>O<sub>4</sub> and NiFe<sub>2</sub>O<sub>4</sub>/CNT

NiFe<sub>2</sub>O<sub>4</sub> nanoparticles cross-linked with carbon nanotubes (CNTs) were synthesized via a one-step solvothermal method. 0.035 g multiwall carbon nanotubes (Bayer) were suspended in 6 mL H<sub>2</sub>O in an ultrasonic bath for 1 h. A solution of 0.484 g Fe(NO<sub>3</sub>)<sub>3</sub>·9H<sub>2</sub>O (Grüssing), 0.174 g Ni(NO<sub>3</sub>)<sub>2</sub>·6H<sub>2</sub>O (Merck) and 6 mL H<sub>2</sub>O were added. To this mixture 4.5 mL of 6 M NaOH solution (Grüssing) was added drop wise under continuous stirring. The solution was transferred into a Teflon-lined steel autoclave with an inner volume of 30 mL and heated for 24 h at 150 °C. The product was magnetically decanted, washed three times with H<sub>2</sub>O followed by ethanol (Walter CMP) and dried at 60 °C. Same synthesis was performed with CNTs (NiFe<sub>2</sub>O<sub>4</sub>/CNT) and without (NiFe<sub>2</sub>O<sub>4</sub>). For experimental methods and sample preparation see section 2.3.

#### 4.1.3 Characterization of as-prepared NiFe<sub>2</sub>O<sub>4</sub>/CNT and NiFe<sub>2</sub>O<sub>4</sub>

XRD powder patterns of as-prepared NiFe<sub>2</sub>O<sub>4</sub>/CNT and NiFe<sub>2</sub>O<sub>4</sub> are displayed in Figure 17. Both patterns were refined in the cubic spinel structure (space group *Fd* $\bar{3}$ *m*) using TOPAS Academic. The volume-weighted average particle sizes are  $d = 43.9(2)$  nm for NiFe<sub>2</sub>O<sub>4</sub> and  $d = 36.1(2)$  nm for NiFe<sub>2</sub>O<sub>4</sub>/CNT. The lattice parameter  $a$  is similar for both samples,  $a = 8.3558(1)$  Å for NiFe<sub>2</sub>O<sub>4</sub> and  $a = 8.3604(2)$  Å for NiFe<sub>2</sub>O<sub>4</sub>/CNT. These results are in accordance with literature data.<sup>[190]</sup>

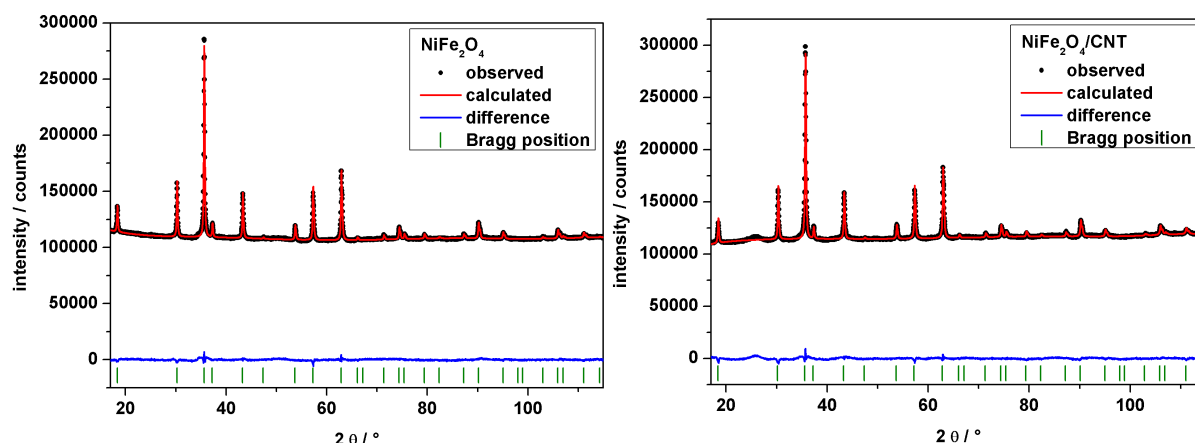


Figure 17: XRD powder pattern (black) of the as-prepared NiFe<sub>2</sub>O<sub>4</sub> (left) and NiFe<sub>2</sub>O<sub>4</sub>/CNT (right). Refined pattern (red), difference curve (blue) and Bragg positions (green).



The lognormal domain size distribution of the coherently scattering domains (Figure 18, middle) reveals that both samples consist of particles in the range of 2-80 nm, while the most particles (ca. 60 %) are in a narrow range from 10 to 20 nm. From the  $(hkl)$ -dependent domain sizes a cube-like shape with rounded edges was extracted (Figure 18 left and right) which is independent from addition of CNTs.

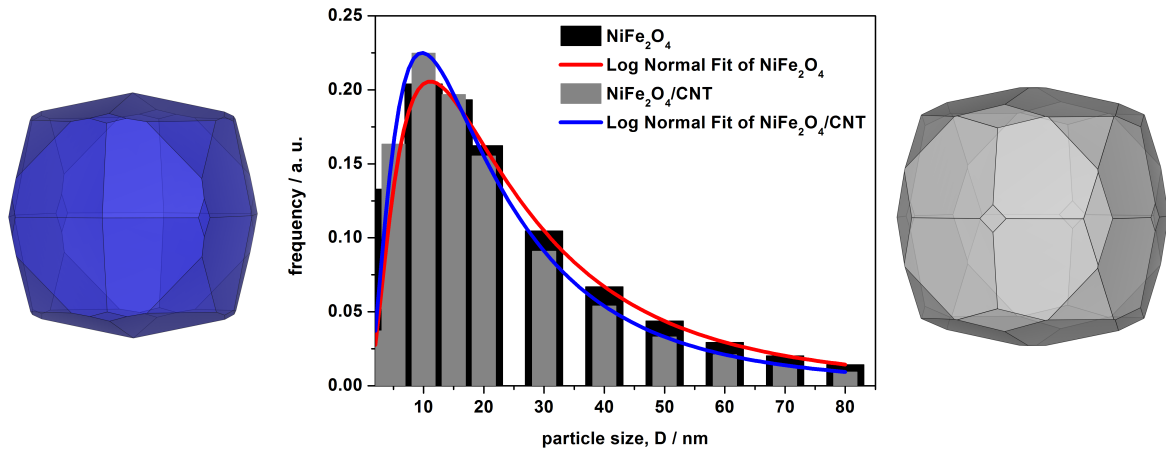


Figure 18: Lognormal domain size distribution (middle) of the as-prepared NiFe<sub>2</sub>O<sub>4</sub> (black) and NiFe<sub>2</sub>O<sub>4</sub>/CNT (grey) nanoparticles. Particle shape of the NiFe<sub>2</sub>O<sub>4</sub> (left) and NiFe<sub>2</sub>O<sub>4</sub>/CNT (right) nanoparticles.

In the TEM image nanoparticles are seen with sizes ranging from ca. 10 to 80 nm (Figure 19, left), in accordance with the size distribution obtained by evaluation of XRD data. NiFe<sub>2</sub>O<sub>4</sub> crystallites are mainly cubes in agreement with the  $(hkl)$ -dependent anisotropic particle morphology. The nanoparticles are interconnected via a network of CNTs. EDX data yield a Fe to Ni ratio of 2:1 (three different positions, Table 5). The representative SAED pattern confirms cubic symmetry (space group:  $Fd\bar{3}m$ , Figure 19, right).

Elemental analysis yields a carbon content of 19.4 wt. % ( $\pm 0.5$  wt. %, average of 3 measurements).

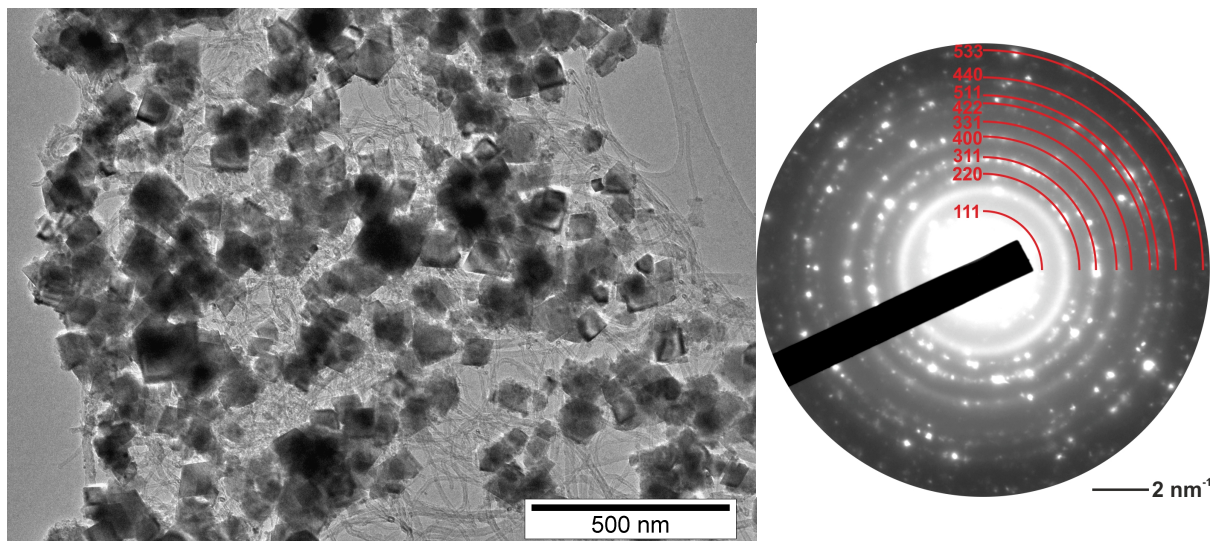
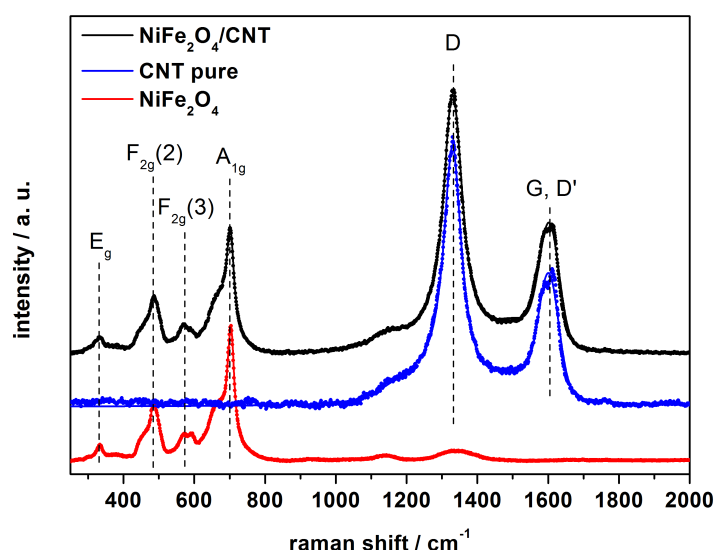


Figure 19: TEM image of the as-prepared NiFe<sub>2</sub>O<sub>4</sub>/CNT nanocomposite (left) and corresponding SAED pattern (right).

**Table 5: Results of the EDX measurements at three different positions of the sample.**

position	NiFe <sub>2</sub> O <sub>4</sub>		NiFe <sub>2</sub> O <sub>4</sub> /CNT	
	Fe / At %	Ni / At %	Fe / At %	Ni / At %
1	67.74	32.26	66.71	33.29
2	70.16	29.84	65.96	34.04
3	66.92	33.08	65.62	34.38
<b>average</b>	<b>68.27</b>	<b>31.73</b>	<b>66.10</b>	<b>33.90</b>

The Raman spectra of NiFe<sub>2</sub>O<sub>4</sub>, NiFe<sub>2</sub>O<sub>4</sub>/CNT and pure CNT are presented in Figure 20. For pure CNTs (blue) three characteristic bands are observed, namely the D-band at 1332 cm<sup>-1</sup>, the G-band (1593 cm<sup>-1</sup>) and the D'-band (1613 cm<sup>-1</sup>). The intensity and energy of the resonances are in agreement with literature data for multiwall carbon nanotubes.<sup>[191-194]</sup> For NiFe<sub>2</sub>O<sub>4</sub> nanoparticles (red) four asymmetric bands are visible. The asymmetric shape with a shoulder on the low energy side of the resonances is characteristic for an inverse spinel structure and a polydisperse size-distribution of nanoparticles respectively.<sup>[195]</sup> The bands can be assigned to E<sub>g</sub>, F<sub>2g</sub>(2), F<sub>2g</sub>(3) and A<sub>1g</sub>. Symmetric bending of oxygen atoms along the Fe-O bond (and Ni-O) can be assigned to the E<sub>g</sub> mode, while asymmetric bending belongs to F<sub>2g</sub>(3). The A<sub>1g</sub> mode is due to symmetric stretching of Fe-/Ni-O bonds and the F<sub>2g</sub>(2) mode is due to asymmetric stretching.<sup>[196,197]</sup> The Raman spectrum of NiFe<sub>2</sub>O<sub>4</sub>/CNT appears as a combination of the two spectra of CNT and NiFe<sub>2</sub>O<sub>4</sub>. The resonances of the spinel and of the CNTs are visible, evidencing that both constituents are intact in the composite.



**Figure 20: Raman spectra of NiFe<sub>2</sub>O<sub>4</sub> (red), NiFe<sub>2</sub>O<sub>4</sub>/CNT (black) and CNT (blue).**

Summarizing the samples NiFe<sub>2</sub>O<sub>4</sub> and NiFe<sub>2</sub>O<sub>4</sub>/CNT contain particles with similar sizes, chemical composition and morphology.

#### 4.1.4 Electrochemical performance

NiFe<sub>2</sub>O<sub>4</sub>/CNT and NiFe<sub>2</sub>O<sub>4</sub> were mixed with carbon black and CMC as binder in 80/10/10 ratio (detailed description is given in section 2.3). In Figure 21 (left) the first and second discharge/charge cycles of the two samples are shown. During the first cycle a fast drop to a long plateau at 0.8 V is observed. The plateau corresponds to an uptake of 6.0 Li per f. u. for NiFe<sub>2</sub>O<sub>4</sub>/CNT and 6.5 Li per f. u. for NiFe<sub>2</sub>O<sub>4</sub>. During the first charge process (Li release) a sloping plateau at about 1.8 V occurs for both samples. The reversible capacity is similar for both materials (1001 mAh g<sup>-1</sup> for NiFe<sub>2</sub>O<sub>4</sub>/CNT and 1092 mAh g<sup>-1</sup> for NiFe<sub>2</sub>O<sub>4</sub>). The irreversible capacity loss during the first cycle is mainly caused by the formation of a solid electrolyte interphase (SEI).<sup>[198]</sup> During the second discharge, the potential drops more slowly to a potential located at 1.0 V, while the charge process is similar for both samples. These results indicate a similar reaction pathway for NiFe<sub>2</sub>O<sub>4</sub>/CNT and NiFe<sub>2</sub>O<sub>4</sub>. We note that pure NiFe<sub>2</sub>O<sub>4</sub> has a larger initial and reversible capacity, indicating that CNTs are inactive and not involved in the reversible Li uptake and release. After the second charge process the reversible capacity of 949 mAh g<sup>-1</sup> is close to the theoretical value (915 mAh g<sup>-1</sup>). The additional capacity may be a result of reversible reactions with the electrolyte or Li adsorption on the large surface of the nanoparticles.<sup>[199–202]</sup>

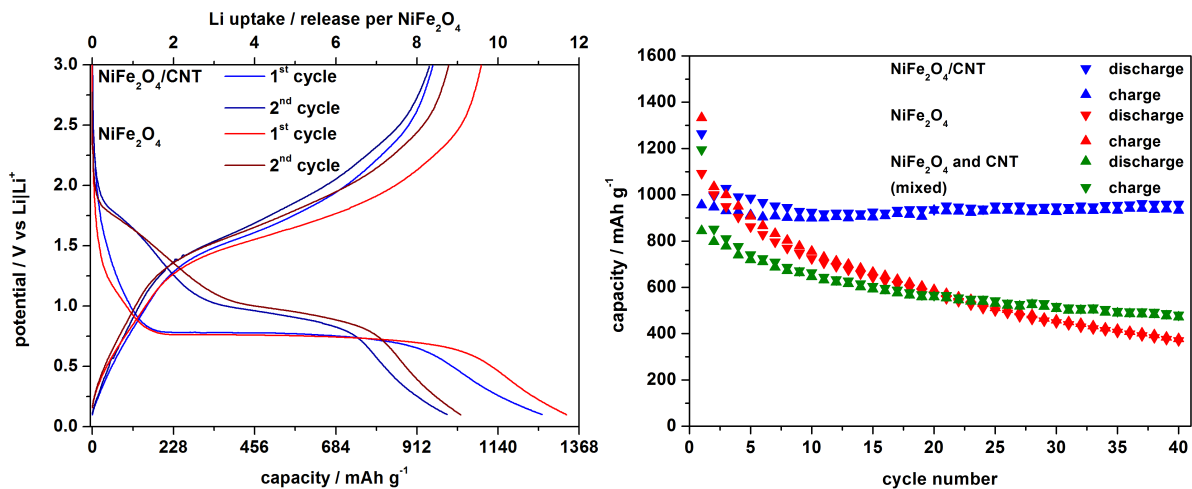


**Figure 21: First and second cycle of NiFe<sub>2</sub>O<sub>4</sub> and NiFe<sub>2</sub>O<sub>4</sub>/CNT (left). Evolution of the capacity during the first 40 cycles for NiFe<sub>2</sub>O<sub>4</sub>, NiFe<sub>2</sub>O<sub>4</sub>/CNT and NiFe<sub>2</sub>O<sub>4</sub> + CNT (ball milled for 30 min at 15 Hz) (right).**

Repeated cycling from 0.1 to 3.0 V lead to a capacity fading for pure NiFe<sub>2</sub>O<sub>4</sub> nanoparticles during the first 40 cycles (Figure 21 right, red triangles). Notably, the NiFe<sub>2</sub>O<sub>4</sub>/CNT composite shows the best cycling stability (Figure 21 right, blue triangles). After 40 cycles the capacity is still 933 mAh g<sup>-1</sup> being larger than the theoretical one and significantly better compared to reports for pure NiFe<sub>2</sub>O<sub>4</sub> nanoparticles.<sup>[92,175–177]</sup> The capacity obtained in the 40<sup>th</sup> cycle is also superior compared to NiFe<sub>2</sub>O<sub>4</sub>/graphene and NiFe<sub>2</sub>O<sub>4</sub>/C, showing similar performance like NiFe<sub>2</sub>O<sub>4</sub> nanofibers.<sup>[90,180,181]</sup> The pure NiFe<sub>2</sub>O<sub>4</sub> nanoparticles were also ball milled with CNTs for 30 min at 15 Hz. This additional experiment did not improve the cycling stability finally yielding 600 mAh g<sup>-1</sup> (Figure 21 right, green triangles). This result demonstrates that

only the synthesis of an interconnected NiFe<sub>2</sub>O<sub>4</sub>/CNT composite stabilizes successfully the cycling capacity, which is in agreement with results for CoFe<sub>2</sub>O<sub>4</sub>/CNT.<sup>[183]</sup>

Cyclic voltammetry curves of NiFe<sub>2</sub>O<sub>4</sub>/CNT and NiFe<sub>2</sub>O<sub>4</sub> exhibit similar shapes for both samples (Figure 22). During the first discharge an intense peak occurs at about 0.5 V. During charging two peaks are visible at 1.7 and 1.9 V. Subsequent cycles show different anodic signals (1.6 V, 0.8 V), while the cathodic peaks occur at an identical potential. After the first cycle new species are formed, which are reversibly cycled during successive Li uptake and release. For NiFe<sub>2</sub>O<sub>4</sub>/CNT the signals are more intense and narrow suggesting a better conductivity of the material. For pure NiFe<sub>2</sub>O<sub>4</sub> nanoparticles a capacity fading is signalled between the second and fifth cycle observable by the decrease of the integrated area between charge and discharge curves. The CV curves measured here are in agreement with data presented in literature.<sup>[90,181,182]</sup>

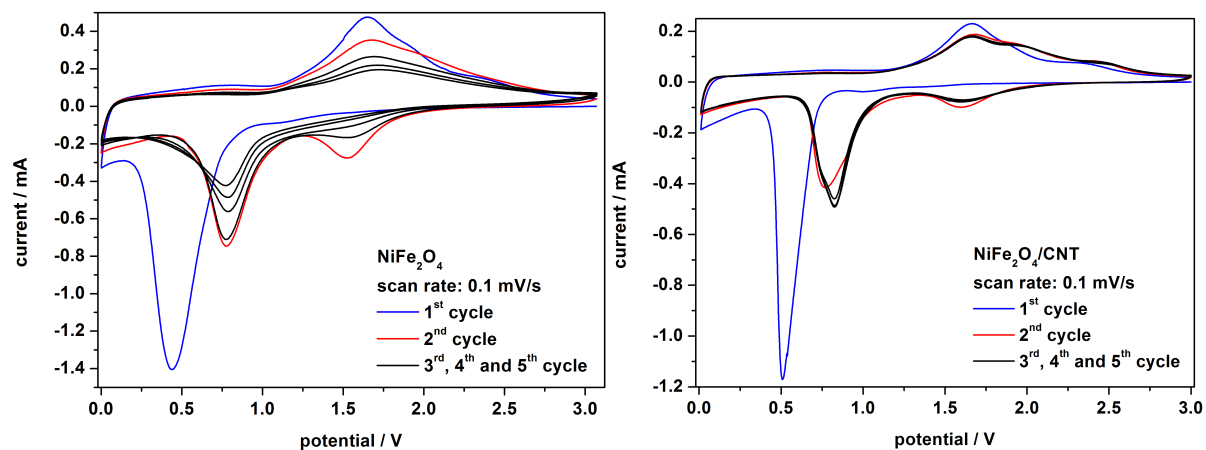


**Figure 22:** CV of the first five cycles measured from 0.0 to 3.0 V at scan rate of 0.1 mV/s for NiFe<sub>2</sub>O<sub>4</sub> (left) and NiFe<sub>2</sub>O<sub>4</sub>/CNT (right).

The composite NiFe<sub>2</sub>O<sub>4</sub>/CNT shows a superior electrochemical performance compared to results presented in literature and pure NiFe<sub>2</sub>O<sub>4</sub> nanoparticles. In the next sections the results of the investigations of the reaction mechanisms occurring during Li uptake and release are discussed.

### 4.1.5 Operando XRD and XAS

The setup of beamline B18 at Diamond Light Source (UK) allows recording *operando* XAS data at the Fe K- and Ni K-edge as well as *operando* XRD patterns simultaneously using one cell. The XAS spectra were collected within 3 min each (Quick EXAFS scan). Afterwards, the energy was adjusted to 8940 eV ( $\lambda = 1.3868 \text{ \AA}$ ) and powder patterns were recorded with a 6K Mythen detector within 3 Min. The reflection positions were corrected using silicon (NIST 640c) as standard reference material. The potential profile of the *in situ* cell is presented in Figure 23. Only marginal differences compared to the Swagelock test cell used in section 4.1.4 are visible which can be explained by the different cell setups (without spring). The first



discharge process (Figure 23, blue) is subdivided into two regions. Region I embodies the uptake of the first 2.5 Li per f. u. and region II covers the discharge to 0.1 V. Region III comprises the first charge up to 3.0 V (Figure 23, red).

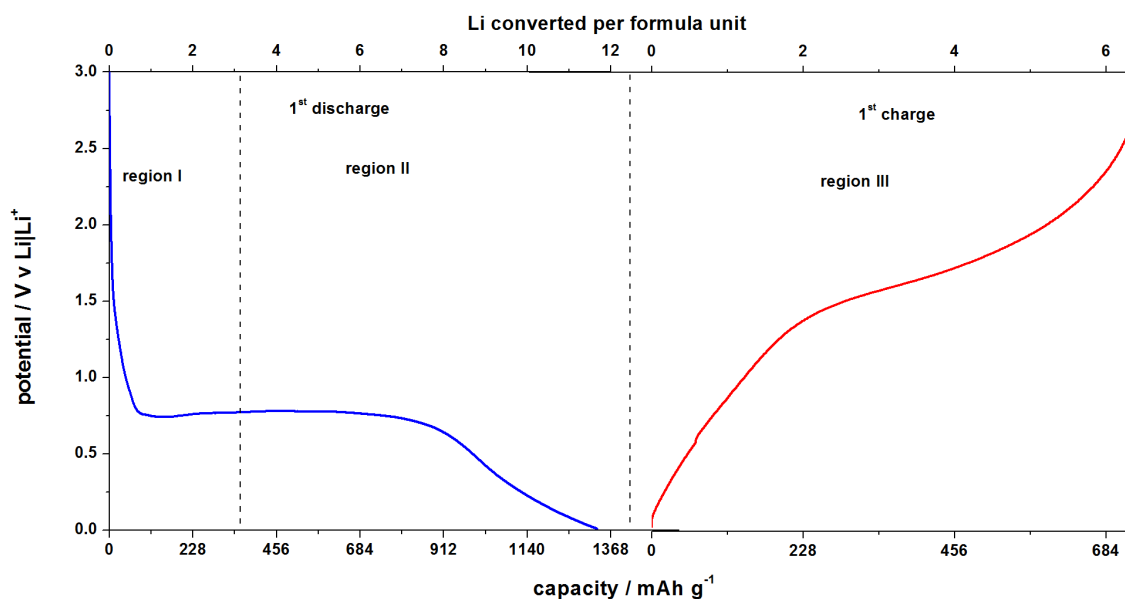


**Figure 23:** Potential curve of the *in situ* cell during first discharge (Li uptake, blue) and first charge (Li release, red). 1 Li converted per formula unit  $\approx 114 \text{ mAh g}^{-1}$ .

*Operando* XRD patterns are displayed in Figure 24. Every second scan is displayed collected during Li uptake (regions I and II, black) and Li release (region III, blue). The XRD pattern of the as-prepared  $\text{NiFe}_2\text{O}_4/\text{CNT}$  (Figure 24, red) is typical for cubic spinel nanoparticles. During region I a fast drop of the potential to 0.8 V occurs. The spinel phase is successively transformed to a new phase as can be seen by the intensity loss of the (311) and (220) reflections, and the simultaneous appearance of new reflections at  $33$  and  $38^\circ 2\theta$ . Similar to  $\text{Mn}_3\text{O}_4$ ,  $\text{ZnFe}_2\text{O}_4$ ,  $\text{MnFe}_2\text{O}_4$ ,  $\text{MgFe}_2\text{O}_4$  and  $\text{CoFe}_2\text{O}_4$  we propose the formation of a monoxide phase.<sup>[68,140,203–205]</sup> During Li uptake  $\text{Fe}^{3+}$  ions are reduced to  $\text{Fe}^{2+}$  accompanied by movement of  $\text{Ni}^{2+}$  and  $\text{Fe}^{2+}$  ions located on tetrahedral sites to neighbouring empty octahedral sites. The phase fraction of the spinel and monoxide phases was determined by quantitative Rietveld analysis (Figure 24, bottom left). The reflection of Cu was used as internal standard for the intensity quantification and the intensity of the reflections of the as-prepared spinel were used as 100 % standard. During Li uptake up to about 0.6 Li the spinel phase fraction decreases, while reflections of the monoxide could not be detected. The ‘consumption’ of the spinel starts at about 0.2 Li which is lower than observed for  $\text{CoFe}_2\text{O}_4$  nanoparticles.<sup>[205]</sup> The lattice parameter  $a$  increases linearly during Li uptake by about 0.3 % up to ca. 2 Li per formula unit. As mentioned above Li uptake is accompanied by reduction of  $\text{Fe}^{3+}$  ions which move from tetrahedral sites to neighboured octahedral sites. It can be assumed that the lattice parameter expansion is due to the larger ionic radius of  $\text{Fe}^{2+}$  residing on the octahedral sites. For the uptake of more than 2  $\text{Li}^+$  the intensity of the reflections of the spinel was too low for reliable lattice parameter refinements. (Figure 24, bottom right).

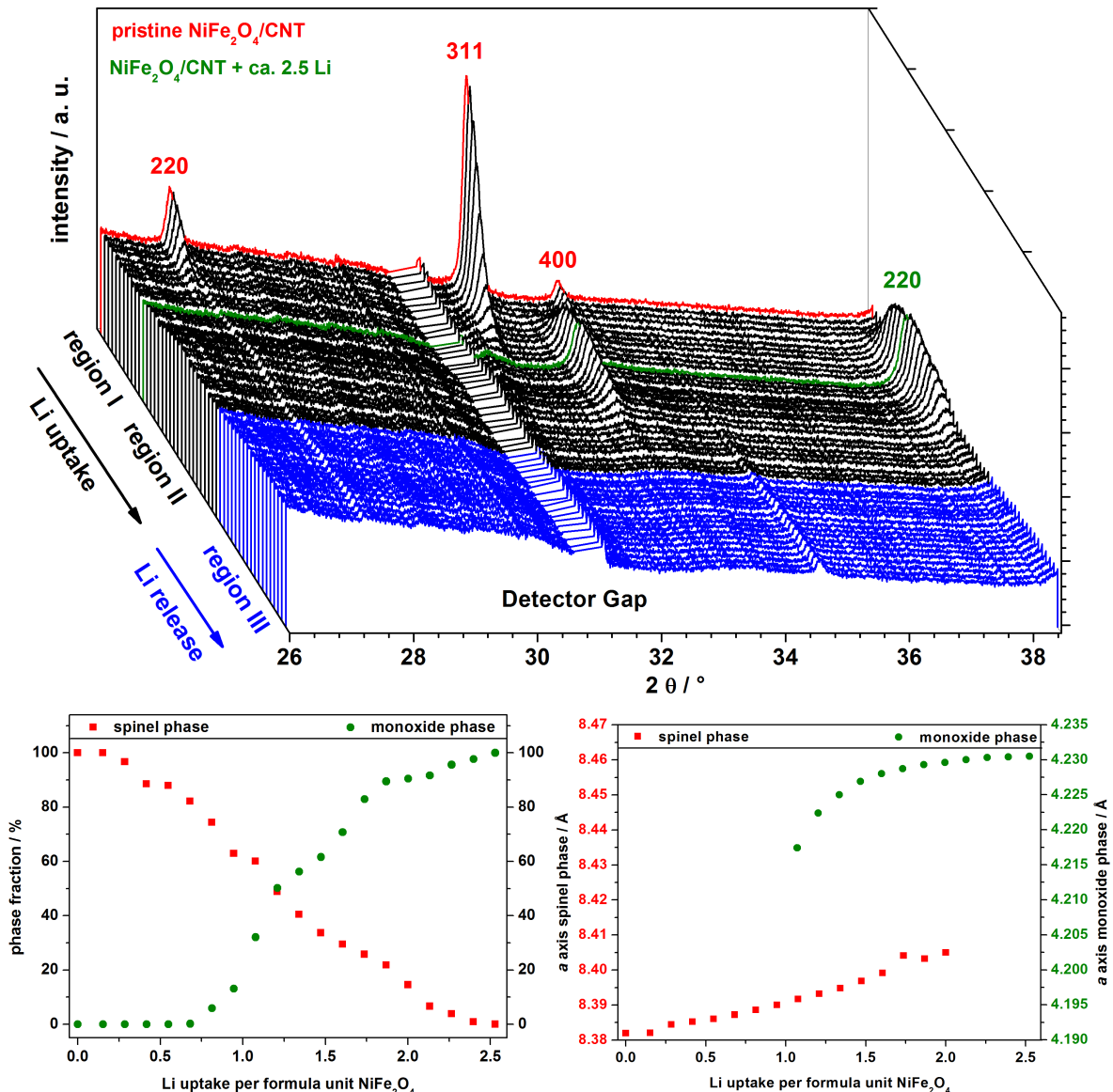


Figure 24: *Operando* XRD powder patterns collected during the first cycle (top); results of quantitative Rietveld refinement (bottom left) and variation of the lattice parameters (bottom right) of the spinel and monoxide phases.

At about 0.7 Li per f. u. reflections of the monoxide phase could be detected with subsequent increasing phase fraction with increasing Li content. At earlier stages of Li uptake the size of coherently scattering domains may be too small to be detected via XRD. After uptake of 2 Li per f. u. the amount of the spinel phase dropped to less than 10 % and reflections of the monoxide phase are dominating. The lattice parameter of the monoxide (cubic,  $Fm\bar{3}m$ ) increases rapidly at the beginning and stays constant after uptake of 2 Li per f. u.. No reflections of the spinel could be detected after uptake of 2.4 Li per f. u.. The cell parameter of the monoxide was refined to 4.231(1) Å with a particle size of 21(4) nm. A comparison with *a*-axis values of NiO (22 nm, 4.179 Å)<sup>[206]</sup> and of nearly stoichiometric FeO nanoparticles (18 nm, 4.305 Å)<sup>[207]</sup> shows that the lattice parameter of the monoxide is in between, *i.e.*, most likely the mixed Ni<sub>x</sub>Fe<sub>y</sub>O phase has been formed. Interestingly, under a thermodynamic point of view formation of a mixed monoxide Ni<sub>1/3</sub>Fe<sub>2/3</sub>O is not possible.<sup>[208]</sup> The formation of

the oxide may be a result of reaction on the nanoscale where classical thermodynamics may play a less dominating role. Phase separation into two separated oxides would require a type of “concerted” movements of  $\text{Fe}^{2+}$  *resp.*  $\text{Ni}^{2+}$  which seems to be not reasonable.

Further Li uptake (region II) transforms the monoxide phase into an amorphous product or into particles which are too small to be detected via XRD. During charge (Li release, region III) no reflections appeared in the XRD patterns, an observation made earlier for several other spinel materials.<sup>[68,203–205]</sup>

*Operando* XAS spectra collected at the Fe and Ni K-edges during region I are presented in Figure 25. For the Fe K-edge spectrum of as-prepared  $\text{NiFe}_2\text{O}_4/\text{CNT}$  the main absorption is located at 7126 eV with a pre-edge signal at 7112 eV. Identical values were reported for  $\text{Fe}^{3+}$  in  $\text{NiFe}_2\text{O}_4$ .<sup>[209,210]</sup> The Ni K-edge is located at 8345 eV with a large intensity of the  $1s \rightarrow 4p$  transition and very weak pre-edge signal which is typical for  $\text{Ni}^{2+}$  in octahedral environment.<sup>[209,211]</sup> The pre-edge feature in the Fe spectrum highly suggests that  $\text{Fe}^{3+}$  ions are at least partially located on tetrahedral sites (Wyckoff position 8a). These observations are in agreement with the inverse spinel structure of  $\text{NiFe}_2\text{O}_4$ .<sup>[190]</sup>

The Li uptake leads to a significant shift of the Fe K-edge to lower energy, while the Ni K-edge is only slightly affected. After uptake of about 2.3 Li the Fe K-edge reached the energy position of  $\text{Fe}^{2+}$  at 7124 eV.<sup>[212]</sup> Simultaneously the pre-edge feature disappeared indicating that  $\text{Fe}^{2+}$  left the non-centrosymmetric tetrahedral position.

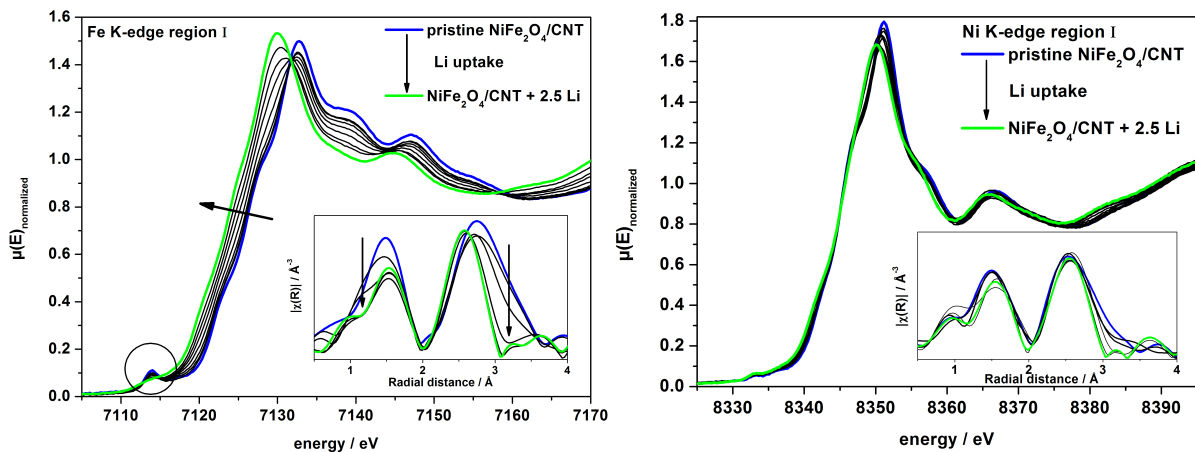


**Figure 25:** *Operando* XAS spectra at Fe K-edge (left) and Ni K-edge (right) during region I. The inset represents FT R-space of the data (not phase shift-corrected).

The insets in Figure 25 display the Fourier transformed (FT R-Space) spectra recorded in region I. Two broad signals are visible representing the first and second neighbours of the absorber atoms. In the crystal structure the first neighbour is  $\text{O}^{2-}$  and hence the signal at 1.5 Å and the shoulder corresponds to M-O bonds. The second signal at 2.7 Å is caused by the next-nearest neighbour, which is a metal cation. While for Ni no changes are seen, the Fe signal becomes more narrow due to movement of Fe cations from the tetrahedra to octahedra. After uptake of about 2.5 Li the shoulder at  $<1.5$  Å is still visible which is may be an effect of the poor crystallinity of the monoxide.

During region II the shape of both spectra changes (Figure 26): the intensity of the  $1s \rightarrow 4p$  transition decreases while a signal typical for metals develops during discharge to 0.1 V. A rotation around isobestic points located at 7124 eV for Fe and 8344 eV for Ni are visible typical for simultaneously reduction of  $\text{Fe}^{2+}$  and  $\text{Ni}^{2+}$  to the metallic state without additional intermediate phases. At the end of region II the spectra at both edges are very similar to that of the metallic reference foils (see also 4.1.6). In the FT R-space the M-O and M-M shells disappear and a peak at about 2 Å appears which is typical for metallic M-M.

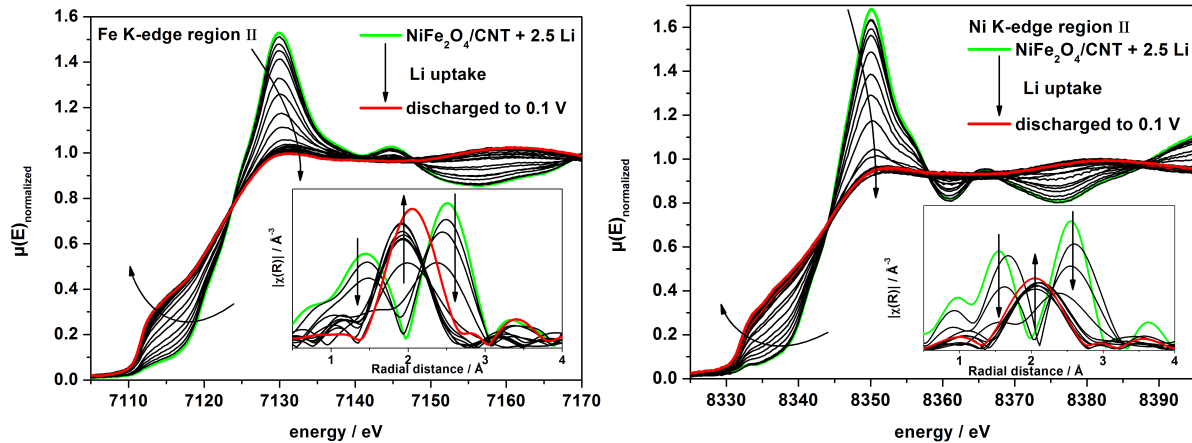


Figure 26: *Operando* XAS spectra at Fe K-edge (left) and Ni K-edge (right) during region II. The inset represents FT R-space curves of the data (not phase-shift corrected).

In region III the *in situ* cell is charged to 3.0 V and Li is released. The Fe and Ni K-edge spectra exhibit a backward rotation around isobestic points at 7126 eV (Fe) and 8343 eV (Ni) (Figure 27), indicating oxidation of metallic Fe and Ni particles. We note that the oxidation of the metallic Fe starts slightly earlier compared to Ni. In the FT R-space the intensity of the metallic M-M shells slightly decreases suggesting oxidation of the metals.

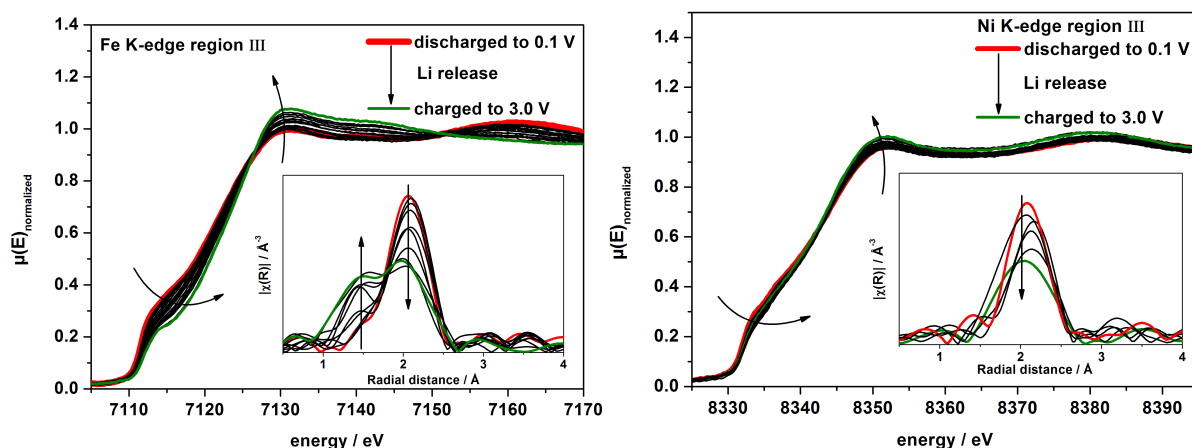


Figure 27: *Operando* XAS spectra at Fe K-edge (left) and Ni K-edge (right) collected during charge operation (region III). The inset represents FT R-space curves of the data (not phase-shift corrected).



#### 4.1.6 $^7\text{Li}$ MAS NMR

$^7\text{Li}$  MAS NMR spectra of  $\text{NiFe}_2\text{O}_4/\text{CNT}$  after uptake of 2.5 Li per f. u., first discharge and first cycle show isotropic peaks near 0 ppm (Figure 28, right). This observation indicates that Li is present as  $\text{Li}_2\text{O}$  in all three samples. If Li-O-M (M = Ni, Fe) bonds would be formed a much larger shift is expected. In all three spectra a large sideband pattern is visible revealing paramagnetic phases in close vicinity of  $\text{Li}_2\text{O}$ . The sample after uptake of 2.5 Li per formula unit displays a narrow sideband pattern and a shift very close to 0 ppm, indicating the formation of  $\text{Li}_2\text{O}$  (Figure 28, blue). After the first discharge the sideband pattern is extremely broadened and shifted towards -10 ppm characteristic for the presence of paramagnetic metallic Ni and Fe nanoparticles (Figure 28, black). After the first cycle the sideband patterns are narrower again and the shift is at 0 ppm (Figure 28, red). Irreversibly consumed Li generates  $\text{Li}_2\text{O}$  and the metallic nanoparticles are oxidized to oxidic species. These results are in good agreement with those reported for Li uptake into  $\text{MnFe}_2\text{O}_4$  and  $\text{MgFe}_2\text{O}_4$  nanoparticles.<sup>[203,204]</sup>

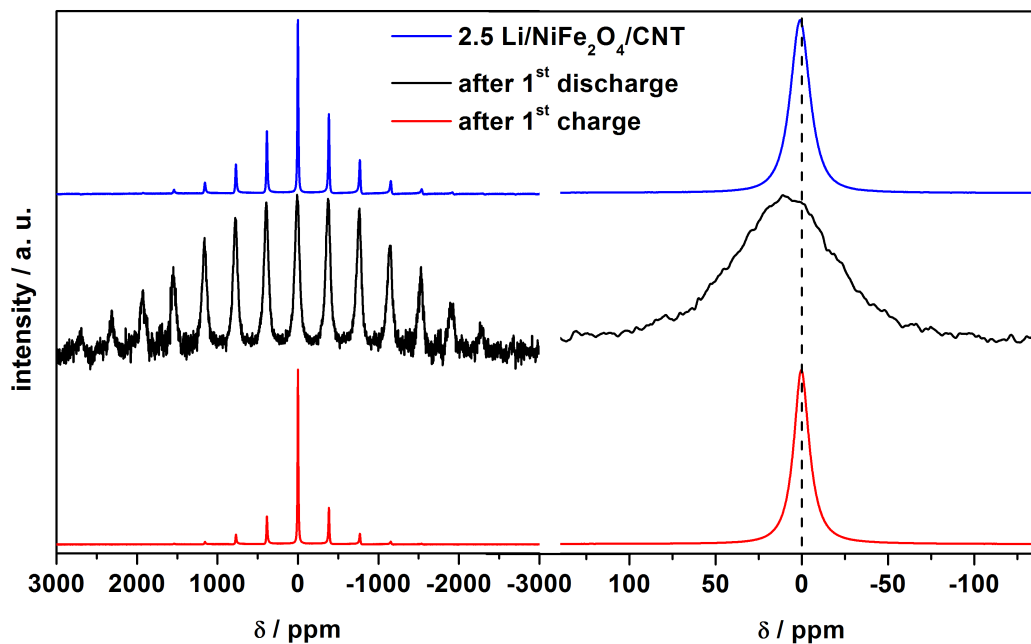
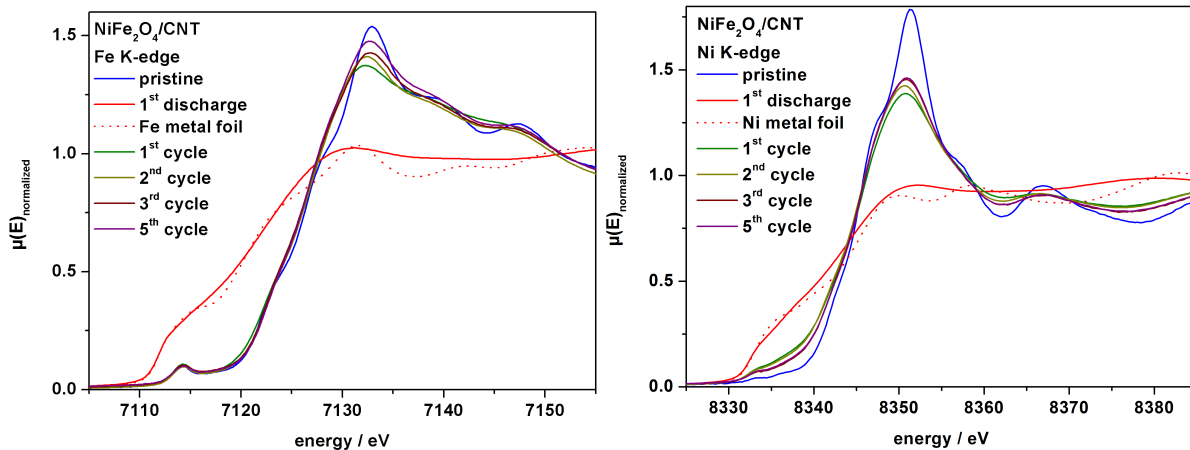


Figure 28:  $^7\text{Li}$  MAS NMR spectra of  $\text{NiFe}_2\text{O}_4$  after uptake of 2.5 Li (blue), first discharge to 0.1 V (black) and first cycle (red).

#### 4.1.7 *Ex situ* XAS

With *in situ* and *operando* investigations only the first cycle could be investigated due to limited availability of beam time at synchrotron sources. Therefore XAS spectra were collected *ex situ* after one, two, three and five cycles. The XANES regions for Fe and Ni K-edges are displayed in Figure 29. As already discussed in section 4.1.5 in pristine  $\text{NiFe}_2\text{O}_4$  the  $\text{Ni}^{2+}$  cations are mainly located on octahedral sites and  $\text{Fe}^{3+}$  resides on tetrahedral and octahedral sites in a nearly 1:1 ratio. The spectra of the metallic reference foils and the material after first discharge are very similar (Figure 29, straight and dotted red line), *i.e.* the cations are converted to the metallic state (see section 4.1.5). The spectra of the Fe K-edge after one, two, three and five cycles (Figure 29) are obviously very similar indicating that after each cycle an identical oxidation state is reached. Compared with the spectrum of the pristine material  $\text{Fe}^{3+}$  is formed after each cycle. Hence, we conclude that the  $\text{Fe}^0 \leftrightarrow \text{Fe}^{\text{III}}$  redox shuttle is stable over many cycles. In addition, a pre-edge feature is always observed at 7114 eV suggesting that  $\text{Fe}^{3+}$  ions are located in a non-centrosymmetric environment after each cycle. The Ni K-edge energy after one, two, three and five cycles is always observed at 8343 eV, *i.e.* identical with that determined for pristine  $\text{NiFe}_2\text{O}_4/\text{CNT}$  containing  $\text{Ni}^{2+}$ . The most pronounced difference between the spectra before and after cycling is the significantly lower intensity of the  $1s \rightarrow 4p$  transition observed for the cycled materials. This depression of the transition is caused by the nanosized or amorphous character of the cycled material.



**Figure 29:** *Ex situ* XAS spectra of pristine  $\text{NiFe}_2\text{O}_4/\text{CNT}$  and after 1<sup>st</sup> discharge, one, two, three and five cycles at Fe K-edge (left) and Ni K-edge (right).

The radial distribution function (FT R-spaces) for Fe and Ni in pristine  $\text{NiFe}_2\text{O}_4$  and after the first discharge are identical with those obtained from the *operando* XAS investigations (Figure 30 and section 4.1.5). After the first, second, third and fifth cycle Fe-O and Ni-O bonds are formed with slightly different distances according to different bond lengths. The second maximum is shifted to lower radial distance representing somewhat shorter M-O-M distances. The newly formed phase is less crystalline compared to the pristine material leading to a lower intensity and broader signals.

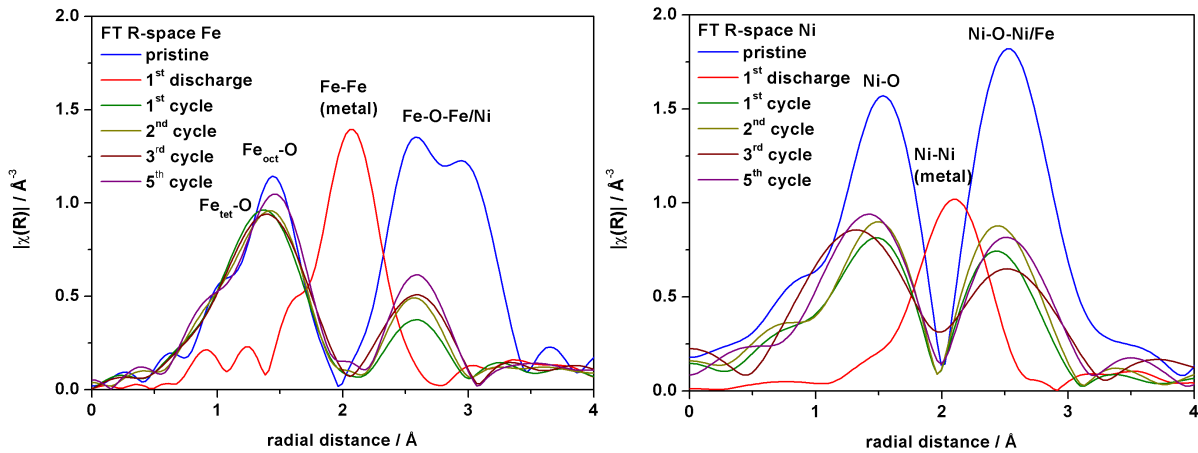


Figure 30: FT radial distance for Fe and Ni absorber atoms for pristine  $\text{NiFe}_2\text{O}_4/\text{CNT}$ , after first discharge and after first, second, third and fifth cycle.

#### 4.1.8 Conclusion of chapter 4.1

$\text{NiFe}_2\text{O}_4$  nanoparticles cross-linked by CNTs were successfully synthesized.  $\text{NiFe}_2\text{O}_4$  nanoparticles crystallizes as inverse spinel with an average volume-weighted size  $d = 36.1(2)$  nm ( $\text{NiFe}_2\text{O}_4/\text{CNT}$ ). The two samples  $\text{NiFe}_2\text{O}_4$  and  $\text{NiFe}_2\text{O}_4/\text{CNT}$  display similar lognormal size distributions, particle shapes and lattice parameters. The electrochemical performance of  $\text{NiFe}_2\text{O}_4/\text{CNT}$  shows a superior increase of the cycling stability compared to pure  $\text{NiFe}_2\text{O}_4$ . The capacity of  $\text{NiFe}_2\text{O}_4/\text{CNT}$  after 40 cycles is still constant at  $933 \text{ mAh g}^{-1}$  a value which is competitive to other spinel oxides (see section 1.2.5).

*Operando* XRD and XAS were performed to study the reaction mechanisms during Li uptake and release of the composite material in detail. At the beginning of the first discharge process only a very small amount of  $\text{Li}^+$  ions is either “consumed” by a surface layer of the spinel or by CNTs. At this stage a fast potential drop to 0.8 V is visible. During further Li uptake  $\text{Fe}^{3+}$  ions are reduced to  $\text{Fe}^{2+}$  accompanied by a movement from tetrahedral 8a site to neighbouring vacant 16c sites. A complete transformation of the spinel structure into a distorted NaCl-like phase is observed after uptake of about 2.4 Li per f. u..  $^7\text{Li}$  MAS NMR supports the assumption that during this process  $\text{Li}_2\text{O}$  is formed. A successive reduction of the intermediate monoxide occurs during further Li uptake and  $\text{Fe}^{2+}$  and  $\text{Ni}^{2+}$  are simultaneously reduced to metallic nanoparticles embedded in a  $\text{Li}_2\text{O}$  matrix. During the charge process  $\text{Li}^+$  ions are released out of the material which is accompanied by oxidation of metallic Ni and Fe to X-ray amorphous  $\text{Ni}^{2+}/\text{Fe}^{3+}$  oxides. The newly generated oxides/CNT species can be reversible cycled many times as evidenced by galvanostatic cycling and CV. The present results suggest that the inability of oxidation of metallic Ni can be overcome by addition of CNTs, which form a conductive interconnected network. <sup>[189]</sup>

### 4.2 The exceptional reaction mechanism during Li uptake into and release out of $\text{Ni}^{\text{II}}\text{Fe}^{\text{III}}\text{Mn}^{\text{III}}\text{O}_4$ nanoparticles

#### 4.2.1 Short introduction

In comparison to the huge number of investigations about transition metal (TM) oxides, reports about spinel oxides with three transition metals are scarce, and reaction mechanisms occurring during Li uptake and release have not been investigated yet. The spinel oxides  $\text{NiFe}_2\text{O}_4$  and  $\text{NiMn}_2\text{O}_4$  show high theoretical and experimental reversible capacities as anode materials in LIBs.<sup>[90,121,123,180,213–216]</sup> A combination of the elements of both spinels may lead to interesting synergistic effects. Moreover, manganese and iron are earth abundant and environmental friendly.

The only report about  $\text{NiMnFeO}_4$  nanoparticles (< 100 nm) showed a reversible capacity of  $750 \text{ mA h g}^{-1}$  after 50 cycles, comparable to  $\text{NiFe}_2\text{O}_4$  and better than  $\text{NiMn}_2\text{O}_4$ .<sup>[217]</sup> To the best of my knowledge, reaction mechanisms with  $\text{NiMnFeO}_4$  as anode material in LIBs were never investigated before.

The binary spinels  $\text{MgFe}_2\text{O}_4$ ,  $\text{CoFe}_2\text{O}_4$ ,  $\text{MnFe}_2\text{O}_4$  and  $\text{ZnFe}_2\text{O}_4$  crystallize in a cubic structure. For this type of spinels a NaCl-type intermediate monoxide phase was identified during the first discharge (Li uptake).  $\text{NiFe}_2\text{O}_4$  crystallizes as an inverse spinel ( $Fd\bar{3}m$ ) while  $\text{NiMn}_2\text{O}_4$  as normal spinel ( $Fd\bar{3}m$ ) or tetragonally distorted ( $I4_1/amd$ ).<sup>[218,219]</sup> Combining these spinels,  $\text{NiMnFeO}_4$  forms a disordered spinel structure, which is discussed in detail later.<sup>[215]</sup> Therefore, the reactions mechanisms are expected to be different compared to already investigated materials  $\text{MFe}_2\text{O}_4$  (M = Mg, Co, Mn, Zn).

Normally, PVDF is used as binder dissolved in toxic N-methylpyrrolidone. Hence, substitution by an environmental-friendly and water-soluble binder is recommended. Here we present the simple synthesis of  $\text{NiMnFeO}_4$  nanoparticles and investigated the anode material for future application in LIBs. The electrode was prepared applying the environmental-friendly and water-soluble NaPAA binder. The focus of the study is to clarify the reaction mechanisms. The material was characterized with XRD, ESEM, EDX and TEM. The reaction pathway during Li uptake and release was investigated in detail by *operando* XRD and XAS, *ex situ*  $^7\text{Li}$  MAS NMR, XAS and TEM.



#### 4.2.2 Synthesis of NiFeMnO<sub>4</sub> Nanoparticles

The NiFeMnO<sub>4</sub> nanoparticles were synthesized by dissolving 5 mmol Ni(NO<sub>3</sub>)<sub>2</sub>·6H<sub>2</sub>O (97 %, Merck), 5 mmol Fe(NO<sub>3</sub>)<sub>3</sub>·9H<sub>2</sub>O (98 %, Riedel-de Haen), and 5 mmol Mn(NO<sub>3</sub>)<sub>2</sub>·4H<sub>2</sub>O (98 %, Grüssing) in 20 ml deionized water. 5 ml nitric acid (65%, p.A., Grüssing) was added to the solution by stirring at room temperature. Afterwards 10 mL Ethylenglycol (99 %, Merck Millipore) was added and the mixture was heated at 80 °C until a viscous gel is formed. Afterwards the gel was dried at 120 °C for 24 h. The solid was ground in an agate mortar and heated at 400 °C in a pre-heated oven in air for 3 h.<sup>[220]</sup>

#### 4.2.3 Characterization of the as-prepared product

The XRD pattern of the as-prepared NiMnFeO<sub>4</sub> nanoparticles (Figure 31 left) suggests an ordered cubic spinel structure (space group: *Fd* $\bar{3}m$ ). But a closer inspection reveals that the relative intensity of the (400) reflection is different compared to the calculated value and the (440) reflection is significantly broadened. These observations indicate a disorder in the spinel structure which is caused by atoms residing on “forbidden” (interstitial) sites.<sup>[221]</sup> The best refinement of the powder pattern was achieved assuming an interwoven structure consisting of the spinel and the rock salt structure (space group: *Fm* $\bar{3}m$ ). Similar observations were reported for MgAl<sub>2</sub>O<sub>4</sub> and ZnAl<sub>2</sub>O<sub>4</sub>.<sup>[222–224]</sup> The lattice parameter of the NaCl-like component is refined to  $a = 4.1694(2)$  Å, which matches with the data of Bunsenite (NiO) nanoparticles, indicating that mainly Ni<sup>2+</sup> ions occupy octahedral sites.<sup>[206]</sup> The lattice parameter of the spinel phase is  $a = 8.3903(2)$  Å.

The lognormal size distribution of the coherently scattering domains reveals particles in the range of nanometers with most crystallites between 4 and 8 nm (Figure 31 right). It is noteworthy that both the ordered and disordered spinel phase exhibit a similar size distribution.

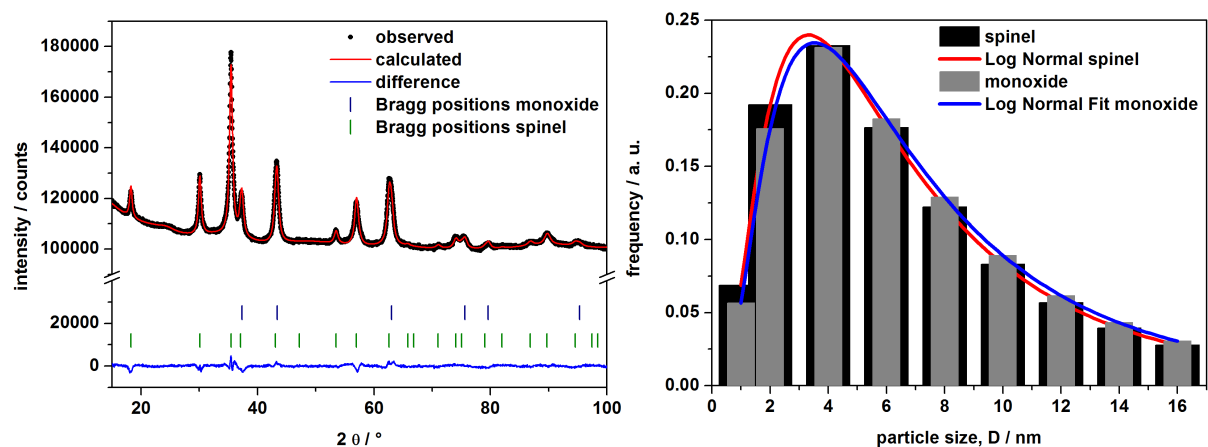


Figure 31: LEFT: XRD powder pattern (black) of the as-prepared NiMnFeO<sub>4</sub> nanoparticles with the refined intensities (red), difference curve (blue) and Bragg positions (green). RIGHT: Lognormal size distribution of the coherently scattering domains for the spinel phase (black) and crystallites adopting the NaCl-type structure (grey).

The EDX measurements performed at four different positions of the NiMnFeO<sub>4</sub> sample yields Mn: 35.5 At%, Fe: 32.4 At%, Ni: 32.1 At % (Table 6) which is close to the theoretical values.

**Table 6: EDX results at four different positions of the NiMnFeO<sub>4</sub> sample.**

Position	Mn / At %	Fe / At %	Ni / At %
I	35.5	33.1	31.6
II	35.7	32.6	31.7
III	35.5	33.0	31.4
IV	35.1	31.0	33.8
average	<b>35.5</b>	<b>32.4</b>	<b>32.1</b>

A transmission electron microscopy (TEM) image of NiMnFeO<sub>4</sub> nanoparticles is displayed in Figure 32 (top left). The sample consists of polydisperse agglomerated particles in a range from 8 to 12 nm, which is in agreement with the lognormal size distribution of the coherently scattering domains determined from the XRD powder pattern.

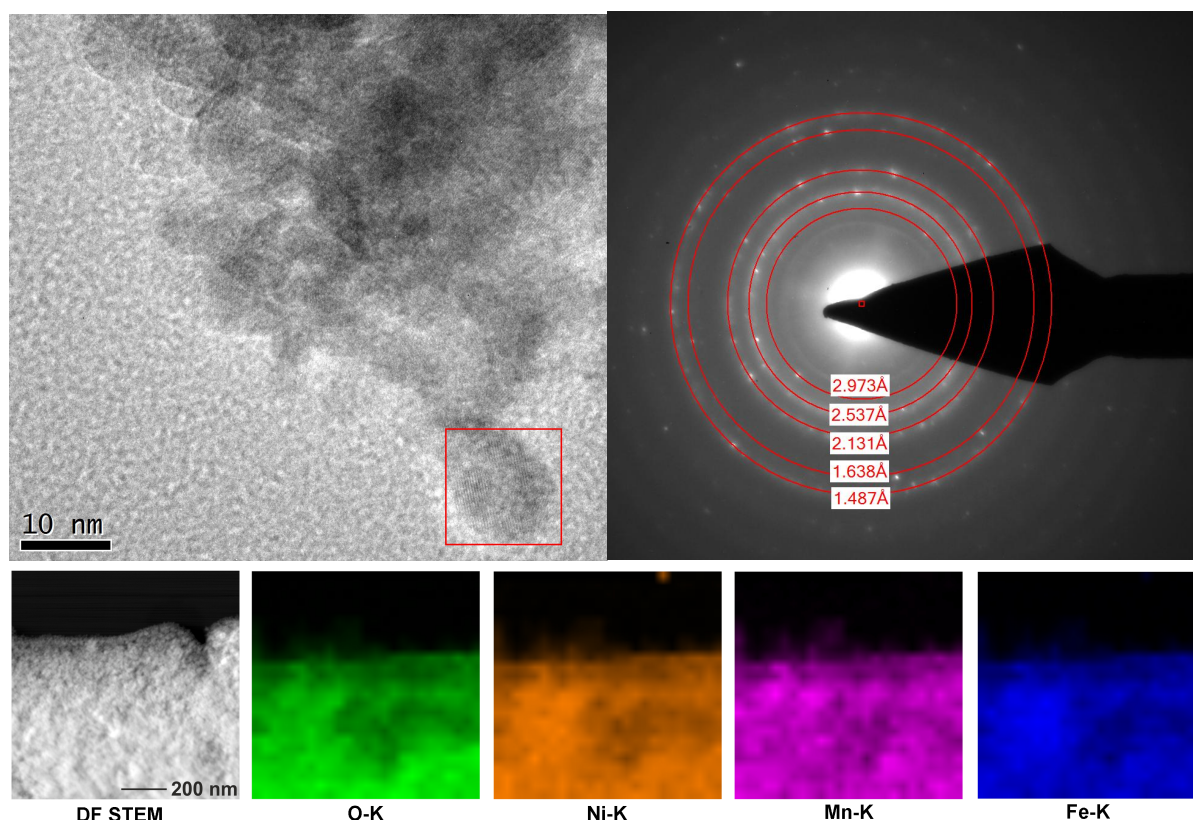


**Figure 32: HRTEM image (top left) and SAED pattern (top right) of pristine NiMnFeO<sub>4</sub> nanoparticles. Bottom: EDX mapping at oxygen, nickel, manganese and iron K-edge in a 0.6 x 1.0 μm area.**

The representative selected area electron diffraction (SAED) pattern (Figure 32, top right) can be assigned to the cubic spinel phase. The TEM-EDX mapping evidences a homogenous distribution of Ni, Mn, Fe and oxygen (Figure 32 bottom), *i.e.* no separation of

NaCl-like domains and the spinel is suggesting that the model of interwoven ordered and disordered spinel structure is correct.

#### 4.2.4 Electrochemical performance

For the investigation of the electrochemical performance NiMnFeO<sub>4</sub> nanoparticles were mixed with C65 and NaPAA (ratio: 70/20/10). In a potential range from 0.1 to 3.0 V the capacity slightly decreases during the first 10 cycles (Figure 33 a and b). Stabilization of the capacity occurs after the 10<sup>th</sup> cycle leading to a constant value of about 830 mAh g<sup>-1</sup> and a Coloumb efficiency near 100 %. The preparation of the electrode with water-soluble NaPAA binder leads to a superior cycling stability compared to electrodes prepared with PVDF.<sup>[217]</sup>

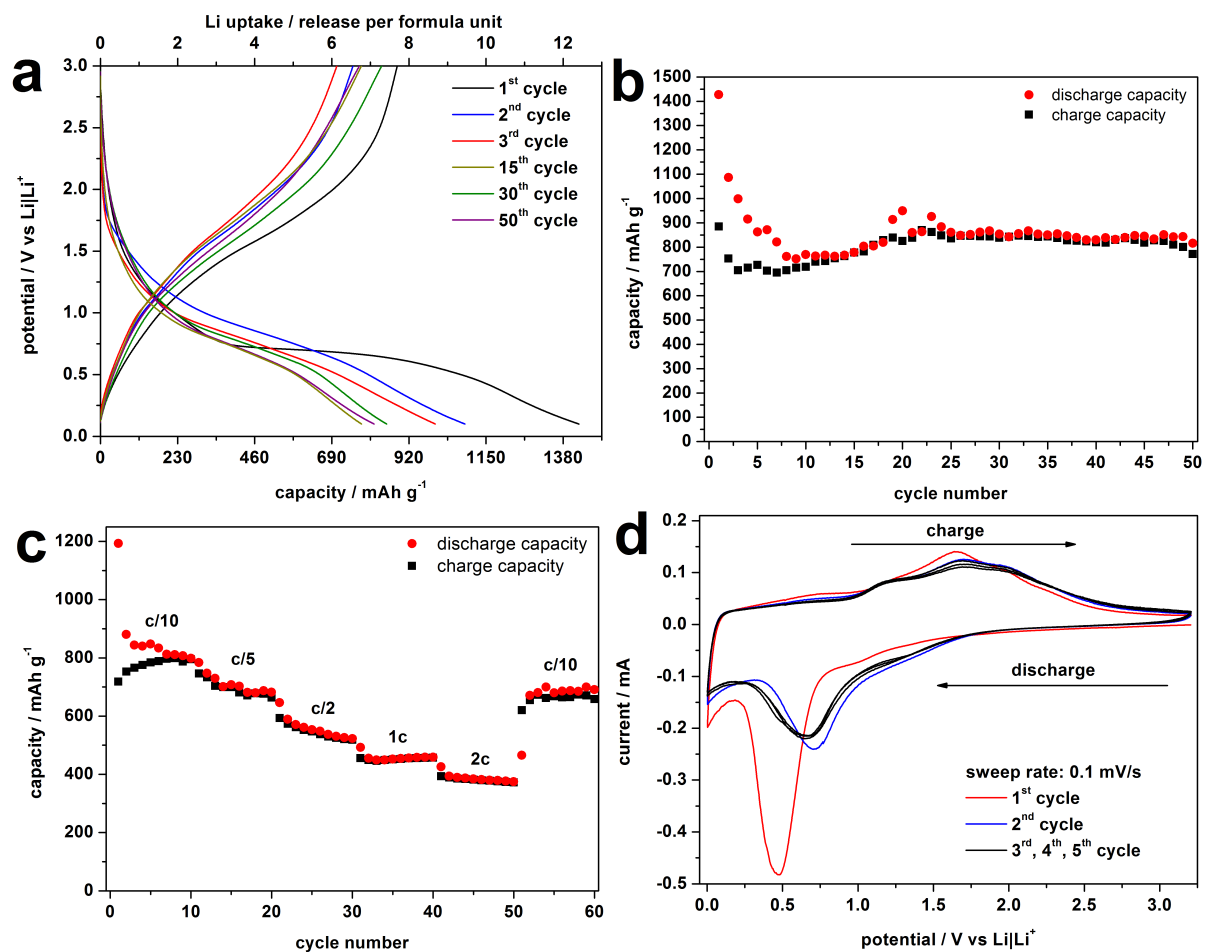


**Figure 33: Electrochemical performance of NiMnFeO<sub>4</sub> nanoparticles in a potential range from 0.1-3 V: a) Potential curves during galvanostatic 115 mAh g<sup>-1</sup> ≈ 1 Li cycling, b) capacity of galvanostatic cycling during first 50 cycles, c) capacity during cycling at different currents, d) cyclic voltammetry (CV) in a potential range from 0 to 3.2 V with a sweep rate of 0.1 mV/s.**

The discharge and charge curves clearly differ between the first and all following cycles (Figure 33a). The discharge curve displays first a steep drop followed by a plateau at 0.8 V (Figure 33a, black line). The capacity for the first discharge of 1427 mAh g<sup>-1</sup> is larger than the theoretical value, which is a common observation for most transition metal spinel oxides (compare Table 2). The reversible capacity for the first cycle of 885 mAh g<sup>-1</sup> (capacity loss 38 %) is close to the theoretical capacity (918 mAh g<sup>-1</sup>). The irreversible capacity loss during

the first cycle is caused by side reactions of the electrolyte, *i.e.* due to the formation of the SEI.<sup>[198]</sup>

Discharge and charge curves of the material at different currents (different C-rates) are displayed in Figure 33c. For the C/10 rate the capacity is about 830 mAh g<sup>-1</sup>. An increase of the current leads to a decrease of the capacity: C/5 about 700 mAh g<sup>-1</sup>, C/2 ca. 550 mAh g<sup>-1</sup>, 1C ca. 450 mAh g<sup>-1</sup>, 2C ca. 380 mAh g<sup>-1</sup>. After the fast cycling of the material the capacity is still about 700 mAh g<sup>-1</sup> for the cycles 50 - 60, indicating that the large capacity recovers after cycling at high current density.

In the CV curve (Figure 33d) the first 5 cycles are presented measured in a potential range from 3.2 to 0 V. In the first discharge curve a strong signal is observed at 0.5 V. The first and following charge curves show a broad signal ranging from about 1.2 to 2.3 V. These events consist of more than one signal indicating that more than one oxidation process takes place during charging. For the second and following discharge curves the signal shifts to about 0.8 V and becomes slightly broader. Obviously, during the first cycle new products are formed which can be reversibly cycled for many times.

### 4.2.5 Operando XAS

*Operando* XAS spectra were collected at ANKA XAS beamline in transmission mode. The Mn, Fe and Ni K-edges have only a small energy difference enabling quick XAS measurements with just one cell. In Figure 34 (left) the potential curve during the first discharge of the XAS cell is shown which is similar to that obtained during the galvanostatic measurement (see section 4.2.4). The slightly smaller capacity is a result of the absence of a spring in the *in situ* cell, causing the inactivation of a small amount of the material. Each start of a XAS scan is marked with colored circles (Mn = red, Fe = blue, Ni = green).

In the XANES spectra (Figures 34 & 35) the thick blue line represents the spectra of the pristine material. The Mn K-edge is located at 6551 eV (determined by the maximum of the first derivative) and a pre-edge feature occurs at 6539 eV (Figure 34, thick blue line). These values match with those reported for Mn<sup>3+</sup> in Mn<sub>2</sub>O<sub>3</sub> indicating that Mn is trivalent in NiMnFeO<sub>4</sub>.<sup>[225]</sup> For the Fe K-edge a pre-edge signal is located at 7113 eV and the main peak at 7124 eV, in agreement with data observed for Fe<sup>3+</sup> in MFe<sub>2</sub>O<sub>4</sub> (M = Co, Mn, Ni) nanoparticles.<sup>[209,226,227]</sup> For Ni no pre-edge signal is observed and the main resonance is located at 8343 eV. The XANES spectrum resembles that observed for Ni<sup>2+</sup> in NiFe<sub>2</sub>O<sub>4</sub> nanoparticles.<sup>[209,211]</sup> The most intense signal bases on the 1s→4p transition. The pre-edge is either a very weak quadrupole transition 1s→3d or a dipole allowed more intense 1s→3d/4p transition (hybridized orbital). The latter is observed for absorbers in non-centrosymmetric symmetry (*e.g.* tetrahedron) because p orbitals with t<sub>2</sub> symmetry can mix with d orbitals with symmetry t<sub>2</sub> and e. For absorber atoms in octahedral environment pre-edge features may occur by the weak 1s→3d transition with an intensity which is only between 1 and 3 % of the



dipole allowed transition. Because no pre-edge peak occurs for Ni it must be assumed that  $\text{Ni}^{2+}$  is located on octahedra and Mn and Fe are partially located on tetrahedral sites. This assumption is in line with results reported for bulk  $\text{NiMnFeO}_4$ .<sup>[228]</sup>

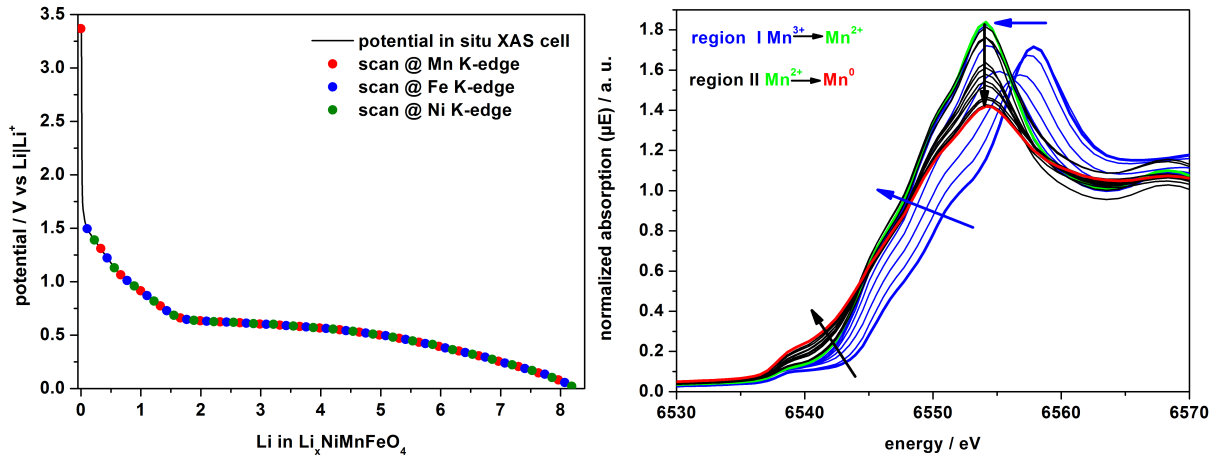


**Figure 34:** Potential curve of the discharge process recorded with the *in situ* XAS cell. Colored cycles mark XAS scans at Mn (red), Fe (blue) and Ni (green) K-edges (left). *Operando* XAS spectra (right) at the Mn K-edge collected during the first discharge process. Blue lines (region I) spectra for uptake of about 2 Li per formula unit; black lines (region II): spectra for Li uptake from 2 to 8 Li per formula unit; red line: end of discharge.

In the beginning of Li uptake, no significant changes are observed for the Ni and Fe K-edges, while the Mn XANES spectra exhibit a strong shift to lower energies (Figure 34 right) indicative for reduction of  $\text{Mn}^{3+}$ . After uptake of about 1 Li per formula unit the edge energy is 6548 eV similar to the value for  $\text{Mn}^{2+}$  in  $\text{MnO}$ .<sup>[229]</sup> Increasing the Li content per f. u. the Fe K-edge shifts to lower energy (Figure 35 left) and after uptake of about 2 Li per f. u.  $\text{Mn}^{3+}$  and  $\text{Fe}^{3+}$  are both reduced to the divalent state. During the reduction the intensity of the pre-edge signal decreases for Fe and Mn suggesting a change of the local symmetry, most probably the ions moved from tetrahedral to octahedral sites.

Further Li uptake (>2 Li per formula unit) leads to a continuous decrease of the  $1s \rightarrow 4p$  transition for all three elements and a signal develops below the absorption edge typical for the metallic state. Furthermore, the spectra rotate around isosbestic points located at 6545 eV for Mn, at 7123 eV for Fe and at 8341 eV for Ni similar to prior observations. At the end of the first discharge process all spectra are very similar to those of the metallic reference foils, indicating metallic nanoparticles are formed. We note that similar mechanisms were observed for  $\text{NiCo}_2\text{O}_4$ : first trivalent  $\text{Co}^{3+}$  ions were reduced to  $\text{Co}^{2+}$  and afterwards metallic Co and Ni were formed.<sup>[230]</sup> The reduction of  $\text{Mn}^{3+}$  to  $\text{Mn}^{2+}$  in a first step was also reported for  $\text{Mn}_3\text{O}_4$  with subsequent reduction of the intermediate product  $\text{MnO}$  followed by formation of metallic Mn at the end of discharge.<sup>[68]</sup>

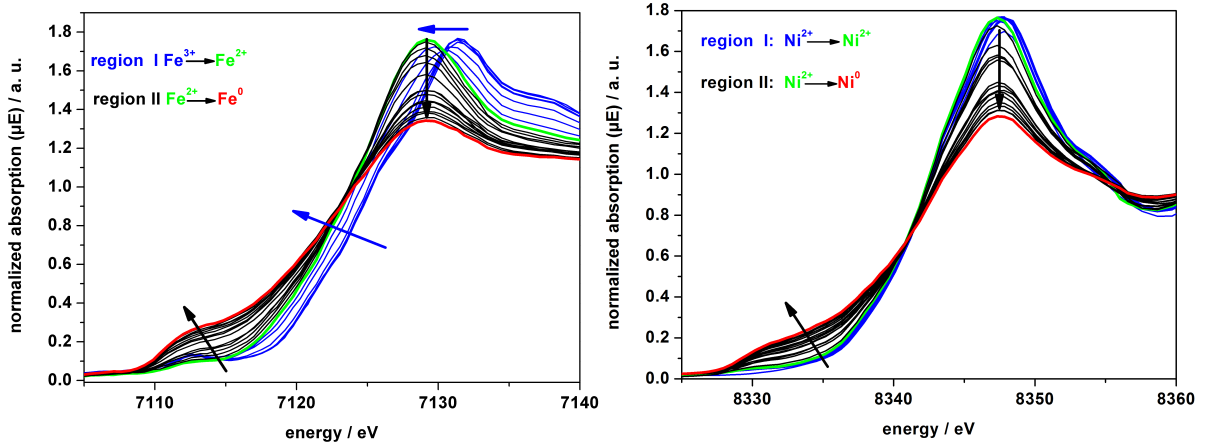


Figure 35: *Operando* XAS spectra at Fe K-edge (left) and Ni K-edge (right) collected during the first discharge process. Blue lines (region I) spectra for uptake of about 2 Li per formula unit; black lines (region II): spectra for Li uptake from 2 to 8 Li per formula unit; red line: end of discharge.

#### 4.2.6 *Ex situ* XAS

The limited beam time at the synchrotron source allowed *operando* XAS experiments only for the first cycle. Additional *ex situ* XAS spectra were collected after 1, 2, 3 and 5 cycles (Figure 36 and 37). The spectra of the pristine material are similar for all three K-edges (Figure 36 and 37, blue line) compared with those collected *operando*. At the end of the first discharge all cations are reduced to the metallic state and like in the spectra obtained with *operando* XAS the spectra resemble that of the metallic reference foils (Figure 36 and 37, black straight and dashed line). After the first cycle the Mn K-edge (Figure 36 left) is shifted to lower energy (6548 eV) with a typical value for  $\text{Mn}^{2+}$ .<sup>[229]</sup> A similar observation was made for the other Mn containing materials demonstrating that metallic Mn cannot be oxidized to  $\text{Mn}^{3+}$  but only  $\text{Mn}^{2+}$ , *i.e.* the capacity loss reported for Mn oxides is partially due to the inability of the formation of  $\text{Mn}^{3+}$ .

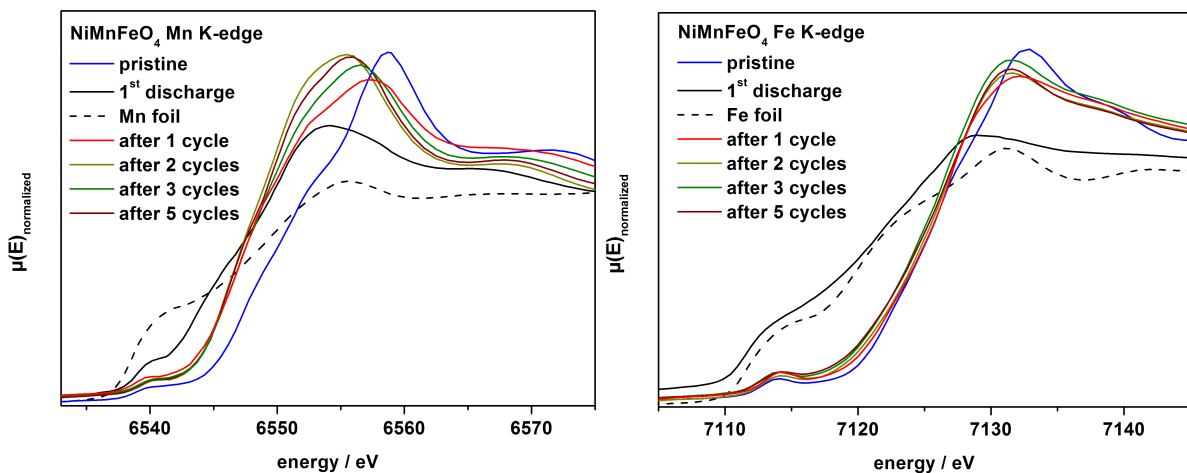


Figure 36: *Ex situ* XAS spectra at the Mn (left) and Fe K-edges (right) of pristine  $\text{NiMnFeO}_4$  (blue), after first discharge (black straight line) and after 1 (red), 2 (yellow), 3 (green) and 5 cycles (dark red).

In contrast, the Fe K-edge spectra after 1, 2, 3 and 5 cycles (Figure 36 right) are very similar to the pristine material suggesting that the reaction  $\text{Fe}^0 \leftrightarrow \text{Fe}^{3+}$  is reversible over many

cycles. In Figure 37 (right), the Ni K-edge spectra are shown after 1, 2, 3 and 5 cycles. After the first cycle metallic Ni is oxidized to  $\text{Ni}^{2+}$  during charge process (edge energy: 8342 eV). But after 2, 3 and 5 cycles the shape of the spectra is successively changing and the signal of the  $1s \rightarrow 4p$  transition continuously loose intensity, *i.e.* the  $\text{Ni}^0 \leftrightarrow \text{Ni}^{2+}$  redox reaction is not stable over many cycles, and a part of Ni remains in the metallic state. This is another reason for the capacity loss, observed during repeated cycling up to more than 50 cycles (see section 4.2.4).

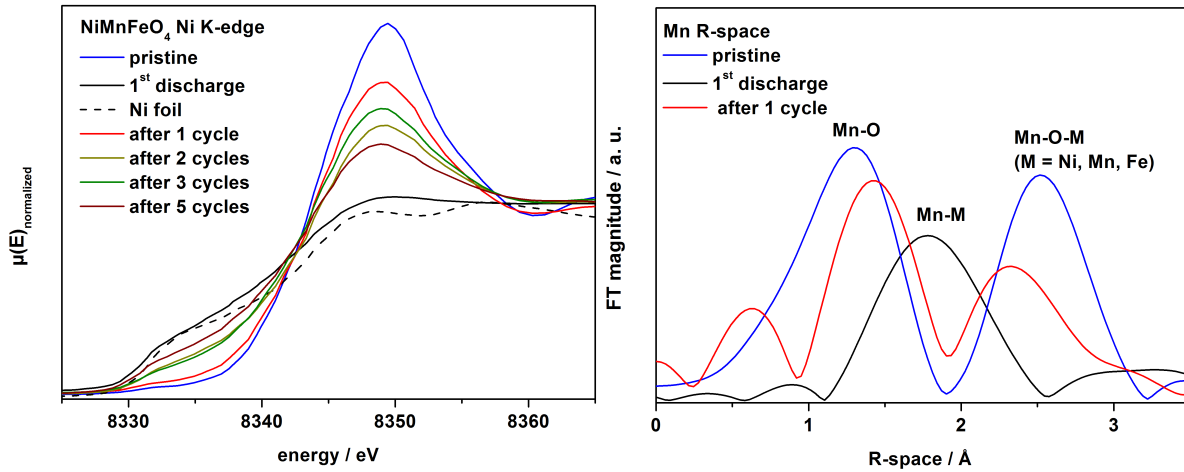


Figure 37: Left: *Ex situ* XAS spectra at the Ni K-edge of pristine  $\text{NiMnFeO}_4$  (blue), after first discharge (black straight line) and after 1 (red), 2 (yellow), 3 (green) and 5 cycles (dark red). Right: FT R-Space for Mn of pristine (blue), after first discharge (black) and after first cycle (red).

The Fourier transformed EXAFS spectra for the pristine material, after the first discharge and after the first cycle are shown in Figures 37 right and 38. For  $\text{NiMnFeO}_4$  the two signals represent the M-O distance at 1.4 Å ( $M = \text{Fe, Mn, Ni}$ ) and the M-M distance cross-linked by  $\text{O}^{2-}$  at about 2.6 Å.

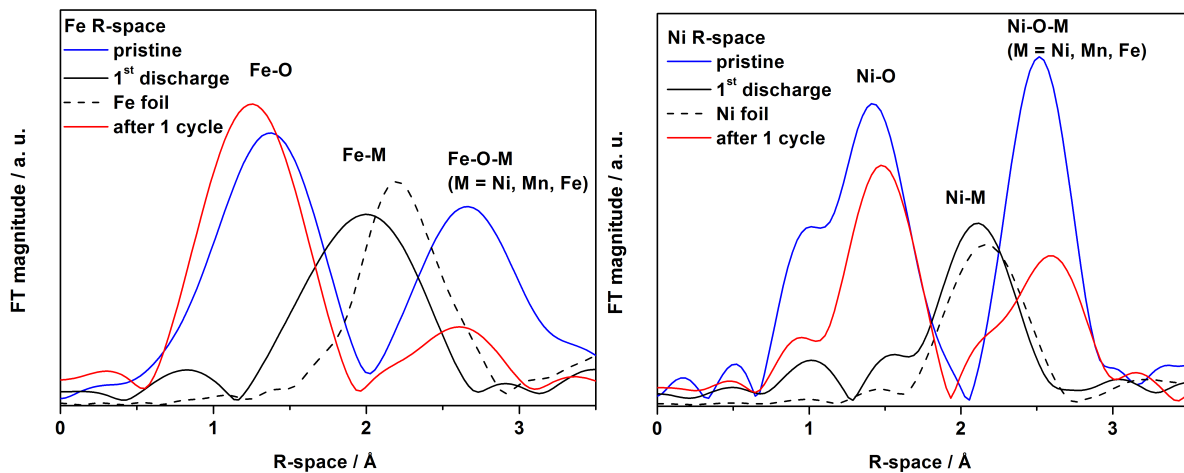


Figure 38: FT R-Space of Fe (left) and Ni (right) for pristine (blue), after first discharge (black) and after the first cycle (red).

After discharge to 0.1 V the M-O and M-O-M signals disappeared and a new path representing direct M-M bonds developed at about 2.0 Å in each spectrum (Figure 37 & 38). After charging the sample to 3.0 V (after one cycle) the signal for the M-M paths decreased.

Simultaneously the signals representing M-O/M-O-M bonds appear again. Summarizing, the *ex situ* XAS results indicate reversible M-O bond formation after one cycle for all three cations.

### 4.2.7 Ex situ Li MAS NMR

The XAS experiments yield information about the transition metal ions but no information about the direct environment of the  $\text{Li}^+$  ions is available.  $^7\text{Li}$  MAS NMR closes this gap of information. Paramagnetic ions in the direct neighbourhood of  $\text{Li}^+$  ions can have strong effects on the NMR spectra leading to large shift values.<sup>[231]</sup>  $^7\text{Li}$  MAS NMR spectra of  $\text{NiMnFeO}_4$  nanoparticles after uptake of 2 Li per f. u. and after complete discharge are displayed in Figure 39. The spectrum after uptake of 2 Li per f. u. shows narrow signals with the most intense peak close to 0 ppm (Figure 39, black). The small shift excludes paramagnetic neighbours in the direct environment of  $^7\text{Li}$  and indicates the formation of a Li containing phase without transition metals. The most probable conclusion is that after uptake of 2 Li per f. u.  $\text{Li}_2\text{O}$  is formed.<sup>[203,204]</sup> For the material discharged to 0.1 V a similar shift close to 0 ppm is observed. Nevertheless, the isotropic peaks are broadened and the width of the spinning sideband pattern is increased (Figure 39, red line). This phenomenon is caused by the formation of metallic Ni, Mn and Fe particles.

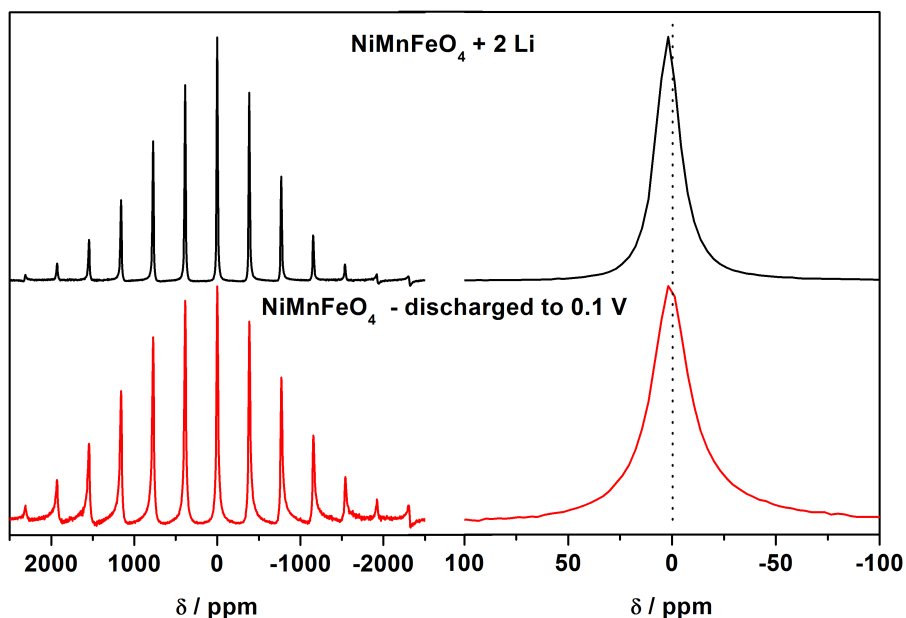


Figure 39:  $^7\text{Li}$  MAS NMR spectra of  $\text{NiMnFeO}_4$  nanoparticles after insertion of 2 Li (black) and after discharge to 0.1 V (red). Left: full spinning sideband patterns; right: magnified view of the region of the isotropic peaks.

### 4.2.8 Operando XRD

In Figure 40 powder patterns collected during Li uptake up to about 2 Li per f. u. are presented together with the galvanostatic potential of the *in situ* cell. As mentioned above the



pattern of pristine material was refined as a mixture of spinel and a NaCl-type structure (section 4.2.3). The reflections of elemental Cu are caused by the setup of the *in situ* cell (see section 2.2.2).

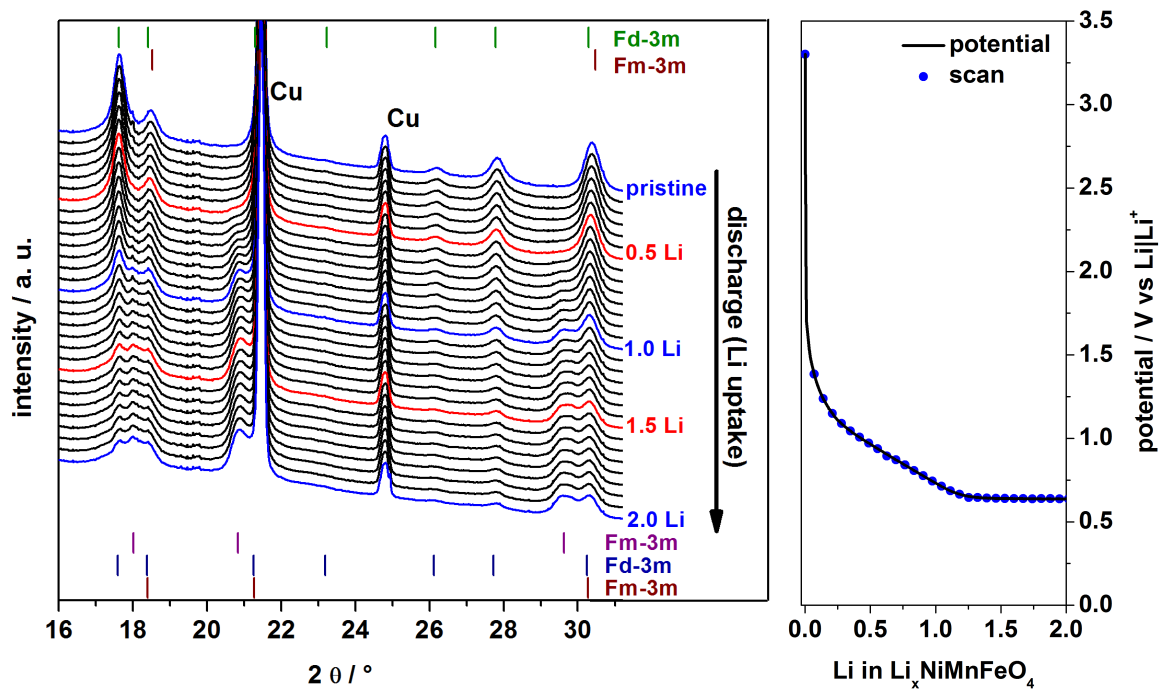


Figure 40: *Operando* XRD patterns (left) and galvanostatic potential of the *in situ* cell (right) during Li uptake up to 2 Li per formula unit  $\text{NiMnFeO}_4$ .

During uptake of the first 0.5 Li per f. u. the intensity of the reflections of the spinel phase decreases (Figure 41 left). But an enlargement of the unit cell volume or Li insertion into the surface of the nanoparticles is not observed, which is different compared to Li uptake by  $\text{CoFe}_2\text{O}_4$ .<sup>[205]</sup> Obviously,  $\text{NiMnFeO}_4$  particles are directly converted into a new intermediate phase, which is either not crystalline or the size of the coherent scattering domains is too small to be detected by XRD. After uptake of 1 Li per f. u., new reflections can be identified (Figure 40) which can be assigned to a new cubic NaCl-type structure with  $a = 4.286(1)$  Å. The lattice parameter is in between  $\text{Fe}_{1-x}\text{O}$  (4.30 Å) and NiO (4.18 Å).<sup>[206]</sup> Because for bulk material a homogenous solid solution  $\text{Fe}_{1-x}\text{Ni}_x\text{O}$  does not exist and may be only a small amount of Fe is substituted by Ni, leading to the observed lattice parameter.<sup>[208]</sup> The formation of the NaCl-type structure requires that cations located on the tetrahedral 8a sites in the spinel phase moving to empty neighbored octahedral sites. On the basis of the results presented above it is highly likely that first  $\text{Mn}^{2+}$  moves to octahedral sites because  $\text{Mn}^{3+}$  is simultaneously reduced to  $\text{Mn}^{2+}$  during Li uptake at the early stages (see section 4.2.5). Increasing the Li content  $\text{Fe}^{3+}$  is reduced to  $\text{Fe}^{2+}$  (visible via *operando* XAS), and these cations are also located on octahedral sites which offer more space (longer Fe-O distance) compared to tetrahedral sites in spinel structure.

After uptake of 2 Li per formula unit the trivalent cations are reduced to the divalent state (see section 4.2.5) and  $\text{Li}_2\text{O}$  is formed (see section 4.2.7). The X-ray powder pattern is

refined as a mixture of three different cubic phases (Figure 41 right). The main phase fraction (about 54 %) crystallizes as the above-mentioned NaCl-type structure (space group:  $Fm\bar{3}m$ ). The lattice parameter (4.286(1) Å) suggests that this mixed monoxide mainly consists of  $Fe^{2+}$  with a small amount of  $Ni^{2+}$ . The second phase (about 29 % phase fraction) most likely consists of a strained spinel structure (space group:  $Fd\bar{3}m$ ). In the structure less than half of the tetrahedral sites are occupied, while  $Mn^{2+}$  mainly occupies the octahedral sites. The third phase, NiO, contributes about 17 % to mixtures of oxides. These observations indicate that no MnO is formed.

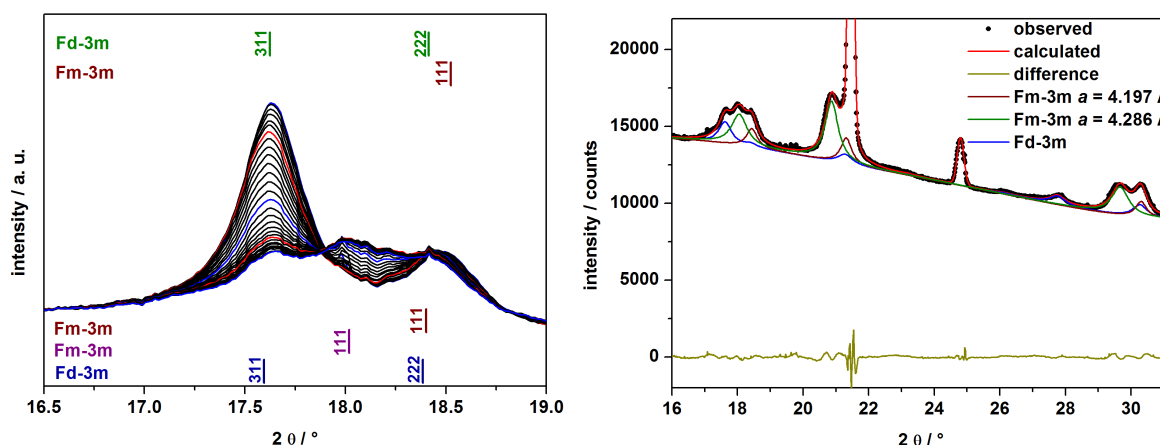


Figure 41: Magnification of the 16.5 to 19 ° 2θ range (left) and Rietveld refinement of the powder pattern recorded after uptake of 2 Li per formula unit including separated calculated powder pattern for all three observed cubic phases (right).

These results are in clear contrast to observations made for  $MnFe_2O_4$ ,  $MgFe_2O_4$ ,  $CoFe_2O_4$ ,  $ZnFe_2O_4$  and  $CoMnFeO_4$ : Instead of one monoxide phase an interwoven/intergrowth structure consisting of three disordered cubic monoxides occur as intermediate phases during discharge. A possible reason may be the clearly different lattice parameters of the pure monoxides, NiO:  $a = 4.179 \text{ Å}$ <sup>[206]</sup>, FeO:  $a = 4.317 \text{ Å}$ <sup>[207]</sup>, MnO:  $a = 4.488 \text{ Å}$ <sup>[232]</sup>, thus preventing the formation of one mixed monoxide under the reaction conditions. In contrast to our previous studies the crystal structure of the pristine material is different which may also be a reason for the different mechanisms.

Increasing the Li content >2 Li per f. u. leads to a simultaneous and successive decrease of the intensity of all reflections (Figure 42). During the long potential plateau at 0.8 V, the intermediate phases are transformed to an amorphous product or particles being too small to be detected by XRD. An identical behaviour was observed for  $MnFe_2O_4$ ,  $MgFe_2O_4$ ,  $CoFe_2O_4$ ,  $ZnFe_2O_4$  and  $Mn_3O_4$ .<sup>[68,140,203–205]</sup>

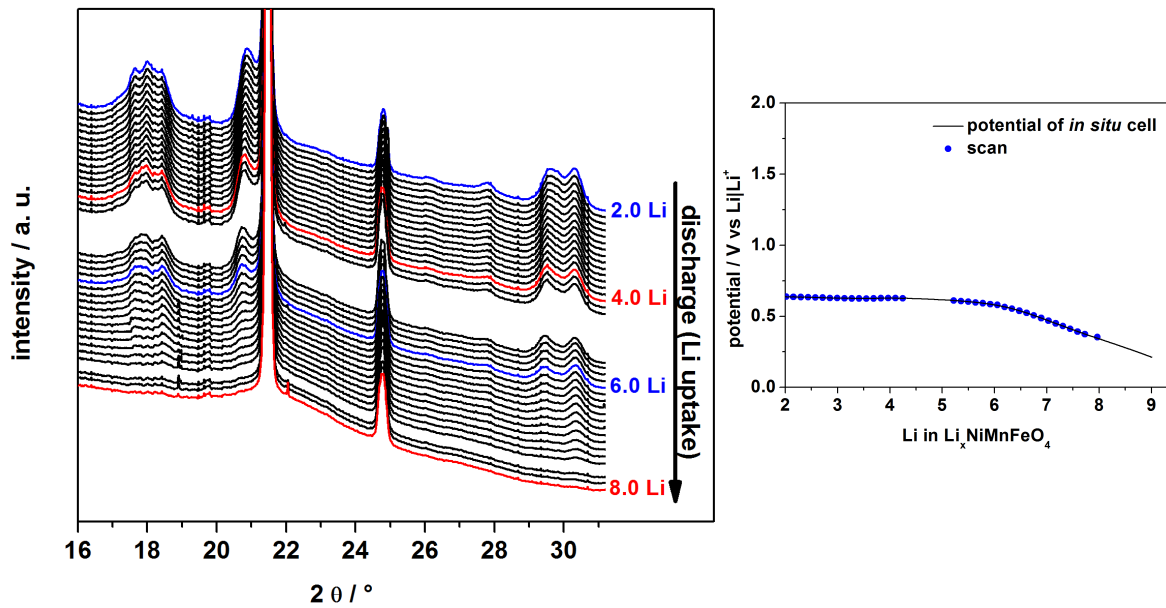


Figure 42: *Operando* XRD patterns collected during Li uptake from 2 to 8 Li per formula unit and associated galvanostatic potential of the *in situ* cell (every second scan is shown).

#### 4.2.9 TEM investigations after uptake of 2 Li / $\text{NiMnFeO}_4$

After uptake of 2 Li per  $\text{NiMnFeO}_4$ , STEM EDX mapping was performed (Figure 43) demonstrating a principal homogenous distribution of oxygen, iron, nickel, manganese and fluor. Fluor is a residue of the  $\text{LiPF}_6$  electrolyte on the surface of the nanoparticles. The homogenous distribution of the elements supports the *operando* XRD results.

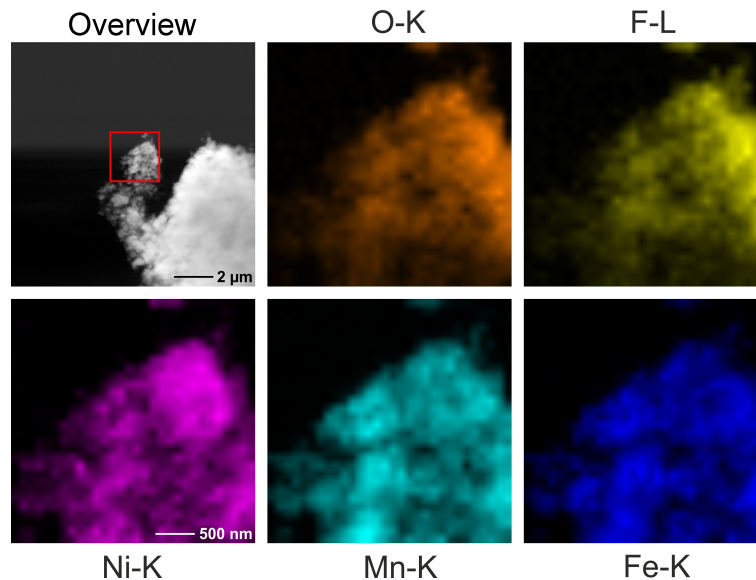


Figure 43: STEM EDX mapping of  $\text{NiMnFeO}_4$  nanoparticles after uptake of 2 Li per formula unit, evidencing the homogenous distribution of O, Ni, Mn and Fe. Fluor is a residue of the electrolyte.

#### 4.2.10 Conclusion of chapter 4.2

$\text{NiMnFeO}_4$  nanoparticles were successfully synthesized by an easy sol-gel combustion method. The material was characterized by TEM, EDX and XRD. In contrast to the other

spinel nanoparticles investigated during the thesis, the material exhibits a special structural property: NiMnFeO<sub>4</sub> nanoparticles crystallize in an interwoven disordered ordered spinel structure which affects the reaction pathway during first discharge.

The already investigated spinel oxides MnFe<sub>2</sub>O<sub>4</sub>, MgFe<sub>2</sub>O<sub>4</sub>, CoFe<sub>2</sub>O<sub>4</sub>, ZnFe<sub>2</sub>O<sub>4</sub> and CoMnFeO<sub>4</sub> form one mixed monoxide phase consisting of bivalent transition metals after uptake of about 2 Li per formula unit.<sup>[140,203–205]</sup> At this stage of discharge NiMnFeO<sub>4</sub> nanoparticles form an interwoven/intergrowth structure consisting of three cubic phases. During discharge, first Mn<sup>3+</sup> is reduced followed by the reduction of Fe<sup>3+</sup>. An identical sequence of reduction was also observed for CoMnFeO<sub>4</sub> nanoparticles and seems to be a general property for Mn<sup>3+</sup> containing spinels. The cations are reduced to the metals during further Li uptake (>2 Li per f. u.). After discharge to 0.1 V Ni, Fe and Mn metallic nanoparticles are embedded in a Li<sub>2</sub>O matrix. During Li release all transition metals are oxidized and M-O (M = Ni, Fe, Mn) bonds are formed. *Ex situ* XAS investigations on samples cycled several times evidence that the reaction Fe<sup>3+</sup> ↔ Fe<sup>0</sup> is reversible, while Ni<sup>0</sup> ↔ Ni<sup>2+</sup> is only reversible at the beginning of cycling. Mn<sup>0</sup> is always only oxidized to Mn<sup>2+</sup>, an observation also made for CoMnFeO<sub>4</sub> nanoparticles. The lesson is clear: oxidic spinels containing Mn<sup>3+</sup> are not recommended for conversion anode materials because 1 Li per formula unit is irreversible consumed.

Nevertheless, the cycling stability is superior compared to other materials (constant capacities about 830 mAh g<sup>-1</sup> at C/10). Another exciting result is the replacement of PVDF as binder by the water-soluble binder NaPAA which is important for environmental-friendly production of batteries.



### 4.3 Fe<sub>3</sub>S<sub>4</sub> nanoparticles - a new anode material for sodium ion batteries

#### 4.3.1 Short introduction

As already mentioned in the introduction (see section 1.2.7) SIBs are a cheap alternative to LIBs. For the commercialization the development of suitable anode materials is very important. One approach to enable graphite acting as anode material is the usage of co-intercalation phenomena e.g. expandable graphite.<sup>[9,149,150]</sup> An alternative is the identification of completely new materials suitable as anodes in SIBs. Recent research focuses on conversion materials forming alloys, such as Sb-, Sn-, Ge- and In-based materials. Phosphorus and phosphides as well as metal sulphides and oxides are also investigated.<sup>[151]</sup> Most metal oxides M<sub>x</sub>O<sub>y</sub> show relative low reversible capacities compared to their theoretical capacities.<sup>[233]</sup> The strong Na-O bond in Na<sub>2</sub>O is may be one reason for the irreversible capacity loss. One alternative is to substitute O<sup>2-</sup> by S<sup>2-</sup>, which may form Na<sub>2</sub>S during sodium uptake. The lattice energy of Na<sub>2</sub>S is smaller compared to Na<sub>2</sub>O thus facilitating the reversible reaction during Na release.<sup>[233]</sup> Therefore metal sulphides are interesting candidates as potential new anode materials for SIBs.

In the last few years different metals sulphides like e.g. MoS<sub>2</sub>, Sb<sub>2</sub>S<sub>3</sub> or Ni<sub>3</sub>S<sub>2</sub> were investigated showing superior reversible capacities compared to oxide-based materials.<sup>[234–236]</sup> Pyrite (FeS<sub>2</sub>) was also intensively investigated as promising high-rate and long-life anode in SIBs.<sup>[152,154]</sup> Furthermore, the components iron and sulphur are earth abundant, cheap and environmental friendly.

In this study we synthesized Fe<sub>3</sub>S<sub>4</sub> nanoparticles and tested this material as a new anode material for SIBs for the first time. The high theoretical capacity (725 mAh g<sup>-1</sup>) and the cheap and earth abundant components were the motivation for the studies. The group of Palstra et al. synthesized Fe<sub>3</sub>S<sub>4</sub> microcrystals and observed good cycling stability against Li metal. During Li uptake Fe<sup>2+</sup> and Fe<sup>3+</sup> are reduced to the metallic state and Li<sub>2</sub>S is formed. During Li release first the formation of Li<sub>2</sub>FeS<sub>2</sub> and subsequent FeS was postulated on the basis of the CV data. After decrease of the capacity to 310 mAh g<sup>-1</sup> in the 25<sup>th</sup> cycle the capacity increased to 563 mAh g<sup>-1</sup> after 100 cycles. Using Fe<sub>3</sub>S<sub>4</sub> as anode material for SIBs may reach similar high capacities and superior cycling stability compared to other materials.

Fe<sub>3</sub>S<sub>4</sub> nanoparticles were synthesized via a solvothermal synthesis route. The electrochemical performance as anode material for SIBs is investigated for the first time and the reaction mechanisms occurring during Na uptake and release are elucidated in detail.

#### 4.3.2 Synthesis of Greigite ( $\text{Fe}_3\text{S}_4$ ) nanoparticles

Greigite ( $\text{Fe}_3\text{S}_4$ ) nanoparticles were synthesized via solvothermal method. 2 mmol  $\text{FeCl}_3 \cdot 6 \text{H}_2\text{O}$  (Grüssing) and 4 mmol thiourea ( $\text{CH}_4\text{N}_2\text{S}$ , Merck) were dissolved in 20 mL ethylene glycol (Merck Millipore) and transferred to a 30 mL Teflon-lined stainless steel autoclave. Argon gas was passed through the solution for 10 Min to minimize oxygen contamination. Afterwards the autoclave was closed, sealed and kept at 200 °C for 12 h. The resulting black powder was magnetically decanted, washed five times with ethanol, and then dried at 50 °C for 12 h under vacuum.<sup>[237]</sup>

#### 4.3.3 Characterization of the Greigite ( $\text{Fe}_3\text{S}_4$ ) nanoparticles

The X-ray powder pattern of the as-prepared sample shows the presence of  $\text{Fe}_3\text{S}_4$  nanoparticles (Figure 44 left) crystallizing in the cubic spinel structure (space group  $Fd\bar{3}m$ ). The obtained lattice parameter ( $a = 9.8559(4) \text{ \AA}$ ) is in agreement with recent data reported for greigite.<sup>[59,238]</sup> The lognormal size distribution reveals polydisperse  $\text{Fe}_3\text{S}_4$  nanoparticles in the range from 2 to 18 nm, while most particles are between 4 and 8 nm in diameter (Figure 44 right). The anisotropic ( $hkl$ )-dependant domain size analysis yields truncated cuboctahedrons (Figure 44 right), which was also observed for microcrystalline  $\text{Fe}_3\text{S}_4$ .<sup>[59]</sup>

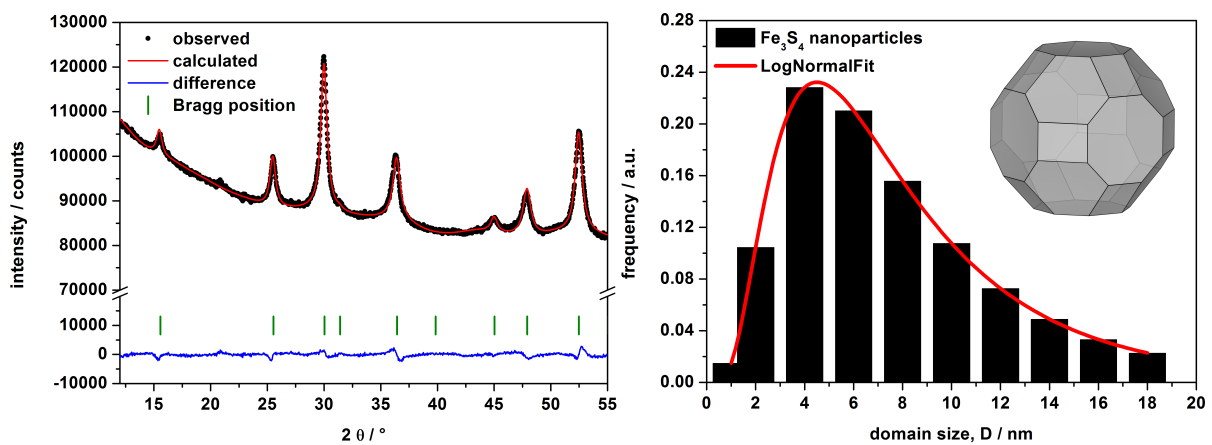


Figure 44: Rietveld Refinement (left) and Lognormal domain size distribution with particle shape of the as-prepared  $\text{Fe}_3\text{S}_4$  nanoparticles (right).

The molar ratio of Fe and S is 3.05:3.95 (EDX) being close to the expected composition. The average was calculated from EDX analysis of the Fe and S K lines, collected at three different positions of the sample (Table 7).

**Table 7: EDX results of Fe and S of the as prepared Fe<sub>3</sub>S<sub>4</sub> nanoparticles.**

position	Fe / At %	S / At %
I	43.60	56.40
II	42.15	57.85
III	44.80	55.20
<b>average</b>	<b>43.52</b>	<b>56.48</b>

The TEM image of Fe<sub>3</sub>S<sub>4</sub> shows agglomeration of the particles (Figure 45). Unfortunately the particle size and shape is not clearly visible. EDX nanoprobe analysis confirmed the ratio of Fe and S of 3:4. The corresponding SAED pattern can be assigned to the cubic spinel (Figure 45 right).

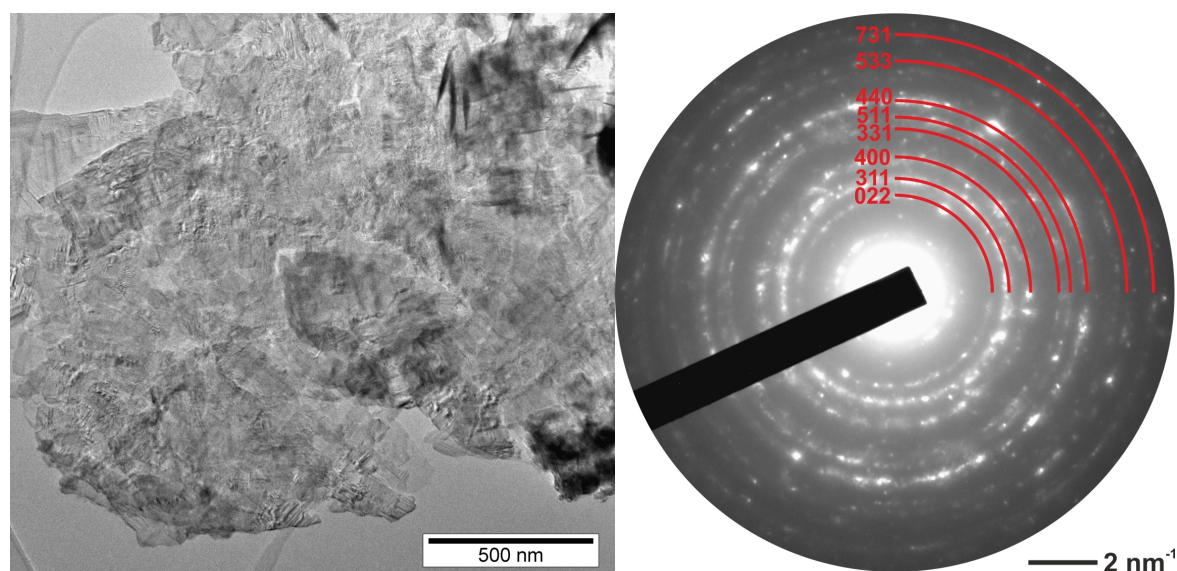


**Figure 45: TEM image of the as-prepared Fe<sub>3</sub>S<sub>4</sub> nanoparticles and corresponding SAED pattern.**

The room temperature (RT)  $^{57}\text{Fe}$  Mössbauer spectrum of the as-prepared material exhibits two sextets (Figure 46) due to Fe cations on octahedral (16d) and tetrahedral (8a) sites. The hyperfine field of the first sextet is 31.1 T with an isomer shift of 0.40 mm/s which can be ascribed to  $\text{Fe}^{3+}$  ions in the high-spin state on the tetrahedral sites (Table 8). The second sextet reveals a larger isomer shift of 0.47 mm/s and a slightly smaller hyperfine field (29.2 T) corresponding to an average oxidation state  $\text{Fe}^{2.5+}$  for the cations on octahedral sites. The oxidation state cannot be discriminated due to fast electron hopping which was also observed for magnetite.<sup>[239]</sup> The results demonstrate that  $\text{Fe}_3\text{S}_4$  nanoparticles crystallize as inverse spinel. The values for hyperfine fields and isomer shifts are in agreement with RT data of greigite microcrystals reported in the literature.<sup>[59,240]</sup> For natural greigite a third sextet was attributed to hexagonal smythite.<sup>[241]</sup> In the spectrum of the present sample two doublets with isomer shifts of  $0.35 \pm 0.2$  mm/s (Table 8) are observed which may be explained by the presence of small superparamagnetic  $\text{Fe}_3\text{S}_4$  particles (Table 8, Figure 46). A similar  $^{57}\text{Fe}$  Mössbauer spectrum obtained at RT for 9 nm  $\text{Fe}_3\text{S}_4$  nanoparticles was reported recently.<sup>[242]</sup> The results of the Mössbauer spectroscopy are in agreement with the polydisperse particle size distribution observed by XRD.

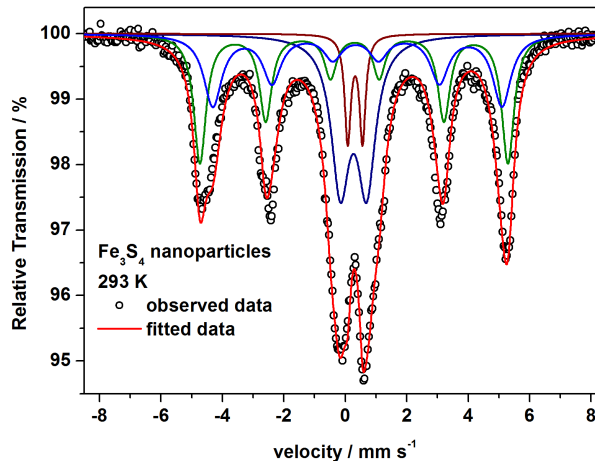


Figure 46:  $^{57}\text{Fe}$  Mössbauer spectra collected at RT of as-prepared  $\text{Fe}_3\text{S}_4$  nanoparticles.

Table 8: Fitting parameters of the contributions used to fit the Mössbauer spectra of  $\text{Fe}_3\text{S}_4$  in the pristine state. Isomer shift (IS), quadrupole splitting (QS), and line widths are given in mm/s.  $B_{\text{HF}}$  is given in T.

	IS	QS	line width	$B_{\text{HF}}$
$\text{Fe}^{3+}$	$0.402 \pm 0.003$	$-0.029 \pm 0.005$	$0.484 \pm 0.012$	$31.1 \pm 0.1$
$\text{Fe}^{2.5+}$	$0.472 \pm 0.004$	$0.055 \pm 0.007$	$0.714 \pm 0.013$	$29.2 \pm 0.1$
$\text{Fe}^{2.5+}$	$0.373 \pm 0.002$	$0.858 \pm 0.013$	$0.711 \pm 0.007$	-
$\text{Fe}^{3+}$	$0.327 \pm 0.005$	$0.481 \pm 0.011$	$0.243 \pm 0.032$	-



#### 4.3.4 Electrochemical properties of Fe<sub>3</sub>S<sub>4</sub> nanoparticles

For the electrochemical characterization 70 wt % Fe<sub>3</sub>S<sub>4</sub> were mixed with 20 wt % carbon and 10 wt % binder as described in Section 2. The electrodes were cycled against Na metal using Natriflate in diglyme as electrolyte. Sodium alginate and PVDF were identified as promising binders (Figure 47). During the first discharge a not well resolved plateau at 1.5 V is observed, followed by a sloping plateau beginning from 1.0 V and ending at 0.1 V. For both binders a capacity larger than 900 mAh g<sup>-1</sup> for the first discharge is reached. During the first charge a sloping plateau is observed at about 1.8 V. The reversible capacity after the first cycle is about 700 mAh g<sup>-1</sup> for the electrode with PVDF and 800 mAh g<sup>-1</sup> using Na-alginate binder. The capacity loss during the first cycle is mainly caused by irreversible reactions on particle surfaces. The formation of an SEI analogous layer is not reported for SIBs yet. The 10<sup>th</sup> and 20<sup>th</sup> cycles are very similar independent from the binder with capacities of about 700 mAh g<sup>-1</sup> being close to the theoretical value (725 mAh g<sup>-1</sup>).

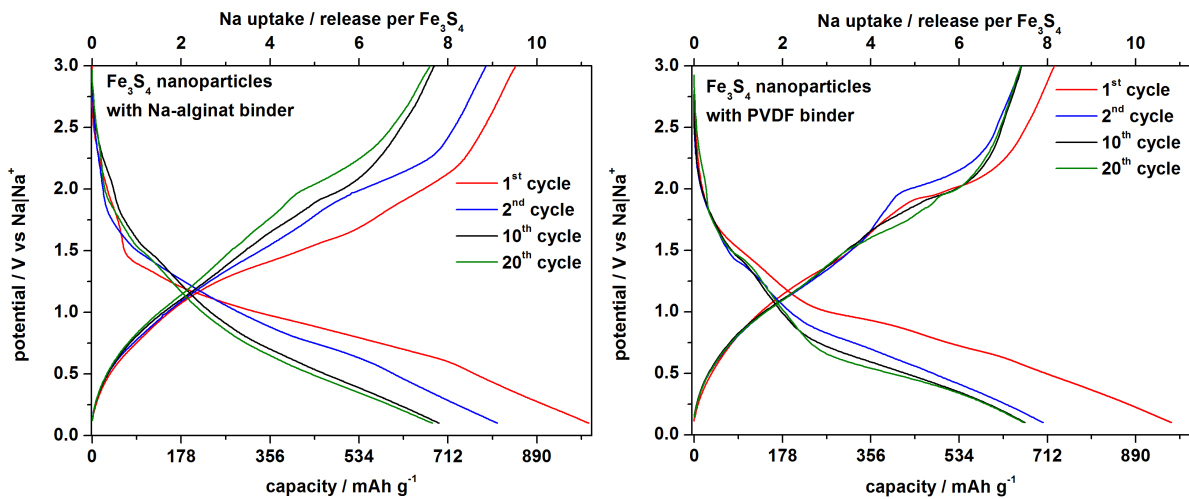


Figure 47: Potential curve of the first (red), second (blue), 10<sup>th</sup> (black) and 20<sup>th</sup> cycle (green) for Fe<sub>3</sub>S<sub>4</sub> nanoparticles electrode using Na-Alginate (left) and PVDF (right).

Using Na-alginate as binder yields higher capacities in the beginning compared to PVDF (Figure 47) and after about 10 cycles the capacity is identical and stable up to the 20<sup>th</sup> cycle (Figure 48) independent from the binder. Stable capacities of 700 mAh g<sup>-1</sup> at C/5 are significantly larger compared to reports for graphite.<sup>[9,149,150]</sup> The results are also superior compared to TiO<sub>2</sub><sup>[243,244]</sup>, Co<sub>3</sub>O<sub>4</sub><sup>[245]</sup>, FeV<sub>2</sub>S<sub>4</sub><sup>[246]</sup>, Ni<sub>3</sub>S<sub>2</sub><sup>[236]</sup>, hollow carbon nanowires<sup>[247]</sup>, MoS<sub>2</sub>/rGO<sup>[248]</sup> and Sn/C<sup>[249]</sup>. Only some recent materials like e.g. rGO/Sb<sub>2</sub>S<sub>3</sub><sup>[234]</sup> and MoS<sub>2</sub>/C<sup>[250]</sup> show similar high capacities.

The CV (Figure 48 right) exhibits significant differences between the cycles. During the first discharging 3 signals occur at 1.5, 1.2 and 0.5 V indicating different processes during Na uptake. Subsequent charging shows also three signals at 1.1, 1.5 and 2.2 V with identical intensity and potentials for all cycles. For the second discharging only one signal at about 1.0 V is visible. During the first charging new species are formed, which represent the active material for the subsequent cycles. During further cycling the signals are broadened and

loose intensity. In comparison, Li uptake by  $\text{Fe}_3\text{S}_4$  shows signals in the CV appearing at different potentials indicating that the mechanisms of Na uptake are different.<sup>[251]</sup>

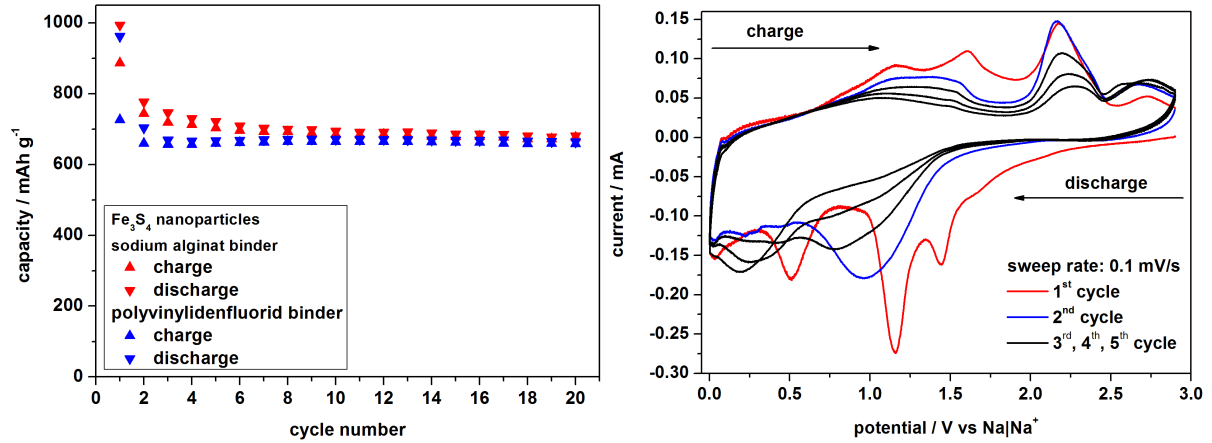


Figure 48: Capacity of the first 20 cycles for PVDF and Na-Alginate as binders at C/5 (left). The CV curves recorded during the first 5 cycles are also shown (right).

The electrodes were also cycled at 1C and 2C (Figure 49). For the first 3 cycles the capacity is significantly lower compared to C/5. Then the capacity increases yielding 430 mAh g<sup>-1</sup> at 2C and 500 mAh g<sup>-1</sup> at 1C after 20 cycles. These values present a capacity loss of 29 % and 39 % respectively, which are very good values for a material based on a conversion reaction.<sup>[252]</sup> Further cycling at the high C-rates leads to a slight capacity loss (Figure 49)

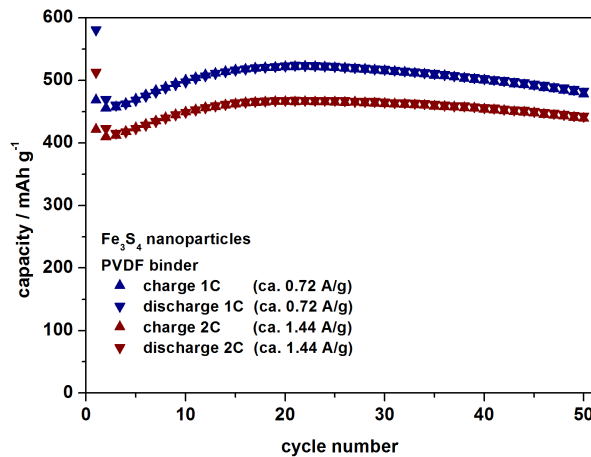


Figure 49: Specific capacity during the first 50 cycles at 1C (blue) and at 2C (brown).

#### 4.3.5 Elucidation of the reaction mechanism

*Ex situ* XRD investigations were performed with a STOE Stadi P diffractometer equipped with Mo X-ray source ( $\lambda = 0.7107 \text{ \AA}$ ) and a Mythen detector. For the pristine  $\text{Fe}_3\text{S}_4$  nanoparticles (Figure 50, left)  $a = 9.8558(4)$  and  $d = 10 \text{ nm}$  are in good accordance with the results presented in section 4.3.3. After uptake of 1 Na/f. u. the (222), (220) and (440) Bragg reflections are significantly broadened which may be caused by a distortion of the structure. To model the structure the symmetry was reduced from cubic to trigonal (space group:  $R\bar{3}m$ ) in agreement with literature.<sup>[253]</sup> A possible explanation for the distortion is that  $\text{Na}^+$  ions enter

the octahedral sites and simultaneous Fe ions move to neighbored empty tetrahedral sites. In addition, Bragg reflections of tetragonal FeS (mackinawite, space group:  $P4/nmm$ ) are detected. Most likely, the new phase forms by the reduction of  $\text{Fe}^{3+}$  ions to  $\text{Fe}^{2+}$  and a reorganization of the crystal structure.

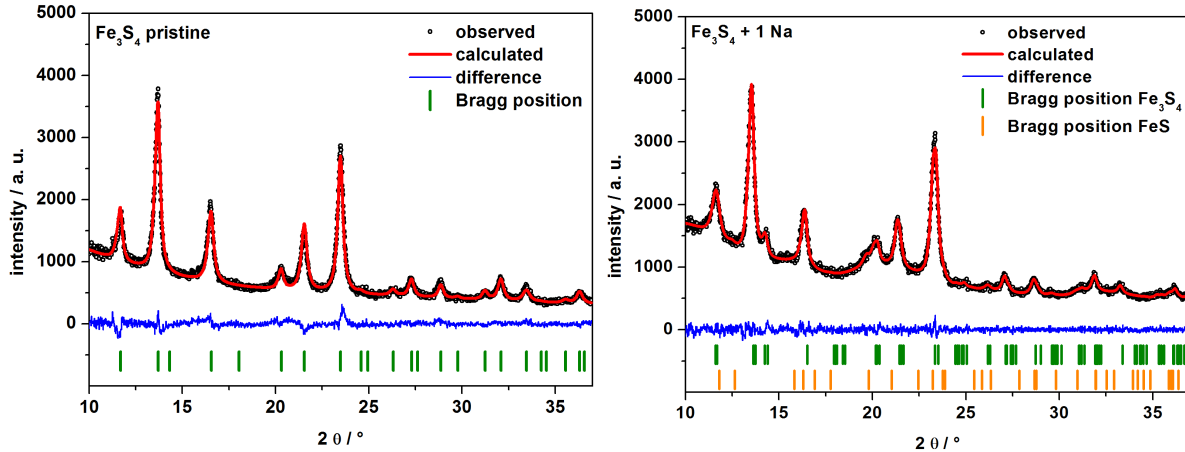


Figure 50: Rietveld refinement of the as-prepared  $\text{Fe}_3\text{S}_4$  nanoparticles (left) and after uptake of 1 Na per formula unit (right).

In the X-ray powder pattern after uptake of 2 Na/f. u. no reflections of greigite could be detected and the reflection pattern can be explained with two highly distorted mackinawite phases (Figure 51 left). At this stage of Na uptake all  $\text{Fe}^{3+}$  ions are reduced to  $\text{Fe}^{2+}$  ions, which is in agreement with the oxidation states of Fe in mackinawite. The structure of mackinawite is layered with the  $c$  axis representing the interlayer separation. The significantly broadened reflections and the highly distorted nature of mackinawite indicate a variety of different layer-to-layer distances. The difference between the two mackinawite phases is the length of the  $c$  axis (phase 1: 6.036(3) Å; phase 2: 6.85(1) Å). We note that similar results were reported for freeze-dried FeS.<sup>[254]</sup>

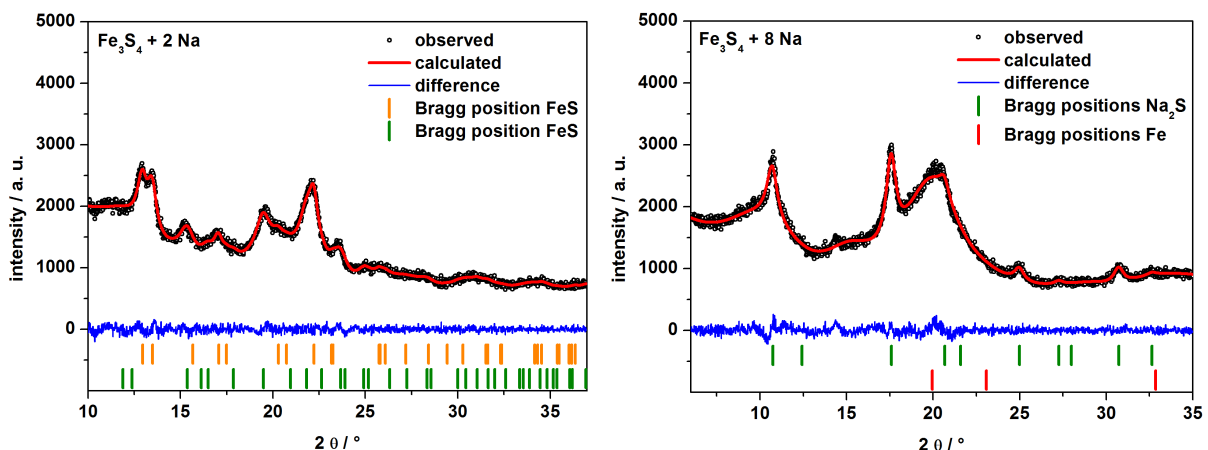


Figure 51: Pawley fit of the  $\text{Fe}_3\text{S}_4$  nanoparticles after uptake of 2 Na per formula unit (left) and after discharging to 0.1 V (uptake of 8 Na per formula unit, right).

During discharging to 0.1 V, about 8 Na per formula unit are stored. The powder pattern was refined (Figure 51 right, Pawley fit) with two phases: cubic  $\text{Na}_2\text{S}$  (space group  $Fm\bar{3}m$ ,  $a = 6.558(1)$ ) with a volume-weighted average domain size of  $d = 4.3(1)$  nm, and

nanocrystalline metallic Fe particles with a domain size of about 1 nm, crystallizing in the same cubic space group ( $Fm\bar{3}m$ ). The lattice parameter was refined to  $a = 3.547(3)$  Å.

*Operando* XAS spectra recorded at the Fe K-edge during the first discharge and the corresponding potential curve of the *in situ* cell are presented in Figure 52 (left and right). The Fe K-edge of the as-prepared material is located at 7119 eV (Figure 52 left, blue) with a pre-edge peak at 7112 eV. Both observations are in perfect agreement with data reported for greigite.<sup>[255]</sup> Obviously Fe ions are in mixed oxidation state  $Fe^{2+}/Fe^{3+}$  and they are located on tetrahedral and octahedral sites which is in agreement with the results of Mössbauer spectroscopy. During Na uptake the Fe K-edge shifts to lower energies (Figure 52 left, green arrow) because  $Fe^{3+}$  ions are reduced to a lower oxidation state. This result is in agreement with the new FeS phases identified via XRD. After uptake of about 5 Na/f.u. the Fe K-edge is shifted to about 7116 eV. Increasing the Na content the parallel shift of the spectrum stopped and the shape changes (Figure 52 left, red arrow): The intensity of the  $1s \rightarrow 4p$  transition decreases and the first minimum located at 7160 eV is less pronounced. This is typical for the formation of very small metallic Fe nanoparticles and is in accordance with the observations of metallic Fe nanoparticles in the XRD patterns.

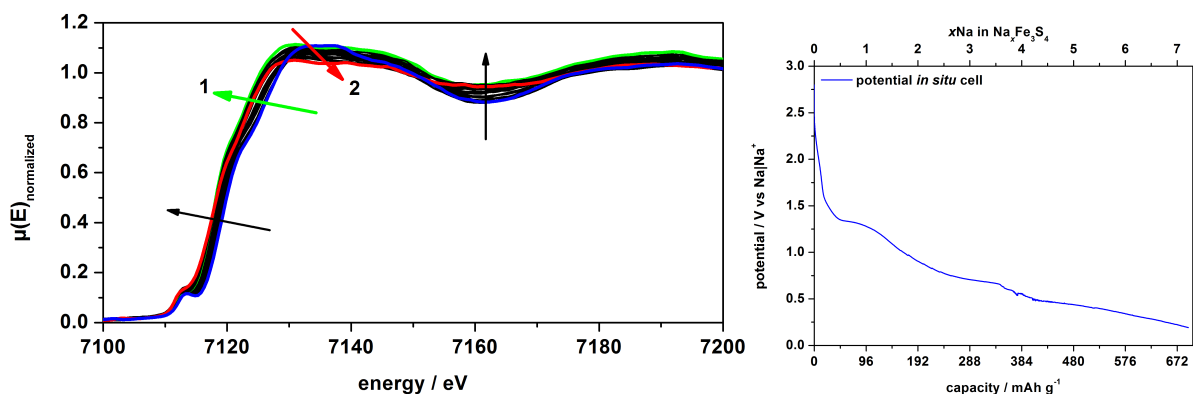


Figure 52: Operando XAS spectra (left) and potential curve of the *in situ* cell (right) during the first discharge of the  $Fe_3S_4$  nanoparticles.

Additional *ex situ* XAS spectra were collected of the as-prepared  $Fe_3S_4$  nanoparticles, after first discharge and after the first cycle (Figure 53). The first signal at 1.6 Å in the FT R-space represents the Fe-S bond, which is clearly broadened due to slightly different Fe-S bonds for Fe ions located on tetrahedral and octahedral sites. After the first discharge the first signal is now located at 1.8 Å being in between the pristine state and the metallic reference foil. The differences between the spectra may be caused by the very small Fe particles ( $d = 1$  nm, see XRD) and similar observations were also reported for  $FeS_2$  after uptake of 3.5 Na per formula unit.<sup>[256]</sup>



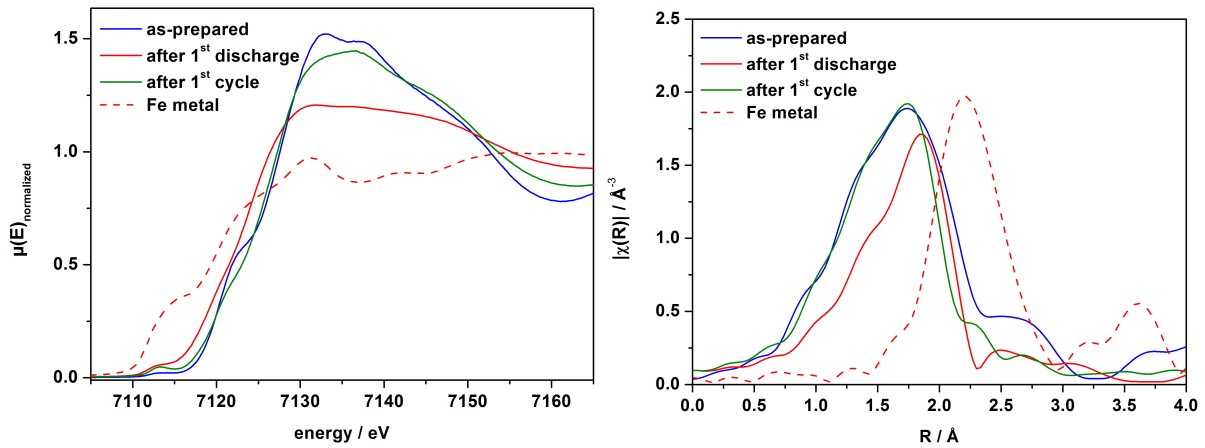
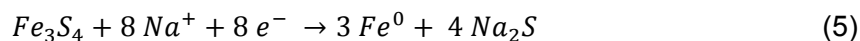


Figure 53: XAS spectra at Fe K-edge (left) and FT R-space (right) of the pristine state (blue), after first discharge (red), after first cycle (green) and metallic reference foil.

#### 4.3.6 Conclusion of chapter 4.3

The  $\text{Fe}_3\text{S}_4$  nanoparticles were synthesized in an easy solvothermal process. The as-prepared  $\text{Fe}_3\text{S}_4$  particles show a sizes distribution between 2 and 18 nm and have a cuboctahedron-like shape. The chemical composition was confirmed by EDX and the oxidation states and local environments of the Fe ions were determined with Mössbauer spectroscopy.

The electrochemical performance of the  $\text{Fe}_3\text{S}_4$  nanoparticles outperforms many anode materials recently discussed in literature (see section 4.3.4). The capacity is superior and the cycling stability is significantly better compared to other conversion materials. Especially the capacity at high currents (2C) is significantly larger compared to materials recently reported. A closer look on the reaction mechanisms during Na uptake and release revealed that in the early stage of the Na uptake a small amount of Na is intercalated into the greigite phase. It can be assumed that  $\text{Na}^+$  enters empty octahedral sites, while Fe ions move to empty neighbored tetrahedral sites, which results in a distorted greigite structure observed in XRD patterns. Further discharging leads to formation of intermediate FeS phases. After uptake of 2 Na per formula unit all  $\text{Fe}^{3+}$  ions are reduced to  $\text{Fe}^{2+}$ . The spinel structure is transformed into two mackinawite (FeS) phases exhibiting different values for the *c*-axis. Discharging to 0.1 V corresponds to an uptake of about 8 Na/ $\text{Fe}_3\text{S}_4$ . The spinel and intermediate phases are transformed into Fe nanoparticles (*d* = 1 nm) embedded in  $\text{Na}_2\text{S}$  (*d* = 4 nm). The overall reaction can be described by equation 5:



During charging no crystalline phase could be detected. An amorphous phase or particles below the coherence length of the X-rays developed during Na release. The *ex situ* XAS spectrum and FT R-space plot are similar to the pristine  $\text{Fe}_3\text{S}_4$  nanoparticles. These observations indicate that metallic Fe particles form Fe-S bonds again, while Na is reversibly released. The mechanisms occurring during Na uptake and release are different compared

## Further Projects

---

to those reported for  $\text{Li}^+$  ions.<sup>[59]</sup> For Li uptake the intermediate phase  $\text{Li}_2\text{FeS}_2$  was observed while a comparable intermediate  $\text{Na}_2\text{FeS}_2$  phase can be excluded. The uptake of 8 Li per formula unit leads to metallic Fe nanoparticles embedded in a  $\text{Li}_2\text{S}$  matrix, similarly to the observations made here. During Li release the intermediate  $\text{Li}_2\text{FeS}_2$  phase is reversibly formed during cycling. Cycling against Na leads to an amorphous product with a mixed oxidation state similar to the pristine material.

### 5 Conclusions and Outlook

The spinel oxide conversion anode materials exhibit during the first discharge (Li uptake) a transformation of the pristine materials into new intermediate nanocrystalline species. Further discharging and during charging (Li release) the generated species are either amorphous or the crystallites are too small to be detected by XRD. In all CV curves and galvanostatic experiments the first discharge differs significantly from the subsequent discharge curves, while the first charge curve is identical compared with subsequent cycles. These observations indicate that the electrochemical active material is formed during the first discharge. The first Li uptake takes place on the large amorphous surface of the nanoparticles. For  $\text{MnFe}_2\text{O}_4$ ,  $\text{MgFe}_2\text{O}_4$ ,  $\text{CoFe}_2\text{O}_4$ ,  $\text{NiFe}_2\text{O}_4$  and  $\text{CoMnFeO}_4$  nanoparticles a mixed monoxide with NaCl-like structure is formed during uptake of the first ca. 2 Li per formula unit. The monoxide is generated by reduction of  $\text{M}^{3+}$  ions to  $\text{M}^{2+}$  combined with the movement of reduced ions located on tetrahedral sites to neighbored empty octahedral sites. The  $\text{NiMnFeO}_4$  nanoparticles exhibit an exceptional mechanism. Instead of one mixed monoxide phase an interwoven/intergrowth structure consisting of three cubic phases is observed.

The first discharge capacity of the spinel oxides is in general significantly larger than the theoretical values, which is caused by side reactions. The intermediate monoxide phases are transformed to metallic nanoparticles embedded in a  $\text{Li}_2\text{O}$  matrix. These observations are similar for all spinel oxides investigated in this thesis. All results suggest that the mechanisms seem to be a general reaction during Li uptake for spinel oxides. During charging new species are formed which are either amorphous or too small to be detected by XRD. Therefore, these species were characterized with XAS, solid state  $^7\text{Li}$  NMR and TEM. During charging the metallic nanoparticles are oxidized to  $\text{M}^{2+}$  and/or  $\text{M}^{3+}$ . Mn is generally only oxidized to  $\text{Mn}^{2+}$  independent of the pristine oxidation state, *i.e.* for a spinel with  $\text{Mn}^{3+}$  in the pristine state 1/3 Li is lost during cycling. Hence, as a general advice in the field of using TM oxides as anode materials, oxides containing  $\text{Mn}^{3+}$  are not recommended. In contrast  $\text{Fe}^{3+}$  shows good reversibility during repeated charging.  $\text{Co}^{2+}$ ,  $\text{Ni}^{2+}$  and  $\text{Mn}^{2+}$  exhibit also reversible cycling stability over several cycles. But extended cycling of the spinel oxides require carbon additives or special morphologies to prevent the materials from drastic capacity loss.

Besides pure spinel oxide nanoparticles, also composites containing carbon nanotubes or reduced graphite oxide were synthesized and investigated. The use of CNTs or rGO significantly reduces the capacity loss during repeated cycling. In addition, the capacity stability during cycling at higher currents could be significantly improved. The question whether the carbon species also influence the reaction mechanism could not be

## Conclusion and Outlook

---

unambiguously answered yet. Application of *operando* XRD and XAS revealed similar reaction mechanisms for the composites like observed for the pure oxides. Therefore, the carbon species do not influence the reaction mechanisms but most likely facilitate the oxidation of the metallic nanoparticles during repeated cycling. Mainly the reversibility of the redox couple  $M^0 \leftrightarrow M^{2+}$  ( $M = \text{Ni}, \text{Co}$ ) is significantly improved. The results suggest that CNTs and/or rGO help to improve the conductivity and keep the nanoparticles in electrical contact. Understanding the reaction mechanisms during Li uptake and release is an important milestone for the commercialization of spinel oxides as anode materials for LIBs because cut-off potentials can be identified and the knowledge about the products and its properties allow calculation of the volume expansion during Li uptake and shrinking during Li release. Using a conversion anode material and a flexible separator a complete cell based on conversion reactions on both cathode and anode side seems to be possible. Using for e.g.  $\text{MnFe}_2\text{O}_4$  as anode and  $\text{FeF}_3$  as cathode the specific capacity of the cell can be doubled. But for commercialization the separator and electrolytes have to be improved or adapted to the requirements for conversion materials.

As discussed above TM oxides are not suitable as anode material for SIBs due to the fact that only about half of the theoretical capacity is reached. In contrast  $\text{Fe}_3\text{S}_4$  nanoparticles exhibit good reversible capacity and very well cycling stability at high currents. These results could be even improved by electrolyte and separator optimization. TM sulphide nanoparticles as anode materials are highly interesting and the results presented are just a first attempt in this new field of research.



**6 References**

- [1] D. A. Notter, M. Gauch, R. Widmer, P. Wäger, A. Stamp, R. Zah, H.-J. Althaus, *Environ. Sci. Technol.* **2010**, *44*, 6550–6556.
- [2] *Zeitreihen Zur Entwicklung Der Erneuerbaren Energien in Deutschland*, **2015**.
- [3] *Key World Energy Statistics 2014*, **2014**.
- [4] N. L. Panwar, S. C. Kaushik, S. Kothari, *Renew. Sustain. Energy Rev.* **2011**, *15*, 1513–1524.
- [5] D. H. Doughty, P. C. Butler, A. A. Akhil, N. H. Clark, J. D. Boyes, *Electrochem. Soc. Interface* **2010**, *19*, 49–53.
- [6] “Agora Energiewende - Agorameter,” can be found under <http://www.agora-energiewende.de/de/themen/-agorathem-/Produkt/produkt/76/Agorameter/>, **2016**.
- [7] B. L. Ellis, L. F. Nazar, *Curr. Opin. Solid State Mater. Sci.* **2012**, *16*, 168–177.
- [8] D. Kundu, E. Talaie, V. Duffort, L. F. Nazar, *Angew. Chem.* **2015**, *127*, 3495–3513.
- [9] S. Wenzel, T. Hara, J. Janek, P. Adelhelm, *Energy Environ. Sci.* **2011**, *4*, 3342–3354.
- [10] M. Armand, J.-M. Tarascon, *Nature* **2008**, *451*, 652–657.
- [11] J. M. Tarascon, D. Guyomard, *Electrochimica Acta* **1993**, *38*, 1221–1231.
- [12] K. Mizushima, P. C. Jones, P. J. Wiseman, J. B. Goodenough, *Mater. Res. Bull.* **1980**, *15*, 783–789.
- [13] A. Du Pasquier, I. Plitz, S. Menocal, G. Amatucci, *J. Power Sources* **2003**, *115*, 171–178.
- [14] I. Bloom, S. A. Jones, V. S. Battaglia, G. L. Henriksen, J. P. Christophersen, R. B. Wright, C. D. Ho, J. R. Belt, C. G. Motloch, *J. Power Sources* **2003**, *124*, 538–550.
- [15] Y. Itou, Y. Ukyo, *J. Power Sources* **2005**, *146*, 39–44.
- [16] F. Lin, D. Nordlund, T.-C. Weng, Y. Zhu, C. Ban, R. M. Richards, H. L. Xin, *Nat. Commun.* **2014**, *5*, 3358–3367.
- [17] M. M. Thackeray, L. A. de Picciotto, A. de Kock, P. J. Johnson, V. A. Nicholas, K. T. Adendorff, *J. Power Sources* **1987**, *21*, 1–8.
- [18] M. M. Thackeray, *J. Am. Ceram. Soc.* **1999**, *82*, 3347–3354.
- [19] M. S. Whittingham, *Science* **1976**, *192*, 1126–1127.
- [20] M. S. Whittingham, *Chem. Rev.* **2004**, *104*, 4271–4302.
- [21] W. Xu, J. Wang, F. Ding, X. Chen, E. Nasybulin, Y. Zhang, J.-G. Zhang, *Energy Environ. Sci.* **2014**, *7*, 513–537.
- [22] N. Nitta, F. Wu, J. T. Lee, G. Yushin, *Mater. Today* **2015**, *18*, 252–264.
- [23] N. A. Kaskhedikar, J. Maier, *Adv. Mater.* **2009**, *21*, 2664–2680.
- [24] M. Winter, P. Novak, A. Mannier, *J. Electrochem. Soc.* **1998**, *145*, 428–435.
- [25] F. Wang, H.-C. Yu, M.-H. Chen, L. Wu, N. Pereira, K. Thornton, A. Van der Ven, Y. Zhu, G. G. Amatucci, J. Graetz, *Nat. Commun.* **2012**, *3*, 1201–1209.
- [26] F. Wang, R. Robert, N. A. Chernova, N. Pereira, F. Omenya, F. Badway, X. Hua, M. Ruotolo, R. Zhang, L. Wu, et al., *J. Am. Chem. Soc.* **2011**, *133*, 18828–18836.
- [27] F. Badway, A. N. Mansour, N. Pereira, J. F. Al-Sharab, F. Cosandey, I. Plitz, G. G. Amatucci, *Chem. Mater.* **2007**, *19*, 4129–4141.
- [28] F. Badway, F. Cosandey, N. Pereira, G. G. Amatucci, *J. Electrochem. Soc.* **2003**, *150*, A1209–A1218.
- [29] T. Li, Z. X. Chen, Y. L. Cao, X. P. Ai, H. X. Yang, *Electrochimica Acta* **2012**, *68*, 202–205.

## References

- [30] J. Liu, W. Cui, C. Wang, Y. Xia, *Electrochem. Commun.* **2011**, *13*, 269–271.
- [31] F. Wu, H. Kim, A. Magasinski, J. T. Lee, H.-T. Lin, G. Yushin, *Adv. Energy Mater.* **2014**, *4*, 1614–1623.
- [32] M.-Q. Zhao, Q. Zhang, J.-Q. Huang, G.-L. Tian, J.-Q. Nie, H.-J. Peng, F. Wei, *Nat. Commun.* **2014**, *5*, 3410–3418.
- [33] C. Luo, Y. Xu, Y. Zhu, Y. Liu, S. Zheng, Y. Liu, A. Langrock, C. Wang, *ACS Nano* **2013**, *7*, 8003–8010.
- [34] T. D. Hatchard, J. R. Dahn, *J. Electrochem. Soc.* **2004**, *151*, A838–A842.
- [35] U. Kasavajjula, C. Wang, A. J. Appleby, *J. Power Sources* **2007**, *163*, 1003–1039.
- [36] M. Holzapfel, H. Buqa, W. Scheifele, P. Novak, F.-M. Petrat, *Chem. Commun.* **2005**, 1566–1568.
- [37] H. Kim, B. Han, J. Choo, J. Cho, *Angew. Chem.* **2008**, *120*, 10305–10308.
- [38] Y.-S. Hu, R. Demir-Cakan, M.-M. Titirici, J.-O. Müller, R. Schlögl, M. Antonietti, J. Maier, *Angew. Chem. Int. Ed.* **2008**, *47*, 1645–1649.
- [39] G. Wang, B. Wang, X. Wang, J. Park, S. Dou, H. Ahn, K. Kim, *J. Mater. Chem.* **2009**, *19*, 8378–8384.
- [40] G. Derrien, J. Hassoun, S. Panero, B. Scrosati, *Adv. Mater.* **2007**, *19*, 2336–2340.
- [41] Y. Idota, *Science* **1997**, *276*, 1395–1397.
- [42] Y. Hwa, J. H. Sung, B. Wang, C.-M. Park, H.-J. Sohn, *J. Mater. Chem.* **2012**, *22*, 12767–12773.
- [43] M. I. Purcell, T. D. Hatchard, R. J. Sanderson, M. N. Obrovac, *J. Electrochem. Soc.* **2014**, *161*, A643–A647.
- [44] T. Fujieda, S. Takahashi, S. Higuchi, *J. Power Sources* **1992**, *40*, 283–289.
- [45] M. N. Obrovac, V. L. Chevrier, *Chem. Rev.* **2014**, *114*, 11444–11502.
- [46] H. Pfeiffer, F. Tancret, M.-P. Bichat, L. Monconduit, F. Favier, T. Brousse, *Electrochem. Commun.* **2004**, *6*, 263–267.
- [47] Y. Lu, J.-P. Tu, Q.-Q. Xiong, J.-Y. Xiang, Y.-J. Mai, J. Zhang, Y.-Q. Qiao, X.-L. Wang, C.-D. Gu, S. X. Mao, *Adv. Funct. Mater.* **2012**, *22*, 3927–3935.
- [48] J. Y. Xiang, X. L. Wang, J. Zhong, D. Zhang, J. P. Tu, *J. Power Sources* **2011**, *196*, 379–385.
- [49] S. Boyanov, J. Bernardi, F. Gillot, L. Dupont, M. Womes, J.-M. Tarascon, L. Monconduit, M.-L. Doublet, *Chem. Mater.* **2006**, *18*, 3531–3538.
- [50] V. Pralong, D. C. S. Souza, K. T. Leung, L. F. Nazar, *Electrochem. Commun.* **2002**, *4*, 516–520.
- [51] M. Nishijima, *J. Electrochem. Soc.* **1994**, *141*, 2966–2971.
- [52] M. Nishijima, *Solid State Ion.* **1996**, *83*, 107–111.
- [53] T. Shodai, *Solid State Ion.* **1996**, *86-88*, 785–789.
- [54] J. L. C. Rowsell, V. Pralong, L. F. Nazar, *J. Am. Chem. Soc.* **2001**, *123*, 8598–8599.
- [55] S.-C. Han, K.-W. Kim, H.-J. Ahn, J.-H. Ahn, J.-Y. Lee, *J. Alloys Compd.* **2003**, *361*, 247–251.
- [56] D. Zhang, Y. J. Mai, J. Y. Xiang, X. H. Xia, Y. Q. Qiao, J. P. Tu, *J. Power Sources* **2012**, *217*, 229–235.
- [57] Y. Gu, Y. Xu, Y. Wang, *ACS Appl. Mater. Interfaces* **2013**, *5*, 801–806.
- [58] X. Chen, Z. Wang, X. Wang, J. Wan, J. Liu, Y. Qian, *Inorg. Chem.* **2005**, *44*, 951–954.
- [59] G. Li, B. Zhang, F. Yu, A. A. Novakova, M. S. Krivenkov, T. Y. Kiseleva, L. Chang, J. Rao, A. O. Polyakov, G. R. Blake, et al., *Chem. Mater.* **2014**, *26*, 5821–5829.

## References

- [60] P. L. Taberna, S. Mitra, P. Poizot, P. Simon, J.-M. Tarascon, *Nat. Mater.* **2006**, *5*, 567–573.
- [61] P. Poizot, P., S. Laruelle, L. Dupont, J.-M. Tarascon, *Nature* **2000**, *407*, 496–499.
- [62] P. Poizot, S. Laruelle, S. Grugeon, L. Dupont, J.-M. Tarascon, *J. Power Sources* **2001**, *97-98*, 235–239.
- [63] M. V. Reddy, G. V. Subba Rao, B. V. R. Chowdari, *Chem. Rev.* **2013**, *113*, 5364–5457.
- [64] K. E. Sickafus, J. M. Wills, N. W. Grimes, *J. Am. Ceram. Soc.* **2004**, *82*, 3279–3292.
- [65] T. F. W. Barth, E. Posnjak, *Z. Für Krist. - Cryst. Mater.* **1932**, *82*, 325–341.
- [66] S. Hafner, F. Laves, *Z. Für Krist. - Cryst. Mater.* **1961**, *115*, 321–330.
- [67] S.-D. Mo, W. Y. Ching, *Phys. Rev. B* **1996**, *54*, 16555–16561.
- [68] M. A. Lowe, J. Gao, H. D. Abruña, *J Mater Chem A* **2013**, *1*, 2094–2103.
- [69] G. Binotto, D. Larcher, A. S. Prakash, R. Herrera Urbina, M. S. Hegde, J.-M. Tarascon, *Chem. Mater.* **2007**, *19*, 3032–3040.
- [70] K. M. Shaju, F. Jiao, A. Debart, P. G. Bruce, *Phys. Chem. Chem. Phys.* **2007**, *9*, 1837–1842.
- [71] Z.-S. Wu, W. Ren, L. Wen, L. Gao, J. Zhao, Z. Chen, G. Zhou, F. Li, H.-M. Cheng, *ACS Nano* **2010**, *4*, 3187–3194.
- [72] Y.-H. Jin, S.-D. Seo, H.-W. Shim, K.-S. Park, D.-W. Kim, *Nanotechnology* **2012**, *23*, 125402–125408.
- [73] C. Ban, Z. Wu, D. T. Gillaspie, L. Chen, Y. Yan, J. L. Blackburn, A. C. Dillon, *Adv. Mater.* **2010**, *22*, E145–E149.
- [74] G. Zhou, D.-W. Wang, F. Li, L. Zhang, N. Li, Z.-S. Wu, L. Wen, G. Q. (Max) Lu, H.-M. Cheng, *Chem. Mater.* **2010**, *22*, 5306–5313.
- [75] Q. Fan, M. S. Whittingham, *Electrochem. Solid-State Lett.* **2007**, *10*, A48–A51.
- [76] H. Wang, L.-F. Cui, Y. Yang, H. Sanchez Casalongue, J. T. Robinson, Y. Liang, Y. Cui, H. Dai, *J. Am. Chem. Soc.* **2010**, *132*, 13978–13980.
- [77] J. Gao, M. A. Lowe, H. D. Abruña, *Chem. Mater.* **2011**, *23*, 3223–3227.
- [78] R. Alcántara, M. Jaraba, P. Lavela, J. L. Tirado, *Chem. Mater.* **2002**, *14*, 2847–2848.
- [79] Y. Sharma, N. Sharma, G. V. Subba Rao, B. V. R. Chowdari, *Adv. Funct. Mater.* **2007**, *17*, 2855–2861.
- [80] X. Guo, X. Lu, X. Fang, Y. Mao, Z. Wang, L. Chen, X. Xu, H. Yang, Y. Liu, *Electrochem. Commun.* **2010**, *12*, 847–850.
- [81] J. Cabana, L. Monconduit, D. Larcher, M. R. Palacín, *Adv. Mater.* **2010**, *22*, E170–E192.
- [82] V. Etacheri, R. Marom, R. Elazari, G. Salitra, D. Aurbach, *Energy Environ. Sci.* **2011**, *4*, 3243–3262.
- [83] J. Li, S. Xiong, Y. Liu, Z. Ju, Y. Qian, *ACS Appl. Mater. Interfaces* **2013**, *5*, 981–988.
- [84] P. Lavela, J. L. Tirado, C. Vidal-Abarca, *Electrochimica Acta* **2007**, *52*, 7986–7995.
- [85] C. Fu, G. Li, D. Luo, X. Huang, J. Zheng, L. Li, *ACS Appl. Mater. Interfaces* **2014**, *6*, 2439–2449.
- [86] Y. Sharma, N. Sharma, G. Subbarao, B. Chowdari, *Solid State Ion.* **2008**, *179*, 587–597.
- [87] S. G. Mohamed, C.-J. Chen, C. K. Chen, S.-F. Hu, R.-S. Liu, *ACS Appl. Mater. Interfaces* **2014**, *6*, 22701–22708.

## References

- [88] M. V. Reddy, C. Yu, F. Jiahuan, K. P. Loh, B. V. R. Chowdari, *RSC Adv.* **2012**, *2*, 9619–9625.
- [89] B. Liu, J. Zhang, X. Wang, G. Chen, D. Chen, C. Zhou, G. Shen, *Nano Lett.* **2012**, *12*, 3005–3011.
- [90] Y. Fu, Y. Wan, H. Xia, X. Wang, *J. Power Sources* **2012**, *213*, 338–342.
- [91] Y. Zhao, J. Li, Y. Ding, L. Guan, *J. Mater. Chem.* **2011**, *21*, 19101–19105.
- [92] P. Lavela, J. L. Tirado, *J. Power Sources* **2007**, *172*, 379–387.
- [93] Y. Wang, D. Su, A. Ung, J. Ahn, G. Wang, *Nanotechnology* **2012**, *23*, 055402–055408.
- [94] M. Li, Y.-X. Yin, C. Li, F. Zhang, L.-J. Wan, S. Xu, D. G. Evans, *Chem Commun* **2012**, *48*, 410–412.
- [95] S. Liu, J. Xie, C. Fang, G. Cao, T. Zhu, X. Zhao, *J. Mater. Chem.* **2012**, *22*, 19738–19743.
- [96] Y. Xiao, J. Zai, L. Tao, B. Li, Q. Han, C. Yu, X. Qian, *Phys. Chem. Chem. Phys.* **2013**, *15*, 3939–3945.
- [97] F. Jiang, X. Du, S. Zhao, J. Guo, B. Huang, X. Huang, Q. Su, J. Zhang, G. Du, *J. Nanoparticle Res.* **2015**, *17*, 173–182.
- [98] Y. Pan, Y. Zhang, X. Wei, C. Yuan, J. Yin, D. Cao, G. Wang, *Electrochimica Acta* **2013**, *109*, 89–94.
- [99] Y. Yin, B. Zhang, X. Zhang, J. Xu, S. Yang, *J. Sol-Gel Sci. Technol.* **2013**, *66*, 540–543.
- [100] L. Jin, Y. Qiu, H. Deng, W. Li, H. Li, S. Yang, *Electrochimica Acta* **2011**, *56*, 9127–9132.
- [101] F. Mueller, D. Bresser, E. Paillard, M. Winter, S. Passerini, *J. Power Sources* **2013**, *236*, 87–94.
- [102] G. Zhang, X. W. D. Lou, *Angew. Chem.* **2014**, *126*, 9187–9190.
- [103] Z. Zheng, Y. Cheng, X. Yan, R. Wang, P. Zhang, *J Mater Chem A* **2014**, *2*, 149–154.
- [104] A. M. Bruck, C. A. Cama, C. N. Gannett, A. C. Marschilok, E. S. Takeuchi, K. J. Takeuchi, *Inorg Chem Front* **2016**, *3*, 26–40.
- [105] J. N. Reimers, *J. Electrochem. Soc.* **1992**, *139*, 2091.
- [106] H. Liu, F. C. Strobridge, O. J. Borkiewicz, K. M. Wiaderek, K. W. Chapman, P. J. Chupas, C. P. Grey, *Science* **2014**, *344*, 1252817–1252817.
- [107] X. Zhang, M. van Hulzen, D. P. Singh, A. Brownrigg, J. P. Wright, N. H. van Dijk, M. Wagemaker, *Nat. Commun.* **2015**, *6*, 8333–8340.
- [108] X. Zhang, M. van Hulzen, D. P. Singh, A. Brownrigg, J. P. Wright, N. H. van Dijk, M. Wagemaker, *Nano Lett.* **2014**, *14*, 2279–2285.
- [109] W. C. Chueh, F. El Gabaly, J. D. Sugar, N. C. Bartelt, A. H. McDaniel, K. R. Fenton, K. R. Zavadil, T. Tyliszczak, W. Lai, K. F. McCarty, *Nano Lett.* **2013**, *13*, 866–872.
- [110] A. Van der Ven, J. Bhattacharya, A. A. Belak, *Acc. Chem. Res.* **2013**, *46*, 1216–1225.
- [111] Z. Lu, J. R. Dahn, *J. Electrochem. Soc.* **2003**, *150*, A1044–A1051.
- [112] M. M. Thackeray, *Prog. Solid State Chem.* **1997**, *25*, 1–71.
- [113] S. A. Wicker, E. H. Walker, *Inorg. Chem.* **2013**, *52*, 1772–1779.
- [114] D. Li, H. Zhou, *Mater. Today* **2014**, *17*, 451–463.
- [115] H. Arai, K. Sato, Y. Orihara, H. Murayama, I. Takahashi, Y. Koyama, Y. Uchimoto, Z. Ogumi, *J. Mater. Chem. A* **2013**, *1*, 10442–10449.
- [116] Q. Wu, Y. Liu, C. S. Johnson, Y. Li, D. W. Dees, W. Lu, *Chem. Mater.* **2014**, *26*, 4750–4756.

## References

- [117] O. Dolotko, A. Senyshyn, M. J. Mühlbauer, K. Nikolowski, H. Ehrenberg, *J. Power Sources* **2014**, *255*, 197–203.
- [118] M. Herklotz, J. Weiß, E. Ahrens, M. Yavuz, L. Mereacre, N. Kiziltas-Yavuz, C. Dräger, H. Ehrenberg, J. Eckert, F. Fauth, et al., *J. Appl. Crystallogr.* **2016**, *49*, 340–345.
- [119] M. S. Whittingham, *Chem. Rev.* **2014**, *114*, 11414–11443.
- [120] G. G. Amatucci, N. Pereira, *J. Fluor. Chem.* **2007**, *128*, 243–262.
- [121] H. Zhao, Z. Zheng, K. W. Wong, S. Wang, B. Huang, D. Li, *Electrochem. Commun.* **2007**, *9*, 2606–2610.
- [122] S. Jin, H. Deng, D. Long, X. Liu, L. Zhan, X. Liang, W. Qiao, L. Ling, *J. Power Sources* **2011**, *196*, 3887–3893.
- [123] F. M. Courtel, H. Duncan, Y. Abu-Lebdeh, I. J. Davidson, *J. Mater. Chem.* **2011**, *21*, 10206–10218.
- [124] M. Morcrette, Y. Chabre, G. Vaughan, G. Amatucci, J.-B. Leriche, S. Patoux, C. Masquelier, J.-M. Tarascon, *Electrochimica Acta* **2002**, *47*, 3137–3149.
- [125] J. Wontcheu, M. Behrens, W. Bensch, S. Indris, M. Wilkening, P. Heitjans, *Solid State Ion.* **2007**, *178*, 759–768.
- [126] W. Bensch, J. Opey, H. Hain, H. Gesswein, D. Chen, R. Mönig, P. A. Gruber, S. Indris, *Phys. Chem. Chem. Phys.* **2012**, *14*, 7509–7516.
- [127] W. Bensch, T. Bredow, H. Ebert, P. Heitjans, S. Indris, S. Mankovsky, M. Wilkening, *Prog. Solid State Chem.* **2009**, *37*, 206–225.
- [128] M. Behrens, O. Riemenschneider, W. Bensch, S. Indris, M. Wilkening, P. Heitjans, *Chem. Mater.* **2006**, *18*, 1569–1576.
- [129] M. Behrens, J. Wontcheu, R. Kiebach, W. Bensch, *Chem. - Eur. J.* **2008**, *14*, 5021–5029.
- [130] M. Behrens, R. Kiebach, J. Opey, O. Riemenschneider, W. Bensch, *Chem. - Eur. J.* **2006**, *12*, 6348–6355.
- [131] Y. Terada, K. Yasaka, F. Nishikawa, T. Konishi, M. Yoshio, I. Nakai, *J. Solid State Chem.* **2001**, *156*, 286–291.
- [132] J. B. Leriche, S. Hamelet, J. Shu, M. Morcrette, C. Masquelier, G. Ouvrard, M. Zerrouki, P. Soudan, S. Belin, E. Elkaïm, et al., *J. Electrochem. Soc.* **2010**, *157*, A606–A610.
- [133] J. Nelson, S. Misra, Y. Yang, A. Jackson, Y. Liu, H. Wang, H. Dai, J. C. Andrews, Y. Cui, M. F. Toney, *J. Am. Chem. Soc.* **2012**, *134*, 6337–6343.
- [134] X. Liu, D. Wang, G. Liu, V. Srinivasan, Z. Liu, Z. Hussain, W. Yang, *Nat. Commun.* **2013**, *4*, 2568–2576.
- [135] C. Marino, B. Fraisse, M. Womes, C. Villevieille, L. Monconduit, L. Stievano, *J. Phys. Chem. C* **2014**, *118*, 27772–27780.
- [136] U. Boesenberg, M. A. Marcus, A. K. Shukla, T. Yi, E. McDermott, P. F. Teh, M. Srinivasan, A. Moewes, J. Cabana, *Sci. Rep.* **2014**, *4*, 7133–7142.
- [137] M. M. Thackeray, W. I. F. David, J. B. Goodenough, *Mater. Res. Bull.* **1982**, *17*, 785–793.
- [138] C. J. Chen, M. Greenblatt, J. V. Waszczak, *Mater. Res. Bull.* **1986**, *21*, 609–619.
- [139] D. Larcher, G. Sudant, J.-B. Leriche, Y. Chabre, J.-M. Tarascon, *J. Electrochem. Soc.* **2002**, *149*, A234–A241.
- [140] D. Bresser, E. Paillard, R. Kloepsch, S. Krueger, M. Fiedler, R. Schmitz, D. Baither, M. Winter, S. Passerini, *Adv. Energy Mater.* **2013**, *3*, 513–523.
- [141] P. Barpanda, G. Liu, C. D. Ling, M. Tamaru, M. Avdeev, S.-C. Chung, Y. Yamada, A. Yamada, *Chem. Mater.* **2013**, *25*, 3480–3487.



## References

- [142] M. Xu, L. Wang, X. Zhao, J. Song, H. Xie, Y. Lu, J. B. Goodenough, *Phys. Chem. Chem. Phys.* **2013**, *15*, 13032–13037.
- [143] D. Su, C. Wang, H. Ahn, G. Wang, *Chem. - Eur. J.* **2013**, *19*, 10884–10889.
- [144] Z. Liu, Y.-Y. Hu, M. T. Dunstan, H. Huo, X. Hao, H. Zou, G. Zhong, Y. Yang, C. P. Grey, *Chem. Mater.* **2014**, *26*, 2513–2521.
- [145] X. Liu, X. Wang, A. Iyo, H. Yu, D. Li, H. Zhou, *J. Mater. Chem. A* **2014**, *2*, 14822–14826.
- [146] J. Song, M. Xu, L. Wang, J. B. Goodenough, *Chem. Commun.* **2013**, *49*, 5280–5282.
- [147] P. Ge, *Solid State Ion.* **1988**, *28-30*, 1172–1175.
- [148] D. A. Stevens, J. R. Dahn, *J. Electrochem. Soc.* **2001**, *148*, A803–A811.
- [149] B. Jache, P. Adelhelm, *Angew. Chem. Int. Ed.* **2014**, *53*, 10169–10173.
- [150] Y. Wen, K. He, Y. Zhu, F. Han, Y. Xu, I. Matsuda, Y. Ishii, J. Cumings, C. Wang, *Nat. Commun.* **2014**, *5*, 4033–4043.
- [151] Y. Kim, K.-H. Ha, S. M. Oh, K. T. Lee, *Chem. - Eur. J.* **2014**, *20*, 11980–11992.
- [152] Z. Hu, Z. Zhu, F. Cheng, K. Zhang, J. Wang, C. Chen, J. Chen, *Energy Env. Sci* **2015**, *8*, 1309–1316.
- [153] Y. Zhu, L. Suo, T. Gao, X. Fan, F. Han, C. Wang, *Electrochem. Commun.* **2015**, *54*, 18–22.
- [154] A. Douglas, R. Carter, L. Oakes, K. Share, A. P. Cohn, C. L. Pint, *ACS Nano* **2015**, *9*, 11156–11165.
- [155] T. Marks, S. Trussler, A. J. Smith, D. Xiong, J. R. Dahn, *J. Electrochem. Soc.* **2011**, *158*, A51–A57.
- [156] M. Newville, *Rev. Mineral. Geochem.* **2014**, *78*, 33–74.
- [157] J. Als-Nielsen, D. McMorrow, *Elements of Modern X-Ray Physics*, Wiley, Hoboken, **2011**.
- [158] D. C. Koningsberger, R. Prins, Eds. , *X-Ray Absorption: Principles, Applications, Techniques of EXAFS, SEXAFS, and XANES*, Wiley, New York, **1988**.
- [159] B. Ravel, M. Newville, *J. Synchrotron Radiat.* **2005**, *12*, 537–541.
- [160] H. M. Rietveld, *J. Appl. Crystallogr.* **1969**, *2*, 65–71.
- [161] P. Scherrer, in *Kolloidchem. Ein Lehrb.*, Springer Berlin Heidelberg, Berlin, Heidelberg, **1912**, pp. 387–409.
- [162] G. . Williamson, W. . Hall, *Acta Metall.* **1953**, *1*, 22–31.
- [163] T. H. de Keijser, J. I. Langford, E. J. Mittemeijer, A. B. P. Vogels, *J. Appl. Crystallogr.* **1982**, *15*, 308–314.
- [164] M. Leoni, R. Maggio, S. Polizzi, P. Scardi, *J. Am. Ceram. Soc.* **2004**, *87*, 1133–1140.
- [165] P. Scardi, M. Leoni, *Acta Crystallogr. A* **2001**, *57*, 604–613.
- [166] W. I. F. David, M. Leoni, P. Scardi, *Mater. Sci. Forum* **2010**, *651*, 187–200.
- [167] A. A. Coelho, *TOPAS-Academic V5*, Coelho Software, **2012**.
- [168] J. S. O. Evans, *Mater. Sci. Forum* **2010**, *651*, 1–9.
- [169] J. Lande, *The Area Diffraction Machine*, **2008**.
- [170] P. W. Hawkes, Ed. , *The Beginnings of Electron Microscopy*, Academic Press, Orlando, **1985**.
- [171] D. D. Laws, H.-M. L. Bitter, A. Jerschow, *Angew. Chem. Int. Ed.* **2002**, *41*, 3096–3129.
- [172] I. J. Lowe, *Phys. Rev. Lett.* **1959**, *2*, 285–287.
- [173] E. R. Andrew, A. Bradbury, R. G. Eades, *Nature* **1958**, *182*, 1659–1659.
- [174] T. Zhang, H. Cao, J. Peng, Q. Xiao, Z. Li, G. Lei, *Funct. Mater. Lett.* **2011**, *04*, 327–331.

## References

- [175] R. Alcántara, M. Jaraba, P. Lavela, J. . Tirado, J. . Jumas, J. Olivier-Fourcade, *Electrochem. Commun.* **2003**, *5*, 16–21.
- [176] X. D. Li, W. S. Yang, F. Li, D. G. Evans, X. Duan, *J. Phys. Chem. Solids* **2006**, *67*, 1286–1290.
- [177] C. Vidal-Abarca, P. Lavela, J. L. Tirado, *J. Phys. Chem. C* **2010**, *114*, 12828–12832.
- [178] P. G. Bruce, B. Scrosati, J.-M. Tarascon, *Angew. Chem. Int. Ed.* **2008**, *47*, 2930–2946.
- [179] L. Luo, R. Cui, K. Liu, H. Qiao, Q. Wei, *Ionics* **2015**, *21*, 687–694.
- [180] C. T. Cherian, J. Sundaramurthy, M. V. Reddy, P. Suresh Kumar, K. Mani, D. Pliszka, C. H. Sow, S. Ramakrishna, B. V. R. Chowdari, *ACS Appl. Mater. Interfaces* **2013**, *5*, 9957–9963.
- [181] Y. Ding, Y. Yang, H. Shao, *J. Power Sources* **2013**, *244*, 610–613.
- [182] E. K. Heidari, B. Zhang, M. H. Sohi, A. Ataie, J.-K. Kim, *J. Mater. Chem. A* **2014**, *2*, 8314–8322.
- [183] Z. Zhang, Y. Wang, M. Zhang, Q. Tan, X. Lv, Z. Zhong, F. Su, *J. Mater. Chem. A* **2013**, *1*, 7444–7450.
- [184] Y. He, L. Huang, J.-S. Cai, X.-M. Zheng, S.-G. Sun, *Electrochimica Acta* **2010**, *55*, 1140–1144.
- [185] Y. Wang, J. Park, B. Sun, H. Ahn, G. Wang, *Chem. - Asian J.* **2012**, *7*, 1940–1946.
- [186] Z. Wang, D. Luan, S. Madhavi, Y. Hu, X. W. (David) Lou, *Energy Env. Sci* **2012**, *5*, 5252–5256.
- [187] S.-F. Zheng, J.-S. Hu, L.-S. Zhong, W.-G. Song, L.-J. Wan, Y.-G. Guo, *Chem. Mater.* **2008**, *20*, 3617–3622.
- [188] F. D. Wu, Y. Wang, *J. Mater. Chem.* **2011**, *21*, 6636–6641.
- [189] G. Balachandran, D. Dixon, N. Bramnik, A. Bhaskar, M. Yavuz, L. Pfaffmann, F. Scheiba, S. Mangold, H. Ehrenberg, *ChemElectroChem* **2015**, *2*, 1510–1518.
- [190] I. H. Gul, E. Pervaiz, *Mater. Res. Bull.* **2012**, *47*, 1353–1361.
- [191] V. Datsyuk, M. Kalyva, K. Papagelis, J. Parthenios, D. Tasis, A. Siokou, I. Kallitsis, C. Galiotis, *Carbon* **2008**, *46*, 833–840.
- [192] C. Gao, Y. Z. Jin, H. Kong, R. L. D. Whitby, S. F. A. Acquah, G. Y. Chen, H. Qian, A. Hartschuh, S. R. P. Silva, S. Henley, et al., *J. Phys. Chem. B* **2005**, *109*, 11925–11932.
- [193] S. Osswald, M. Havel, Y. Gogotsi, *J. Raman Spectrosc.* **2007**, *38*, 728–736.
- [194] F. Wen, F. Zhang, Z. Liu, *J. Phys. Chem. C* **2011**, *115*, 14025–14030.
- [195] A. Ahlawat, V. G. Sathe, V. R. Reddy, A. Gupta, *J. Magn. Magn. Mater.* **2011**, *323*, 2049–2054.
- [196] Z. Z. Lazarevic, C. Jovalekic, D. Sekulic, M. Slankamenac, M. Romcevic, A. Milutinovic, N. Z. Romcevic, *Sci. Sinter.* **2012**, *44*, 331–339.
- [197] V. G. Ivanov, M. V. Abrashev, M. N. Iliev, M. M. Gospodinov, J. Meen, M. I. Aroyo, *Phys. Rev. B* **2010**, *82*, 24104–24108.
- [198] K. Xu, *Chem. Rev.* **2014**, *114*, 11503–11618.
- [199] E. Bekaert, P. Balaya, S. Murugavel, J. Maier, M. Ménétrier, *Chem. Mater.* **2009**, *21*, 856–861.
- [200] L. Gireaud, S. Grugeon, S. Pilard, P. Guenot, J.-M. Tarascon, S. Laruelle, *Anal. Chem.* **2006**, *78*, 3688–3698.
- [201] A. Ponrouch, P.-L. Taberna, P. Simon, M. R. Palacín, *Electrochimica Acta* **2012**, *61*, 13–18.

## References

- [202] S. Laruelle, S. Grugeon, P. Poizot, M. Dollé, L. Dupont, J.-M. Tarascon, *J. Electrochem. Soc.* **2002**, *149*, A627–A634.
- [203] S. Permien, H. Hain, M. Scheuermann, S. Mangold, V. Mereacre, A. K. Powell, S. Indris, U. Schürmann, L. Kienle, V. Duppel, et al., *RSC Adv.* **2013**, *3*, 23001–23015.
- [204] S. Permien, S. Indris, M. Scheuermann, U. Schürmann, V. Mereacre, A. K. Powell, L. Kienle, W. Bensch, *J Mater Chem A* **2015**, *3*, 1549–1561.
- [205] S. Permien, S. Indris, U. Schürmann, L. Kienle, S. Zander, S. Doyle, W. Bensch, *Chem. Mater.* **2016**, *28*, 434–444.
- [206] F. H. Aragón, P. E. N. de Souza, J. A. H. Coaquira, P. Hidalgo, D. Gouvêa, *Phys. B Condens. Matter* **2012**, *407*, 2601–2605.
- [207] O. Crisan, A. D. Crisan, *J. Alloys Compd.* **2011**, *509*, 6522–6527.
- [208] P. Schmidt, *Eur. J. Inorg. Chem.* **2008**, *2008*, 2847–2855.
- [209] C. Nordhei, A. L. Ramstad, D. G. Nicholson, *Phys Chem Chem Phys* **2008**, *10*, 1053–1066.
- [210] D. Carta, D. Loche, G. Mountjoy, G. Navarra, A. Corrias, *J. Phys. Chem. C* **2008**, *112*, 15623–15630.
- [211] S. Chkoundali, S. Ammar, N. Jouini, F. Fiévet, P. Molinié, M. Danot, F. Villain, J.-M. Grenèche, *J. Phys. Condens. Matter* **2004**, *16*, 4357–4372.
- [212] G. Jain, M. Balasubramanian, J. J. Xu, *Chem. Mater.* **2006**, *18*, 423–434.
- [213] W. Kang, Y. Tang, W. Li, X. Yang, H. Xue, Q. Yang, C.-S. Lee, *Nanoscale* **2015**, *7*, 225–231.
- [214] Y.-N. NuLi, Q.-Z. Qin, *J. Power Sources* **2005**, *142*, 292–297.
- [215] Y. Ma, C.-W. Tai, R. Younesi, T. Gustafsson, J. Y. Lee, K. Edström, *Chem. Mater.* **2015**, *27*, 7698–7709.
- [216] H. Zhao, L. Liu, Z. Hu, L. Sun, S. Han, Y. Liu, D. Chen, X. Liu, *Mater. Res. Bull.* **2016**, *77*, 265–270.
- [217] P. Lavela, N. A. Kyeremateng, J. L. Tirado, *Mater. Chem. Phys.* **2010**, *124*, 102–108.
- [218] A. Sagua, G. M. Lescano, J. A. Alonso, R. Martínez-Coronado, M. T. Fernández-Díaz, E. Morán, *Mater. Res. Bull.* **2012**, *47*, 1335–1338.
- [219] O. Bodak, L. Akselrud, P. Demchenko, B. Kotur, O. Mrooz, I. Hadzaman, O. Shpotyuk, F. Aldinger, H. Seifert, S. Volkov, et al., *J. Alloys Compd.* **2002**, *347*, 14–23.
- [220] I. Khosravi, M. Yazdanbakhsh, E. K. Goharshadi, A. Youssefi, *Mater. Chem. Phys.* **2011**, *130*, 1156–1161.
- [221] P. Barpanda, S. K. Behera, P. K. Gupta, S. K. Pratihari, S. Bhattacharya, *J. Eur. Ceram. Soc.* **2006**, *26*, 2603–2609.
- [222] M. Ishimaru, I. V. Afanasyev-Charkin, K. E. Sickafus, *Appl. Phys. Lett.* **2000**, *76*, 2556–2558.
- [223] K. E. Sickafus, *J. Nucl. Mater.* **2003**, *312*, 111–123.
- [224] A. Feltz, W. Pölzl, *J. Eur. Ceram. Soc.* **2000**, *20*, 2353–2366.
- [225] P. Aitchison, B. Ammundsen, D. J. Jones, G. Burns, J. Rozière, *J. Mater. Chem.* **1999**, *9*, 3125–3130.
- [226] D. Carta, M. F. Casula, A. Falqui, D. Loche, G. Mountjoy, C. Sangregorio, A. Corrias, *J. Phys. Chem. C* **2009**, *113*, 8606–8615.
- [227] S. Ammar, A. Helfen, N. Jouini, F. Fiévet, I. Rosenman, F. Villain, P. Molinié, M. Danot, *J. Mater. Chem.* **2001**, *11*, 186–192.
- [228] A. Feltz, J. Töpfer, B. Neidnicht, *Z. Für Anorg. Allg. Chem.* **1993**, *619*, 39–46.
- [229] K. Zhong, B. Zhang, S. Luo, W. Wen, H. Li, X. Huang, L. Chen, *J. Power Sources* **2011**, *196*, 6802–6808.

## References

- [230] A. V. Chadwick, S. L. P. Savin, S. Fiddy, R. Alcántara, D. Fernández Lisbona, P. Lavela, G. F. Ortiz, J. L. Tirado, *J. Phys. Chem. C* **2007**, *111*, 4636–4642.
- [231] C. P. Grey, N. Dupré, *Chem. Rev.* **2004**, *104*, 4493–4512.
- [232] M. J. Radler, J. B. Cohen, G. P. Sykora, T. Mason, D. E. Ellis, J. Faber, *J. Phys. Chem. Solids* **1992**, *53*, 141–154.
- [233] F. Klein, B. Jache, A. Bhide, P. Adelhelm, *Phys. Chem. Chem. Phys.* **2013**, *15*, 15876–15887.
- [234] D. Y. W. Yu, P. V. Prikhodchenko, C. W. Mason, S. K. Batabyal, J. Gun, S. Sladkevich, A. G. Medvedev, O. Lev, *Nat. Commun.* **2013**, *4*, 2922–2929.
- [235] C. Zhu, X. Mu, P. A. van Aken, Y. Yu, J. Maier, *Angew. Chem. Int. Ed.* **2014**, *53*, 2152–2156.
- [236] J.-S. Kim, G.-B. Cho, K.-W. Kim, J.-H. Ahn, G. Wang, H.-J. Ahn, *Curr. Appl. Phys.* **2011**, *11*, S215–S218.
- [237] Z. J. Zhang, X. Y. Chen, *J. Alloys Compd.* **2009**, *488*, 339–345.
- [238] R. Flaig-Baumann, G. H. Moh, B. Nuber, *Naturwissenschaften* **1970**, *57*, 192–193.
- [239] I. S. Lyubutin, C. R. Lin, Y. V. Korzhetskiy, T. V. Dmitrieva, R. K. Chiang, *J. Appl. Phys.* **2009**, *106*, 034311–034317.
- [240] L. Chang, A. P. Roberts, Y. Tang, B. D. Rainford, A. R. Muxworthy, Q. Chen, *J. Geophys. Res.* **2008**, *113*, 6104–6120.
- [241] R. E. Vandenberghe, E. de Grave, P. M. A. de Bakker, M. Krs, J. J. Hus, *Hyperfine Interact.* **1992**, *68*, 319–322.
- [242] I. S. Lyubutin, S. S. Starchikov, C.-R. Lin, S.-Z. Lu, M. O. Shaikh, K. O. Funtov, T. V. Dmitrieva, S. G. Ovchinnikov, I. S. Edelman, R. Ivantsov, *J. Nanoparticle Res.* **2013**, *15*, 1397–1410.
- [243] L. Wu, D. Bresser, D. Buchholz, S. Passerini, *J. Electrochem. Soc.* **2015**, *162*, A3052–A3058.
- [244] D. Bresser, B. Oschmann, M. N. Tahir, F. Mueller, I. Lieberwirth, W. Tremel, R. Zentel, S. Passerini, *J. Electrochem. Soc.* **2014**, *162*, A3013–A3020.
- [245] Y. Liu, Z. Cheng, H. Sun, H. Arandiyani, J. Li, M. Ahmad, *J. Power Sources* **2015**, *273*, 878–884.
- [246] M. Krengel, P. Adelhelm, F. Klein, W. Bensch, *Chem Commun* **2015**, *51*, 13500–13503.
- [247] Y. Cao, L. Xiao, M. L. Sushko, W. Wang, B. Schwenzer, J. Xiao, Z. Nie, L. V. Saraf, Z. Yang, J. Liu, *Nano Lett.* **2012**, *12*, 3783–3787.
- [248] L. David, R. Bhandavat, G. Singh, *ACS Nano* **2014**, *8*, 1759–1770.
- [249] M. K. Datta, R. Epur, P. Saha, K. Kadakia, S. K. Park, P. N. Kumta, *J. Power Sources* **2013**, *225*, 316–322.
- [250] J. Wang, C. Luo, T. Gao, A. Langrock, A. C. Mignerey, C. Wang, *Small* **2015**, *11*, 473–481.
- [251] J. Zheng, Y. Cao, C. Cheng, C. Chen, R.-W. Yan, H.-X. Huai, Q.-F. Dong, M.-S. Zheng, C.-C. Wang, *J Mater Chem A* **2014**, *2*, 19882–19888.
- [252] W. Xu, K. Zhao, L. Zhang, Z. Xie, Z. Cai, Y. Wang, *J. Alloys Compd.* **2016**, *654*, 357–362.
- [253] H. Stanjek, J. Schneider, *Am. Mineral.* **2000**, *85*, 839–846.
- [254] M. Wolthers, S. J. Van der Gaast, D. Rickard, *Am. Mineral.* **2003**, *88*, 2007–2015.
- [255] J. H. . Watson, B. A. Cressey, A. P. Roberts, D. C. Ellwood, J. M. Charnock, A. K. Soper, *J. Magn. Magn. Mater.* **2000**, *214*, 13–30.
- [256] A. Kitajou, J. Yamaguchi, S. Hara, S. Okada, *J. Power Sources* **2014**, *247*, 391–395.

## 7 Appendix

### 7.1 Reports for beamtime at synchrotron sources

User Reports 2013 · 7. Nano and Micro Technologies [NMT]

#### MFe<sub>2</sub>O<sub>4</sub> (M = Co, Mg, Mn, Ni, Zn) nanoparticles as anode materials in Li-ion batteries: An in-situ study of the reaction pathway

S. Permien<sup>1)</sup>, S. Indris<sup>2)</sup>, W. Bensch<sup>1)</sup>

<sup>1)</sup> University of Kiel, Institute of Inorganic Chemistry, Max-Eyth-Str. 2, D-24118 Kiel, Germany

<sup>2)</sup> Karlsruhe Institute of Technology, Hermann-von-Helmholtz-Platz 1, D-76344 Eggenstein-Leopoldshafen, Germany

##### Introduction

While hundreds of papers are published every year where new and better electrode materials for Li-based batteries are claimed, investigations of the reaction mechanisms during charge and discharge of such materials are scarce. A challenge for future applications of Li-batteries is the identification of materials which are composed of earth abundant, environmentally friendly and sustainable elements. Classically the batteries on the market work on the basis of Li intercalation and deintercalation reactions. During the last few years so-called “conversion” reactions are in focus of research.<sup>[1]</sup> Spinel with general formula MFe<sub>2</sub>O<sub>4</sub> (M = Co, Ni, Mn, and Zn) are promising candidates showing high capacity because of the complete reduction of M and Fe to the metallic state.<sup>[2]</sup> A promising anode material is CoFe<sub>2</sub>O<sub>4</sub> with high capacities of more than 1000 mAh/g.<sup>[3]</sup> Addition of carbon helps to stabilize capacity over many cycles.<sup>[4]</sup> But up to now the structural changes during Li insertion/deinsertion were not investigated in detail. The results of in-situ XRD studies (PDIFF beamline at ANKA) during Li insertion into nanosized CoFe<sub>2</sub>O<sub>4</sub> are presented as a representative for spinels of the type MFe<sub>2</sub>O<sub>4</sub>.

CoFe<sub>2</sub>O<sub>4</sub> nanoparticles were synthesized by mixing Co(NO<sub>3</sub>)<sub>2</sub>\*6H<sub>2</sub>O, Fe(NO<sub>3</sub>)<sub>3</sub>\*9H<sub>2</sub>O and citric acid in a ball mill for 2 h at 500 rpm. The viscous mixture was decomposed at 400 °C for 3 h.

##### Experimental

A custom built cell (40x40x15 mm) consisting of two aluminium plates with rectangular apertures (14x3 mm) in the centre and two sheets of Kapton foil windows glued on both sides was used. The active anode material was mixed with carbon (C65) and polyvinylidene fluoride as binder. The mixture was suspended in NMP (N-methylpyrrolidone), deposited on a thin Cu foil and dried. Li metal as counter electrode is attached on a Cu foil. A microporous polyethylene/polypropylene membrane was used as separator and 1 M LiPF<sub>6</sub> in an ethylene carbonate/dimethyl carbonate mixture is used as electrolyte. PDIFF Beamline was operated at 16 keV with a Princeton CCD detector. Powder patterns were collected within 5 min. Copper diffraction peaks were masked and 2D spectra were transformed with Area Diffraction machine.<sup>[5]</sup>

##### Results and Discussion

During insertion of the first 0.5 Li per formula unit all reflections shift to smaller 2θ angles (Fig. 1, left) and the *a*-axis of CoFe<sub>2</sub>O<sub>4</sub> increases linearly from 8.376 Å to 8.427 Å (Fig. 2, top right). The potential of the cell is dropping and a not well developed plateau at 1.5 V can be seen (Fig. 2, bottom right). Afterwards two phases can be identified and the spinel structure is successively transformed to a rock salt-like structure, which is accompanied by a significant intensity drop of the (311) peak of the spinel phase (17.4 °2θ). Simultaneously, the intensity of the (111) reflection of the new phase Co<sub>0.33</sub>Fe<sub>0.66</sub>O rises. After insertion of 2 Li per formula unit the reflections of the spinel phase cannot be detected anymore. Most likely Co on tetrahedral sites in the spinel moves to neighbouring empty octahedral sites, thus forming the NaCl-type structure. The *a*-axis lattice constant of the newly formed Co<sub>0.33</sub>Fe<sub>0.66</sub>O is 4.245 Å.



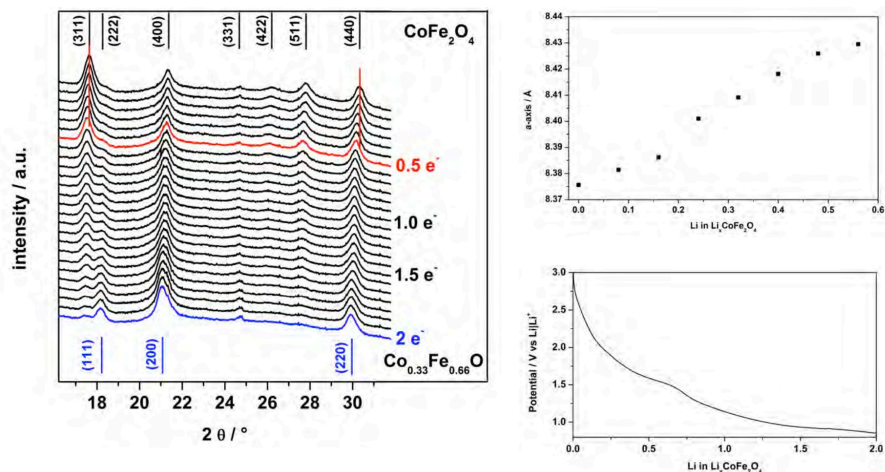


Fig. 1: *In-situ* XRD of  $\text{CoFe}_2\text{O}_4$  during Li uptake of 2 Li per formula unit (left), increase of the a-axis during insertion of the first 0.6 Li (top right) and change of the cell potential during Li uptake (bottom, right).

After insertion of 2 Li a long plateau at 0.8 V has been observed (Fig. 2, right). During insertion of the next 6 Li per formula unit, the intensity of the reflections decreases. Probably  $\text{Co}_{0.33}\text{Fe}_{0.66}\text{O}$  is transformed to metallic Fe, Co and  $\text{Li}_2\text{O}$  with particles being too small to be detected by XRD which was also reported for  $\text{MnFe}_2\text{O}_4$ .<sup>[2]</sup>

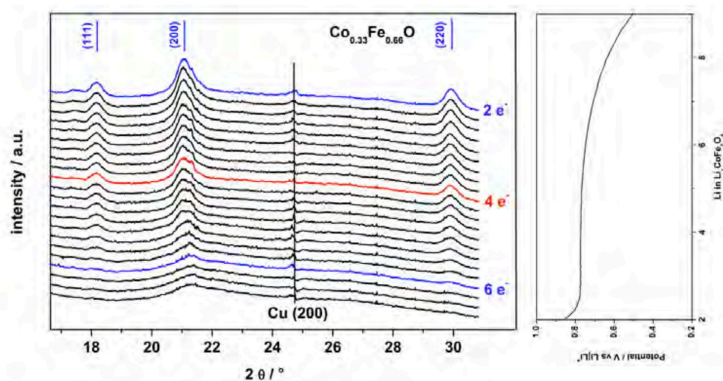


Fig. 2: *In-situ* XRD of  $\text{CoFe}_2\text{O}_4$  during Li uptake between 2 and 6.5 Li per formula unit (left) and change of the cell potential (right)

### Conclusion

It seems that Li insertion into  $\text{CoFe}_2\text{O}_4$  nanoparticles is first accompanied by an intercalation and at a distinct Li content a structural transformation to a mono-oxide with NaCl-type structure occurs ( $\text{Co}_{0.33}\text{Fe}_{0.66}\text{O}$ ) followed by full conversion to iron, cobalt and lithium oxide.

### Reference

- [1] J. Cabana, L. Monconduit, D. Larcher, M. Rosa Palacin, *Adv. Energy Mater.*, **2010**, 22, 170–192.
- [2] S. Permien, H. Hain, M. Scheuermann, S. Mangold, V. Mereacre, A. K. Powell, S. Indris, U. Schürmann, L. Kienle, V. Duppel, S. Harm and W. Bensch, *RSC Adv.*, **2013**, 3, 23001-23014.
- [3] P. Lavela, J.L. Tirado, *J. Power Sources.*, **2007**, 172, 379-387.
- [4] H. Xia, D. Zhu, Y. Fu, X. Wang, *Electrochim. Acta*, **2012**, 83, 166-174.
- [5] Area Diffraction Machine Version 2 Beta248, **2007**.

## In operando XAS studies on $\text{CoFe}_2\text{O}_4$ nanoparticles as anode materials in Li-ion batteries

Stefan Permien<sup>1)</sup>, Sylvio Indris<sup>2)</sup>, Wolfgang Bensch<sup>1)</sup>

<sup>1)</sup> University of Kiel, Institute of Inorganic Chemistry, Max-Eyth-Str. 2, D-24118 Kiel, Germany

<sup>2)</sup> Karlsruhe Institute of Technology, IAM-EES, Hermann-von-Helmholtz-Platz 1, D-76344 Eggenstein-Leopoldshafen, Germany

### Introduction

For batteries with higher capacity, faster charging and more power for portable consumer electronics or the next generation of electro-mobility vehicles several materials are identified, which can access more than one lithium per formula unit. The so-called “conversion” reactions are in focus of research in which redox reactions lead to a full conversion of the host materials providing capacities larger than 1200 mAh/g, being three times larger than for commercially used graphite. Spinel with general formula  $\text{MFe}_2\text{O}_4$  ( $\text{M} = \text{Co}, \text{Ni}, \text{Mn}, \text{and Zn}$ ) are promising candidates showing high capacity because of the complete reduction of M and Fe to the metallic state.<sup>[1]</sup> A promising anode material is  $\text{CoFe}_2\text{O}_4$  with high capacities of more than 1000 mAh/g<sup>[2]</sup>. Addition of carbon helps to stabilize capacity over many cycles.<sup>[3]</sup> During charge and discharge processes local structure and electronic state of elements change dramatically and are not intensively investigated yet. In operando XAS shed light on the mechanisms during Li insertion and Li removal, especially for partially converted and fully converted products which do not exhibit structural long-range order.

### Experimental

A custom built cell (40x40x15 mm) consisting of two aluminium plates with rectangular apertures (14x3 mm) in the centre and two sheets of Kapton foil windows glued on both sides was used. The active anode material was mixed with carbon (C65) and polyvinylidene fluoride as binder. The mixture was suspended in NMP (N-methylpyrrolidone), deposited on Cu foil and dried. Li metal as counter electrode is attached on a Cu foil deflector. A microporous polyethylene/polypropylene membrane was used as separator and 1 M  $\text{LiPF}_6$  in an ethylene carbonate/dimethyl carbonate mixture is used as electrolyte. X-ray absorption spectra were collected at KMC2 Beamline in transmission mode. Spectra were background subtracted, normalized and  $k^2$ -weighted with Athena software package.<sup>[4]</sup>

### Results and Discussion

Fig. 1 displays the change of the potential of the electrochemical cell during in operando XAS investigations. Discharge process was realized with  $I = 160 \mu\text{A}$  and is subdivided in two regions. Obviously the charge process is faster compared to the discharge process because the current was set to  $I = 220 \mu\text{A}$ . Also formation of SEI and irreversible reactions with the electrolyte lead to irreversible capacity loss during the first cycle.<sup>[1]</sup>

In **region I** the potential drops fast to 1.5 V and a not well resolved plateau is reached at about 1.1 V. At the beginning of discharge the Fe K-edge shifts significantly to lower energy and the pre-edge feature starts to disappear (Fig. 2, left), while the Co K-edge does not exhibit a pronounced shift (Fig. 2, right). At the end of **region I** all

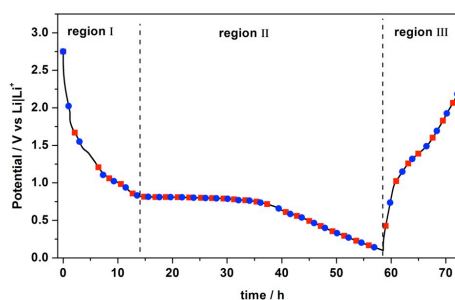


**Fig. 1: Cell potential (black line) during in operando investigation. Blue cycles mark XAS scans at the Co K-edge and red squares at the Fe K-edge.**

$\text{Fe}^{3+}$  ions are reduced to  $\text{Fe}^{2+}$ . This is associated with structural changes observed in FT-EXAFS data (Fig. 3). The Fe-O and Co-O distances increase slightly due to formation of a rock salt-like structure observed in the *in situ* XRD investigations.

During **region II**  $\text{Fe}^{2+}$  and  $\text{Co}^{2+}$  are reduced to the metallic state. This is clearly visible in FT-EXAFS data where the intensity of Co-O/Fe-O shell decrease and vanish, and formation of M-M shells develop which exhibit a pronounced intensity at the end of discharge process (Fig. 3).

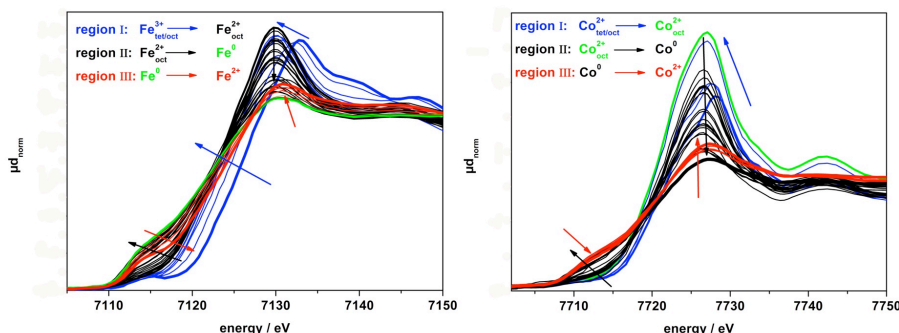


**Fig 2:** Scans at Fe k-edge (left) and Co k-edge (right) regions are marked in different colours and arrows should illustrated the shift.

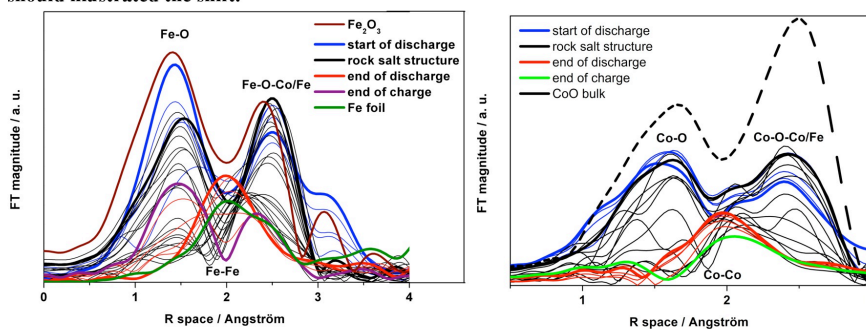


**Fig. 3:** FT-EXAFS data during first cycle for Fe (left) and Co (right).

**Region III** describes the charge process after reducing Co and Fe to the metallic state and formation of  $\text{Li}_2\text{O}$ . During charging the pre-edge region is shifting to higher energy and the maximum of the XANES region increases, i.e.  $\text{Fe}^{2+}$  and  $\text{Co}^{2+}$  are formed. This effect is more pronounced at the Fe K-edge. Formation of  $\text{Fe}^{3+}$  can be excluded. In FT-EXAFS data the intensity of Fe-Fe and Co-Co shells drops (Fig. 3) and the Fe-O shell returns.

### Conclusion

The results suggest that during Li insertion into  $\text{CoFe}_2\text{O}_4$  nanoparticles first  $\text{Fe}^{3+}$  is reduced to  $\text{Fe}^{2+}$  with a structural transformation to a structure where Fe-O and Co-O distances are slightly larger. Afterwards  $\text{Co}^{2+}$  and  $\text{Fe}^{2+}$  are simultaneously reduced to metallic Fe and Co nanoparticles. During charge process metallic Fe and Co are oxidised to  $\text{Fe}^{2+}$  and  $\text{Co}^{2+}$ .

### Reference

- [1] S. Permien, H. Hain, M. Scheuermann, S. Mangold, V. Mereacre, A. K. Powell, S. Indris, U. Schürmann, L. Kienle, V. Duppel, S. Harm, W. Bensch, *RSC Adv.*, **2013**, *3*, 23001-23014.
- [2] P. Lavela, J.L. Tirado, *J. Power Sources*, **2007**, *172*, 379-387.
- [3] H. Xia, D. Zhu, Y. Fu, X. Wang, *Electrochim. Acta*, **2012**, *83*, 166-174.
- [4] Athena Software package, Athena Version 0.8.056, **2008**.

## Appendix

Diamond User Office	SP10411	SCI-USO-DOC-0009.doc
Experimental Report		Issue: 4

<b>Principal Investigator</b>	Mr. Stefan Permien, Prof. Dr. Wolfgang Bensch, University of Kiel		
<b>Experiment Team</b>	Mr. Stefan Permien, University of Kiel Dr. Sylvio Indris, Karlsruhe Institute of Technology Mr. Diego Gianolio		
<b>Local contact</b>	Mr. Diego Gianolio		
<b>Date of Experiment</b>	Wed 25 Feb 2015	<b>Beamlines</b>	B18

**1 - Abstract** Please summarise the purpose of your experiment at Diamond for the **non-specialist** (100 - 200 words in Times New Roman, size 12, black)

Electric vehicles and large-scale applications (e.g. for storage of solar and wind energy) are in need of batteries with higher capacity, lighter weight and the ability to discharge/charge much faster. Especially high capacities are needed, and to solve this problem new materials like e.g. transition metal oxides are in focus of research. The specific capacity of these materials is three times higher than for commercially used graphite.<sup>[1]</sup> A laptop could operate for 18 h instead of just 6 h and an electric car could drive more than 1000 miles without the necessity to charge the battery.

For optimization a deep understanding of the changes during discharge and charge processes are very important to identify benefits and weaknesses of these new types of batteries. The excellent radiation of Diamond Light source enabled us monitoring changes during operation of the battery.

**2 - Experiment details** Please include any relevant details e.g. sample stage, detectors, white or monochromatic beam  
For *operando* XAS investigations of NiFe<sub>2</sub>O<sub>4</sub> custom built cells (40x40x7 mm) consisting of two aluminium plates with rectangular apertures (14x3 mm) in the centre and two sheets of Kapton foil windows glued on both sides were used. The active anode material was mixed with carbon and binder. The mixture was dispersed with NMP (N-methylpyrrolidone), deposited on Cu foil and dried. Li metal as counter electrode was attached on a Cu foil ring. A microporous polyethylene/polypropylene membrane was used as separator and 1 M LiPF<sub>6</sub> in an ethylene carbonate/dimethyl carbonate mixture (1:1) was used as electrolyte. Cells were discharged/charged with the Biologic VSP-300 potentiostat/galvanostat.

For investigation of NiFe<sub>2</sub>O<sub>4</sub> QEXFAS spectra at Fe and Ni K-edges were collected within 3 min (each) in transmission mode. Spectra were started 100 eV before and 900 eV after each K-edge. Afterwards XRD patterns were collected in 3 min using the Mythen 6K detector at 8940 eV in transmission. For data reliability two cells (with same material and same C-rate) were measured at the same time by moving the two cells with a xyz-stage.

**3 - Results** Please include actual data where possible.

Combination of X-ray diffraction (XRD) and X-ray absorption spectroscopy (XAS) yields a comprehensive picture about alterations of the long-range order, the chemical state and of the local environment of the absorbers. Due to oxygen and water sensitivity of Li, the electrolyte and Li containing samples it is very important to perform *operando* measurements. Ex situ experiments are difficult to realize because other phases or species can be formed during preparation of/ or transportation to the beamline. In the present study, NiFe<sub>2</sub>O<sub>4</sub> nanoparticles are connected with multiwall carbon nanotubes and were used as anode material.

In Fig. 1 the potential curve of the *in situ* cell during the first cycle is shown. The theoretical capacity for full conversion (8 Li = 915 mAh/g) is clearly exceeded after the first discharge, a typical observation for conversion reactions due to formation of a solid electrolyte interphase (SEI). In region I the potential drops very fast, followed by a long plateau at 0.8 V. During charge process a sloping plateau at 1.7 V is observed (region III).

## Appendix

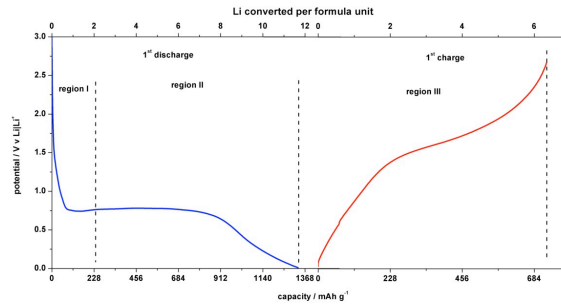


Fig. 1: Potential curve of the *in situ* cell.

During insertion of the first 2 Li,  $\text{Fe}^{3+}$  is reduced to  $\text{Fe}^{2+}$  indicated by the strong shift in XAS scans at the Fe K-edge (Fig. 2). Simultaneously a new phase (monoxide with NaCl-type structure) is formed evidenced by disappearance of reflections of the spinel and formation of new reflections in XRD scans. Insertion of more Li leads to reduction of the cations to the metallic state visible by rotation around an isosbestic point at 7124 eV for Fe and 8344 eV for Ni. At the end of discharge Ni and Fe metal nanoparticles are embedded in a  $\text{Li}_2\text{O}$  matrix. After the 1<sup>st</sup> charge process Fe and Ni return to their original oxidation states. In the XRD pattern no reflection can be observed, i.e. the material is either X-ray amorphous or nanoparticles are formed being too small to be detected. In earlier investigations we observed similar mechanisms for Li insertion into  $\text{MnFe}_2\text{O}_4$  and  $\text{MgFe}_2\text{O}_4$ .<sup>[1, 2]</sup>

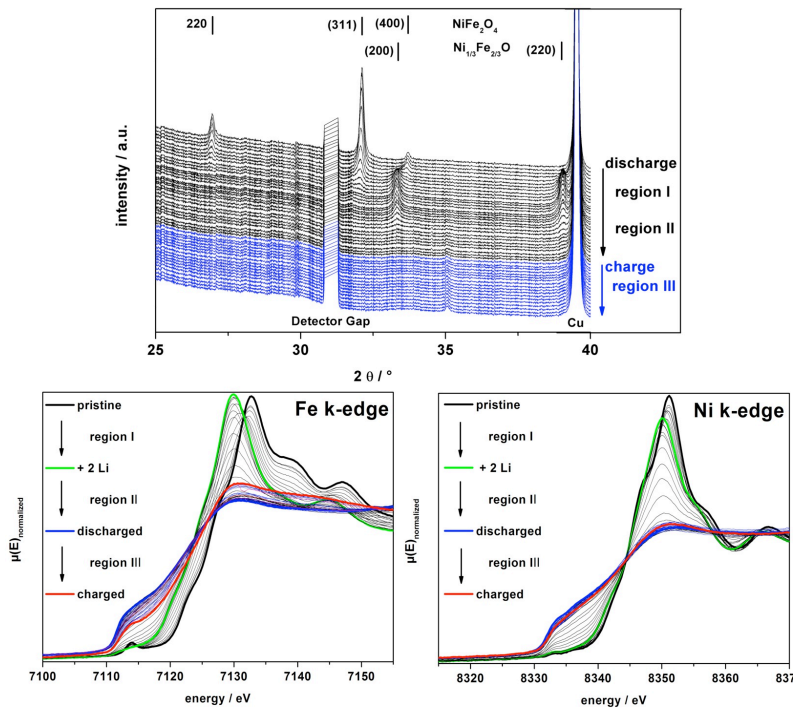


Fig. 2 Operando XRD pattern of the first cycle (top) and Operando XAS at Fe and Ni K-edges (bottom).



### 4 – Conclusion and future work

What will this enable you to do? Do you plan to apply for further beamtime at Diamond??

The excellent radiation coming from diamond light source enables very fast QEXAFS and XRD scans. Instrumentations at Beamline B18 give the possibility to measure XRD and XAS at the same time in just one cell and therefore high quality data can be collected yielding a detailed picture of the reaction mechanism. The first results presented here will be published in a high impact journal. In combination with TEM investigations we hope to formulate a general reaction mechanism and investigate the positive influence of carbon nanotubes in combination with oxide nanoparticles.

### 5 - Publications resulting from work

Please add any publications, submitted or published that have used data obtained from Diamond into the Diamond Publication database

<http://publications.diamond.ac.uk/>

You will need your fed id to enter the publication database

<http://publications.diamond.ac.uk/>

You will need your fed id to enter the publication database

### 6 - References

- [1] S. Permien, H. Hain, M. Scheuermann, S. Mangold, V. Mereacre, A. Powell, S. Indris, U. Schürmann, L. Kienle, V. Duppel, S. Harm, W. Bensch, „Electrochemical insertion of Li into nanocrystalline MnFe<sub>2</sub>O<sub>4</sub>: a study of the reaction mechanism“, *RSC Adv.*, **2013**, 3, 23001–23014.
- [2] S. Permien, S. Indris, M. Scheuermann, U. Schürmann, V. Mereacre, A. K. Powell, L. Kienle, W. Bensch, „Is there a universal reaction mechanism of Li insertion into oxidic spinels: a case study using MgFe<sub>2</sub>O<sub>4</sub>“, *J. Mater. A*, **2015**, 3, 1549-1561.

Note:

1. We understand that not all details of the analysis can be included in a report requested so soon after an experiment run but please be as complete as possible.
2. All reports are classed as confidential and will only be made available to Principal Beamline Scientists, the local contact, the Directors, the Peer Review Panel and the Communications team.
3. You may be contacted by our Communications team to obtain authorisation to publish details of your experiment on the external company website or in company literature.

### Which is the active phase during reversible Li uptake/release of $\text{CuFe}_2\text{O}_4$ at high potential? An *in situ* XRD study of the reaction

S. Permien<sup>1)</sup>, S. Indris<sup>2)</sup>, W. Bensch<sup>1)</sup>

<sup>1)</sup> University of Kiel, Institute of Inorganic Chemistry, Max-Eyth-Str. 2, D-24118 Kiel, Germany

<sup>2)</sup> Karlsruhe Institute of Technology, Hermann-von-Helmholtz-Platz 1, D-76344 Eggenstein-Leopoldshafen, Germany

#### Introduction

Commercial Lithium-Ion-Batteries (LIBs) are based on reversible Li intercalation/deintercalation reactions. But recently battery materials with higher capacities were identified operating on conversion reactions. During a conversion reaction, Li uptake is accompanied by transformation of the crystal structure of the pristine material to new phases. The involved transition metals are reduced to metallic nanoparticles and anions e.g. oxide reacts with Li to form  $\text{Li}_2\text{O}$ . Li intercalation into e.g. layered oxides is reasonable understood and reaction steps were described in detail. In contrast, the chemical and physical reaction pathways of conversion materials are not investigated in detail yet. A class of anode materials for LIBs based on conversion reactions are spinels with the general formula  $\text{MFe}_2\text{O}_4$  (M = Cu, Co, Ni, Mn, and Zn). These anode materials are promising candidates showing high capacities of more than 1000 mAh/g.<sup>[1,2]</sup> In recent studies on nanoparticles of  $\text{CoFe}_2\text{O}_4$  and  $\text{MnFe}_2\text{O}_4$  we identified three individual reaction steps during the first discharge process: i) the first ca. 0.5 Li per formula unit is inserted into an amorphous surface covering the nanoparticles; ii) further Li uptake reduces  $\text{M}^{\text{III}}$  to  $\text{M}^{\text{II}}$  being accompanied by movement of M ions located on tetrahedral sites to empty neighbouring octahedral sites resulting in formation of a NaCl-type phase; iii) for more than 2 Li per formula unit metallic nanoparticles are successively formed and embedded in a  $\text{Li}_2\text{O}$  matrix.<sup>[2,3]</sup> The present study focuses on the beginning of the discharge process: Nanosized  $\text{CuFe}_2\text{O}_4$  showed reversible capacities for cycling at high potentials between 1.6 and 3.0 V). *In situ* XRD studies at PDIFF beamline should answer the question whether Li uptake by crystalline  $\text{CuFe}_2\text{O}_4$  leads to structural changes and whether other “active” species are formed.  $\text{CuFe}_2\text{O}_4$  nanoparticles (Sigma-Aldrich) were mixed with 30 wt % graphite nanoparticles (ACS materials) in an agate mortar for 30 minutes.

#### Experimental

For *in situ* XRD a custom-built cell (40x40x15 mm) consisting of two aluminium plates with rectangular apertures (14x3 mm) in the centre and two sheets of Kapton foil windows glued on both sides was used. The active anode material was mixed with polyvinylidene fluoride (PVDF) as binder. The mixture was suspended in NMP (N-methylpyrrolidone), deposited on a thin Cu foil and dried. Li metal as counter electrode is attached on a Cu foil ring. A microporous polyethylene/polypropylene membrane was used as separator and 1 M  $\text{LiPF}_6$  in an ethylene carbonate/dimethyl carbonate mixture was used as electrolyte. The PDIFF Beamline was operated at 16 keV with a Princeton CCD detector. Powder patterns were collected within 60 seconds. 2D patterns were calibrated with  $\text{LaB}_6$  and transformed with Area Diffraction machine.<sup>[4]</sup>

#### Results and Discussion

In Fig. 1 (top) *in situ* XRD patterns from 16 to 18.5 °2 $\theta$  are displayed. The (311) reflection of the spinel is located at 17.3 °2 $\theta$  and the (222) at 17.7 °2 $\theta$ . In addition to the XRD patterns the change of the cell voltage of each scan range is shown (Fig. 1, bottom). During the first discharge, a quasi-plateau at 2.3 V could be observed while the intensity and position of both reflections is not altered. It seems that the first 0.5 Li per formula unit are inserted into the surface of the nanoparticles as it was observed for  $\text{CoFe}_2\text{O}_4$  in an earlier study.<sup>[3]</sup> Increasing the amount of Li

per formula up to 1 Li results in a sloping plateau from 2.1 to 1.6 V. The Li uptake is accompanied by a decrease of the intensity of the (311) and (222) reflections by about 20 %. Afterwards, the *in situ* cell is charged from 1.6 V to 3 V. Only about 0.4 Li are reversibly released. During the first charge, second discharge, and second charge process the intensity of both reflections stay constant.

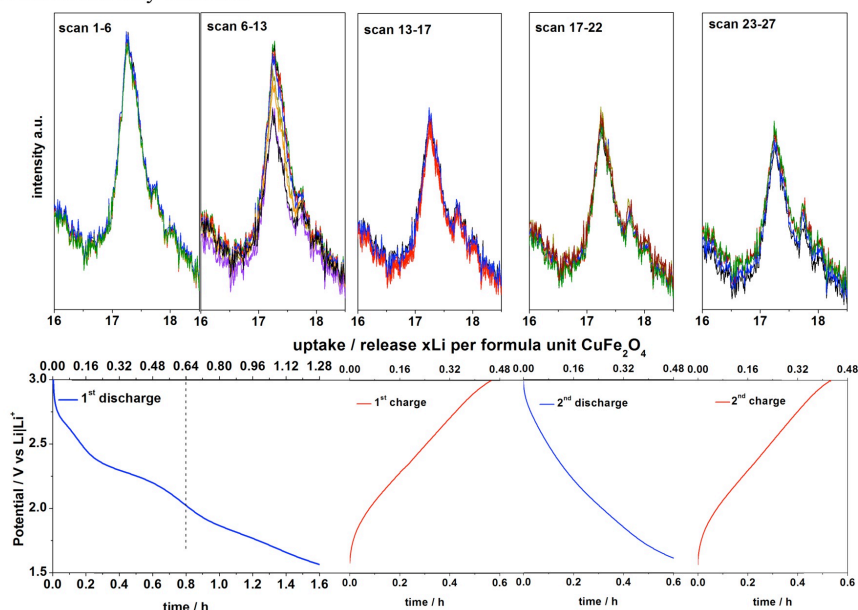


**Fig. 1:** *In situ* XRD of  $\text{CuFe}_2\text{O}_4$  during first and second cycle. Detailed view of the (311) and (222) reflections of  $\text{CuFe}_2\text{O}_4$  (top). Potential process during the first 2 cycles in a potential range from 3.0 to 1.55 V (bottom).

During first discharge a part of the spinel is transformed to an amorphous product and/or crystallites being too small to be detected via XRD. A shift of all spinel reflections as observed for the Li uptake into  $\text{CoFe}_2\text{O}_4$ <sup>[3]</sup> could not be observed for  $\text{CuFe}_2\text{O}_4$ , suggesting a different mechanism. Most probably, the Li uptake occurs in a surface layer of  $\text{CuFe}_2\text{O}_4$  nanoparticles without inducing stress/strain in the crystallites. Further Li uptake leads to an intensity drop of the reflections of the spinel. In the spinel structure Li ions could enter empty octahedral sites (16c) or empty tetrahedral sites (48f, 8b). Independent which site would be occupied by Li, the Li-Cu<sup>2+</sup>/Fe<sup>3+</sup> distance is below 2 Å leading to strong repulsive interactions. Reversible Li uptake and release can only be envisaged if Li occupies empty 16c site and the cation on the tetrahedral site simultaneously moves also to 16c. This scenario leads to formation of  $(\text{LiCu})_{16c}(\text{Fe}_2)_{16d}\text{O}_4$  with a NaCl-type structure. At the present stage of investigation we exclude this scenario because no new crystalline phase could be detected. During the 1<sup>st</sup> and 2<sup>nd</sup> charge and 2<sup>nd</sup> discharge no changes of the crystalline spinel phase could be observed. The constant intensity and position of the reflections indicates that the spinel phase is not the active part of the material during repeated cycling in high potential ranges from 1.6 to 3.0 V. The results suggest that an amorphous phase is the active material.

#### Reference

- [1] Z. Xing, Z. Ju, J. Yang, H. Xu, Y. Qian, *Electrochim. Acta*, **2013**, *102*, 51–57.
- [2] S. Permién, H. Hain, M. Scheuermann, S. Mangold, V. Mereacre, A. K. Powell, S. Indris, U. Schürmann, L. Kienle, V. Duppel, S. Harm and W. Bensch, *RSC Adv.*, **2013**, *3*, 23001-23014.
- [3] S. Permién, S. Indris, U. Schürmann, L. Kienle, S. Zander, S. Doyle, W. Bensch, *Chem. Mater.*, **2015**, *accepted*
- [4] Area Diffraction Machine Version 2 Beta248, **2007**.

### 7.2 Acknowledgements

Prof. Dr. Bensch is grateful acknowledged for four years of science, discussion, cooperation, publishing and the very good food & barbeque at our workgroup meetings.

I want to thank Dr. Sylvio Indris for the support during my research in Karlsruhe and the excellent work during long nights at synchrotron sources in Berlin and England.

Especially my colleges John, Felix, Markus, Björn, Svenja, David (Team Nano) and the whole work group are thankfully acknowledged. The state Schleswig Holstein is acknowledged for the financial support. All synchrotron institutions are thankful acknowledged for beam time allocation and beam time scientist are acknowledged for their great support.

I also want to say “thank you” to all Bachelor students: Diana Hennings, Tobias Neumann, Jonas van Dinter and Matthias Fesser. Additional all students making their advanced courses in the same field of research are thankful acknowledged. Additional Björn Richter is thankful acknowledged for helping me with some synthesis.

The most important supporter of my studies and work were my family. I want to thank my parents and my grandfather for the mental and financial support in the beginning of my study.

A very special thank goes to my girlfriend Annika Sellin enduring my bad mood and motivating & supporting me if things are not going the way I want. Also my son Leander is acknowledged. Smiling at his dad is enough motivation for many hours of hard work.

### 7.3 List of Publications

1) Stefan Permien, Holger Hain, Marco Scheuermann, Stefan Mangold, Valeriu Mereacre, Annie K. Powell, Sylvio Indris, Ulrich Schürmann, Lorenz Kienle, Viola Duppel, Svenja Harm, Wolfgang Bensch, *RSC Advances*, **2013**, 3, 23001-23014.

DOI:10.1039/c3ra44383c

2) Stefan Permien, Sylvio Indris, Marco Scheuermann, Ulrich Schürmann, Valeriu Mereacre, Annie K. Powell, Lorenz Kienle, Wolfgang Bensch, *Journal of Material Chemistry A*, **2015**, 3, 1549-1561.

DOI: 10.1039/c4ta05054a

3) Stefan Permien, Sylvio Indris, Ulrich Schürmann, Lorenz Kienle, Stefan Zander Stephen Doyle, Wolfgang Bensch, *Chemistry of Materials*, **2016**, 28, 434-444.

DOI: 10.1021/acs.chemmater.5b01754

4) Stefan Permien, Sylvio Indris, Anna-Lena Hansen, Marco Scheuermann, Dirk Zahn, Ulrich Schürmann, Gero Neubüser, Lorenz Kienle, Eugen Yegudin, Wolfgang Bensch, *ACS Applied Materials & Interfaces*, **2016**, 8, 15320-15332.

DOI: 10.1021/acsami.6b03185

5) Stefan Permien, Sylvio Indris, Gero Neubüser, Andy Fiedler, Lorenz Kienle, Stefan Zander, Stephen Doyle, Björn Richter, Wolfgang Bensch, *Chemistry – A European Journal*, **2016**, *submitted*.

#### Co-Authorship:

6) Nicole Pienack, Henning Lühmann, John Djamil, Stefan Permien, Christian Näther, Sebastian Haumann, Richard Weihrich, Wolfgang Bensch, *Chem. Eur. J.* **2015**, 21, 13637-13645. DOI: 10.1002/chem.201501796



### 7.4 Curriculum Vitae

Name: Stefan Alexander Permien  
Date of birth: 22.08.1985  
Place of birth: Hamburg

#### **Work experience**

May 2016 - now Senior Project Manager at Custom Cells Itzehoe  
2012 – May 2016 Christian-Albrechts-university Kiel, institute for inorganic Chemistry as an academic assistant  
2009 – 2015 CEO of a small-scale enterprise as an professional athlete including marketing and product development  
2005 – 2006 Civilian service at Lebenshilfe Schenefeld car pool and care

#### **Education**

2012 – August 2016 Christian-Albrechts-Universität zu Kiel, institute for inorganic Chemistry as an academic assistant  
2012 Diploma thesis at the institute for inorganic Chemistry (grade: 1.6)  
2006 – 2012 Course of studies at the Christian-Albrechts-university Kiel  
1996 – 2005 High School and college – university-entrance diploma (grade: 2.2)

#### **Special skills:**

Foreign language: English fluent writing and speaking  
Social Engagement: Coach and adviser at the Kids camp pro (2007-2013) – encouragement of young talents in kite surfing  
Sportive results: Four times German vice master in kite surfing (2007, 2008, 2009, 2013)  
3. Place European championships (2010)  
1. Place World championships Canada (2009)  
Two times German vice champion in snow kiting (2009 und 2012)  
Winner of the German kite-tour (2008)

### 7.5 Erklärung

Hiermit versichere ich, dass ich die vorliegende Arbeit selbständig an – abgesehen von der Beratung durch meinen wissenschaftlichen Lehrer – und nur unter Verwendung der angegebenen Hilfsmittel angefertigt habe.

Die Dissertation wird ausschließlich an dieser Stelle zur Promotion vorgelegt. Zusätzlich erkläre ich, dass ich bisher noch keinen Promotionsversuch, weder an dieser oder an einer anderen Hochschule unternommen habe. Die vorliegende Arbeit wurde unter Einhaltung der Regeln guter wissenschaftlicher Praxis der Deutschen Forschungsgemeinschaft erstellt.

I certify that I prepared this work on my own. I have only used the tools indicated in this work - apart from the advice of my scientific teacher.

The thesis is presented exclusively for the promotion at this institution. In addition, I declare that I do not have a promotion attempt either at this or at another university.

Kiel, July 2016

Stefan Permien